MONASH UNIVERSITY
THESIS ACCEPTED IN SATISFACTION OF THE
REQUIREMENTS FOR THE DEGREE OF
DOCTOR OF PHILOSOPHY
ON............. ..... 6 September 2002 ....

.... ▮▮▮▮▮▮▮▮▮▮ ......
Sec., Research Graduate School Committee

Errata

p 30, paragraph 4, line 3: change "form" to "from"
p 33, paragraph 2, line 8: change "Similar" to "Similarly"
p 42, paragraph 3, line 1: change "is" to "was"
p 59, paragraph 2, line 4: change "150°C" to "150°C/0.5h"
p 61, paragraph 3, line 9: change "Based" to "Based on"
p 62, paragraph 2, line 1: change "measure" to "measured"
p 98, paragraph 3, line 2: delete "that"
p 111, Table 5.2, change the units for erosion rate from "10^{-10} m^3 kg^{-1}" to "(m^3/kg)x10^{10}"
p 229, paragraph 1, line 4: change "is also found play" to "is also found to play"
p 234, last line, Should be "α-sialon ceramics","
p 239, first line, change "plastic impact." to "plastic impact,"
p 240, line 31, change "*mater*" to "*Mater*"
p 243, line 17, change "Si$_3$N$_4$-AlN-Al$_2$O$_3$." to "Si$_3$N$_4$-AlN-Al$_2$O$_3$,"
p 246, line 4, change "brittle materials" to "brittle materials,"
p 246, line 8, change "ceramics" to "ceramics,"

Addendum

p 48: Add at the end of the second sentence of paragraph 3: "The small load used here is due to the size of the erodent particles, ~400 μm in diameter."

p 61 paragraph 1: Comment: Commercial grade alumina, zirconia and silicon infiltrated silicon carbide materials were used here.

p 62: Add at the beginning of paragraph 2: "For the alumina materials,"

p 63 paragraph 3: Comment: The values of elastic modulus of the present materials were obtained from literature and suppliers.

p 89 paragraph 1: Comment: ↑ and ↓ represent increase and decrease in the content, respectively.

p 101: Add at the end of the second point: ", which impede the devitrification process."

P 108: Comment: The estimated error in this testing method is about 5%, which was stated in section 3.3.2.3 (p 53-54).

p 194 & 195 Figs 6.27 & 6.28: Comment: (a) Upon the solid particle impact, and (b) after impact.

p 228: Add at the end of the third point: "due to the increased severity of erosion."

p 244: delete lines 17 & 18.

Erosion Behaviour of Engineering Ceramics

A thesis submitted in fulfilment of the requirements
for the degree of Doctor of Philosophy

Yu Zhang

B.Sc.

M.Sc.

School of Physics and Materials Engineering

Monash University

Victoria, 3800

Australia

March 2002

To My Wife Josette,

Son Denzil and Daughter Elyzia

TABLE OF CONTENTS

CHAPTER 6 – EROSION BEHAVIOUR OF ENGINEERING CERAMICS

DECLARATION

This thesis contains no material which has been accepted previously for the award of any other degree or diploma in any university or other institution. To the best of my knowledge and belief, it contains no material published previously or written by any other person, except where due reference is made in the text.

Yu Zhang

March 2002

ACKNOWLEDGMENTS

SUMMARY

Although it has long been recognized that microstructure has a significant effect on the erosion performance of ceramic materials, the role of microstructure in the erosion process is not understood in detail. Most of the previous studies on the effect of microstructure on erosion response used alumina ceramics as the model material. However, alumina ceramics, in general, contain an equiaxed grain morphology and high residual stresses at the grain boundaries and are, therefore, not representative of other engineering ceramics, especially the self-reinforced ceramics. In addition, many of the previous studies were carried out on commercial materials in which there is little scope for independent control of microstructures. Thus in the current research, the role of microstructure in the erosion process has been studied using silicon nitride based sialon ceramics which offer great potential for microstructural tailoring.

Ca α-sialon ceramics with well-tailored microstructures were prepared for evaluating the role of microstructure on their erosion behaviour. The microstructural design of these materials was achieved by careful selection of the starting compositions and control of the processing conditions. It was found that compositions located inside the single-phase α-sialon forming region of the Ca α-sialon phase diagram produced a microstructure consisting of predominantly equiaxed grains coupled with a small amount of intergranular glass, while those outside the single-phase region on the Al rich side gave a microstructure containing elongated α-sialon grains, minor secondary phases and a relatively high glass content. Hot pressing gave a higher grain growth rate and density and also redistributed the intergranular glass. A longer dwell time at the sintering temperature resulted in a coarser grain size and larger unit cell dimensions of α-sialon and thus reduced the amount of intergranular glass, while a higher sintering temperature assigned a higher grain aspect ratio and a larger unit cell dimension of α-sialon.

The erosion behaviour of Ca α-sialon ceramics with tailored microstructures was investigated using silicon carbide and garnet erodents at various impact angles. It was

found that dense materials containing an optimum amount of intergranular glassy phase exhibited good erosion resistance. Fine-grained materials had better erosion resistance than the coarse-grained ones, while materials consisting of elongated interlocking grains were favored for erosion resistant applications compared to those consisting of an equiaxed grain morphology.

The understanding of the role of microstructure in erosion of sialon ceramics was extended to erosion of a variety of engineering ceramics, including alumina, partially stabilized zirconia, silicon nitride and silicon carbide. The erosion performance of these materials was directly compared. In the light of detailed SEM examinations of the eroded surfaces of all target materials, a qualitative model, based on fracture mechanics using the energy dissipation/energy balance approach, was proposed to account for the erosion behaviour of ceramic materials in general.

Alumina and alumina-based ceramics are the most commonly used materials in applications requiring wear and erosion resistance. Many of these applications involve erosion by abrasive particle-entrained slurries. Therefore dry and wet erosion behaviours of alumina ceramics were directly compared. It was found that under similar conditions, wet erosion was much more severe than dry erosion due to the deleterious effect of water on the crack propagation of alumina ceramics.

LIST OF PUBLICATIONS

Refereed Publications

1. Y. Zhang, Y.-B. Cheng, S. Lathabai, (2001) "Influence of microstructure on the erosive wear behaviour of Ca α-sialon materials", *Journal of the European Ceramic Society*, **21**, 2435-2445.

2. Y. Zhang, Y.-B. Cheng, S. Lathabai, (2001) "Erosion behaviour of advanced ceramics", *Journal of the Australasian Ceramic Society*, **37**(1), 39-44.

3. Y. Zhang, Y.-B. Cheng, S. Lathabai, (2000) "Erosion of alumina ceramics by air- and water-suspended garnet particles", *Wear*, **240**, 40-51.

4. Y. Zhang, Y.-B. Cheng, S. Lathabai, (1998) "The effects of impact angle on slurry erosion rates of alumina ceramics", *Journal of the Australasian Ceramic Society*, **34**(2), 146-151.

5. Y. Zhang, Y.-B. Cheng, "Grain boundary devitrification of Ca α-sialon ceramics", accepted for publication by *Journal of Materials Science*.

6. Y. Zhang, Y.-B. Cheng, "Densification, microstructure and mechanical properties of Ca α-sialon ceramics", submitted to *Journal of the European Ceramic Society*.

7. Y. Zhang, Y.-B. Cheng, S. Lathabai, "Effects of grain size and grain morphology on the erosion behaviour of Ca α-sialon ceramics", submitted to *Journal of the American Ceramic Society*.

8. Y. Zhang, Y.-B. Cheng, S. Lathabai, "A study on erosion response of highly anisotropic silicon nitride", submitted to *Journal of the American Ceramic Society*.

Conference Proceedings

Y. Zhang, Y.-B. Cheng, S. Lathabai, "The role of microstructure in erosion of engineering ceramics", Proceeding of the Conference on International Symposium on SiAlONS. Chiba, Japan, Dec. 2001. (accepted for publication in conference proceeding).

Conference Presentations

1. Y. Zhang, Y.-B. Cheng, S. Lathabai, "Erosion behaviour of advanced ceramics", presented at the International Ceramic Conference & Exhibition, Sydney, NSW., Australia, June 2000.

2. Y. Zhang, Y.-B. Cheng, S. Lathabai, "Solid particle erosion behaviour of ceramic materials", presented at the 102nd Annual Meeting of the American Ceramic Society, St. Louis, USA, May 2000.

3. Y. Zhang, Y.-B. Cheng, S. Lathabai, "Erosion of alumina ceramics and its implications", presented at the annual forum of the Institute of Materials Engineering Australasia Victorian Branch, Melbourne, Vic., Australia, August 1999.

4. Y. Zhang, Y.-B. Cheng, S. Lathabai, "The effects of impact angle on slurry erosion rates of alumina ceramics", presented at the International Ceramic Conference & Exhibition, Melbourne, Vic., Australia, September 1998.

Chapter 1

INTRODUCTION

When solid particles entrained in a fluid stream (gaseous or liquid) impinge on a surface, the target material loses volume due to the repeated impact of particles. This phenomenon is known as erosion. Erosion is one of the severe forms of material degradation generally classified as wear (Lathabai 1995).

Erosive wear has been a serious and continuing problem for many years in many industrial operations, including steam and jet turbines, pipelines and valves used in slurry transportation of matter, and fluidised bed combustion system (Kosel 1992; Finnie 1995). The earliest research on erosion was published in the early 19th century (Young 1807). Since then, many studies have been carried out on various practical erosion problems. However, little research has been done which investigates erosion mechanisms by which particles remove material. The pioneering investigation of this fundamental physical process of erosion started after the Second World War and erosion of ductile metals was the major interest. Finnie (1960) was the first to realize that the erosion mechanisms were different in ductile and brittle materials with plastic flow playing a major role in the former case and microfracture in the latter. After Finnie's work, there has been an extraordinary amount of work in the area of erosion in brittle materials, especially in the past two decades.

Ceramics possess various properties including high hardness, low density, high strength, high chemical stability and high temperature tolerance. These properties suggest the use of ceramics in wear resistant applications, especially where metallic and polymeric components have proved to be inadequate. A possible application is in Australian mining industries, where mineral processing usually involves turbulent flow of gases or liquids with entrained abrasive particles in the presence of corrosive environments and/or elevated temperature. Ceramics, in general, have complicated

1

microstructures and there exists a close association between the microstructures and the properties of ceramics. Even though there has been a great deal of work in the area of erosive wear behaviour of ceramics over the past years, there is not yet a common model which accounts for the effects of the complex microstructure on wear performance. In order to select the best material for a particular use and to develop better wear resistant ceramics, there is an urgent need to develop a better understanding of the influence of microstructure on the erosive wear mechanisms of these materials.

Compared to many other engineering ceramics, sialon ceramics have greater phase complexity and more degrees of freedom for tailoring of microstructures. This offers an ideal system for studying the role of microstructure on erosion of advanced ceramics. More importantly, α-sialon ceramics with an elongated microstructure belong to a promising group of toughened ceramics in which the *in-situ* developed whiskers reinforce the microstructure, activating toughening mechanisms that result in a significant improvement in crack resistance. The improved crack resistance coupled with the excellent hardness of α-sialon ceramics may suggest great potential for erosion resistant applications. However, there has been little research into the erosion behaviour of sialon materials. One possible reason is the lack of interest in using such a high cost material in erosion resistant applications. An approach to this problem is the fabrication of Ca α-sialon materials in which the stabilizing cation Ca can be easily subtracted from the low-cost $CaCO_3$. This has made Ca α-sialon ceramics significantly cheaper than the other α-sialons where the commonly used stabilizing cations are the rare-earth elements which can make up almost 50% of the total cost of the starting materials.

The major aims of this research are:

- To prepare a series of Ca α-sialon ceramics with well-tailored microstructures.

- To study the influence of microstructure on erosion behaviour of Ca α-sialon ceramics.

- To extend the knowledge gained from erosion studies of Ca α-sialon ceramics to other engineering ceramics.

- To develop a new model which accounts for the erosion behaviour of ceramic materials in general.

The following paragraphs outline the structure of this dissertation:

Chapter 2 reviews the relevant theory and previous research. It expands the above introduction by evaluating the current literature and draws together the information that exists in the areas of both fabrication of α-sialon ceramics and the effect of microstructure on the erosion behaviour of advanced ceramics.

Chapter 3 outlines the experimental procedures undertaken in the present study. It includes descriptions of materials and powder processing techniques, the fabrication methods used, the design and calibration of erosion test rigs, erosion testing procedures, and the characterization techniques used.

Chapter 4 reports the fabrication of Ca α-sialon ceramics with well-tailored microstructures. The effects of the starting compositions and processing conditions on the microstructure of these materials are evaluated. A discussion of the correlation between the microstructure and the mechanical properties of these materials is also included.

Chapter 5 details the results of erosion tests on the Ca α-sialon ceramics prepared in Chapter 4. It examines the effects of various aspects including impact angles, erodent particle properties and ceramic microstructures on erosion mechanisms of Ca α-sialon ceramics.

Chapter 6 extends the erosion tests to a number of engineering ceramics and studies the relationship between their microstructure and erosion performance. On the basis of this information a qualitative model, based on the energy dissipation analysis, is

developed which may account for the erosion behaviour of ceramic materials in general.

Chapter 7 presents a direct comparison of dry and wet erosion behaviors of alumina ceramics.

The final chapter summarizes the major achievements of the current research and offers recommendations for future work of this area.

Chapter 2

LITERATURE REVIEW

2.1 Introduction

The aim of the following review of the published literature is to establish the current understandings of the effect of microstructure on the erosion behaviour of ceramic materials. The field of the study can be divided into two main areas: the fabrication of Ca α-sialon ceramics with well-tailored microstructures and the effect of microstructure on the erosion behaviour of advanced ceramics, and hence, this review is written in two parts. Part I explores the origin, aspects of the fundamental properties and current research of sialon ceramics. Emphasis is placed on α-sialon ceramics, especially the tailoring of the microstructure of these materials. Because silicon nitride has close relationships with sialon materials, a brief discussion of the crystal structure of silicon nitride is also included. Part II reviews the theories of solid particle erosion of brittle materials and the studies which have verified the models on single crystals, glasses and advanced ceramics. The present understanding of the mechanisms of material removal in brittle materials is critically reviewed with an emphasis on the effect of microstructure on the erosion behaviour of advanced ceramics.

Part I – Sialon Ceramics

2.2 Background

Ceramic is a very broad term which can be defined as all nonmetallic, inorganic materials. However, when the scope of the definition is restricted to the high-performance engineering ceramics which exhibit excellent mechanical and chemical properties at high temperatures, the list of the ceramics is very limited and among

which silicon nitride based materials are one of the prime candidates (Jack 1976).

Silicon nitride (Si_3N_4) possesses many excellent properties. It is light, hard, strong, wear-resistant and stable at high temperatures. It also has low coefficients of friction and thermal expansion, and superb resistance to thermal shock, oxidation and corrosive environments (Lee and Rainforth 1994). However, it is very difficult to fabricate dense Si_3N_4 ceramic with these desirable properties. This is because the predominantly covalent nature of the atomic bonds in Si_3N_4 hinders atom migration and thus the temperature required to move the atoms is so high that it causes this material to decompose. Hence, sintering Si_3N_4 is extremely difficult as proved by the long and tortuous history of the development of Si_3N_4 as an engineering ceramic. The earliest report on synthetic Si_3N_4 was published in 1859 (Deville and Wöhler) and early patents for the mechanically strong Si_3N_4 as an engineering material took almost a century to appear (Carborundom Co. 1952, 1953 and 1954).

Densification of Si_3N_4 powder can be facilitated by adding 1-5 wt% metal oxide which reacts with the silica present on the surface of Si_3N_4 particles to form a low-melting-point silicate phase (Deeley et al. 1960). The covalent Si_3N_4 dissolves in this silicate liquid at fabrication temperatures and subsequently precipitates as Si_3N_4 grains. This sintering process is classified as liquid phase sintering and the liquid cools to give an amorphous grain boundary phase which is deleterious to the high temperature properties.

The solid solubility of Al_2O_3 in the Si_3N_4 lattice was discovered independently in Japan (Oyama and Kamigaito 1971; Oyama 1972) and in England (Jack and Wilson 1972). It was found that some of the Si-N bonds in Si_3N_4 could be replaced by Al-O bonds while the material still retained the crystal structure of Si_3N_4. This solid solution was denoted as Si-Al-O-N. One of the reasons for exploration of this system was to produce a material which combined the excellent properties of Si_3N_4 with the sinterability of Al_2O_3, and hence, to overcome the major disadvantage of liquid phase sintering of Si_3N_4, i.e. the residual grain boundary phase. Since then, sialon ceramics have been investigated in parallel with Si_3N_4 materials to establish the better understanding which is needed to obtain optimum processability and properties of

these materials, and there remains much work to be done in both classes of materials (Riley 2000).

2.3 Sialons and Their Properties

For engineering ceramic alloys involving solid solutions, a clear understanding of the crystal structure and the related phase fields of the various phases is necessary. Such knowledge enables: (1) the selection of effective sintering aids; (2) the selection of optimal sintering conditions; (3) the design of optimal compositions of the final products; and (4) the tailoring of microstructures of the fabricated materials with desirable mechanical properties for various applications (Weiss and Lukas 1989; Yen 1994). In the following sections, the crystal structures and the phase relationships of sialons will be discussed.

2.3.1 Crystal structures

2.3.1.1 Silicon nitride

In order to better understand the crystal structure of sialon ceramics, it is helpful to consider the structure of Si_3N_4 first. The unit block of Si_3N_4 is a SiN_4 tetrahedron, with the Si atom located in the centre with a hybridized state sp^3 configuration producing a tetrahedral arrangement of valence orbital electrons bonding covalently with four N atoms (Lee and Rainforth 1994). Each N atom (in trigonal) also coordinates with three Si atoms to link up three SiN_4 tetrahedra. Thus, the structure of Si_3N_4 can be considered to be a three-dimensional SiN_4 tetrahedron network. It is important to note that many properties of Si_3N_4, such as high strength, high hardness, high temperature resistance, as well as poor sinterability, are due to this strong Si-N covalent bond.

Traditionally, two crystallographic modifications of Si_3N_4 are known: α and β, both of an hexagonal structure (Turkdogan et al. 1958; Riley 2000). The two idealized hexagonal structures are close packed arrays which consist of layers of Si and N atoms in the sequence of ABCDABCD... for α-Si_3N_4 (Fig. 2.1(b)) or ABAB... for β-Si_3N_4 (Fig. 2.1(a)) along the c-axis. The AB layer is identical in both phases and the

CD layer in the α phase is related to the AB layer by a c-glide plane (Ekström and Nygren 1992). Hence the c dimension of α-Si_3N_4 is approximately twice that of β-Si_3N_4 (Fig. 2.2). The unit cell of α-Si_3N_4, ideally $Si_{12}N_{16}$, contains two large cavities which can accommodate cations and allow for substantial alloying. The unit cell of β-Si_3N_4, on the other hand, consists of Si_6N_8 and the SiN_4 tetrahedra are linked up to form a phenacite-like structure (Fig. 2.2(b)) which contains a long tunnel running parallel to the c-axis of the unit cell (Ekström and Nygren 1992). Thus β-Si_3N_4 allows only limited solubility of cations other than Al^{3+}. Some useful crystallographic data of Si_3N_4 polymorphs are summarized in Table 2.1 (Wild et al. 1972; Kato et al. 1975; Grun 1979; Lee and Rainforth 1994).
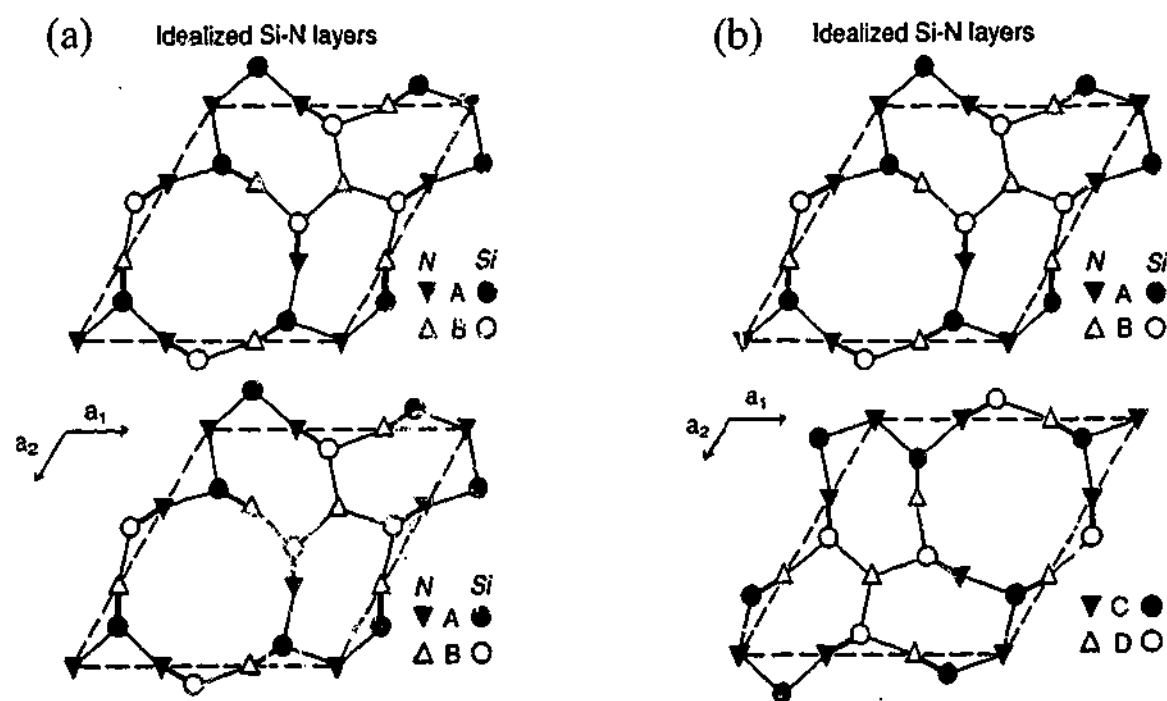
Fig. 2.1. (a) The AB layers in the β-Si_3N_4 crystal structure and (b) the AB and CD layers in the α-Si_3N_4 crystal structure (Hampshire 1993; Lee and Rainforth 1994).
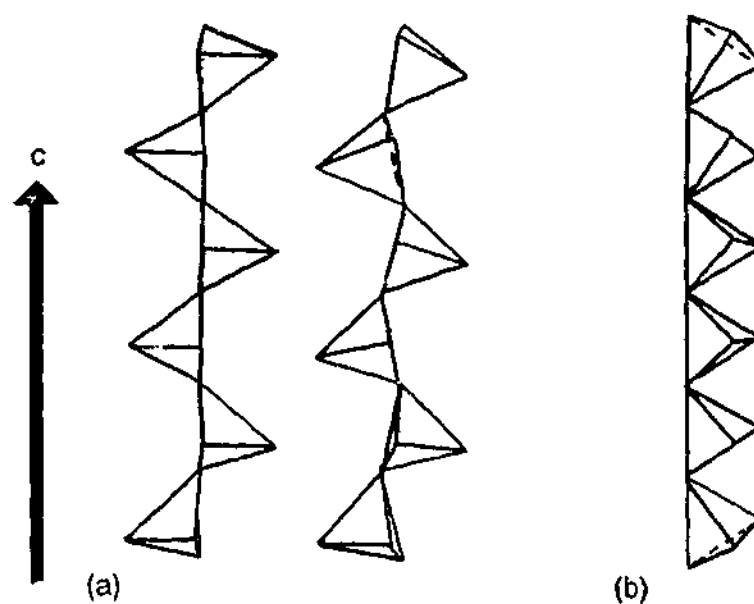
Fig. 2.2. (a) The two tetrahedra sequences of α-Si₃N₄ and (b) the one tetrahedron sequence of β-Si₃N₄ along the *c*-axis (Grun 1979; Lee and Rainforth 1994).

Table 2.1 Crystallographic data of Si_3N_4 and sialon polymorphs

Polymorphs	Space group	Crystallographic system	Unit cell dimensions (Å)	Theoretical density (g/cm³)
α-Si_3N_4	P3lc	Hexagonal	$a = 7.818$ $c = 5.591$	3.168
β-Si_3N_4	P6₃ or P6₃/m	Hexagonal	$a = 7.595$ $c = 2.902$	3.192
α-sialon	P3lc	Hexagonal	Composition dependent	Composition dependent
β-sialon	P6₃ or P6₃/m	Hexagonal	Composition dependent	Composition dependent

α-Si_3N_4, mainly observed when silicon is nitrided at 1150-1350°C, can be transformed to β-Si_3N_4, the more stable high-temperature form, in the presence of a M(Metal)-Si-O-N liquid at temperatures above 1400°C (Thompson 1989). Such a transformation is a reconstructive process which involves breaking and reforming strong Si-N bonds via the dissolution of α-Si_3N_4 particles into the liquid phase and the subsequent precipitation of β-Si_3N_4 from the liquid. However, no reverse β- to α-Si_3N_4 transformation has been observed experimentally.

9

An exciting discovery of a third polymorph of Si_3N_4 which has a cubic spinel structure has been recently reported by Zerr et al. (1999). The novel cubic Si_3N_4, c-Si_3N_4, is formed at high temperature (2200 K) and high pressure (15 GPa), and is metastable in air at ambient pressure to at least 700 K. Theoretical calculations showed that the modulus (~300 GPa) and hardness (~33 GPa) of c-Si_3N_4 were quite similar to those of stishovite, a high-pressure phase of SiO_2, and were, therefore, significantly higher than those of the α- and β-Si_3N_4. Such high hardness of c-Si_3N_4 suggests its enormous potential in applications where hardness and wear-resistance are crucial. However, this c-Si_3N_4 is not directly related to the sialon ceramics under examination in the present study and thus it will not be discussed in greater detail.

When metal oxides were used to facilitate the densification of Si_3N_4 ceramics, a range of solid solutions were produced, among which the "SiAlONs", a solid solution with Si-N bonds substituted by Al-O bonds, have attracted the most attention.

2.3.1.2. Sialons

The replacement of Si^{4+} by Al^{3+} in SiN_4 tetrahedra was predicted by Grieveson, Jack and Wild (1968). Valency balance is achieved either by the substitution of N^{3-} by O^{2-} or by the introduction of additional metal cations with or without the substitution of N^{3-} by O^{2-}. The former mechanism occurs in β-sialons and the latter in α-sialons. Some crystallographic data of α- and β-sialons are summarized in Table 2.1 (Lee and Rainforth 1994).

β-sialons are isostructural with β-Si_3N_4 and are based on an arrangement of $(Si,Al)(O,N)_4$ tetrahedra identical to that of β-Si_3N_4. The β-sialon crystal structure is derived from β-Si_6N_8 by the replacement of $Z(Si^{4+}-N^{3-})$ bonds with $Z(Al^{3+}-O^{2-})$ bonds. Therefore no additional cations are required to give charge balance. The general formula for the β-sialon solid solution is:

$$Si_{6-z}Al_zO_zN_{8-z} \qquad (2.1)$$

where $0 < Z < 4.2$.

The transformation from β-Si_3N_4 to β-sialons can result in a small expansion in the unit cell dimension with a low lattice strain due to the slightly longer bond length of Al-O (1.75 Å) than that of Si-N (1.74 Å) (Cao and Metselaar 1991). The unit cell dimensions of β-sialons can be expressed as a function of Z (Ekström 1989):

$$a \text{ (Å)} = 7.603 + 0.0296Z$$
$$c \text{ (Å)} = 2.907 + 0.0255Z \tag{2.2}$$

where $0 < Z < 4.2$.

α-sialons are isostructural with α-Si_3N_4 and are based on an identical arrangement of $(Si,Al)(O,N)_4$ tetrahedra as in α-Si_3N_4 (Slasor et al. 1991). In α-Si_3N_4, when $(m+n)$(Si-N) bonds are replaced by m(Al-N) and n(Al-O) bonds in each unit cell, a charge deficiency occurs which requires additional cations to compensate for the charge unbalance. These compensating cations, M, such as Li, Mg, Ca, Y and the rare-earth elements except La, Pr and Eu, are incorporated into the large interstices of the structure to form α-sialon solid solutions (Huang et al. 1985; Hampshire et al. 1978; Thompson 1989; Mandal 1999). The general formula for α-sialon is:

$$M_x^{v+}Si_{12-(m+n)}Al_{m+n}O_nN_{16-n} \tag{2.3}$$

where $x \leq 2$ and is related to the valency, v, of the compensating cation, M, according to the relationship $x = m/v$ (Hampshire et al. 1978).

In α-sialons, significant amounts of Si-N bonds are substituted by Al-N bonds and this results in a large expansion in unit cell dimension with a high lattice strain due to the greater bond length of Al-N (1.87 Å) than that of Si-N (1.74 Å) (Cao and Metselaar 1991). Hampshire and colleagues (1978) were the first to propose that the increment in unit cell dimension could be plotted as a function of substitution numbers m and n:

$$\Delta a \text{ (Å)} = 0.045m + 0.009n$$
$$\Delta c \text{ (Å)} = 0.040m + 0.008n \tag{2.4}$$

Later studies (Sun et al. 1991; Wang et al. 1999a) showed that the increment in unit cell dimension was governed not only by the m and n values, but also by the size of the compensating cations and their solubility in α-sialons. Therefore, a number of

formulas have been determined for various cation stabilized systems (Sun et al. 1991; Ekström et al. 1997; Wang et al. 1999a).

α-sialon exhibits higher hardness than β-sialon because of the longer stacking sequence in α-sialon resulting in the longer Burgers vector required for slip of dislocations (Lewis et al. 1981). α-sialons can accommodate some of the sintering additives or impurities into the α-sialon lattice, thus reducing the overall amounts of intergranular glassy phase and improving the high temperature properties. Despite having the above advantages, traditionally, single-phase α-sialons were not seriously considered for engineering applications. This was primarily due to their highly brittle nature, resulting from their inability to form elongated grains (Rosenflanz 1999). In addition, other factors, such as difficulties in the fabrication of fully dense α-sialons by pressureless sintering and the instability of some α-sialon compositions at relatively low temperatures, also hinder the commercialization of single-phase α-sialons as engineering ceramics. For example, most rare-earth stabilised α-sialons can transform to softer β-sialons and undesirable intergranular glassy phases when the temperature reaches $\sim 1400°C$ (Rosenflanz 1999). It should be noted, unlike the α-$Si_3N_4 \leftrightarrow \beta$-$Si_3N_4$ system, the reverse transformation, i.e. β- to α-sialon, has also been observed (Mandal et al. 1993).

Fully dense β-sialons can be made by pressureless sintering in the presence of large amounts of sintering aids (Ekström and Nygren 1992). These sintering aids react with the SiO_2 present on the surface of Si_3N_4 powder and also with some of the Al_2O_3 in the initial powder mixture to form even greater amounts of intergranular glassy phase in the final material (Ekström and Nygren 1992). The grain boundary glassy phase is particularly deleterious for high temperature applications. However, at low or medium temperatures, this glassy phase coupled with the elongated β-sialon grains can significantly increase the fracture toughness (Ekström 1989). The pressureless sintered β-sialons were the first nitrogen ceramics to achieve large scale commercial viability (Mandal 1999) and are currently largely used in engineering applications (Chen and Rosenflanz 1997).

It is important to note that, in sialon ceramics, there often exist a number of AlN-polytypoid phases. The structure of the AlN-polytypoids is based on the wurtzite type structure of AlN with the incorporation of additional Si and O atoms (Jack 1976; van Tendeloo et al. 1983). The compositional formula for AlN-polytypoids is M_mX_{m+1}, indicating these materials are built up by MX double layers of metal (M = Al, Si) and non-metal (X = N, O) atoms stacking along the c-axis in the sequence of AB and ABC with MX_2 layers at periodic intervals (Thompson et al. 1983; Bando et al. 1986). The AlN-polytypoid phases observed in the sialon system are 8H, 15R, 12H, 21H, 27R, 33R, 39R, 24H and $2H^\delta$, where H and R represent hexagonal and rhombohedral crystallographic systems, the numeral denotes the number of M and X layers within each periodic interval, and δ signifies disorder in the sequence of MX_2 layers (Thompson 1977; Thompson 1989; van Tendeloo et al. 1983).

Compared to α-sialon and β-sialon, AlN-polytypoids possess relatively poor mechanical properties. However, unlike many other ceramics, these materials display an increased flexural strength at high temperature (Wang et al. 1999b). In addition, AlN-polytypoids appear in fiber-like or long lath-like grain morphologies (Wang et al. 1999b; Wood and Cheng 2000), which indicates that sialon composites containing AlN-polytypoid phases may exhibit improved fracture toughness.

The relation between sialon and Si_3N_4 is analogous to that between brass and copper (Jack 1986). Pure copper is soft and weak, but up to 40% of Cu atoms can be replaced by Zn atoms without changing the structure. The resultant alloy has improved hardness and strength coupled with a lower melting temperature and thus is easier to fabricate (Lee and Rainforth 1994). Likewise, sialon ceramics have the strength and thermal shock resistance of silicon nitride with the additional advantages of higher hardness, toughness and wear-resistance as well as improved chemical stability and sinterability (Ekström and Nygren 1992). Furthermore, sialon ceramics can incorporate some of the sintering additives into the lattice and thus reduce the amounts of intergranular glassy material. More significantly, compared to Si_3N_4, sialon ceramics have greater phase complexity and more degrees of freedom for tailoring of microstructures and consequently mechanical properties. Thus, the possible microstructural tailoring of sialon ceramics means that these materials offer

an excellent modeling system in any investigation of the effect of various microstructural aspects on the erosion behaviour of ceramic materials.

2.3.2 Representation of the M-Si-Al-O-N system

As already stated, sialon ceramics exhibit complex phases. The phase diagram of sialon ceramics involves a five-component system, M-Si-Al-O-N, and can be illustrated by a so-called Jänecke prism (Gauckler and Petzow 1983). The base of the prism is the Si_3N_4-AlN-Al_2O_3-SiO_2 square and the third dimension is a consequence of the metal oxide or nitride addition. Fig. 2.3(a) shows an example of the Jänecke prism for the Ca-Si-Al-O-N system (Hewett et al. 1998a).
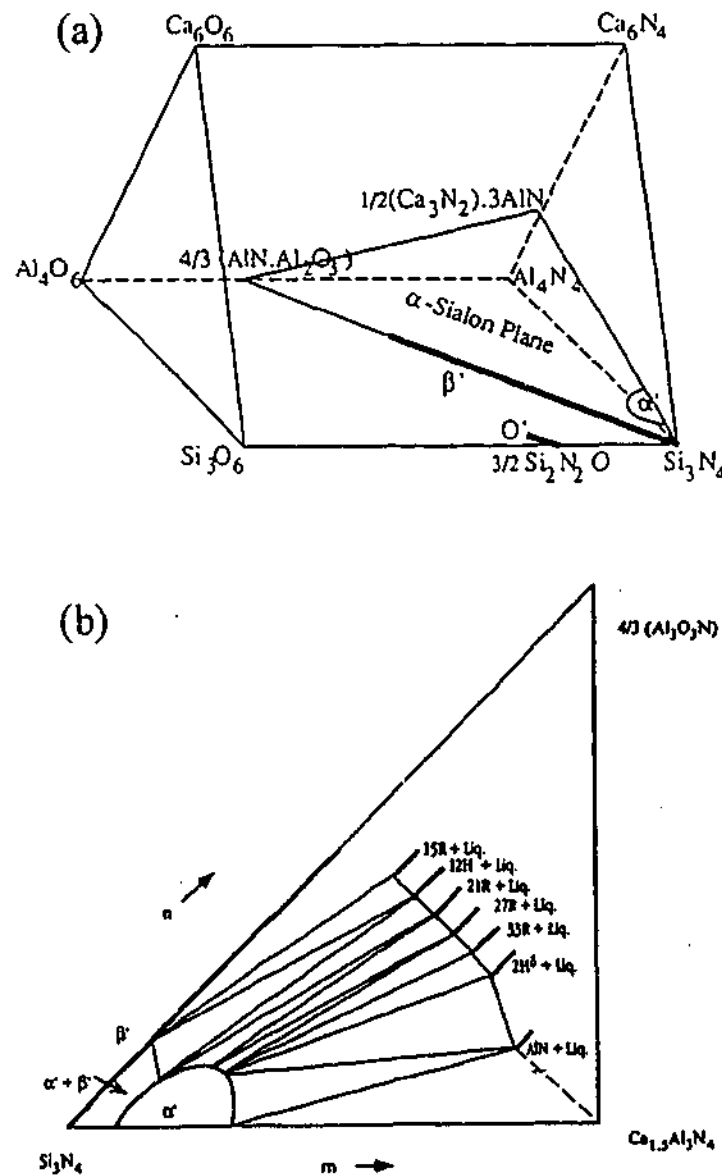
Fig. 2.3. (a) Jänecke prism for the Ca-Si-Al-O-N system indicating the two-dimensional α-sialon plane (Hewett et al. 1998a) and (b) Ca α-sialon phase behaviour diagram (Hewett et al. 1998a).

In Fig. 2.3(a), three distinct phase regions can be distinguished: α-sialon, β-sialon and O-sialon. The α-sialon phase region has a two-dimensional (2D) extension in the plane Si_3N_4-$4/3(AlN \cdot Al_2O_3)$-$1/2(Ca_3N_2) \cdot 3AlN$. The β-sialon phase extends along the line Si_3N_4-$4/3(AlN \cdot Al_2O_3)$ and thus falls on one border of the so-called α-sialon plane. The O-sialon phase forms a narrow solid solution range on the Si_3N_4-AlN-Al_2O_3-SiO_2 plane and has the structure of Si_2N_2O. According to the phase relationship, it is not possible for the O-sialon phase to be in equilibrium with the α-sialon phase. Interest in O-sialon as an engineering ceramic is driven by its excellent oxidation/corrosion resistance at high temperatures. An excellent review paper presented by Ekström and Nygren (1992) summarised much work on O-sialons. Since the present study focuses on the microstructural tailoring of α-sialon ceramics, O-sialons will not be further discussed here.

The behavioural phase relationships on the 2D α-sialon plane for Ca α-sialon system were studied initially by Jack (1983) and later by Hewett and coworkers (1998a) and Wood and Cheng (2000). These phase relationships are shown graphically in Fig. 2.3(b). As can be seen in Fig. 2.3(b), α-sialon and β-sialon coexist in the low m-value compositions near the Si_3N_4 corner. This indicates that α- and β-sialon phases are fully compatible and α/β-sialon composites with various α-sialon:β-sialon phase ratios can be prepared. α/β-sialon composites are another important Si_3N_4 based ceramic group in addition to the β-Si_3N_4 and β-sialons that are currently in used for engineering applications. This is mainly because that α/β-sialon composites are easier to fabricate compared to Si_3N_4 and single-phase α-sialon ceramics. More significantly, α/β-sialon composites offer some improved mechanical properties by taking advantage of the high hardness of α-sialon and the good strength and toughness of β-sialon. The properties of α/β-sialon composites will be further discussed in section 2.4.4.

As the m-value increases, a number of compositions containing various amounts of α-sialons, AlN-polytypoids and liquid phases can be obtained. Therefore, with careful selection of the composition, it is possible to fabricate α-sialon ceramics which have

controlled microstructures and thus controlled mechanical properties. One of the approaches to microstructural tailoring of Ca α-sialon ceramics proposed by the present study is indeed based on this philosophy.

2.4 α-Sialon Ceramics

2.4.1 Introduction

Early studies of sialon ceramics mainly focused on β-sialon and its commercial production (Jack 1976; Lewis et al. 1977; Lewis et al. 1980; North et al. 1980). By 1987, a seminal paper published by Jack (1987) presented the entire history of β-sialon ceramics including their discovery, development, production and applications. At that time, research of α-sialon ceramics was still in its early stage. Initial interest in α-sialons as engineering ceramics stemmed from their unique combination of properties. In addition to having remarkably high hardness and outstanding thermal shock resistance, α-sialons offer the possibility of the development of single-phase or composite ceramics without grain boundary glassy phase. However, the promotion of α-sialon ceramics for engineering applications was impeded due to the highly brittle nature, poor sinterability and poor stability (at elevated temperatures) of these materials. The early work on α-sialon ceramics was summarized by Cao and Metselaar (1991).

A renewed interest in α-sialons appears to have been stimulated by a study by Hwang, Susintzky and Beaman (1995) who reported that elongated grains could be obtained in the multication stabilized α-sialon system containing strontium. Similar findings were also observed in samarium doped α-sialon ceramics (Shen et al. 1996). However, despite the presence of elongated grains, no significant improvements in the fracture toughness of these materials were reported until very recently. Shen and colleagues (1997) examined the formation of elongated grains in various α-sialon systems. They found that a high fraction of transient liquid phase coupled with a larger stabilizing cation was more likely to lead to the formation of the elongated α-sialons. Improved fracture resistance was observed in some of these compositions. Since then, many studies concerning the development of elongated α-sialons have

been published by a number of research groups. Among these the research of the Michigan group in the USA (led by I.-W. Chen) and the research of the Monash group in Australia (led by Y.-B. Cheng) are the most significant.

Chen and Rosenflanz (1997) reported a novel technique for fabricating α-sialon materials with elongated microstructure from β-Si_3N_4 powder using the gas-pressure sintering method. Microstructures containing up to 40% elongated α-sialon grains were obtained in Y and a range of rare-earth stabilized α-sialon materials by practising nucleation control. Much improved fracture toughness, exceeding 6 MPa $m^{1/2}$ compared to the typical 3 MPa $m^{1/2}$ for equiaxed α-sialons, was observed in some of these compositions. Remarkably, the values for the hardness of these materials were almost identical regardless of the various compositions and the various amounts of elongated grains contained. In addition, these materials contained very little grain boundary glass phase. At the same time, a truly remarkable finding by Zhao, Swenser and Cheng (1997) showed that an elongated microstructure could be readily obtained in Ca stabilized α-sialon systems using more conventional α-Si_3N_4 powder and the pressureless sintering method. Further studies (Wood et al. 1999; Wood and Cheng 2000) showed that the formation of α-sialon grains with an elongated morphology was more favoured in compositions rich in AlN and glass. Fracture toughness greater than 6 MPa $m^{1/2}$ was routinely observed in Ca α-sialon materials containing elongated grains.

From these studies, it can be concluded that the development of elongated α-sialons is controlled by either the nucleation rates of α-sialon phase or the phase assembly of the α-sialon compositions. Furthermore, the nucleation rate is dependent on: (1) the choice of starting powder; (2) the type of stabilizing cation; and (3) the control of the sintering conditions which include the heating rate, the dwell temperature and the dwell time.

In the remainder of this section, the stabilising cations and the reaction mechanism of α-sialon ceramics will be discussed. A brief survey of the published literature on the

tailoring of microstructural and mechanical properties of these materials will be included. Emphasis will be placed on Ca α-sialon ceramics.

2.4.2 Stabilising cations

As outlined in section 2.2, Si_3N_4 is a highly covalently bonded material. To achieve full densification of Si_3N_4, additional sintering aids, such as metal oxides, are essential. The added metal oxides react with the silica on the surface of Si_3N_4 particles to form an oxynitride liquid which assists densification and also cools to give an intergranular glassy phase. On the other hand, α-sialons require additional cations to stabilise. This indicates that the transient liquid phase can be absorbed by the α-sialon lattice during sintering and results in a material with significantly reduced intergranular glassy phase. Therefore, by careful selecting the optimal oxide additive, it is possible to produce a dense, single-phase ceramic with a minimum of grain boundary phase.

There have been extensive studies carried out concerning the possibility of using various cations to stabilise α-sialon during the last two decades (Huang et al. 1986; Thompson 1989; Kuang et al. 1990; Huang and Yan 1992; Ekström and Shen 1995; Mandal and Thompson 1996; Mandal 1999). It is now well appreciated that metal cations, such as Li^+, Mg^{2+}, Ca^{2+}, Y^{3+} and lanthanide elements with atomic number Z ≥ 60, are readily incorporated into the α-sialon lattice, and thus formation of single-phase α-sialon is possible. Larger cations Nd^{3+} and Ce^{3+}, with ionic radii of 0.99 Å and 1.03 Å respectively, can also enter the α-sialon structure alone, but both show a low percentage of cation accommodation within the α-sialon lattice. Thus, single-phase Nd and Ce α-sialons are difficult to obtain (Mandal and Thompson 1996; Mandal 1999). Even larger cations La^{3+} ($r = 1.06$ Å) and Sr^{2+} ($r = 1.26$ Å) cannot enter the α-sialon structure alone; single-phase La and Sr α-sialons do not exist, but both can form multi-cation α-sialon in the presence of Ca^{2+} or Y^{3+} cations (Mandal 1999).

Ideally, α-sialon can be synthesized entirely from nitrides with no oxides contained in the starting powder mixture. Hence a negative charge imbalance resulting from the

partial replacement of Si^{4+} by Al^{3+} in SiN_4 tetrahedra is compensated for solely by the introduction of the stabilising cations. Since each α-Si_3N_4 unit cell contains two large cavities, at most two stabilising cations can be incorporated into the α-sialon lattice. However, in reality, such a limit has never been achieved (Cao and Metselaar 1991). This is because the presence of the oxygen in the Si_3N_4 particles inevitably results in some substitution of N^{3-} by O^{2-} as well. The highest solubility reported in the literature is 1.83 Ca^{2+} cations per unit cell in the Ca α-sialon when Ca_3N_2 was used as the calcium source (Jack 1983). The maximum solubility of 1.5 Li^+ cations per unit cell was also observed in Li α-sialon (Kuang et al. 1990), while the maximum solubility of the rare earth and Yttrium cations, as shown in Fig. 2.4, varies between 1.0 to 0.6 (Huang et al. 1986). In general, the maximum solubility in α-sialons decreases as the radius of the stabilising cations increases (Cao and Metselaar 1991).
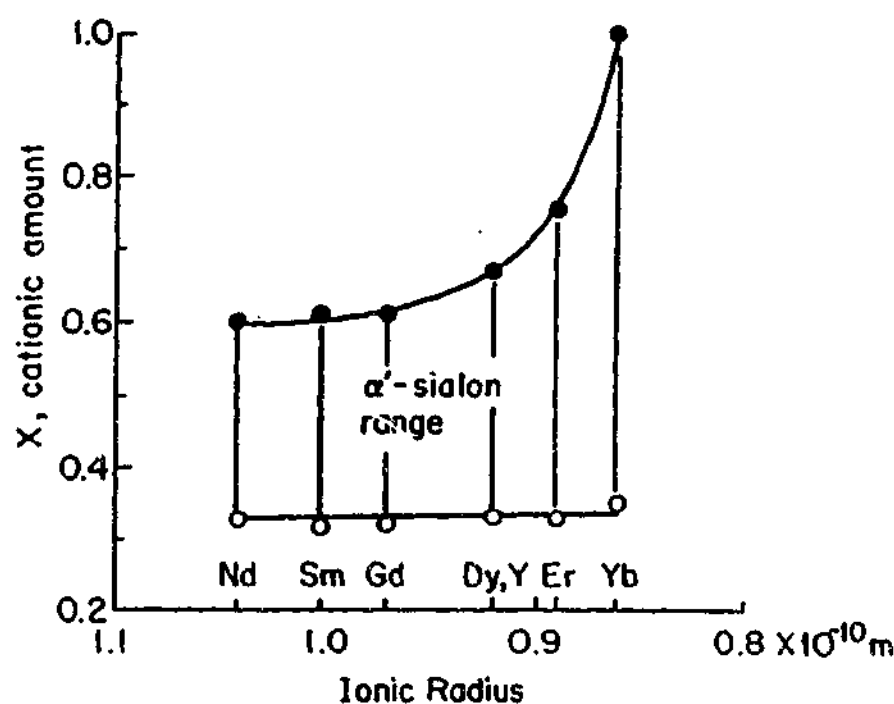
Fig. 2.4. Rare-earth cation ionic radius vs. α-sialon solid solubility limit (Huang et al. 1986).

Early studies of α-sialon ceramics focused on compositions stabilised by Li^+, Mg^{2+} and Y^{3+} cations because of the established role of Mg^{2+} and Y^{3+} as densification aids for hot-pressing of Si_3N_4 (Jack 1976; Riley 2000). The most extensively investigated

systems were yttrium and rare earth sialons due to the formation of refractory phases from the devitrification of intergranular glass. In contrast, Ca α-sialons have received very little attention despite the realization that these materials have a number of advantages over the yttrium or rare earth α-sialons: calcium is more readily obtainable and has a larger solubility in the α-sialon structure, and the resultant material has greater thermal stability. In 1991, a comprehensive review of the work that had been done on α-sialon ceramics during the past twenty years was presented by Cao and Metselaar (1991). Almost two hundred papers on α-sialon ceramics were summarized. Among these, only a few were related to Ca α-sialon ceramics. Most of these were based on the early Newcastle work by Jack, Hampshire and Thompson (Jack 1983; Hampshire et al. 1978; Thompson 1989) with some further research by Huang, Sun and Yan (1985). Until recently, a considerable amount of work has been carried out on Ca α-sialon ceramics (van Rutten et al. 1996; Zhao et al. 1997; Hewett et al. 1994, 1998a and 1998b; Wood et al. 1999; Wood and Cheng 2000; Mandal 1999; Wang et al. 1999a; Zhang et al. 2000a). However, most of this work was concerned with phase formation and related microstructural development of the Ca α-sialon system (Hewett et al. 1998a; Wang et al. 1999a; Wood and Cheng 2000), and there has been little study in the field of microstructural tailoring by manipulating the nucleation rate via altering the sintering conditions (Zhang et al. 2000a).

2.4.3 Reaction and densification mechanisms

It is generally accepted that the densification of silicon nitride ceramics with oxide additives occurs via a liquid-phase sintering process which can be described by three partly overlapped stages: particle rearrangement, solution-precipitation, and coalescence of the grains (Kingery 1959; Cao and Metselaar 1991). However, for densification of α-sialon ceramics, the sintering mechanism becomes much more complicated since during the heating cycle, various reaction pathways may, depending on the acid-base chemistry, occur, some intermediate phases form, and some liquid ingredients are incorporated into the α-sialon structure (Hampshire et al. 1978; Jack 1983; Menon and Chen 1995a).

Based on experimental observations, Menon and Chen (1995a; 1995b) concluded that the sintering mechanisms of α-sialon ceramics involved both reaction and densification. Five temperature dependent stages of the reaction sequence were identified (Menon and Chen 1995b):

1) formation of a ternary oxide eutectic liquid (at temperature T_1)

2) primary wetting of a nitride powder and precipitation of the intermediate phase (at temperature T_2)

3) secondary wetting of the other nitride powder (at temperature T_3)

4) dissolution of the intermediate phase (at temperature T_4)

5) precipitation of the final phase, α-sialon (at temperature T_5)

The wetting behaviour of nitride powders in the ternary oxides was found to obey Pearson's principle: the more basic oxides, such as Li_2O, MgO, CaO, Nd_2O_3, Sm_2O_3 and Gd_2O_3, wetted Si_3N_4, while the more acidic oxides, such as Dy_2O_3, Er_2O_3 and Yb_2O_3, wetted AlN (Menon and Chen 1995a).

Menon and Chen (1995b) also found that the above five characteristic temperatures had a controlling effect on the densification behaviour of α-sialon ceramics (Fig. 2.5). Three major stages of the densification process were observed:

1) formation of the ternary oxide eutectic liquid (at temperature T_1)

2) wetting of the majority nitride powder (at temperature T_2 or T_3)

3) dissolution of the intermediate phase (at temperatures T_4 and T_5)

It should be noted that densification is mainly achieved by massive particle rearrangement, irrespective of wetting and dissolution behaviour (Menon and Chen 1995b). The efficiency of densification is mostly influenced by the amount of liquid available and the degree of its viscosity (Menon and Chen 1995b).

21

(a)

(b)
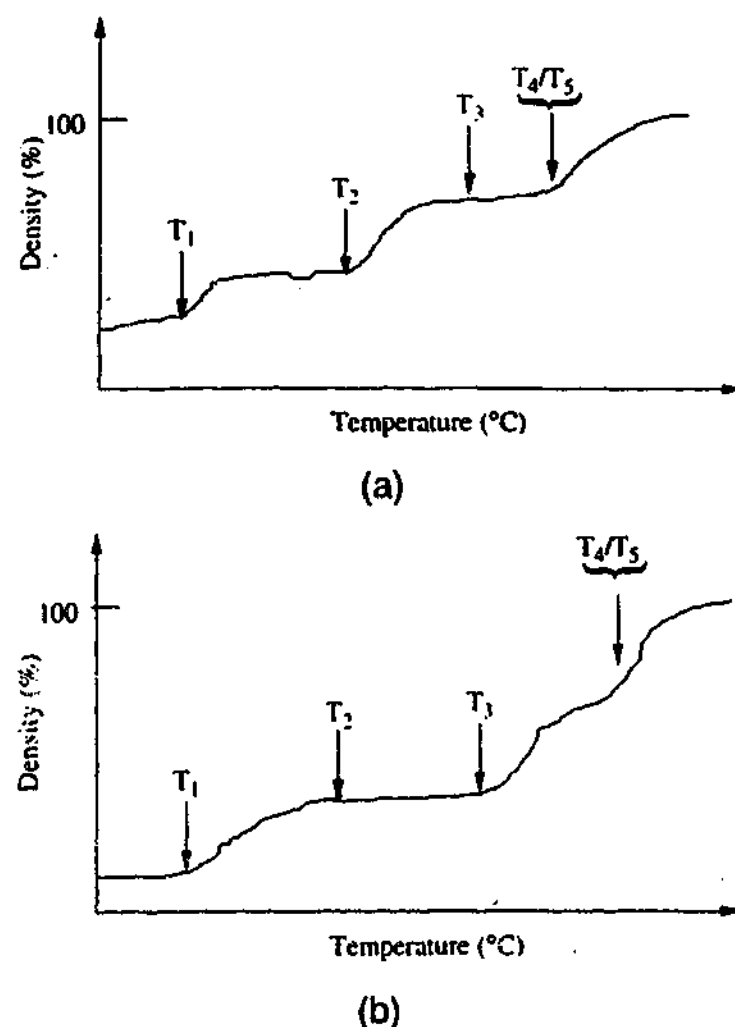
Fig. 2.5. Schematic shrinkage curves when the eutectic melt wets (a) Si_3N_4 and (b) AlN first (Menon and Chen 1995b).

The reaction densification mechanisms proposed in these studies provide a general concept for fabrication of α-sialon ceramics. However, in practice the reaction sequence and densification efficiency could be significantly affected by a number of factors, such as the sintering techniques, the composition of the starting mixtures, the heating rate and the dwell time. Therefore, further studies of reaction densification mechanisms of individual α-sialon systems, and even various compositions within the same system, are necessary.

2.4.4 Microstructures and mechanical properties

To give a comprehensive review of the microstructures and mechanical properties of sialon ceramics would be a formidable task for this limited volume. This section will

therefore be limited to a survey of the most relevant publications on this subject and to a brief summary of representative properties of sialon materials.

Despite the excellent combination of thermal mechanical properties of Si_3N_4 ceramics, the wide application of these materials is still hampered by their relatively low fracture toughness (Lange 1973; Jack 1976; Swain 1994; Kleebe et al. 1999). Improvements in fracture toughness of Si_3N_4 and sialon ceramics are mainly achieved by crack bridging and crack deflection mechanisms (Fairbanks et al. 1987; Bennison and Lawn 1989; Kelly et al. 1991; Chen and Engineer 1999). To enhance crack deflection toughening, high aspect ratio acicular grains and a weak interface between the grains and grain boundary phases are desirable. To enhance crack bridging toughening, high aspect ratio grains with large diameters are required. On the other hand, weak interfaces and subsequently the debonding of large elongated grains result in the development of fracture origins and loss of strength of the material. Therefore, to develop a superior material with both high toughness and strength, optimization of the microstructure is essential.

There has been a large amount of research concerning the correlation between microstructural features and the mechanical properties of Si_3N_4 ceramics during the last two decades (Lange 1979; Himsolt et al. 1979; Li and Yamanis 1989; Mitomo 1991; Kleebe et al. 1999). The outcomes have been quite impressive: materials with elongated β-phase grains exhibited a much improved steady-state fracture toughness of up to 10 MPa $m^{1/2}$, compared to ~3 MPa $m^{1/2}$ in Si_3N_4 with fine, more equiaxed grain structures, reported by numerous groups (Li and Yamanis 1989; Tajima and Urashima 1994; Kleebe et al. 1999). Current best room-temperature values for fracture toughness and strength for Si_3N_4 ceramics exceed 10 MPa $m^{1/2}$ and 1100 MPa (Becher et al. 1998; Sun et al. 1998). This Si_3N_4 with very best properties was prepared by tape casting of a powder mixture of Si_3N_4 ($\geq$95% α-phase), 6.25 wt% Y_2O_3, 1 wt% Al_2O_3 and 2 vol% β-Si_3N_4 seeds and followed by gas pressure sintering at 1850°C for 6 h under a nitrogen gas pressure of 1 MPa (Hirao et al. 1995; Ohji et al. 1995; Becher et al. 1998). The resultant microstructure had a distinct bimodal grain size distribution where large elongated β-sialon grains of an average size of 2 μm were evenly dispersed in a matrix of fine-grained β-Si_3N_4 (0.3 μm in size) and an

amorphous grain boundary phase. The same study also showed that the further coarsening of the fine matrix grains to ~1 μm or the refining of the elongated β-sialon grains to ~0.5 μm both resulted in a lower fracture toughness (~6 MPa m$^{1/2}$) and a lower strength (850-930 MPa). However, the major drawbacks of the β-Si$_3$N$_4$ and β-sialon materials are their relatively low hardness and the considerable amount of grain boundary glassy material present which is known to be deleterious for high temperature applications. The typical hardness value for these materials is 15-16 GPa compared to 19-24 GPa for α-sialons.

The development of α/β-sialon composites was aimed to overcome the low hardness and high glass content problems of the β-Si$_3$N$_4$/sialons ceramics. As mentioned in section 2.3.1, α-sialons have, in general, an equiaxed grain morphology and possess high hardness and good thermal shock resistance, while β-sialons tend to contain elongated grains and exhibit higher toughness and higher strength than α-sialons. α/β-sialon composites can be classified as a case where the elongated β-sialon grains toughen the equiaxed α-sialon matrix. In addition, the α-sialon phase has the ability to incorporate the sintering additive into its structure and thus reduces the amount of grain boundary glassy phase. Therefore, α/β-sialon composites have been found to have excellent mechanical properties at both room temperature and elevated temperature (Yen 1994; Sheu 1994).

It has been long established that α/β-sialon composites offer possibilities for tailoring the phase content, microstructure and consequently the mechanical properties of the final products. The phase content of α/β-sialon composites, such as α to β-sialon phase ratio and the amount of the intergranular glassy phase, can be controlled by changing the overall composition in M-Si-Al-O-N systems (Ekström 1994). The various phase contents of these materials can also be obtained from a single starting composition using different heat-treatment cycles (Mandal et al. 1993). More significantly, in α/β-sialon composites, the size of the α-sialon grains and the aspect ratio of the β-sialon grains can be controlled by careful selection of appropriate sintering conditions (Sheu 1994) and the heat-treatment cycles (Mandal et al. 1993).

One excellent example is a series of studies of the effect of sintering conditions on the mechanical properties of α/β-YAG($Y_3Al_5O_{12}$) sialon composites by Yen (1994) and Wang et al. (1996b). They showed that, for a particular composition, namely α-sialon:β-sialon = 1:1 coupled with 9 wt% YAG, pressureless sintering at 1800°C for 2 h produced a material exhibiting a poor room temperature flexural strength of 612 ± 24 MPa, a poor fracture toughness of 3.9 ± 0.1 MPa $m^{1/2}$, and a low hardness of HV10 1594 kg/mm^2. The flexural strength of this material at elevated temperature (1350°C) was ~500 MPa. The same pressureless sintered material followed by a gas pressure sintering at 2000°C for 1.5 h resulted in a much improved room temperature flexural strength of 925 ± 22 MPa, an improved fracture toughness of 7.2 ± 0.3 MPa $m^{1/2}$, and a remarkable hardness of HV10 1884 ± 74 kg/mm^2. More importantly, the flexural strength of this material at 1350°C was also dramatically improved to ~720 MPa.

Another example is the study of the effect of the composition on the microstructure and mechanical properties of α/β-sialon composites by Sheu (1994). He concluded that the composite contained 30-40 % equiaxed α-sialon grains (~0.2 μm) and fine, elongated β-sialon grains possessed the optimised mechanical properties, which had a flexural strength of 1100 MPa at 25°C, 800 MPa at 1400°C, and a fracture toughness of 6 MPa $m^{1/2}$. The same study also showed that the flexural strength and fracture toughness of the composites increased markedly with increasing β-sialon content whereas the hardness decreased. Furthermore, the high temperature flexural strength of these materials experienced a dramatic decay when the β-sialon content increased from 70% to 80%, indicating that the increasing of β-sialon content was accompanied by an increasing of intergranular glassy material. This is because in order to allow the β-sialon grains to grow without steric hindrance, excessive sintering aids must be added (Ekström 1994; Wang et al. 1998).

Trade-offs between hardness and toughness, as well as between the room temperature and high temperature strength are unfortunate, and it seems very likely that a Si_3N_4 based ceramic exists which exhibits combined excellent properties. To this end, the development of self-reinforced α-sialon ceramics offers great potential. A preliminary

study of α-sialon ceramic with a whisker-like microstructure by Chen and Rosenflanz (1997) showed some encouraging results: a strength of 700 MPa and a fracture toughness of 6.3 MPa m$^{1/2}$ were obtained, which are almost twice the values of the equiaxed α-sialon ceramics. A hardness of 22 GPa was also obtained which is identical to the values of the equiaxed α-sialon ceramics. However, in order to further improve the properties of α-sialon ceramics, a better understanding of microstructural control of these materials is needed.

A final remark ought to be made on the toughening mechanism of elongated α-sialon ceramics which has so far not been addressed in the literature. As discussed above, improvements in fracture toughness of Si_3N_4 and sialons ceramics are mainly achieved by crack bridging and crack deflection mechanisms which require a high aspect ratio acicular grains and a weak bonding between the grains and grain boundary phases. However, unlike in β-Si_3N_4 and β-sialons, both α-sialon grains and grain boundary phases contain identical elements. Thus, the bonding between the α-sialon grains and grain boundary could be strong, which could consequently hinder the crack bridging and crack deflection mechanisms. Therefore, to further improve the fracture toughness of α-sialon ceramics, the interfacial characteristics must be first addressed.

Part II – Solid Particle Erosion

2.5 Background

Most of the research into erosion has been carried out during the last forty years, but some work dates as far back as the 19th century (Young 1807; Reynolds 1873). However, most of the early studies were carried out on various practical erosion problems and little research has been done which investigates erosion mechanisms by which particles remove material. Investigation of this fundamental physical process of erosion started after the Second World War and the erosion of ductile metals was the major interest. Finnie (1960) was the first to realize that the erosion mechanisms were different in ductile and brittle materials with plastic flow playing a major role in

the former case and microfracture in the latter. It was also found that there was a dramatic difference in the response of ductile and brittle materials when the erosion rate was measured as a function of the angle of incidence (Sheldon and Finnie 1966a). Ductile materials, such as metals and polymers, exhibit a maximum erosion rate at low angles of incidence (typically 15-30°), while brittle materials, such as ceramics, have the maximum rate at or near 90°. After Finnie's work, there has been an extraordinary amount of work in the area of erosion in brittle materials, especially in the past two decades.

2.6 Theoretical Models

During erosive wear of brittle materials, material removal occurs via microfractures produced by impacting particles. The proposed fracture mechanisms have been based on the damage pattern produced by the dynamic impact of a single particle on a smooth surface (Finnie 1995). Surprisingly, similar damage features can also be observed in these materials loaded quasistatically with sharp indenters (Wiederhorn and Lawn 1979). This means that the more controllable quasi-static indentation method could be used to model dynamic erosion behaviour in brittle materials (Rowcliffe 1992; Finnie 1995).

The earliest attempt to model the erosion behaviour of brittle materials was made by Sheldon and Finnie (1966b). They assumed that the particle-target interaction was perfectly elastic and thus the volume removed by an impacting particle was calculated based on Hertzian cracking under a spherical indenter. However, a later study observed a zone of plastic deformation containing a high density of dislocations under the impact site in brittle materials, indicating that the assumption of a perfect elastic interaction was not valid (Hockey et al. 1978).

With the development of indentation fracture mechanics, two elastic-plastic theories have been developed to model the erosion behaviour of brittle materials. Evans et al. (1978) considered the dynamic elastic-plastic response of an impacting particle, while Wiederhorn and Lawn (1979) assumed the particle-target contact velocity was slow (relative to sonic velocity), i.e. the quasi-static condition, and the kinetic energy of the

erodent particle was absorbed completely by the plastic flow of the target. However, both theories assumed that the lateral cracks were responsible for material removal and both predicted a power-law dependence for the erosion rate, ΔE, on erodent and target properties given by

$$\Delta E \propto v^n D^{2/3} \rho^p K_C^{-(4/3)} H^q \tag{2.5}$$

where v, D and ρ are the velocity, mean size and density of the erodent particles, and K_c and H are the fracture toughness and hardness of the target material. The exponents n, p and q differ in the two models, being 3.2, 1.3 and -0.25 for dynamic and 2.4, 1.2 and 0.11 for quasi-static model, respectively. Both models suggest that the erosion rate has a strong inverse dependence on the fracture toughness, but exhibits a much weaker dependence on the hardness of the target material. The above expression is valid for normal impacts and for ΔE in units of mass or volume loss per unit mass of erodent used.

The two models have been further extended to predict ΔE for oblique impacts by using the normal component of velocity, $v \cdot \sin\alpha$ (Hockey et al. 1978), and by taking into account of the effects of the velocity and particle size thresholds, in which v and D were replaced by ($v \cdot \sin\alpha - v_0$) and ($D - D_0$), respectively (Routbort et al. 1980a). Here α is the angle of incidence, which is defined as the angle between the incident particle direction and the target surface. The extended version of the two models, which holds for particle sizes greater than 40 μm (Sheldon and Finnie 1966a; Marshall et al. 1981), indicates that in erosion of brittle materials, ΔE increases with increasing impact angle and the maximum erosion rate occurs at 90° impact angle.

2.7 Verification of the Models

The two elastic-plastic models along with their extended versions have been verified on a wide range of materials including glasses, single crystals and advanced ceramics. The research in each of these materials is discussed below.

2.7.1 Single crystals and glasses

Single crystals and glasses serve as the ideal model materials for assessment of the theoretical models without microstructure complications (Routbort and Scattergood 1992). There have been numerous studies on these materials to verify the validity of the theoretical assumptions on which the two models are based and the predictions of the dependence of erosion rate on the erodent particle size, density, velocity and impact angles (Wiederhorn and Lawn 1979; Routbort et al. 1980a; Scattergood and Routbort 1981; Scattergood and Routbort 1983).

Verifications of the theoretical assumptions of the models have been carried out by examining the damage features introduced by single particle impacts on glasses and single crystals (Wiederhorn and Lawn 1979; Routbort et al. 1980a; Wiederhorn and Hockey 1983; Ritter et al. 1984; Srinivasan and Scattergood 1987; Murugesh and Scattergood 1991). All studies showed that when glasses and single crystals were impacted by hard. sharp particles at 90°, the most conspicuous damage revealed was the surface spalling attributable to the lateral cracks. These findings were in very good agreement with the theoretical assumptions that lateral cracks were responsible for material removal.

Verification of the proposed dependence of erosion rate on erodent particle size, density, velocity and impact angles has been carried out mainly on Si (111) single crystals by Scattergood, Routbort and Kay (Routbort et al. 1980a; Scattergood and Routbort 1981; Scattergood and Routbort 1983). They extensively investigated the erosion of Si single crystals using SiC, Al_2O_3 and SiO_2 erodents over a range of particle sizes, D (23 to 270 μm), velocities, v (30 to 150 m/s), and impact angles, α (22° to 90°). Their results showed that for $\alpha \geq 45°$, the erosion rate, ΔE, could be described within the framework of the existing models: $\Delta E = (v \cdot \sin\alpha - v_0)^n (D - D_0)^{0.6}$. The velocity exponent, n, was found to vary with the particle size regardless of the type of the erodent used; varying from closer to the predicted value of the dynamic model for 23 μm particles to near the predicted value of the quasistatic model for 270 μm particles. However, in the study by Routbort et al. (1980a), a higher ΔE was found for lower angles of incidence compared to those predicted from

the theories, a finding which implies that another erosion mechanism is operating. This mechanism is the plastic cutting mechanism which obtained from the tangential component of the velocity, $v \cdot \cos\alpha$, which becomes more significant for small α. In addition, in this study the effect of particle density on erosion rate could not be clearly established due to the considerable scatter in experimental data.

From the above discussion, it can be concluded that the two elastic-plastic theories serve reasonably well in the prediction of the erosion behaviour of glasses and single crystals, i.e. materials which lack microstructural complexity.

2.7.2 Advanced ceramics

Advanced ceramics with complex microstructures are of greater interest for erosion than single crystals and glasses from a practical point of view. Over the past two decades, there has been a large volume of literature concerning the verification of the two theoretical models in predicting the erosion behaviour of advanced ceramics. In the remainder of this section, three aspects of the relevant research will be reviewed: the dependence of erosion rate on particle velocity and size, the dependence of erosion rate on relative properties of erodent and target materials, and the dependence of erosion rate on properties of target materials.

2.7.2.1 Particle velocity and size exponents

The experimental results have supported the theories reasonably well with regard to the particle velocity exponents (Wiederhorn and Hockey 1983; Routbort and Scattergood 1992). Despite the wide range of target materials (form SiC, Si_3N_4 to Al_2O_3) and erodent particles (SiC or Al_2O_3), the velocity exponent, n, varied from 1.8 to 3.5 with a majority falling between the theoretical predictions of $n = 2.4$ and $n = 3.2$ for quasi-static and dynamic conditions, respectively (Murugesh and Scattergood 1991; Routbort and Scattergood 1992). However, the value of n decreased with increasing erodent particle sizes and this trend was ascribed to the blunting effect due to the fragmentation of the large particles (Murugesh and Scattergood 1991; Routbort and Scattergood 1992). The n value was also found to be sensitive to particle hardness, being smaller for the softer erodent (Al_2O_3) than for the harder erodent

(SiC) (Gulden 1981a; Murugesh and Scattergood 1991). The dependence of the n value on the particle hardness indicated that the erodent particle properties could play an important role in determining the rate of erosive wear. However, such an effect could not be accounted for by the theoretical models in which the erodent particles were assumed to be ideally strong and non-deforming.

The dependence of erosion rate on particle size has not been extensively studied. However, exponents close to 2/3 have been observed for a number of target materials, such as silicon carbide whisker reinforced aluminas and partially stabilized zirconias. These values were in accordance with the theoretical predictions of $D^{2/3}$ (Routbort and Scattergood 1992).

2.7.2.2 Relative target-particle properties

The erosion rate depends on the properties of both erodent and target materials. Gulden (1979, 1981b) was the first to investigate the effect of relative target-particle hardness on the erosion mechanism. She studied erosion of hot-pressed and pressureless sintered Si_3N_4 ceramics using both quartz and SiC abrasive grits. It was found that the erosion rate using SiC grits was approximately two orders of magnitude greater than that using quartz particles under otherwise identical conditions. Single impact studies showed that the erosion mechanisms were entirely different as the harder SiC caused lateral fracture, while the softer quartz particles resulted in minor chipping on a much finer scale than that of the particle contact area.

Wada and Watanabe (1987b), using data from previous studies, showed that for many target-particle combinations, the erosion rate, ΔE, can be related to the particle and target hardness, H_p and H_t, respectively, according to $\Delta E \propto (H_t/H_p)^a$, where a is an empirical exponent with a negative value. In a later study, Wada (1992) further pointed out that the erosion mechanisms, in general, were lateral fracture for $H_t/H_p < 1$ and minor chipping for $H_t/H_p > 1$. Similar conclusions were reached by Shipway and Hutchings (1996). In an extensive study of the erosion of a wide range of brittle materials using a number of different erodent particles, they concluded that as the

H_t/H_p ratio approached unity, a small-scale chipping mechanism operated and its associated erosion rate deviated further away from the theoretical predictions.

The view of dependence of erosion mechanism on H_t/H_p ratio was not shared by Srinivasan and Scattergood (1988a). They proposed that erodent particles softer than the target materials could cause erosion by lateral fracture. However, damage accumulation was required to build up the necessary stress level for producing cracks. Other studies (Murugesh et al. 1991; Dimond et al. 1983) suggested that it was the relative fracture toughness of the erodent and target materials, K_{cp}/K_{ct}, that had the dominant influence on erosion rates, not the hardness.

Studies of the dependence of erosion rates and mechanisms on the erodent and target properties have practical importance. When selecting ceramic materials for particular applications, one should be aware that any accelerated erosion tests using erodent particles which are not representative of the proposed service environment might provide completely contrary information. However, many of the investigations reported in the literature seem to focus on the effects of hardness and fracture toughness of the erodent and target on erosion rates and mechanisms of ceramic materials. The fact that hardness and fracture toughness are not independent material variables and that the involvement of material microstructure can obscure the underlying dependence. Therefore, the use of hardness and fracture toughness alone to predict the rate and mechanism of erosive wear would appear to be oversimplified. For example, Roberts and Hutchings (1989) studied the erosion rates and mechanisms of five different glass-bonded aluminas using silica, alumina and silicon carbide erodent particles. It was found that the erosion rates of the aluminas increased as the hardness of the erodent particle increased. More significantly, the ranking of the erosion resistance of the five aluminas varied for different erodents. The change in the ranking of the aluminas for different erodent materials cannot be accounted for by the relative hardness and fracture toughness of the erodent and target scenario proposed by previous researchers. The microstructure of the target aluminas, therefore, must play a significant role.

2.7.2.3 Target material properties

In order to examine the effect of hardness and fracture toughness of the target material on the erosion rate of ceramic materials, Wada (1992) carried out an extensive erosion test on a large number of engineering ceramics using SiC erodent under identical conditions. The erosion rates of sixteen kinds of sintered Si_3N_4 ceramics were determined. The multiple regression analysis showed that the erosion rate, ΔE, can be related to the target hardness, H_t, and fracture toughness, K_{ct}, according to $\Delta E = 24.5\ H_t^{-1.2}\ K_{ct}^{-2.9}$. As can be seen, the values of hardness and toughness exponents differed significantly from the theoretical predictions (see eq. 2.1). In the same study, the erosion rates of twelve kinds of hot-pressed Si_3N_4 ceramics were also determined under the same conditions. The results showed that a relationship of $\Delta E = 6.4 \times 10^3\ H_t^{-0.27}\ K_{ct}^{-7.1}$ could be established. Again the hardness and toughness exponents varied greatly from the theories. More remarkably, significant differences existed in the hardness and toughness exponents in these empirical relationships derived from the two sets of Si_3N_4 ceramics. One of the main purposes of establishing these empirical relationships was to predict the erosion performance of ceramic materials based on their hardness and fracture toughness values. If the exponents for the two sets of very similar materials vary by such a large margin, these empirical approaches become virtually meaningless.

As demonstrated above, the classic models based on hardness and fracture toughness of target materials failed to explain the erosion behaviour of engineering ceramics. Engineering ceramics can vary greatly in microstructure, and their mechanical properties (such as hardness and fracture toughness) may not reflect such differences. Taking alumina ceramics as an example, hardness is dependent on a combination of Al_2O_3 content and grain size (Heath et al. 1990). Therefore, even if two alumina ceramics have identical hardness, they do not necessarily have the same Al_2O_3 content and grain size. Similar, fracture toughness is also associated with a number of microstructural aspects, such as alumina content, porosity, grain size and morphology, and intergranular phases, etc. Hence, the microstructural aspects that are not accounted for by the erosion models may have a controlling effect on the erosion performance of ceramic materials. However, to this end, a clear and complete

33

understanding of the role of microstructure in the erosion process still remains elusive. Thus arises the need of the current research to clarify the effect of the microstructural variables on the erosion behaviour of ceramic materials.

2.8 Effect of Microstructure on Erosion of Ceramics

2.8.1 Introduction

Erosive wear is a complex phenomenon; it is influenced by a number of controlling factors including the properties of erodent particles, the fluid flow conditions and the properties of target materials (Table 2.1). Fortunately, there has been an immense volume of literature produced on all facets of erosion of brittle materials. Since this investigation focuses on the role of microstructure on erosion of ceramic materials, in particular the sialon ceramics, only the literature relevant to these areas will be reviewed.

Table 2.1 Factors which influence erosion in an inert environment (Finnie 1995)

Erodent particle properties
Size; Shape; Hardness; Strength (resistance to fragmentation)

Fluid flow conditions
Angle of impact; Particle velocity; Particle rotation; Particle concentration in the fluid; Nature of the fluid and its temperature

Target material properties
Stress as a function of strain; Strain-rate and temperature; Hardness; Fracture toughness; Stress level and residual stress; Shape; Microstructure; Fatigue; Melting point; etc

There is certainly no shortage of publications in the area of the role of microstructure on solid-particle erosion of ceramics. This can be seen from a series of three review articles that appeared in recent years.

A book, Erosion of Ceramic Materials, edited by Ritter and published in 1992 (Ritter), sums up two of this work. One was a review of solid particle erosion of ceramics and ceramic composites by Routbort and Scattergood (1992) in which it was

concluded that the effects of microstructure on erosion were quite significant and might have often been unrecognized in the earlier studies. The other was on the effect of ceramic second-phase particles on solid particle erosion of ceramic materials by Kosel and Ahmed (1992). Later in 1995, Lathabai (1995) discussed the erosion behaviour of a number of engineering ceramics in which the controlling influence of microstructure on erosion of these materials was highlighted.

Early reports of microstructural effects on erosion of ceramic materials appeared in the early 1980's. When extensive investigations showed that the theoretical models had failed to explain the erosion behaviour of engineering ceramics, it was argued that the reason for this non-correlation could be attributed primarily to microstructural aspects of erosion that were not modeled by the theories. Wiederhorn and Hockey (1983) studied the effect of hardness, H_t, and fracture toughness, K_{ct}, of target materials on the erosion rate for various brittle materials including three kinds of glasses, single crystal silicon and sapphire, sintered and hot-pressed aluminas, hot-pressed silicon nitrides and carbides using SiC erodent. Their results showed that while both theories provided a qualitative description of the erosion data, neither theory is quantitatively correct. It was proposed that one possible source for the rather large dependence of erosion rate on H_t and K_{ct} observed in their work compared to the theoretical predictions was the effect of the microstructure on erosion.

As a part of an extensive series of studies, Wada and Watanabe (1987a) investigated the erosion behaviour of thirteen kinds of commercial alumina ceramics using SiC erodent. They found that alumina ceramics with similar microstructural features exhibited similar erosion rates. Later, Heath et al. (1990) examined the erosion behaviour of fifteen commercial alumina ceramics and showed that no relationship could be established between any of the target properties (hardness, fracture toughness and Al_2O_3 content) and measured erosion rates. In contrast, the erosion behaviour of these aluminas could be related to microstructural parameters such as porosity, grain size, grain boundary chemistry and the bonding strength between the alumina grains and the matrix phase.

2.8.2 Alumina ceramics

Studies of the dependence of erosion behaviour on more controlled microstructures were mainly conducted on alumina ceramics. This is because among the engineering ceramics, alumina and alumina-based ceramics are the most commonly used wear resistant materials (Esposito and Tucci 1997). Miranda-Martinez et al. (1994) and later Franco and Roberts (1996 and 1998) have investigated the effects of grain size on the erosion rate and mechanism using a set of high purity polycrystalline aluminas with tailored microstructures. Dense alumina materials with a range of grain sizes were fabricated from the same batch of high purity, 99.9%, α-Al_2O_3 powder, using various sintering techniques (hot-pressing or pressureless sintering), sintering temperatures and duration. Remarkably, despite a wide range of grain sizes, from 1-14 μm, this set of alumina ceramics had essentially identical hardness and fracture toughness. Their results showed that the measured erosion rate was grain-size-dependent, being about one order of magnitude greater for aluminas of 14 μm grain size than for 1 μm grain size (Miranda-Martinez et al. 1994; Franco and Roberts 1996). An inverse square root dependence of erosion rate on grain size was established by Miranda-Martinez et al. (1994), who also showed that for alumina ceramics with a grain size greater than 2 μm, grain dislodgment event was the main erosion mechanism.

Other studies also showed that the grain size could affect the erosion mechanism of alumina ceramics (Breder et al. 1988; Srinivasan and Scattergood 1988a). Damage in fine-grained alumina ceramics was dominated by radial cracking and lateral chipping and that in the coarse-grained alumina was governed by grain ejection and very irregular radial crack patterns (Breder et al. 1988). Erosion experiments on several commercial and model aluminas by Srinivasan and Scattergood (1988a) have also confirmed that the grain size can affect the erosion mechanism.

The effect of grain boundary phases on erosion rates and mechanisms of alumina ceramics was investigated by Zhou and Bahadur (1991, 1993 and 1995). Five kinds of alumina materials, with and without the silicate glassy phase and zirconia, were subjected to airborne erosion using SiC particles. It was found that the single-phase

alumina exhibited the poorest erosion resistance, and the erosion resistance of the alumina was enhanced by the presence of intergranular secondary phases, such as silicate glass and zirconia. It was concluded that the intergranular secondary phases improved the bonding between the alumina grains and also increased the erosion resistance by absorbing part of the impact energy. However, the presence of large amounts of silicate glassy phase in alumina degraded the erosion resistance due to the much lower resistance to erosion of the glassy phase than that of the alumina grains (Zhou and Bahadur 1991). SEM studies of damage features of these materials by single and multiple particle impacts revealed that the presence of intergranular secondary phases also affected the erosion mechanism. For single-phase alumina, the dominant material removal mechanism was intergranular fracture associated with a high erosion rate, while for alumina containing secondary phases, the damage features were chipping and fragmentation of grains, resulting in a lower rate of material removal (Zhou and Bahadur 1993).

More recently, Zhang et al. (2000b) have examined the effects of grain size and grain boundary glassy phase on erosion rates and mechanisms of alumina ceramics under both airborne and slurry erosions. It was again observed that the erosion rate increased with the increasing grain size, and the presence of a small amount of intergranular glassy phase had a beneficial effect on the erosion resistance of alumina ceramics. The erosion mechanisms in both airborne and slurry erosion were found to depend strongly on the angle of incidence. However, no clear relationship between the erosion mechanism and the alumina grain size could be established.

The porosity of target materials was also found to affect the erosion mechanism (Wada and Watanabe 1987b; Heath et al. 1990). It has been previously observed that erosion damage in alumina ceramics was characterized by grain boundary cracking (Shipway and Hutchings 1991). Extension and linking up of cracks with nearby pores and flaws have been proposed to result in large unit volume removal (Miranda-Martinez et al. 1994).

It is now well appreciated that microstructure can have a controlling influence on erosion of alumina ceramics. Dense, fine-grained alumina materials containing a

small amount of intergranular glassy phase would be good candidates for use in applications requiring erosion resistance. However, whether this model can be applied to other engineering ceramics is questionable. Alumina ceramics generally contain equiaxed grains and exhibit anisotropy of thermal expansion on the crystal axis. The thermal expansion mismatch can induce grain boundary stress upon cooling from the sintering temperature and thus weakens the bonding strength between alumina grains. Both the equiaxed grain morphology and the weak bonds between the grains determine that the erosion mechanism would be grain dislodgment which is often associated with a high erosion rate when alumina ceramics are exposed to solid particle impact at high angles (Ritter 1985; Ritter et al. 1986). The grain dislodgment mechanism may not hold for erosion of *in-situ* reinforced silicon nitride and transformation toughened zirconia ceramics. Therefore, in order to establish the apparent connection between the microstructure and erosion of brittle materials, systematic studies on more representative and flexible model materials are needed.

2.8.3 Other engineering ceramics

Compared to alumina ceramics, much less research has been done on other engineering ceramics in the sense of the dependence of erosion behaviour on microstructure. A few representative studies for the specific cases of ZrO_2-based ceramics, SiC and Si_3N_4 shall be briefly reviewed.

Lathabai (2000) investigated the effects of grain size and varying degree of transformability (from tetragonal to monoclinic ZrO_2) on the slurry erosion behaviour of CeO_2-stabilized tetragonal zirconia polycrystals (Ce-TZP) using SiC, Al_2O_3 and SiO_2 erodents of similar particle size distribution. It was found that the effect of grain size was apparent only in aggressive erosion environments provided by the hard SiC and Al_2O_3 grits, and high slurry velocities. The erosion rate increased as the grain size and transformability of the target materials increased. More significantly, the erosion mechanisms of Ce-TZP with different grain sizes eroded by various erodent particles were essentially the same, involving grain dislodgment, deformation of the grains and delamination of the deformed material. Clearly, further investigations are needed for

feasibility of designing an optimum microstructure for maximum erosion resistance for a given set of conditions.

Routbort and Scattergood (1980b and 1980) compared erosion behaviour of reaction-bonded (RB) and hot-pressed (HP) SiC ceramics. The RB-SiC contained 10.5 wt% Si and possessed a microstructure with coarse SiC grains (~100 μm in size) embedded in a matrix of small SiC grains and free Si, while the HP-SiC was a dense, high purity material consisting of fine equiaxed SiC grains with an average grain size of 2-4 μm. Their results showed that the dependence of erosion rate on the erodent particle size differed significantly for these two materials. The erosion mechanism was also different for the two materials; being transgranular fracture and grain dislodgment for HP-SiC, and lateral cracking and preferential erosion of the softer Si phase for RB-SiC. It was proposed that such differences could be accounted for by the effects of grain size and the presence of weak grain boundaries. However, it was also pointed out that "silicon carbide is not a suitable material for systematically studying the effect of grain size on erosion, because it is difficult to change grain size while keeping everything else constant". More than a decade later, Wang et al. (1995) examined the effects of porosity and grain size on erosion behaviour of three SiC ceramics fabricated using different techniques: pressureless sintering, hot pressing and hot isostatic pressing. It was observed that the erosion rate increased as the porosity and the grain size increased. However, a clear relationship between the erosion mechanism and the microstructure still remain elusive.

There are also a few systematic studies on the dependence of erosion behaviour on the microstructure of Si_3N_4 and sialon ceramics. Since sialon ceramic is the proposed model material in this investigation, the relevant literature will be dealt with in greater detail in the following section.

2.9 Erosion of Silicon Nitride and Sialon Ceramics

Sialon ceramic and its parent material Si_3N_4 offer the possibility of improved fracture resistance by *in-situ* whisker reinforcement. The microstructure of *in-situ* reinforced (ISR) Si_3N_4-based materials includes large, elongated grains that can improve

toughness by crack bridging, crack deflection, crack blunting and grain pullout. Indeed, there has been continuous research into the erosion of Si_3N_4 and Si_3N_4-based materials over the years. Gulden (1981b) investigated the erosion of four commercial Si_3N_4 ceramics. Her results supported the predictions of the quasi-static model. Similar conclusions were also drawn by Wada (1992) in a study of the erosion of 16 kinds of commercial Si_3N_4 ceramics. However, in much of this work, the primary goal seems to have been the verification of the validity of the theoretical models rather than a systematic investigation of the influence of the microstructure.

Until recent years, such an attempt has been made by Ritter and co-workers (Ritter et al. 1991) and later by Routbort and colleagues (Marrero et al. 1993; Karasek et al. 1996; Routbort 1996). Ritter et al. (1991) examined the erosion rates of two sintered silicon nitride ceramics with identical composition but different microstructures. The two Si_3N_4 ceramics were pressureless sintered to 99% theoretical density using the same batch starting powder. The final products possessed a microstructure consisting of fine whisker-like grains with a bimodal size distribution, designated as fine-grained Si_3N_4. The coarse-grained Si_3N_4 was prepared by annealing the fine-grained material at a high temperature. The resultant material had a microstructure containing much coarser grains but with a similar grain aspect ratio to that of the fine-grained material. It was found that, unlike in erosion of alumina and SiC ceramics, the erosion rate of the coarse-grained Si_3N_4 was actually lower than that of the fine-grained material. However, this finding was not explained in terms of the effect of microstructure on erosion mechanism, since the primary goal of the study was to address the correlation between the erosion data and indentation fracture mechanics analysis.

Marrero and co-workers (1993) compared the erosion behaviour of ISR Si_3N_4 and an 'equivalent' fine-grained hot pressed Si_3N_4 fabricated from the same batch of starting powder. The fine-grained Si_3N_4 consisted of a combination of equiaxed and elongated grains with a mean grain size of 1 μm, while the ISR Si_3N_4 contained much coarser grains but with a similar grain aspect ratio. The conventional fracture toughness (long-crack toughness) value of the ISR Si_3N_4 was significantly higher than that of the fine-grained Si_3N_4. However, such a difference did not result in a

significant difference in erosion rates of these materials. It was suggested that the small difference in erosion rate for the two materials could be accounted for by the small differences in other mechanical properties, such as hardness. The role of microstructure on erosion behaviour was again not discussed.

To our knowledge, there have been only three publications on the erosion behaviour of sialon materials. Wada (1992) compared the erosion rate and mechanisms of a series of α/β sialon composites containing 3.5-100 wt% α-sialon phase using both SiC and Al_2O_3 erodent particles. The Vickers hardness of these materials was found to decrease steadily as the α-sialon content decreased; being 23 and 15.3 GPa for materials containing 100 and 3.5 wt% α-phase, respectively. The fracture toughness, however, exhibited an anomalous behaviour; being approximately 7.5 MPa m$^{1/2}$ for composites containing 3.5-71 wt% α-sialon content, and <6.6 MPa m$^{1/2}$ for pure α-sialon materials. A strong dependence of erosion rate, ΔE, on target hardness, H_t, and erodent particle hardness, H_p, was found, and an empirical relationship, $\Delta E = (H_t/H_p)^a$, was developed to describe such dependence. The dependence of the erosion mechanism on H_t and H_p was also observed; being brittle fracture for $H_t/H_p < 1$ and minor scratching for $H_t/H_p > 1$, respectively. As can be seen, such an approach is again an attempt to rectify the theoretical models rather than to clarify the effect of microstructure on erosion. A similar approach was also taken by Liu and co-workers (1998). They investigated the erosion behaviour of α/β sialon composites which contained 0-40 and 90 wt% α-phase using SiC erodent. Their results showed that the erosion rate of these materials decreased with increasing hardness (H) and toughness (K_c) and could be expressed by $\Delta E = 6.53\ H^{1.51}\ K_c^{-3.33}$. Again, the effect of microstructure on erosion was neglected.

The only study on the influence of microstructure on the erosion behaviour of sialon ceramics was carried out by Park and colleagues (1997). They investigated the erosion behaviour of a number of dense sialon-based ceramic materials containing 0-20 wt% Si_3N_4 whiskers using SiC erodent at room temperature and at an elevated temperature (500°C). SEM examinations of the polished and etched sections of these materials revealed that the grain sizes of both the sialon matrix and Si_3N_4 whiskers increased as the whisker content increased. The mechanical property analysis showed

that the fracture toughness increased while the flexural strength decreased as the whisker content increased. The hardness, however, remained almost constant regardless of the various whisker contents. The erosion results showed that the erosion rate increased as the erosion temperature and the content of Si_3N_4 whiskers increased. SEM examinations of the eroded surfaces of these materials revealed that the major erosion mechanism was grain pullout and plastic deformation. It was concluded that the higher erosion rate at the elevated temperature was due to the severe plastic deformation at this temperature, while the higher material removal rate observed for materials containing higher amount of Si_3N_4 whiskers was a result of the grain size effect.

Engineering ceramics possess complex microstructures with varying porosity, grain size, grain morphology, grain boundary chemistry and amount of grain boundary phases. To date, there has been no systematic study into the effects of various microstructural parameters on the erosion behaviour of these materials.

2.10 Summary

Based on this background, the primary goal of the present study is to conduct erosion tests on a carefully prepared model system that allows independent control of the various microstructural parameters and to clarify the effect of these parameters on the erosion behaviour of ceramic materials.

Chapter 3

EXPERIMENTAL METHODOLOGY

3.1 Introduction

This chapter outlines the experimental details relevant to this work. Section 3.2 describes the methods for processing Ca α-sialon ceramics. It involves the selection of starting powders, composition calculations, powder processing, green powder compaction, and various sintering methods employed to densify the compact as well as the post-sintering heat treatment for devitrification of the intergranular glassy material. Section 3.3 provides the details of the erosion test methods. It includes descriptions of the erodent materials and the erosion test rigs, as well as the calibrations of the erodent particle impact velocity and feed rate or flux. The final section, 3.4, focuses on the characterization techniques utilized to analyze the relevant materials.

3.2 Ceramic Processing

3.2.1 Powders

Compositions of Ca α-sialon can be represented by the formula $Ca_{m/2}Si_{12-(m+n)}Al_{m+n}O_nN_{16-n}$. The Ca α-sialon samples designed for the present work are located on the $m:n$ = 2:1 line within the modified phase diagram (Fig. 2.3b). The designation CA1005 refers to a design composition of m = 1.0 and n = 0.5, and CA2613 and CA3618 describe the materials of compositions m = 2.6, n = 1.3 and m = 3.6, n = 1.8, respectively. The starting powders used were commercial Si_3N_4 (H. C. Starck, Goslar, Germany), AlN (H. C. Starck, Goslar, Germany) and $CaCO_3$ (APS Chemicals, NSW, Australia). Their grades and relevant properties are listed in Table 3.1. Powder mixtures were calculated based on molar balancing of the Ca α-sialon formula (see

above), taking into account the presence of a surface layer of oxides on nitride powders, in particular, the SiO_2 and Al_2O_3 layers on the Si_3N_4 and AlN particles, respectively. The weight percentages of the starting powders of the three selected compositions are shown in Table 3.2.

Table 3.1 Grades and relevant properties of the starting powders

Powder	Grade	Description*	Oxygen Content in Nitride Particles (wt%)*	d_{50} (μm)	Specific Surface Area $(m^2/g)^*$
Si_3N_4	M11	α-phase>90%	1.2	0.7*	12-15
AlN	AT	Fe<500ppm	1.14	6-10*	<2
$CaCO_3$	Lab	98-99%	–	4.2^+	–

* Manufacturer's data sheet. $^+$ Measured by SEM analysis.

Table 3.2 Weight percentages of the starting powders of the three compositions

Composition	Si_3N_4 (M11) (wt%)	AlN (AT) (wt%)	CaO (wt%)
CA1005	84.602	10.590	4.808
CA2613	61.981	26.148	11.871
CA3618	48.964	35.105	15.931

100 g batches of powder mixture for each composition were measured and ball milled in 110 ml isopropanol with 250 g Si_3N_4 milling media for 30 h in a polyethylene jar on a roller bench. The amounts of isopropanol and Si_3N_4 media required for ball milling are crucial. The quantity of isopropanol determines the viscosity of the mixture slurry. A low viscosity slurry results in more abrasive wear of Si_3N_4 media and hence affects the composition of the mixture, while a high viscosity obstructs the formation of a uniform slurry. Similarly, an excessive or an insufficient Si_3N_4 media causes greater abrasion of the milling media or non-uniform slurry, respectively.

Once the milling was completed, the slurry was drained into a shallow pan with a large surface area to reduce powder segregation and it was then dried in a fan-forced

oven at 84°C. This temperature is just under the boiling point of the isopropanol to avoid splashing of the slurry. The dried powder mixture was further hand mixed in an alumina mortar and pestle for 10 minutes to prevent any powder segregation induced from the drying course.

3.2.2 Powder compaction

To date, the most traditional process for powder compaction is dry pressing, either uniaxially or isostatically (Reed and Runk 1976; Reed 1988; McEntire 1991). A uniaxial press usually involves a die cavity with a rigid frame and moveable upper and lower punches. Ceramic powder is filled into the die cavity and pressure is applied through the pressing punch to compact powder to a specific size and shape via the rearrangement and the deformation of the particles. It is a simple and cheap process. However, interface friction caused by the particle-particle interaction and, more significantly, the powder-die-wall interaction diminishes the pressure available for compaction (Briscoe and Rough 1998). Such an effect becomes more pronounced as the distance from the pressing punch increases and, hence, results in non-uniform density along the length of the pressed green body (Glass and Ewsuk 1997; Briscoe and Rough 1998).

A Cold Isostatic Press (CIP), on the other hand, offers a hydrostatic powder compaction method which avoids the powder–die-wall frictional effect. As a result, the density gradients in the green body are significantly minimized, but not completely eliminated since interparticle friction forces exist. However, CIP requires special airtight soft moulds to house the powder and then to immerse in a pressurized vessel filled with water suspended oil during the operation. The leakage as well as the cleaning process of such moulds between different sample batches are significant concerns.

To avoid the drawbacks from the uniaxial press and the complications of the sample mould in CIP, in the present work, a two-stage powder compaction process was employed. That is a low pressure uniaxial pressing followed by a higher pressure CIP. The powders, approximately 7 g for each sample, were uniaxially pressed into 25 mm

diameter pellets under 10-15 MPa pressure, aiming to produce a defect free (apart from the density gradients) green body with sufficient strength for sample handling. The aspect ratio of the pellets, i.e. the height over the diameter, was kept low to minimize the powder-die-wall friction and the density gradients (Glass and Ewsuk 1997; Briscoe and Rough 1998). The green pellets were then vacuum-sealed in airtight plastic bags and subjected to CIP at a much higher pressure, 200 MPa, for further compaction. The resultant green densities are usually above 60% of their sintered counterparts. SEM examination on the sintered samples showed that there is no notable density variation across the samples.

3.2.3 Sintering

Fabrication of engineering ceramics involves high-temperature treatment of the green powder compacts. Such a process is called sintering, or more casually densification. Densification of the Ca α-sialon ceramics can be achieved by both pressureless sintering and hot pressing.

3.2.3.1 Pressureless sintering

In order to clarify the effect of composition on microstructure, the three Ca α-sialon compositions used were pressureless sintered. Four green pellets were packed in a cylindrical graphite crucible. To avoid decompositions of the starting materials at elevated temperatures, the green compacts were embedded in a 50 wt% Si_3N_4:50 wt% BN packing powder mixture. The green compacts were first calcined at 900°C for 1 h under vacuum to decompose $CaCO_3$ to CaO. Sintering was carried out in a nitrogen atmosphere in a graphite sintering furnace (Thermal Technology U.S.A.) equipped with a control system. The temperature was monitored using a radiation pyrometer. The sintering schedule can be summarized as follows:

(1)   evacuate the chamber to $< 2 \times 10^{-2}$ Torr

(2)   flush the chamber with high purity N_2 and then pump the chamber down again

(3)   heat the furnace to 900°C at 20°C/min and dwell for 1 h for calcination

(4)   backfill the chamber with N_2 to just above atmospheric pressure and maintain a positive gas flow

(5)   heat the furnace to 1800°C at 20°C/min and dwell for 4 h for sintering

(6)   switch off the furnace power and allow rapid cooling. The cooling rate was estimated to be approximately 40°C/min from 1800 to 1500°C and 25°C/min between 1500 and 1200°C.

3.2.3.2 Hot pressing

In order to elucidate the effects of sintering conditions on microstructures, two Ca α-sialon compositions, namely CA1005 and CA2613, were selected for hot pressing. Pellets of 8 g each were packed into a graphite die of 25 mm diameter with moveable upper and lower plungers. Prior to packing, the plungers as well as the inner wall of the graphite die were painted with a thin ethanol suspended BN coating to prevent reactions between the sample and the die assembly. Hot pressing was performed in a nitrogen atmosphere in a Thermal Technology hot pressing/sintering furnace equipped with a control system. The temperature was again monitored using a radiation pyrometer. The pressure was applied when the temperature first reached 1000°C, kept constant at 25 MPa during the sintering stage and was released at 1000°C upon cooling. The sintering/pressing schedule can be summarized as follows:

(1)   evacuate the chamber to $< 2 \times 10^{-2}$ Torr

(2)   flush the chamber with high purity N_2 and then pump the chamber down again

(3)   heat the furnace to 900°C at 20°C/min and dwell for 1 h for calcination

(4)   backfill the chamber with N_2 to just above atmospheric pressure and maintain a positive gas flow

(5)   heat the furnace to desired sintering temperature at 20°C/min

(6)   once the temperature reaches 1000°C, start to apply the pressure at a rate of 1 MPa/min to 25 MPa

(7)   keep the pressure at 25 MPa during sintering

(8)   switch off the furnace power for rapid cooling and release the pressure at 1000°C.

3.2.3.3 Heat treatment

Post-sintering heat treatment devitrifies the grain boundary glass which alternatively modifies the microstructure and hence the mechanical properties of the materials. In order to investigate the effect of intergranular glassy phase on the material properties,

heat treatments were carried out on all three pressureless sintered Ca α-sialon compositions.

Sintered samples were packed in a 50 wt% Si_3N_4:50 wt% BN powder bed in a cylindrical graphite crucible. Heat treatment was carried out in a nitrogen atmosphere in a graphite furnace. The following heat treatment schedule was utilized:

(1)   evacuate the chamber to $< 2 \times 10^{-2}$ Torr

(2)   flush the chamber with high purity N_2 and then pump the chamber down again

(3)   backfill the chamber with N_2 to just above atmospheric pressure and maintain a positive gas flow

(4)   heat the furnace to 1300°C at 20°C/min and dwell for 12 h

(5)   switch off the furnace power and allow rapid cooling.

3.3 Erosion Tests

3.3.1 Erodent materials

The erodent particles used were commercial grade SiC and garnet abrasive grits, supplied by Carborundum Australia and Australian Mining, respectively. Both grits were angular in shape although the corners of the garnet particles were slightly rounded. The SiC particles had a size distribution between 210-500 μm and the garnet grits a size distribution between 200-600 μm (Fig. 3.1). The particle size distribution analysis, as determined by the laser diffraction technique, showed the median diameter, d_{50}, to be 388 and 400 μm for the SiC and garnet particles, respectively. The chemical compositions and the mechanical properties of the erodent particles are given in Table 3.3.

The apparent solid density of the erodent particles was determined using a helium pycnometer (AccuPyc 1330 Micromeritics densitometer). The hardness and indentation fracture toughness were determined by micro-indentation tests at a load of 1.96 N, 15 s. The erodent particles were mounted in thermosetting resin, ground, and polished to a <0.5 μm diamond finish for indentation testing. Morphologies of the two erodent particles were examined with a JEOL JSM-840A scanning electron

microscope in secondary electron (SE) imaging mode. Prior to SEM examination, the samples were gold coated to prevent charge accumulation. The accelerating voltage used was 20 kV.

Fig. 3.1. SEM images of erodent particles: (a) garnet particles and (b) SiC grits.

Table 3.3 Properties of the erodent particles

Property	Garnet	SiC
Chemical Composition* (wt%)	36 SiO_2, 30 FeO, 20 Al_2O_3, 6 MgO, 2 Fe_2O_3, 1 MnO, 1 CaO, and 1 Ti O_2	98.85 SiC, 0.60 (Si+SiO_2), 0.20 Fe, 0.15 Al, and 0.20 Free C
Apparent Solid Density (ⁱ ⅃ ⁄ ᵃ)	4100	3200
Hardness[+] (GPa)	1᠁᠁	30.4
Toughness[+] (MPa $m^{1/2}$)	1.10	2.5
Melting Point* (°C)	1250	–
Particle Size, d_{50} (μm)	400	388

* **Manufacturer's Data Sheet**

[+] **Measured by Vickers Indentation at 1.96 N load**

3.3.2 Airborne erosion tests

3.3.2.1 Experimental system

The experimental system for airborne erosion tests was a gas-blast type erosion rig, shown schematically in Fig. 3.2. It consists of a compressed air supply, a 20 kg capacity erodent holding tank, sections of pipeline (including a T-intersection), an ejector nozzle and a sample holder.

When the driving compressed air passed through the T-intersection, a region of low pressure was created and the erodent particles were sucked up through the suction tube. Consequently, the particles were entrained in the stream of compressed air and accelerated down a 125 mm long, 5.4 mm inner diameter steel nozzle to impact on the stationary target. The particle velocity was controlled by means of the compressed air. The angle of impingement was varied by tilting the ejector nozzle via a mechanical lever.

This type of test rig, in general, provides excellent control over the conditions to which the specimens are exposed. For this reason it has become the most reliable and popular tester for laboratory research into the mechanisms of erosion and the influence of operating variables on wear performance (Zu et al. 1990).

3.3.2.2 Calibration

Investigations of erosion by air-particulate stream involve the measurement of several important parameters, such as angle of impingement, particle flux and particle velocity. In our laboratory, the impingement angle can be adjusted to an accuracy of $\pm$ $2°$ according to a spirit level. The particle flux, f, was measured by collecting the erodent particles from the nozzle exit over a fixed period of time. It was defined as follows: f = the mass of the collected erodent particles divided by the area of the nozzle orifice and the period of time, generally in units of g per $cm^2 s$.
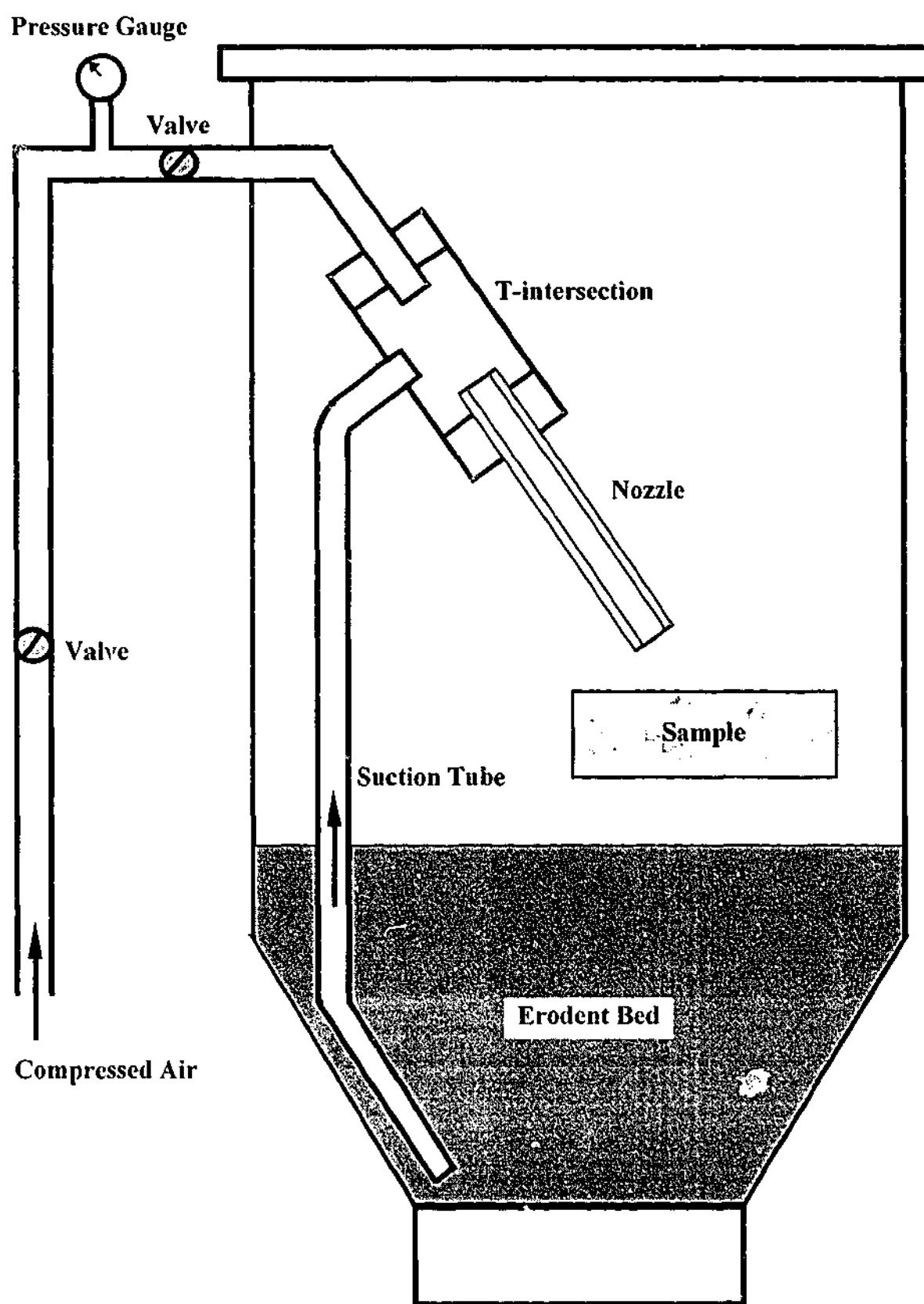
Fig. 3.2 A schematic of the gas-blast erosion test apparatus.

The particle velocity was controlled by means of the compressed air pressure and measured using the rotating double disk technique (Ruff and Ives 1975). Following Ruff and Ives's design, a similar device was made to measure the particle velocity (Fig. 3.3). It consists of two parallel aluminium disks (A and B) mounted on a common steel shaft. Disk A which is closer to the nozzle exit was lined with a thin rubber layer to prevent unwanted erosive wear. A radial slit was made on disk A which permits the air-particulate stream to pass through and eventually leave an erosion mark on disk B.
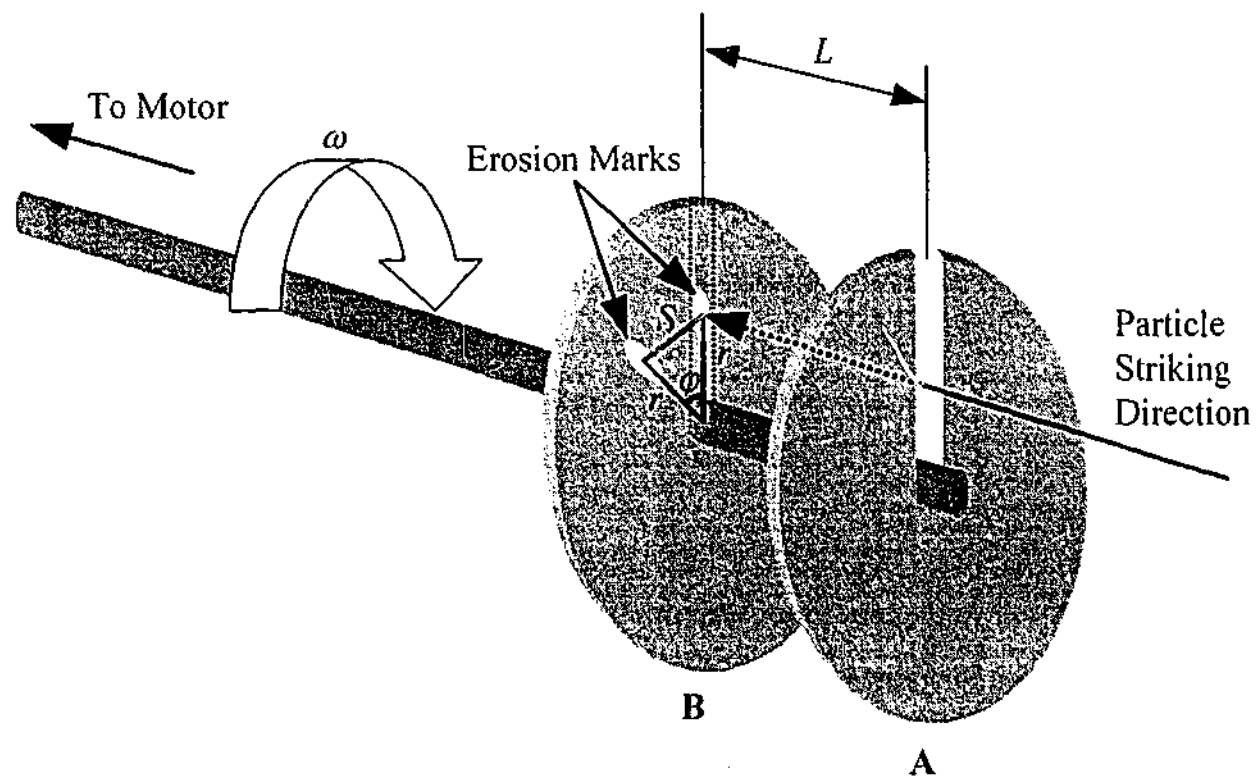
Fig. 3.3. Illustration of the double disk device.

To measure the particle velocity, the device was placed in front of the orifice of the eroding nozzle. Two erosion exposures were made, one with the disks stationary and the other with the disks rotating at a constant angular velocity, ω, which was determined by a stroboscopic light source. Now, if the distance between the two disks, L, is known, according to the time-of-flight rule, the average particle velocity, v, can be obtained by the following relationship:

$$v = L/t \tag{3.1}$$

where t is the time required for particles to travel from disk A to B.

During the time, t, the disks rotated through an angular displacement, θ,

$$\theta = 2\pi\omega\, t \qquad\qquad (3.2)$$

By substituting eq. (3.2) into (3.1), the average particle velocity is given by

$$v = 2\pi\omega L/\theta \qquad\qquad (3.3)$$

For convenience, eq. (3.3) can be further rewritten as:

$$v = 360°\cdot\omega\, L/\varphi \qquad\qquad (3.4)$$

where φ is the angle corresponding to the angular displacement θ and can be calculated by measuring the S and the r values. S is the linear separation between the center of the two erosion marks and r is the distance from the centre of the erosion marks to the centre of the disk B.

In the present work, the average particle velocity was measured as a function of the compressed air pressure. By taking the typical values of the present setup: $L = 24.7$ mm and $\omega = 60.7$ Hz, and determining the φ value corresponding to various air pressures, p, the average particle velocity was readily calculated using eq. (3.4). The v^2-p relationship is plotted in Fig. 3.4. Data presented as mean and standard deviation of three measurements.

From Fig. 3.4, the relation $v^2 \propto p$ was established, indicating that the kinetic energy of the erodent particles ($1/2\cdot mv^2$; m is the mass of the particle) is proportional to air pressure.

3.3.2.3 Experimental procedure

The specimens prepared for erosion tests were machined to dimensions $20\times20\times(3\text{-}10)$ mm^3 or $\phi(20\text{-}25)\times5$ mm^2. All tests were performed on the bulk material whose surface layer was removed by a surface grinder with a resin-bonded diamond cup wheel. Surfaces for erosion testing were further ground to an 800-mesh finish to ensure consistent surface properties.
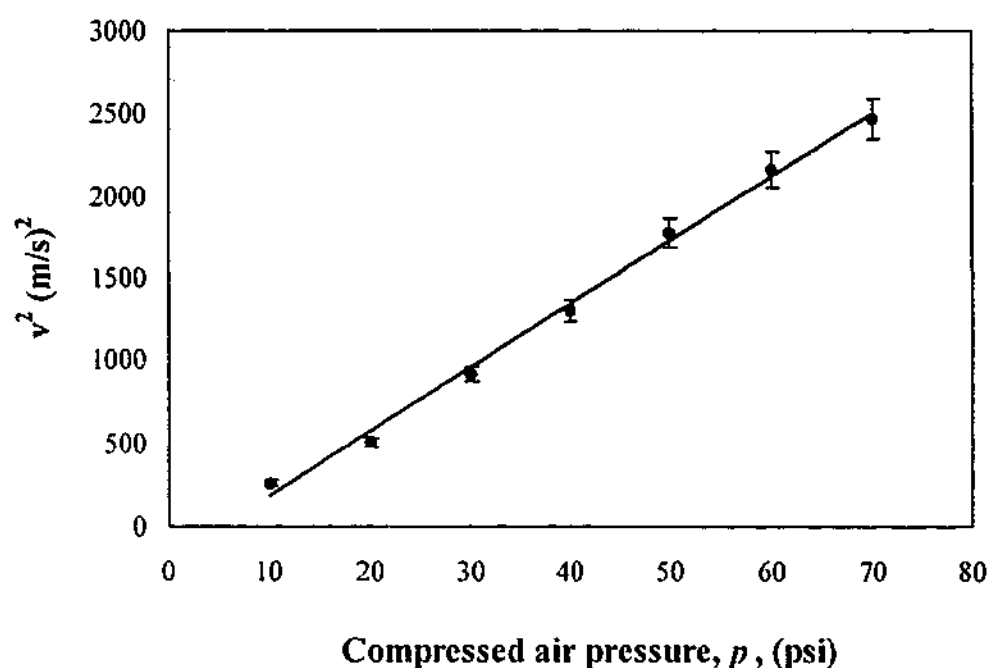
Fig. 3.4. Particle velocity square as a function of compressed air pressure.

The samples were placed 13.8 mm from the nozzle orifice at any impingement angle. The impact angles used were 30°, 45°, 60° and 90° for alumina, zirconia and pressureless sintered sialon ceramics, and 30° and 90° for silicon nitride, silicon carbide and hot-pressed sialon materials. Most samples were eroded with a fixed amount of erodent at 20 m/s in six exposures, although in some cases a higher velocity of 37 m/s was used. Erodent materials used were garnet and silicon carbide grits.

Mass loss from the target material was measured before and after the exposure using an analytical balance with an accuracy to ±0.1 mg. Wear volume was calculated from the weight change and the bulk density of each material. Cumulative volume loss was plotted as a function of the amount of erodent impacting on the surface. The erosion rate (ΔE) was defined as follows: ΔE = volume loss from the specimen divided by the mass of particles used, generally in units of m^3 per kg.

3.3.3 Slurry jet erosion tests

3.3.3.1 Experimental system

Slurry erosion tests were carried out with a custom designed slurry jet apparatus, shown schematically in Fig. 3.5. Briefly, the equipment utilized a compressed air supply, a 60 l capacity slurry holding tank, an agitator, a diaphragm pump, sections of pipeline, an ejector nozzle (inner diameter of 4 mm) and a sample holder.

The slurry, a mixt .   .   .   .   garnet grits, was pumped from the holding tank to the ejector noz .   .   .   .   .ch it emerged as a high velocity jet to strike the target surface. The .   .   .   ..olids and the velocity of this slurry stream were varied by adjusting the agitat.: ..peed and the compressed air pressure, respectively. The angle of impingement was varied by tilting the specimen holder via a mechanical lever.

3.3.3.2 Calibration

The major variables examined were angle of impingement, particle loading (i.e. mass fraction of erodent particles in the slurry), particle flux, and velocity of the slurry jet. The angle of impingement can be adjusted to an accuracy of $\pm 2°$ according to a spirit level.

To determine particle velocity, flux and solid loading, a simple method was developed which involves collecting the amount of slurry released form the nozzle ejector over a fixed period of time and consequently solving the following equations simultaneously:

$$V_S + V_L = V_T \tag{3.5}$$

$$V_S \cdot \rho_S + V_L \cdot \rho_L = M_T \tag{3.6}$$

where V_S and V_L refer to the volumes of the solid particle and the liquid, respectively, while ρ_S and ρ_L correspond to the densities of the solid particle and the liquid. V_T and M_T are the total volume and the total mass of the collected slurry.
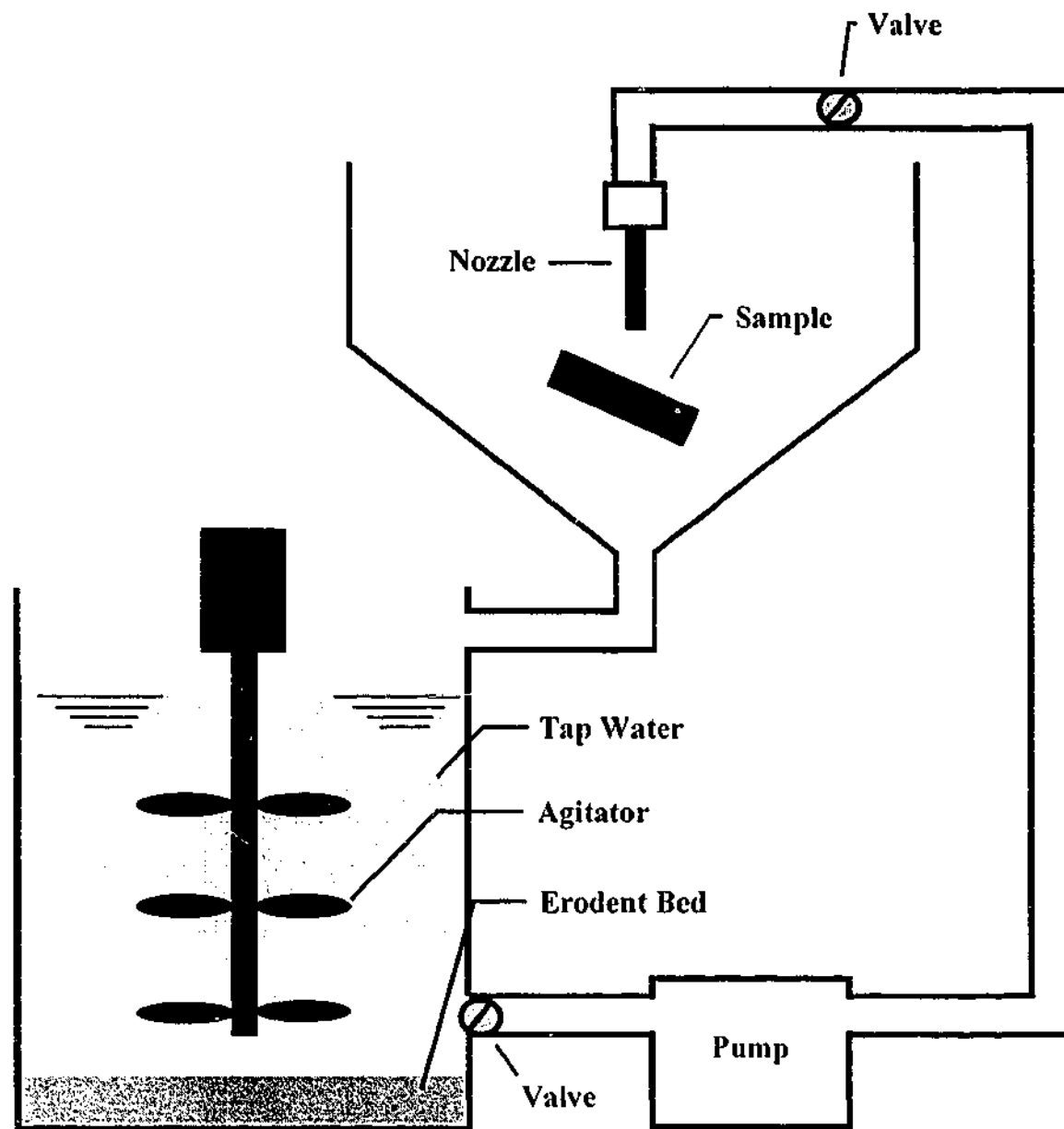
Fig. 3.5 Schematic diagram of the slurry erosion test apparatus.

The apparent solid density of the particle was measured using helium pycnometer. The slurry collecting time, t, was controlled by a stopwatch, and the total volume and the mass of the slurry were determined by analytical beakers and an analytical balance. Assuming the abrasive particle velocity is the same as the slurry velocity, v, it is straightforward to show that

$$v = V_T/[(\pi r^2)\, t] \tag{3.7}$$

where r is the radius of the nozzle orifice.

Consequently, the particle flux F is given by (Turenne et al. 1989)

$$F = v\, \rho_S f \tag{3.8}$$

where f is the particle volume fraction which can be expressed as

$$f = V_S/V_T \tag{3.9}$$

Finally, the solid particle loading, C, can be derived by

$$C = \rho_S V_S/M_T \tag{3.10}$$

The particle velocity corresponding to various compressed air pressures was determined for a range of particle loadings – 3.1 wt%, 7.6 wt% and 11 wt%. The v^2-p relationship is shown in Fig. 3.6. Data presented as mean and standard deviation of three velocity values corresponding to the above three particle loadings. From Fig. 3.6, the relation $v^2 \propto p$ was again established, indicating that the kinetic energy of the erodent particles entrained in a slurry stream is also proportional to air pressure.

It is important to note that, even under the same air pressure, the particle velocity varies slightly with the particle loading, C. The v-C relationship for various air pressures is presented in Fig. 3.7. As can be seen, there is a slight decrease in particle velocity with increasing particle loading. Such phenomenon will be discussed in Chapter 7.
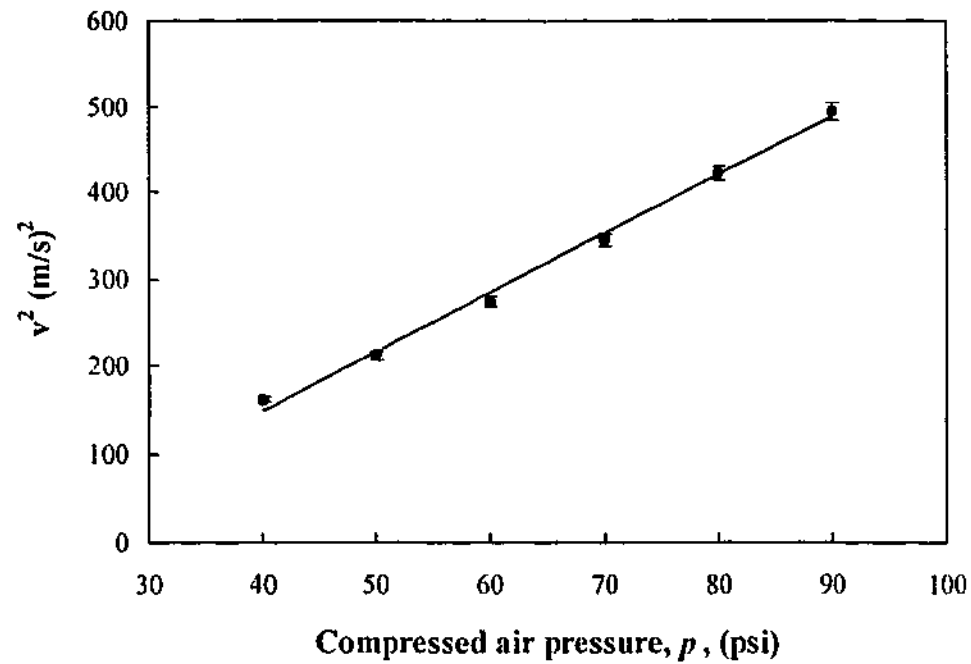
Fig. 3.6. Particle velocity square as a function of compressed air pressure.
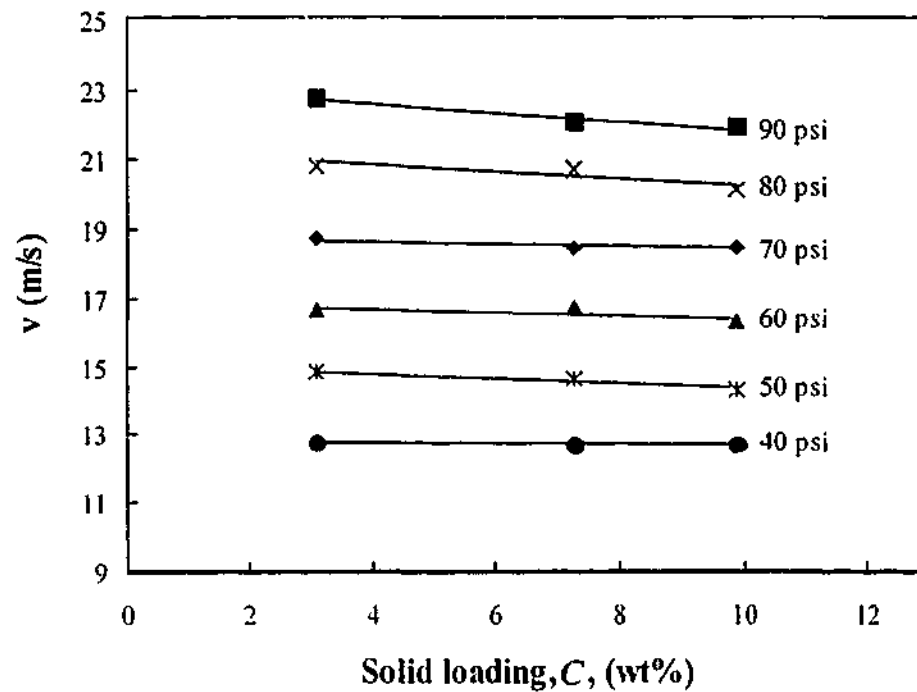
Fig. 3.7. Particle velocity as a function of the particle loading for various air pressures.

3.3.3.3 Experimental procedure

The specimens, with the same dimensions as described in the airborne tests, were mounted directly under the ejector nozzle, approximately 13.8 mm below the nozzle

exit, for all tests. The effect of the angle of impact was studied for alumina ceramics at 15°, 30°, 45°, 60°, 75° and 90°. In this series of tests, the particle loading was held at 7.6 wt% and the slurry velocity was 16.5 m/s. The effect of slurry velocity was determined for a fixed particle loading, 7.6 wt%, at an angle of impact of 30°. The velocities tested were 12.7 m/s, 14.5 m/s, 16.5 m/s, 18.6 m/s, and 20.5 m/s. The effect of particle loading was measured at a fixed slurry velocity of 16.5 m/s, again at a fixed angle of impact, 30°. The different particle loadings used were 3.1 wt%, 7.6 wt% and 11 wt%.

Each sample was eroded with a fixed amount of erodent in five exposures. The amount of erodent used in a single exposure was controlled by timing the release of the slurry as determined by careful pre-calibration. The specimens were ultrasonically cleaned, oven dried at 150°C to eliminate moisture trapped at pores and weighed before and immediately after the erosion test. As in the case of airborne erosion testing, the cumulative erosive volume loss was plotted as a function of the mass of erodent particles used. The steady state slurry erosion rate (ΔE_S) was determined as the ratio of the volume loss from the specimen to the mass of the erodent particles used, again from the slope of the linear part of the cumulative volume loss-erodent mass plot.

3.4 Analytical Techniques

3.4.1 X-ray analysis

The phase analysis of the ceramic materials was made by X-ray diffractometry (XRD), while the lattice parameters of the α-sialon ceramics were determined by the Güinier-Hägg X-ray camera.

3.4.1.1 X-ray diffractometry

The sample surfaces prepared for XRD analyses were bulk internal surfaces with beveled edges to eliminate any surface and edge effects. The analyses were performed on a Rigaku-Geigerflex diffractometer with nickel filtered CuK_α radiation. The X-ray

generator was operated at 40 kV and 22.5 mA. The diffraction spectra were collected at Bragg angles between 10° and 80°, using a scan speed of 0.5°/min and a step size of 0.02°. Analyses of the spectra were performed on the Traces 5.2 program.

Crystalline phases were identified using the JC PDS Powder Diffraction File and the following notations were used to define the intensity of the diffraction peaks: tr = trace (relative peak intensity <3%); vw = very weak (<10%); w = weak (10-20%); mw = medium weak (20-40%); m = medium (40-55%); ms = medium strong (55-70%); s = strong (70-85%); vs = very strong (>85%).

3.4.1.2 Güinier-Hägg X-ray camera

Samples for lattice parameter measurement were crushed to a fine powder. Si was used as an internal standard. The measurements were performed on a Güinier-Hägg X-ray camera with $CuK_{\alpha 1}$ radiation. The recorded X-ray powder diffraction photographs were analysed by a computer-linked line scanner (LS-18) system and program SCANPI (Johansson et al. 1980; Wang et al. 1999a). The lattice parameters were calculated using the least-squares refinement program PIRUM (Werner 1969; Johansson et al. 1980).

3.4.2 Scanning electron microscopy

Microstructures of the bulk material and the eroded surfaces of the samples were examined using scanning electron microscopy (SEM).

The samples for microstructural examinations were wax-mounted onto the stainless steel holders and were ground using a surface grinder with a diamond abrasive impregnated resin cup wheel to remove the surface layers. The samples were then ground with 15 μm diamond paste on a flat glass lap to produce a macroscopically flat surface. Polishing was carried out on the tin laps to produce a mirror-like finish using initially 6 μm and then 0.5 μm diamond paste. The samples were ultrasonically cleaned in water between each polishing stage.

To examine the grain structure of the samples, the polished surfaces were etched when it was needed. For alumina and zirconia ceramics, the samples were thermally etched at 50°C below their sintering temperatures for 15-20 mins in a rapid heating furnace with the heating and cooling rates of 500°C/h. For Ca α-sialon ceramics, the samples were chemically etched in molten NaOH, contained in a Ni crucible, for 10-20 s then rinsed under running water. For silicon nitride materials, the samples were plasma etched (prepared by K. Hirao, the National Industrial Research Institute of Nagoya, Japan). For silicon infiltrated silicon carbide materials, no etching was applied since large differences existed in atomic number between the grains and grain boundary phases which could be resolved by back scattered electron (BSE) images during SEM examinations.

The samples for microstructural examinations along with their eroded surfaces were ultrasonically cleaned, mounted and sputter coated with amorphous carbon. The surface morphology was examined using a JEOL FE6300 SEM equipped with a field emission gun operating in secondary electron (SE) imaging mode with an accelerating voltage of 10 kV. The BSE images as well as qualitative analysis on the elemental composition were performed on a JEOL JSM-840A SEM equipped with an energy dispersive X-ray (EDX) spectrometer operating at 20 kV.

3.4.3 Density determinations

The bulk density quoted in the present work was measured using the boiling water method recommended by Australian Standard AS 1774.5 (1979). The sample was boiled in distilled water for 2 h and then cooled to room temperature while the specimen remained immersed in water. The immersed mass of the sample, M_I, was measured by weighing the saturated specimen submerged in water. The specimen was then withdrawn from the water and the excess water on the surface was removed by a damp cloth. The saturated mass, M_S, was recorded by weighing the saturated specimen suspended in air. The sample was oven-dried at 105-110°C overnight before the dry mass, M_D, was recorded. Based these values, the bulk density, D_b, was calculated using the following relationship (AS 1774.5, 1979)

$$D_b = M_D \cdot D_L / (M_S - M_I) \qquad (3.11)$$

where D_L is the density of the distilled water at room temperature.

The true density of the specimen, D_t, was measure on finely powdered sample using a Helium pycnometer, AccuPyr '330 Micromeritics densitometer. The true porosity, P_t, was calculated as follows (AS 1774.5, 1979)

$$\% P_t = (1 - D_b/D_t) \times 100 \qquad (3.12)$$

3.4.4 Hardness and fracture toughness measurements

Hardness and fracture toughness measurements were carried out on the polished samples using a Vickers diamond pyramid indenter. The standard load conditions were 10 kg, 15 s. However, in some cases, the load was decreased since many lateral cracks developed and disturbed the measurement of the radial cracks. The indentation produced a diagonal impression with cracks extending from the corners (Fig. 3.8).

(a)   (b)
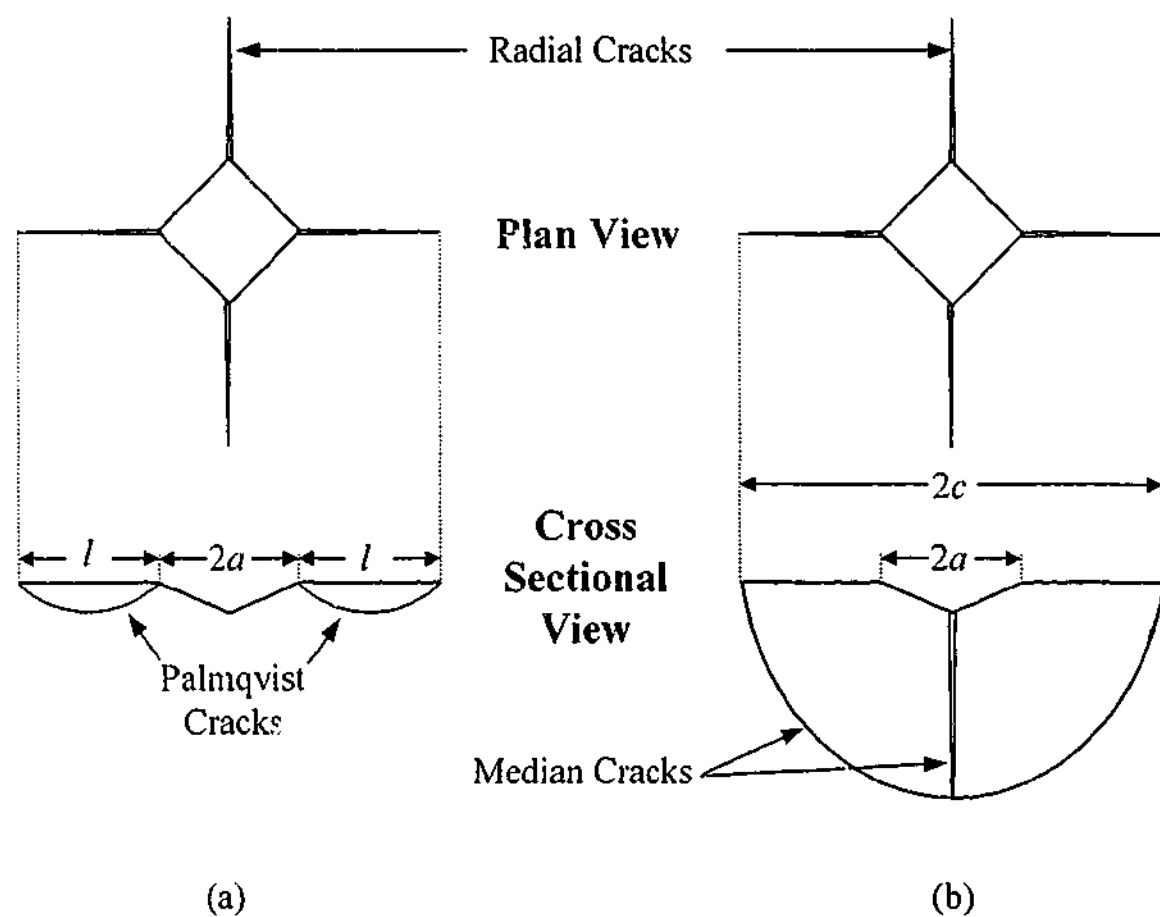
Fig. 3.8. Schematic diagram of a Vickers indent (a) radial palmqvist crack system and (b) radial-median system (Niihara 1983).

The diagonal length, $2a$, the full crack length, $2c$, as well as the Palmqvist crack length, l, were measured in all directions using an optical microscope. Five indents were made for each sample and the means were used to derive the hardness and fracture toughness values.

The hardness, H, was calculated using the following equation

$$H = P/2a^2 \tag{3.13}$$

where P is the load in Newtons.

The fracture toughness, K_{IC}, was calculated according to the crack-to-indent ratios. For $c/a \geq 2$, the method proposed by Anstis et al. (1981) was adopted

$$K_{IC} = 0.016 \, (E/H)^{1/2} \, (P/c^{3/2}) \tag{3.14}$$

where E is the modulus of the specimen.

However, for $1.25 \leq c/a \leq 2$, the Palmqvist crack treatment developed by Niihara (1983) was utilized

$$[K_{IC}\phi /(Ha^{1/2})](H/E\phi)^{2/5} = 0.048(l/a)^{-1/2} \tag{3.15}$$

where ϕ is the constrain factor ($= H/\sigma_y \approx 3$, where σ_y is the yield stress).

Chapter 4

MICROSTRUCTURAL TAILORING OF Ca α-SIALON CERAMICS

4.1 Introduction

Since the focus of the research was an investigation of the relationship between the microstructure and the erosion behaviour of ceramic materials, it was necessary first to ascertain whether ceramics with well-tailored microstructures could be obtained. This chapter reports an evaluation of the effects of the starting compositions and processing conditions on the microstructure of Ca α-sialon ceramics. It then discusses the correlation between the microstructure and the mechanical properties, followed by an examination of the effect of a post-sintering heat treatment on the properties of these materials.

Section 4.2 describes the experimental details involved in the sample preparation, characterisation techniques and property measurements relevant to this work. Section 4.3 presents the results of X-ray diffraction (XRD) analysis which provide the phase content and the lattice parameters of the Ca α-sialon samples, while section 4.4 presents the scanning electron microscope (SEM) observations which show the variations in microstructure of these materials. The measured physical and mechanical properties of these materials are described in section 4.5, and sections 4.6-4.9 form a comprehensive discussion which deals with the nucleation and densification mechanism, the microstructural design and the effect of microstructure on mechanical properties of Ca α-sialon ceramics.

4.2 Experimental Design

4.2.1 Materials preparation

Three Ca α-sialon compositions, namely CA1005, CA2613 and CA3618, with the nominal x ($= m/2 = n$) value of 0.5, 1.3 and 1.8, respectively, were selected for this study. In order to clarify the effect of starting compositions on the microstructure of final products, the three compositions were pressureless-sintered (PLS-ed) at 1800°C for 4 h in nitrogen atmosphere. In order to elucidate the effect of sintering conditions on the microstructure, compositions CA1005 and CA2613 were selected for hot pressing (HP) under various conditions. Finally, in order to identify the effect of grain boundary glass on the erosion response of Ca α-sialon ceramics, a post-sintering heat treatment was carried out on the three PLS-ed compositions at 1300°C for 12 h in nitrogen. Detailed procedures for the sample preparation of Ca α-sialon ceramics are described in section 3.2, while the processing conditions for these samples are summarized in Table 4.1.

Table 4.1 Processing conditions of the Ca α-samples

Samples	Sintering condition
CA1005	PLS @1800°C/4h
CA1005(HT)	PLS @1800°C/4h + HT @1300°C/12h
CA1005F	PLS @1800°C/3h + HP @1700°C/1h
CA1005C	PLS @1800°C/8h + HP @1700°C/1h
CA2613	PLS @1800°C/4h
CA2613(HT)	PLS @1800°C/4h + HT @1300°C/12h
CA2613F	HP @1550°C/0.5h + HP @1600°C/0.5h
CA2613C	PLS @1800°C/3h + HP @1700°C/1h
CA3618	PLS @1800°C/4h
CA3618(HT)	PLS @1800°C/4h + HT @1300°C/12h

where **PLS: Pressureless-sintered; HT: Heat-treated; HP: Hot-pressed.**

4.2.2 Characterisation techniques

XRD was used to determine the lattice parameters and the crystalline phases of the samples fabricated (refer to section 3.4.1). Based on the measured lattice parameters, the actual x value for the Ca α-sialon phase can be obtained as the mean of x_a and x_c given by the following equations (Wang et al. 1999a):

$$\Delta a = 0.156 \, x_a \tag{4.1}$$

$$\Delta c = 0.115 \, x_c \tag{4.2}$$

where $\Delta a = a - a_o$ and $\Delta c = c - c_o$; a and c are the measured unit-cell dimensions of α-sialon along the a and c-axes, respectively, while a_o and c_o represent the unit-cell dimensions of α-Si$_3$N$_4$ which have values of 7.749 Å and 5.632 Å, respectively.

SEM was employed to study the microstructure of the Ca α-sialon ceramics. The samples were polished and etched and then examined using a JEOL FE6300 SEM equipped with a field emission gun. Etching was performed by immersing polished surfaces of the samples into molten NaOH. The temperature of the molten NaOH and the etching duration were determined according to the amount of the glassy phase in the sample. For example, for composition CA1005, the etching condition was 410°C for 20 s, while for compositions CA2613 and CA3618, the condition was 400°C for 10 s. Prior to SEM examination, the samples were carbon coated to prevent charge accumulation. The accelerating voltage used was 10 kV.

The diameter and length of α-sialon grains were determined as the lengths of the shortest and the longest diagonal of the two-dimensional exposed grains, respectively, from the SEM micrographs of polished surfaces. Over 500 grains of each sample were measured. The apparent aspect ratio of the grains was given by the ratio of the average length over average diameter. No stereological factors were considered in the calculation. The volume fraction of the minor AlN-polytypoids and intergranular glassy phase in the samples was estimated from images of the two-dimensional polished sections using the quantitative image analysis technique. The SEM micrographs of the polished sections were enlarged and the area fraction of the AlN-polytypoid phase or the intergranular glassy phase was manually traced onto a

transparent film for quantitative image analysis. The present study showed that the standard deviation of the measured volume fraction using quantitative image analysis technique was less than 10%. The volume fraction of AlN raw material in the sintered body was estimated based on the calibration XRD curve of an AlN and α-Si_3N_4 two-phase system. The volume ratio of AlN to α-Si_3N_4 powders was varied from 0-100%. The X-ray peak areas of AlN and α-Si_3N_4 for (100) and (201) planes, respectively, were calculated using the Traces 5.2 XRD analysis program, and the relative volume fraction of AlN in the AlN–α-Si_3N_4 system was obtained by comparing their peak areas.

The water immersion method was used to determine the bulk density of all samples. The total porosity of the HP-ed samples (CA1005 and CA2613) and the PLS-ed CA3618 was estimated from the SEM micrographs of polished surfaces using the image analysis technique. The true density, d_t, of the three sialon compositions was calculated from (AS 1774.5, 1979)

$$d_t = d_b/(1-P\%) \tag{4.3}$$

where d_b and $P\%$ represent the bulk density and the total porosity, respectively, of the corresponding samples. The total porosity of PLS-ed CA1005 and CA2613 samples was calculated from the derived true density value and the measured bulk density value using equation 4.3.

Vickers indentation, at a peak load of 98 N, was utilized to measure the hardness and fracture toughness of the sialon ceramics (Anstis et al. 1981). A value of 240 GPa for Young's Modulus was used to evaluate the fracture toughness of the Ca α-sialon materials (Ta et al. 2000). The indentation toughness undervalues the actual toughness of these α-sialon ceramics in which an R-curve behaviour, i.e. fracture toughness increases as the crack size increases, is expected (Lawn 1993; Wood et al. 1999). However, such a technique is adequate for a relative comparison of the resistance to crack growth of ceramic materials.

4.3 XRD Analysis

4.3.1 Pressureless-sintered samples

XRD spectra (2θ from $30°$ to $40°$) of the three PLS-ed Ca α-sialon materials are shown in Fig. 4.1. As can be seen, in material CA1005, α-sialon was the only crystalline phase revealed (Fig. 4.1(a)). In material CA2613, α-sialon was the dominant phase but there was also a trace of 33R (AlN-polytypoid) (Fig. 4.1(b)). AlN-polytypoid phases, as discussed in section 2.3.1.2, are AlN defect structures that result from the incorporation of silicon and oxygen into the AlN structure. In material CA3618, α-sialon was again the dominant phase but a minor AlN' phase was also present (Fig. 4.1(c)). The AlN' phase observed here is not the AlN starting powder, rather, it is a precipitated AlN solid solution with a very small concentration of silicon in it (Wood and Cheng 2000).

Fig. 4.1 also shows that there is a slight decrease in the amount of α-sialon phase as the x-value of the composition increases. This decrease was accompanied by the presence of small amounts of 33R and AlN' phases in samples CA2613 and CA3618, respectively. In addition, the α-sialon peaks exhibit a clear shift towards low angles as the x-value of the composition increases, indicating the unit cell dimensions of the α-sialon phase increase as the x-value increases.
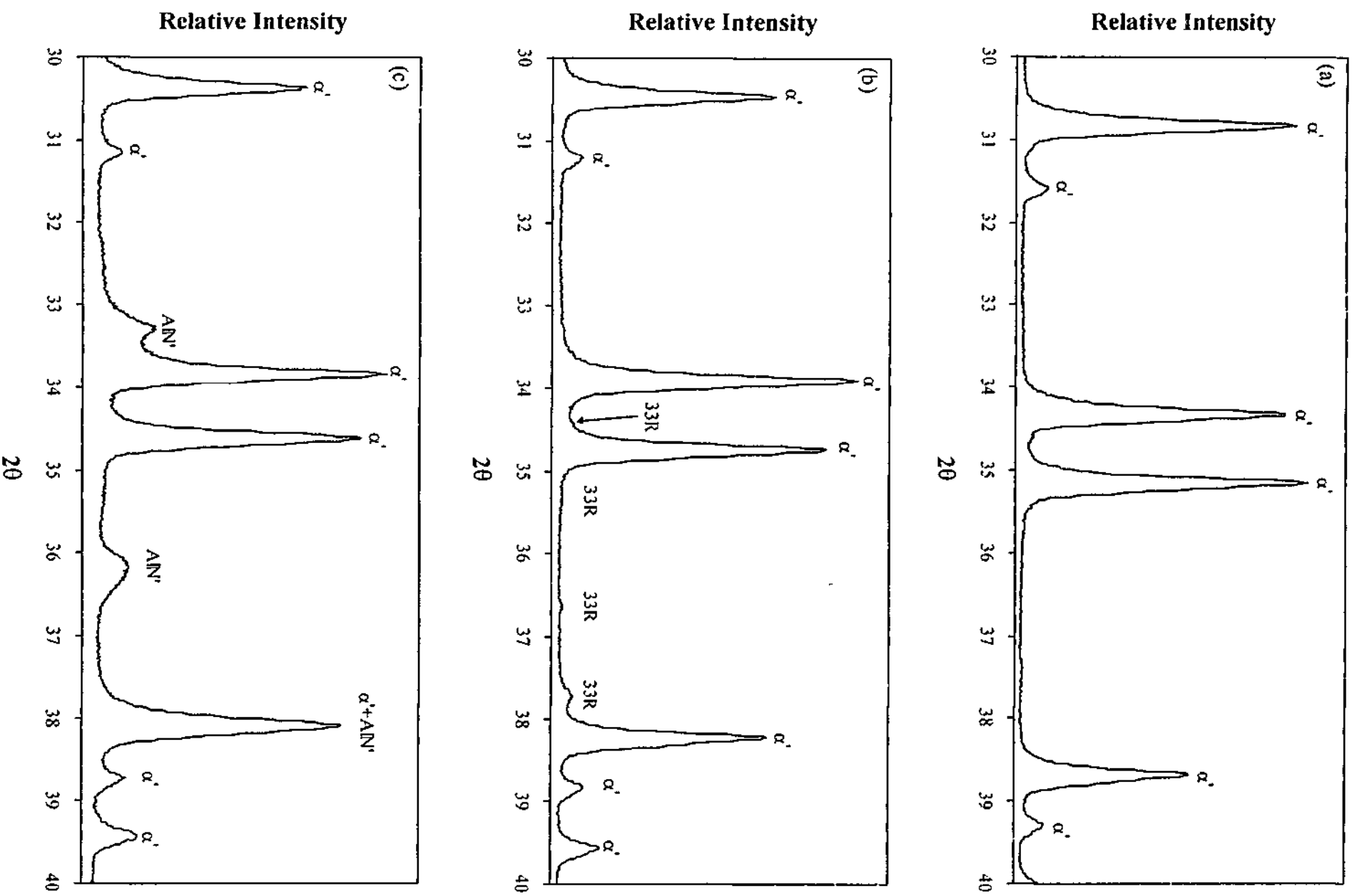
Fig. 4.1. XRD spectra for the three PLS-ed samples: (a) CA1005, (b) CA2613 and (c) CA3618.

4.3.2 Hot-pressed samples

Figs. 4.2 and 4.3 show the XRD spectra (2θ from 30° to 40°) for composition CA2613 fabricated under various conditions: two-stage HP-ed at 1550°C/0.5h and 1600°C/0.5h (CA2613F), and PLS-ed at 1800°C/3h followed by post-sintering HP at 1700°C/1h (2613C). XRD spectra were taken from bulk surfaces both parallel (Fig. 4.2) and perpendicular (Figs. 4.3) to the uniaxial HP direction. Sample CA2613C consisted of a dominant Ca α-sialon phase coupled with a small amount of 33R phase, while sample CA2613F contained a dominant Ca α-sialon phase and a minor AlN phase. The AlN phase observed in the low temperature two-stage HP-ed material CA2613F was probably due to the unreacted aluminium nitride powder. To confirm this, sample CA2613F was post-sintering heat-treated at 1700°C/1h. XRD analysis of the heat-treated sample revealed no AlN phase, though a small amount of 33R was detected.

By comparing XRD spectra taken from bulk surfaces parallel to and perpendicular to the HP direction, some variations in relative intensity ($I/I_{max}\times100\%$) of α-sialon peaks were observed. Table 4.2 lists the relative intensities of the XRD peaks for the Ca α-sialon from the reference powder diffraction file (Thompson 1988) and the present HP-ed CA2613 materials. As can be seen, for materials CA2613F and CA2613C, the diffraction intensities from the crystal planes that are normal or nearly normal to the c-axis of the α-sialon hexagonal unit cell, i.e. planes with indices $l > h$, k, are greater for surfaces parallel to the HP direction than those perpendicular to the HP direction. In contrast, the diffraction intensities from the planes that are parallel to the c-axis of the α-sialon unit cell, i.e. planes with indices (hk0), are stronger for surfaces perpendicular to the HP direction. The XRD results suggest that a textured structure has been developed in samples CA2613F and CA2613C, as a result of the c-axis of the α-sialon grains being preferentially aligned normal to the HP direction. This preferred orientation is associated with the development of the elongated α-sialon grain morphology (Wang et al. 1996a).
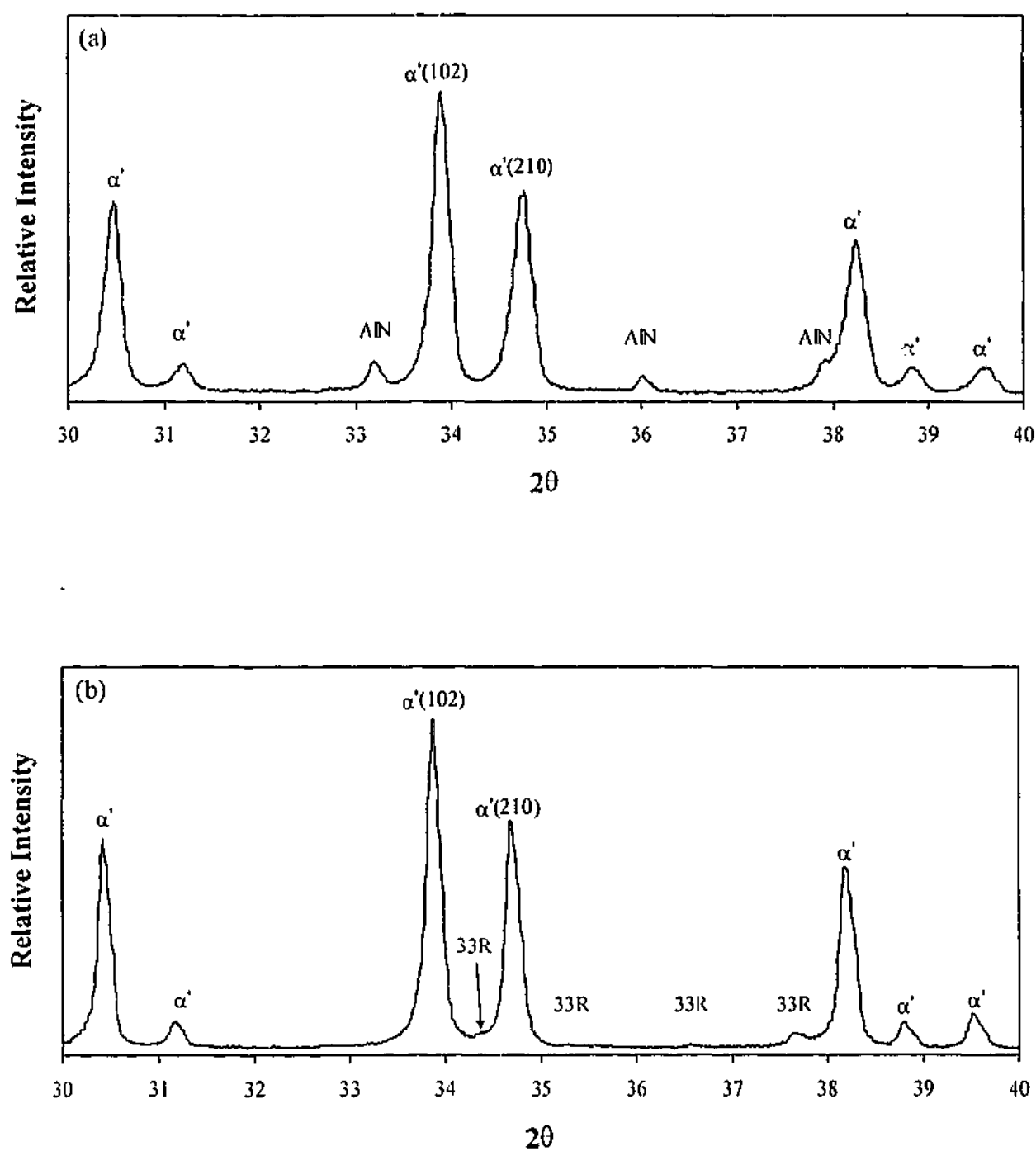
Fig. 4.2. XRD spectra from bulk surfaces parallel to the uniaxial HP direction of samples: (a) CA2613F and (b) CA2613C.
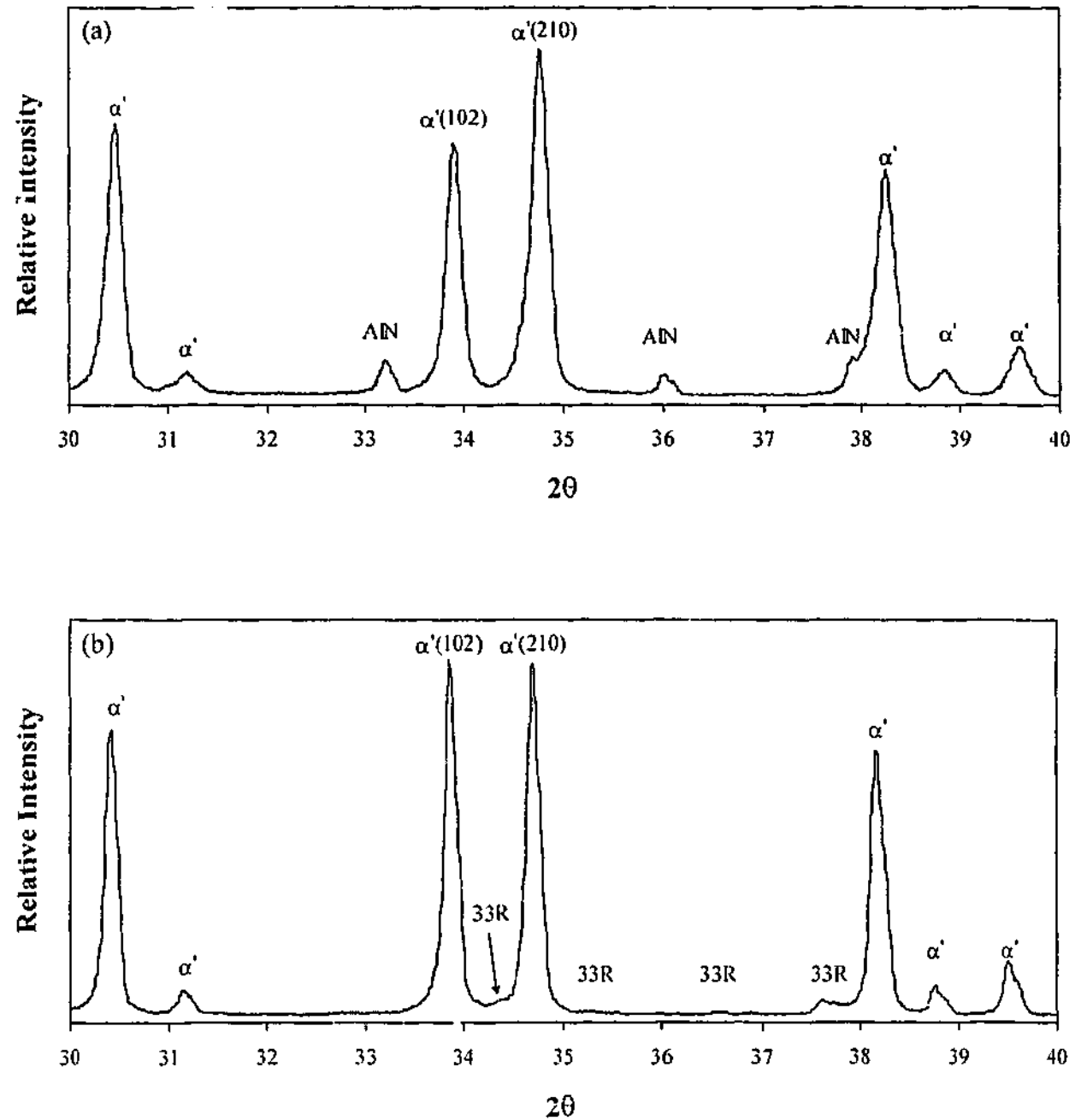
Fig. 4.3. XRD spectra from bulk surfaces perpendicular to the uniaxial HP direction of samples: (a) CA2613F and (b) CA2613C.

The degree of the texture is more significant in material CA2613F than CA2613C. This can be evidenced by comparing the peak intensity ratios of (102) and (210) planes in the XRD diffraction patterns. For sample CA2613F, the ratio of $I_{(102)}/I_{(210)}$ was 1.5 and 0.7 for sections parallel and perpendicular to the HP direction, respectively. On the other hand, for sample CA2613C these ratios became 1.4 and 1, respectively. This is because material CA2613C was initially PLS-ed for 3 h at 1800°C to produce a microstructure consisting of mainly elongated α-sialon grains with random orientations. The post-sintering HP for CA2613C at 1700°C/1h resulted

in further coarsening of elongated α-sialon grains, during which a certain degree of preferential grain orientation could occur. However, the preferred orientation of the α-sialon grains was less than that observed in the sample that was only HP-ed, CA2613F.

Table 4.2 XRD intensities of Ca α-sialon from the reference powder diffraction file (Thompson 1988) and of composition CA2613 fabricated under various conditions

hkl	Relative Intensity: I/I_{max} (%)				
	Powder Diffraction File	CA2613F		CA2613C	
		$//^a$	$\perp^a$	$//^a$	$\perp^a$
201	75	64	79	65	81
002	9	12	10	10	9
102	100	100	74	100	100
210	80	68	100	70	98
211	65	52	66	56	75
112	9	11	10	10	10
300	14	12	17	12	17

[a] //: surface parallel to the HP direction;

$\perp$: surface perpendicular to the HP direction.

4.3.3 Heat-treated samples

Post-sintering heat treatment was carried out at 1300°C for 12 hours on the three PLS-ed materials CA1005, CA2613 and CA3618. X-ray phase analysis of the heat-treated samples revealed a secondary gehlenite phase ($Ca_2Al_2SiO_7$, G') in materials CA2613 and CA3618 (Fig. 4.4). Gehlenite is the crystallised form of the intergranular glass. A higher amount of glass in sample CA3618 produced more gehlenite in the sample comparing to the other samples after the heat-treatment. No obvious evidence of gehlenite was seen in the XRD spectrum of the heat-treated sample CA1005, owing to a very low content of grain boundary glass in this

material. This finding is consistent with the fact that the CA1005 composition is located inside the single-phase α-sialon region.
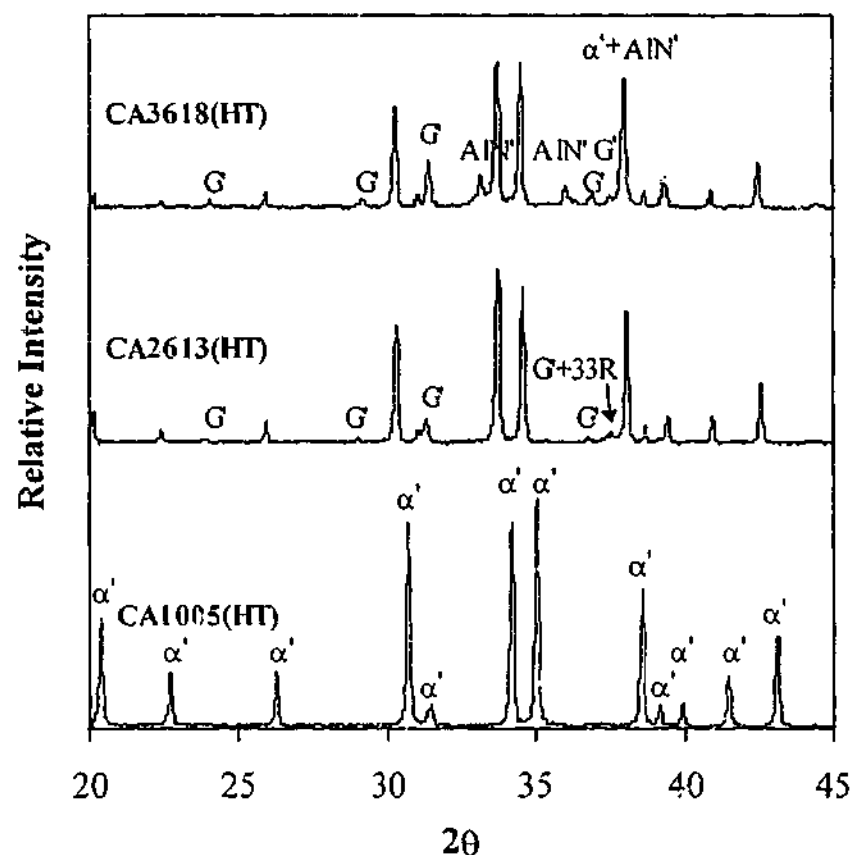
Fig. 4.4. XRD spectra of the heat-treated (HT) samples. G': gehlenite ($Ca_2Al_2SiO_7$).

4.3.4 Unit cell dimensions

The nominal and actual x-values, lattice parameters and crystalline phases of Ca α-sialon samples are presented in Table 4.3. The actual x-value, in all cases, is lower than its nominal value, indicating that there exists a competition for Ca^{2+} between the α-sialon phase and intergranular glassy phase. The three PLS-ed samples, i.e. CA1005, CA2613 and CA3618, provide an ideal system for studying the effect of the design composition, described by the nominal x-value, on the solubility of Ca^{2+}, determined by the actual x-value. The solubility of Ca^{2+} in the α-sialon unit cell increases as the nominal x-value increases. The result is consistent with the measured unit cell dimensions of the three PLS-ed samples. As shown in Table 4.3, the cell dimensions of α-sialon also increase as the x-value increases. The expansion of cell

dimensions in α-sialon is mainly caused by substitution of Si-N bonds by Al-N bonds due to the greater bond length of Al-N (1.87 Å) than that of Si-N (1.74 Å) (Cao and Metselaar 1991). The larger number of Si^{4+} replaced by Al^{3+} (m-value) in SiN_4 tetrahedra results in a greater negative charge imbalance which requires additional stabilising cations to compensate. Therefore, the actual x-value increases as the cell dimensions of the α-sialon increase.

However, the ratio of the soluble Ca^{2+} in the α-sialon lattice to the total added amount of calcium, i.e. the ratio of actual to nominal x-values, is found to decrease when the nominal x-value exceeds 1.3. For example, in material CA2613 ($x = 1.3$), the level of Ca^{2+} in the α-sialon lattice is approximately 70% of the added amount, suggesting that about 30% of added Ca^{2+} remains in the intergranular glassy phase. However, the percentage of Ca^{2+} in the α-sialon lattice decreases to around 60% in material CA3618 ($x = 1.8$) with about 40% of added Ca^{2+} remaining in the glassy phase. The decrease in the percentage of Ca^{2+} in the α-sialon lattice suggests that the amount of the intergranular glassy phase increases as the x-value increases.

From Table 4.3, it can be seen that for the same composition, the sintering conditions, i.e. the sintering time and temperature, also have an impact on the cell dimensions of α-sialon and the solubility of Ca^{2+} in the α-sialon lattice. The longer sintering time, as demonstrated by CA1005F and CA1005C, and the higher sintering temperature, as shown by CA2613F and CA2613C, can result in a larger cell dimensions and thus increase the solubility of Ca^{2+} in the α-sialon lattice and decrease the amount of grain boundary residual glass.

Table 4.3 Nominal and actual x-values, lattice parameters and crystalline phases of Ca α-sialon samples

Sample[a]	Nominal x-value	Actual x-value[b]	a (Å)	c (Å)	V (Å³)	Phase present[c]
CA1005	0.5	0.33	7.8013(5)[d]	5.6696(5)	298.82	α′ vs
CA1005F	0.5	0.33	7.8004(4)	5.6705(6)	298.81	α′ vs
CA1005C	0.5	0.35	7.8024(4)	5.6724(5)	299.06	α′ vs
CA2613	1.3	0.89	7.8886(5)	5.7339(6)	309.01	α′ vs; 33R vw
CA2613F	1.3	0.84	7.8783(10)	5.7302(6)	308.05	α′ vs; AlN vw
CA2613C	1.3	0.89	7.8876(5)	5.7337(5)	308.93	α′ vs; 33R vw
CA3618	1.8	1.06	7.9191(7)	5.7499(7)	312.28	α′ vs; AlN′ w

[a] Sample notation and its sintering condition refer to Table 4.1.

[b] The mean value of x_a and x_c calculated using relationships $\Delta a = 0.156x_a$ and $\Delta c = 0.115x_c$ derived by Wang et al. (1999a).

[c] α′ = α-sialon; 33R = $SiAl_{10}O_2N_{10}$ (AlN-polytypoid); AlN = unreacted aluminium nitride powder; AlN′ = AlN-polytypoid.

[d] The values in the parentheses are the standard deviation of the final decimal place.

X-ray peak intensities: vs = very strong (relative peak intensity >25%), w = weak (10-20%), vw = very weak (<10%).

4.4 SEM Analysis

4.4.1 Pressureless-sintered samples

SEM micrographs of polished and chemically etched surfaces of the three PLS-ed Ca α-sialon ceramics are shown in Fig. 4.5. The average diameter and apparent aspect ratio of α-sialon grains as well as the volume fraction of the intergranular glass of these materials are given in Table 4.4. Sample CA1005 contained more or less equiaxed α-sialon grains coupled with a small amount of intergranular glassy phase (Fig. 4.5(a)). The size of the α-sialon grains varied widely from 0.1 μm to over 2 μm with an average diameter of 0.44 μm. The volume fraction of the intergranular glassy phase was estimated using image analysis to be approximately 3%.

Sample CA2613 displayed two distinct crystalline phases: the α-sialon phase with a smooth trait and the 33R phase with speckled features (Fig. 4.5(b)). The speckled appearance of 33R grains was the result of the faster etching rate of AlN compared to that of α-sialon when NaOH etchant was used (Weimer 1997). The α-sialon grains appeared mainly in an elongated shape and ranged widely in size. The small grains were typically 0.2-0.3 μm in diameter and 0.7-1.2 μm in length, while the large grains were 0.9-1.2 μm in diameter and 3-8 μm in length. The aspect ratios of both large and small grains were, however, very similar, ranging from 3 to 8 with an apparent ratio of 5.2. The 33R AlN-polytypoid phase appeared as long laths with an average thickness and length of 0.6 μm and 4 μm, respectively. Quantitative image analysis on the SEM micrographs of polished sections showed that the area fraction of 33R phase in sample CA2613 was approximately 4%, while the area fraction of the intergranular glassy phase in CA2613 was approximately 7%.
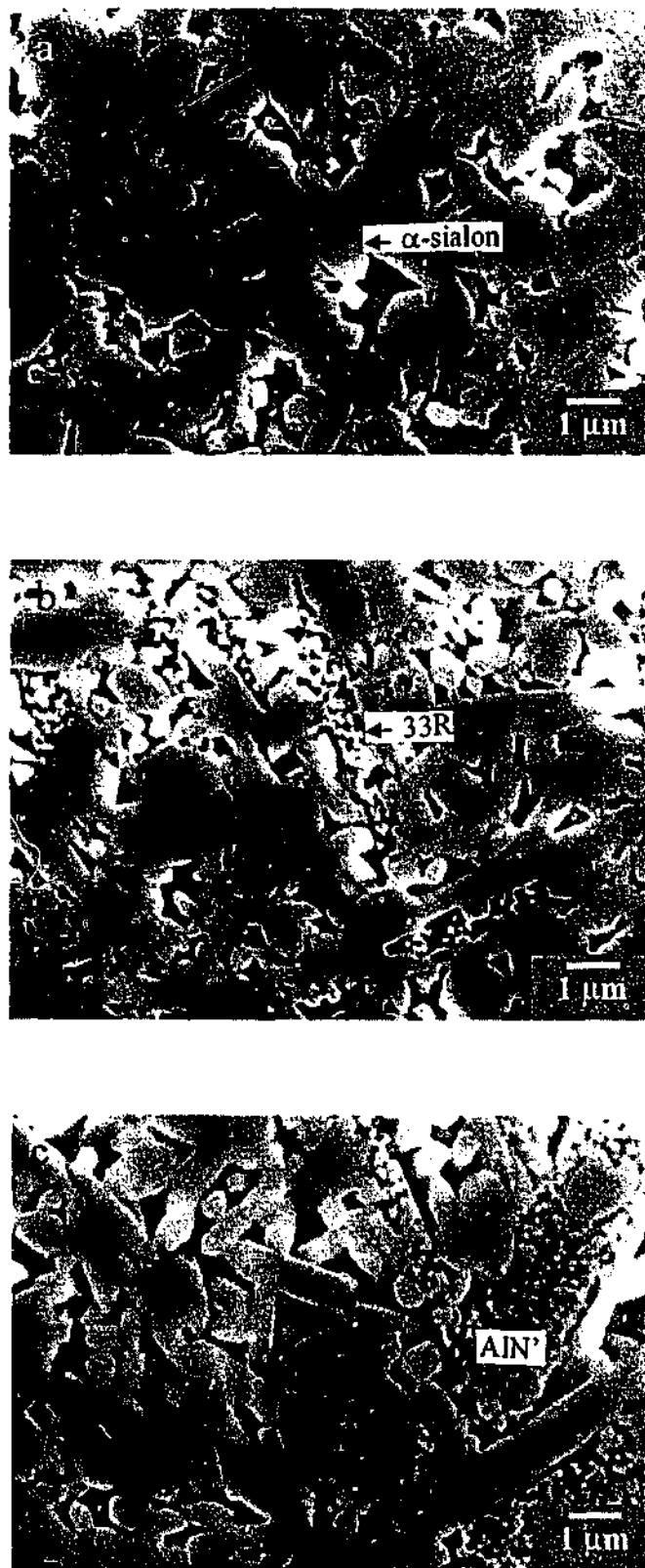
Fig. 4.5. SEM micrographs of the three PLS-ed Ca α-sialon samples: (a) CA1005, (b) CA2613 and (c) CA3618.

Table 4.4 Average diameter and apparent aspect ratio of α-sialon grains as well as the volume fraction of the secondary phases of the Ca α-sialon samples

Sample	Average Diameter (μm)	Apparent Aspect Ratio	Secondary Phases Content (vol%)			
			GB[a]	33R[a]	AlN[b]	AlN'[a]
CA1005	0.44	1.8	3			
CA1005F	0.52	2.1	2			
CA1005C	0.74	2.0	<1			
CA2613	0.46	5.2	7	4		
CA2613F	0.15	3.0	5		3	
CA2613C	0.51	4.1	3	4		
CA3618	0.57	7.3	15			19

[a] The volume fractions of grain boundary glass (GB) and AlN-polytypoids (33R and AlN') were determined using the quantitative image analysis technique, with a standard deviation less than 10%.

[b] The volume fraction of unreacted aluminium nitride powder (AlN) was estimated based on the calibration curve of an AlN and α-Si_3N_4 two-phase system determined using the quantitative XRD analysis technique.

Sample CA3618 also consisted of two crystalline phases: the α-sialon and AlN' phases (Fig. 4.5(c)). The α-sialon phase in CA3618 had a similar elongated grain morphology to that observed in material CA2613 except being much larger and longer in size. The average diameter of α-sialon grains in material CA3618 was 0.57 µm, although some grains were as large as 2 µm in diameter. The apparent aspect ratio was 7.3. The AlN' phase, as shown with speckled features in Fig. 4.5(c), exhibited a similar morphology as the 33R phase observed in CA2613. The size of these AlN' grains was, however, much larger than that of the 33R laths in sample CA2613. Image analysis revealed that the area fraction of the AlN' phase and the intergranular glassy phase in sample CA3618 was approximately 19% and 15%, respectively.

4.4.2 Hot-pressed samples

SEM micrographs of polished and chemically etched surfaces of HP-ed materials CA1005 and CA2613 are presented in Figs. 4.6 and 4.7, respectively. The average diameter and apparent aspect ratio of α-sialon grains as well as the volume fraction of the secondary phases of these materials are given in Table 4.4.

Fig. 4.6(a) shows the microstructure of sample CA1005F (PLS-ed at 1800°C/3h followed by post-sintering HP at 1700°C/1h), while Fig. 4.6(b) is the micrograph of sample CA1005C (PLS-ed at 1800°C/8h followed by post-sintering HP at 1700°C/1h). As can be seen, both materials contained almost equiaxed α-sialon grains with a large fraction of the grains being slightly elongated. Both materials exhibit a wide range of variations in grain sizes, being from 0.1 µm to 4 µm for CA1005F and from 0.2 to over 6 µm for CA1005C. The average diameters of the α-sialon grains were 0.52 and 0.74 µm for materials CA1005F and CA1005C, respectively, which were significantly greater than that (0.44 µm) of their PLS-ed counterpart CA1005. The apparent aspect ratios of the α-sialon grains were 2.1 and 2.0 for materials CA1005F and CA1005C which were also greater than that (1.8) of their PLS-ed counterpart CA1005. Quantitative image analysis showed that materials CA1005F and CA1005C contained approximately 7% and 6% grains, respectively,

with an aspect ratio exceeding 2, while material CA1005 contained less than 5% grains with the aspect ratio greater than 2. The volume fraction of grain boundary glass was, however, found to decrease from approximately 3% for PLS-ed material CA1005 to ~2% and <1% for HP-ed materials CA1005F and CA1005C, respectively.
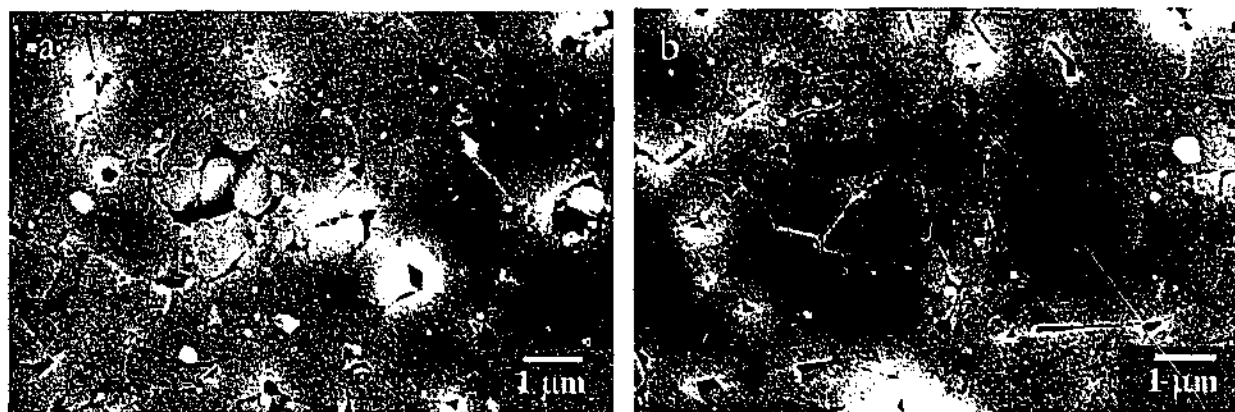
Fig. 4.6. SEM micrographs of the two-stage sintered CA1005 samples: (a) CA1005F and (b) CA1005C.

Figs. 4.7(a) and (b) are the low and high magnification microstructures, respectively, of two-stage HP-ed material CA2613F (1550°C/0.5h followed by 1600°C/0.5h), while Fig. 4.7(c) is the micrograph of sample CA2613C (PLS-ed at 1800°C/3h followed by post-sintering HP at 1700°C/1h).

XRD analysis revealed that material CA2613F consisted predominantly of α-sialon phase together with a small amount of unreacted AlN (section 4.3.2). SEM examinations of a polished and etched section of sample CA2613F showed that the α-sialon grains were mainly elongated in shape and had an average diameter of 0.15 μm, with very few grains approaching the 1 μm mark (Figs. 4.7(a) and (b)). The apparent aspect ratio of these grains was 3. In addition, some isolated regions containing fine particles with a speckled appearance, highlighted by the frame in Fig. 4.7(a), were also observed. EDX analysis indicated that these regions consisted mainly of Al and N (Fig. 4.7(d)). The speckled feature, as discussed in section 4.4.1, is an unique feature of the AlN-polytypoid phase as a result of the NaOH etching. Moreover, these speckled particles were submicrometer in sizes (Fig. 4.7(a)), which were significantly smaller than the starting AlN particles, i.e. 6-10 μm (Table 3.1),

suggesting that they were more likely the precipitated AlN-polytypoid phase. However, the quantity of the precipitated AlN-polytypoid is so small that no diffraction peaks of such phase were revealed by XRD analysis.

Quantitative XRD analysis showed that the volume fraction of unreacted AlN in sample CA2613F was approximately 3%, while image analysis revealed that the volume fraction of the intergranular glass in this material was approximately 5%.
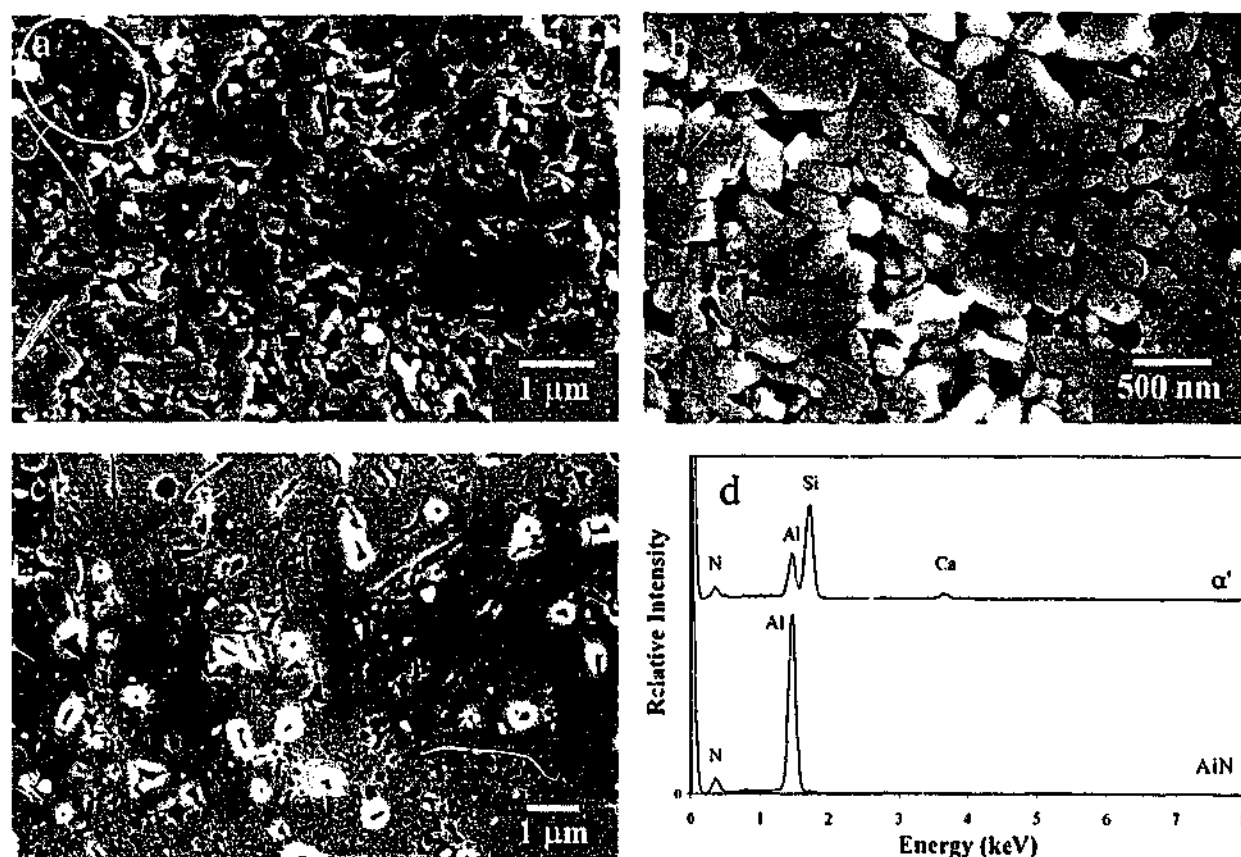
Fig. 4.7. SEM micrographs of the two-stage sintered CA2613 samples: (a) and (b) CA2613F, and (c) CA2613C. EDX analysis (d) revealed that regions containing speckled particles, highlighted by white frame in (a), consisted mainly of Al and N, suggesting that they are probably precipitates of the AlN-polytypoid. Note: EDX spectrum for the Ca α-sialon phase (α') is also shown in (d) for reference.

Material CA2613C consisted of mainly elongated α-sialon grains coupled with a small amount of AlN-polytypoid (33R, as revealed by XRD analysis), which is consistent with the PLS-ed sample CA2613. However, the average diameter of the α-sialon grains in CA2613C was slightly greater than that in PLS-ed sample CA2613 whereas the apparent aspect ratio was lower than that of the latter (Table 4.4). The

volume fraction of the grain boundary glass of CA2613C, as determined using the image analysis technique, was significantly lower than that of the PLS-ed sample CA2613 and the low temperature HP-ed sample CA2613F (Table 4.4).

4.5 Property Evaluation

The physical and mechanical properties of the Ca α-sialon samples are presented in Table 4.5, where some interesting trends can be observed. Compositions with higher x-values are easier to densify than those with lower x-values. The increase in the amount of intergranular glassy phase with increase in the x-value may account for this. For example, in the three PLS-ed materials, sample CA3618 attained a bulk density of above 99% of its true density whereas material CA1005 only achieved a bulk density of 95% of its true density. Clearly, intergranular glassy phase or the liquid phase when it is above the eutectic temperature is crucial for facilitating densification during sintering. The importance of the liquid phase in the densification process is further illustrated by comparing the bulk density of the HP-ed material CA1005 and PLS-ed materials CA2613 and CA3618. The two HP-ed materials CA1005F and CA1005C only achieved a bulk density similar to PLS-ed material CA2613, indicating even with the assistance of applied pressure, densification of composition CA1005 is hindered owing to its low liquid phase content.

In addition, the post-sintering heat treatment resulted in a slight decrease in the bulk density of the samples in comparison to their PLS-ed counterparts. This may be accounted for by an increased porosity resulting from the volume reduction due to the devitrification of the glass located at the multi-grain junctions (Deckwerth and Rüssel 1997a). The increase in porosity at grain boundaries was indeed observed in a previous study on grain boundary devitrification of Sm α-sialon ceramics (Cheng and Thompson 1994).

In Table 4.5, it is also seen that the hardness of the materials decreases as the x-value increases. The decrease in the amount of α-sialon phase and the increase in the intergranular glass content with increasing x-value may account for this. Thus among the three compositions, material CA1005 has the highest hardness, with values of

16.4 and 19.1 GPa for the PLS-ed and HP-ed samples, respectively. This is followed by CA2613 with corresponding values of 15 and 18.3 GPa, respectively. CA3618 exhibits the lowest hardness value of 14.5 GPa. Furthermore, a slight reduction in hardness was noticed for the heat-treated samples compared to the as-sintered ones. This may also be accounted for by the increased porosity resulting from the devitrification of intergranular glass in the heat-treated samples.

In addition, a clear dependence of hardness on ceramic microstructure was also observed. For instance, in the two HP-ed CA2613 samples, the coarse-grained material CA2613C (Fig. 4.7(c)) containing a small amount of intergranular glass possessed a much higher hardness than the fine-grained material CA2613F (Fig. 4.7(a)). A similar trend was obtained in the two HP-ed CA1005 samples where the coarse-grained, less glass containing material CA1005C exhibited a higher hardness than its fine-grained counterpart CA1005F.

Indentation fracture toughness measurements of the three α-sialon compositions indicate that toughness increases as the x-value increases. The improved toughness in samples with higher x-values can be attributed to the presence of the elongated α-sialon grains as well as the large polytypoid laths in these materials. This can be evidenced by previous studies on the fracture surfaces of high x-value Ca α-sialon materials dominated by elongated α-sialon grains in which microstructural toughening mechanisms such as crack deflection, crack bridging, grain debonding and grain pullout were observed (Wood et al. 1999). The scenario of the microstructural toughening mechanism is further supported by comparing the fracture toughness of the HP-ed samples. The coarse-grained materials CA1005C and CA2613C exhibited considerably higher toughnesses than their fine-grained counterparts CA1005F and CA2613F, indicating crack deflection and bridging played an important role in determine the fracture toughness of ceramic materials.

Table 4.5 Physical and mechanical properties of the Ca α-sialon samples

Sample	Bulk Density (kg/m^3)	True Density (kg/m^3)	Total Porosity (%)	Hardness (GPa)	Toughness (MPa m$^{1/2}$)
CA1005	3050	3224	~5.4	16.4 ± 0.3	4.5 ± 0.1
CA1005(HT)	3033	–	~5.9	15.5 ± 0.3	4.6 ± 0.4
CA1005F	3150	3224	~2.3	18.6 ± 0.4	4.3 ± 0.4
CA1005C	3141	3224	~2.6	19.1 ± 0.4	4.7 ± 0.2
CA2613	3160	3233	~2.3	15.0 ± 0.3	5.4 ± 0.5
CA2613(HT)	3158	–	~2.3	14.7 ± 0.2	5.5 ± 0.1
CA2613F	3189	3233	~1.4	16.2 ± 0.2	5.0 ± 0.5
CA2613C	3208	3233	~0.8	18.3 ± 0.2	5.6 ± 0.4
CA3618	3205	3240	~1.1	14.5 ± 0.3	5.7 ± 0.3
CA3618(HT)	3199	–	~1.3	14.1 ± 0.4	5.9 ± 0.2

4.6 Densification of Ca α-Sialon Materials

There has been significant progress made in research into the reaction sequence and densification behaviour of Ca α-sialon ceramics in the past decade (Menon and Chen 1995a and b; van Rutten et al. 1996; Hewett et al. 1998a; Wood et al. 1999; Wang et al. 1999a; Ta et al. 2000; Li et al. 2000). As discussed in section 2.4.3, Menon and Chen (1995b) identified five reaction sequences which controlled the densification behaviour of Ca α-sialon ceramics. They were (1) the eutectic formation, (2) wetting of a nitride powder (Si_3N_4) and intermediate phase precipitation, (3) secondary wetting of the other nitride powder (AlN), (4) dissolution of the intermediate phase, and (5) precipitation of the final phase. Densification of Ca α-sialon ceramics was found to proceed in three major stages corresponding to three characteristic temperatures: 1360°C, 1410°C and 1610°C (Menon and Chen 1995b). Similar results were reported in a study on densification behaviour of Ca α-sialon ceramics using dilatometry (van Rutten et al. 1996) where two major stages of volume shrinkage were observed at temperatures of 1350 and 1450°C which corresponded very well with the first two characteristic temperatures reported by Menon and Chen (1995b). Despite appreciable knowledge of reaction and densification behaviour of Ca α-sialon ceramics, PLS-ed dense Ca α-sialon ceramics were scarcely reported.

Hewett et al. (1998) and Wood et al. (1999) reported two Ca α-sialon compositions densified by PLS. Both materials had a k value, the value describes the atom ratio (Al + Si)/(O + N) of the starting powder composition, of 0.74. This indicates that the design compositions of the two materials were located above the α-sialon plane and toward the oxide end of the prism (Fig. 2.3(a)), and hence was CaO-rich. For compositions on the α-sialon plane, the k value is 0.75 (Hewett et al. 1998). The three PLS-ed Ca α-sialon compositions (CA1005, CA2613 and CA3618) reported in the present work were also CaO-rich with a k value of 0.74. Therefore, it is apparent that the abundant CaO in the starting compositions is the key to achieve a high density of Ca α-sialon materials in the absence of additional pressure. Previous investigations on the reaction sequence of Ca α-sialon materials with excess CaO showed that gehlenite was the only detectable intermediate phase (Hewett 1998; Wood et al.

1999). Based on data from previous studies (Menon and Chen 1995a and b; van Rutten et al. 1996; Hewett 1998; Wood et al. 1999) and the results of the present work, the following reaction densification mechanism can be proposed.

In the case of sintering of Ca α-sialon ceramics, densification begins at around 1200°C (van Rutten et al. 1996), which corresponds closely to the eutectic point of 1170°C in the $CaO-SiO_2-Al_2O_3$ ternary system (Levin et al. 1964). The amount of liquid in the system, which is calcium and oxygen enriched, increases as the temperature increases. There are two major effects of this liquid on the densification process. First, the liquid penetrates in between the nitride particles and results in particle movement (rearrangement) in such a way that an overall shrinkage occurs. Second, the liquid facilitates the formation of the intermediate gehlenite phase which can result in up to 10% volume reduction of the $CaO-SiO_2-Al_2O_3$ eutectic (Malecki et al. 1997). As a result, the first significant volume shrinkage was observed at temperatures ranged between 1350-1360°C by Menon and Chen (1995b) and van Rutten et al. (1996).

The transient intermediate gehlenite ($Ca_2Al_2SiO_7$) phase forms at ~1200°C, peaks at 1300-1400°C and dissolves at ~1600°C (Hewett et al. 1994; van Rutten et al. 1996; Wood et al. 1999; Li et al. 2000). The Ca α-sialon phase, however, appears at temperatures between 1250 and 1350°C, indicating that wetting or at least partial wetting of the nitride particles, especially Si_3N_4 particles according to the acid-base theory (Menon and Chen 1995a), begins as soon as the eutectic liquid is formed. The raw α-Si_3N_4 material may not be completely dissolved into the eutectic liquid before precipitation of the α-sialon phase. In fact Chatfield et al. (1986) investigated the nucleation sites of α-sialon formed at the initial stage and found that a core of unreacted α-Si_3N_4 raw material frequently remained in the α-sialon grains, indicating that the unreacted α-Si_3N_4 raw material acts as nuclei for α-sialon precipitation. The eutectic is, therefore, an N-containing Ca-Si-Al-O-N liquid, suggesting that the intermediate crystalline phase gehlenite is more likely an N-containing compound $Ca_2Al_{2-x}Si_{1+x}O_{7-x}N_x$.

The ternary eutectic (CaO-SiO_2-Al_2O_3) preferentially wets and reacts with Si_3N_4 (Menon and Chen 1995a). However, due to the formation of large amounts of gehlenite, the amount of liquid in the system and the Ca content in the liquid are low at temperatures between 1300-1400°C. The reductions in liquid content and in accessible Ca hinder the further wetting of Si_3N_4 particles and the precipitation of the α-sialon phase or epitaxial growth of α-sialon on α-Si_3N_4 nuclei. As a result, a delay in volume shrinkage was observed at temperatures of ~1400°C (Menon and Chen 1995b; van Rutten et al. 1996). The occurrence of the second stage massive volume shrinkage was delayed until the heating temperature reached ~1450°C (Menon and Chen 1995b; van Rutten et al. 1996). This is because, above 1400°C, the intermediate gehlenite phase begins to melt and forms a large amount of Ca-rich oxynitride liquid with a relatively low viscosity. The abundant low viscosity Ca-rich oxynitride liquid is essential for the further wetting of the remaining nitride particles and consequently for the precipitation of the Ca α-sialon phase.

The α-Si_3N_4 raw material disappears at temperatures between 1550-1600°C (Wang et al. 1999a; Wood et al. 1999; Li et al. 2000), while AlN raw material may persist at these temperatures (see Tables 4.3 and 4.4). The persistence of AlN raw material at 1600°C observed in the present study is partially due to the fact that the hard basic CaO containing melt preferentially reacts with the hard acid Si_3N_4 (Menon and Chen 1995a). However, the large AlN particles in the starting powder mixture may also have contributed to the delay of complete wetting of AlN raw material.

From the above discussions, the reaction densification mechanism of Ca α-sialons can be outlined as follows:

(i)   1200-1400°C

$CaO + SiO_2/Si_3N_4 + Al_2O_3/AlN \rightarrow$ Ca-Si-Al-O-N liquid + gehlenite + Ca α-sialon
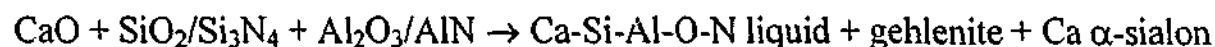
Partial densification is achieved via particle rearrangement and the formation of the gehlenite phase.

(ii)   1400-1600°C

Ca-Si-Al-O-N liquid + gehlenite + Si_3N_4 + AlN →

Ca α-sialon + Ca-Si-Al-O-N liquid
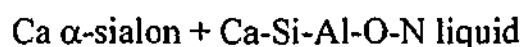
Further densification is achieved via continuous wetting of the nitride particles and the solution/precipitation process involving the phase transformation from α-Si_3N_4 to α-sialon.

(iii) >1600°C

Ca-Si-Al-O-N liquid + Ca α-sialon + AlN →

Ca α-sialon ($x\uparrow$) + Ca-Si-Al-O-N liquid ↓
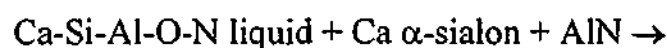
Full densification may be achieved by pore elimination through cooperative flow of the particle-liquid mixture; solution, migration and precipitation of the remnant nitride powders in the viscous oxynitride liquid; and Ostwald ripening where small dissolving grains give way to further densification by rearrangement of small and large α-sialon grains.

4.7 Microstructural Tailoring of Ca α-Sialon Materials

Microstructural development of Ca α-sialon ceramics can be achieved by altering the starting powder compositions and the sintering conditions.

4.7.1 Effect of starting composition

The three PLS-ed samples, i.e. CA1005, CA2613 and CA3618, provide an ideal system for studying the influence of starting composition on the microstructure of the final product. Significant microstructural differences can be revealed among the three compositions. Sample CA1005 contained fine almost equiaxed α-sialon grains coupled with a small amount of intergranular glass and relatively high porosity while CA2613 possesses a fine elongated grain morphology with a higher amount of grain boundary glass and a lower porosity. Sample CA3618 exhibits a coarser and longer grain morphology with the highest amount of grain boundary glass and the lowest porosity. The present results are consistent with the previous findings where microstructures containing elongated α-sialon grains were observed in Ca α-sialon compositions located outside the single-phase α-sialon region (Zhao et al. 1997; Wood et al. 1999), and the aspect ratio and the proportion of elongated α-sialon

grains were found to increase as the x-value increased (Li et al. 2000). It is, therefore, apparent that the nature of the liquid phase during the grain growth process plays an important role in determining the α-sialon grain morphology.

Wood et al. (1999) proposed that the increased liquid content would give more freedom for the elongated α-sialon nuclei to grow with less impingement upon each other. However, the high resolution SEM micrograph of low temperature (1600°C) HP-ed sample CA2613F revealed a microstructure of abundant tiny elongated α-sialon grains (Fig. 4.7(b)), suggesting that Ca α-sialon grains can intrinsically take an elongated morphology even if large amounts of α-sialon nuclei exist. Furthermore, these overpopulated tiny α-sialon nuclei in composition CA2613 could still develop into large elongated α-sialon grains at higher temperature without impinging upon each other, whereas those in CA1005 remained in an almost equiaxed morphology even when fired at 1800°C over 8 h. Li et al. (2000) studied the nucleation and growth mechanism of elongated Ca α-sialon grains using different Si_3N_4 powders with various $\alpha-Si_3N_4:\beta-Si_3N_4$ ratios. They proposed that the nucleation density probably was not the only factor that determined the morphology of α-sialon grains, in fact, the amount and the viscosity of the transient liquid might play a more important role. Indeed, to better understand the growth mechanism of elongated Ca α-sialon grains, the combined role of grain impingement and the nature of the liquid phase in the system at the sintering temperature needs to be considered.

As discussed in section 4.6, the conversion from $\alpha-Si_3N_4$ to α-sialon through the solution/precipitation process was fully completed at temperatures around 1600°C and the abundant tiny α-sialon particles were formed (Fig. 4.7(b)). It is therefore reasonable to assume that grain growth from temperatures above 1600°C is governed by the Ostwald ripening mechanism via the dissolution of the small diameter α-sialon grains. In theory, the population of growing α-sialon particles depends on the critical particle diameter, d_{crit}, and particles with a size below d_{crit} can dissolve in the transient liquid. However, in practice, the critical diameter can be influenced by many factors, such as the amount of the transient liquid and the nitrogen solubility of the oxynitride melt at the operating temperature. Hoffmann (1994a) found that the value

of the critical diameter increased as the nitrogen solubility of the transient liquid increased.

Compared to composition CA1005, CA2613 contains a higher amount of CaO additive and a lower amount of nitride particles (Table 3.2), in particular α-Si_3N_4 particles. The higher CaO and the lower α-Si_3N_4 contents result in larger amounts of transient liquid with relatively low nitrogen content at elevated temperatures, indicating that the oxynitride melt in CA2613 may have a lower viscosity and can dissolve more nitrides than that in CA1005 at the same sintering condition. Thus, the value of the critical diameter for material CA2613 is greater than that for CA1005. The greater d_{crit} value would facilitate the dissolution of the fine α-sialon particles and hence create more space and provide sources for the coarser particles to develop into larger elongated grains. In addition, the large quantity of low viscosity transient liquid existed in composition CA2613 at the sintering temperature also facilitates the densification process of this material via pore elimination and cooperative flow of the particle-liquid mixture, and thus, material CA2613 exhibits a lower porosity than CA1005. The influence of the amount and property of the transient liquid on the grain morphology and porosity of the Ca α-sialon ceramics becomes more pronounced as the x-value of the design composition further increases. As a result, among the three compositions, material CA3618 consists of α-sialon grains with the highest aspect ratio and the greatest diameter together with the lowest porosity. In contrast, the small amounts of oxynitride melt with a high nitrogen content in composition CA1005 leads to a decrease in the d_{crit} value of α-sialon particles and hence results in an over abundance of tiny α-sialon particles which consequently hinders the development of elongated α-sialon grains. Furthermore, the high porosity of sample CA1005 is also attributed to the presence of the small amount of high viscosity oxynitride liquid at the sintering temperature.

4.7.2 Effect of sintering conditions

In the present study, the major microstructural parameters of interest are grain size, grain morphology and the amount of grain boundary glassy phase. Microstructural examination of samples CA1005, CA1005F and CA1005C, fabricated from the same

design composition but under various processing conditions, provides some insights into understanding the effect of sintering technique and dwell time on the microstructure of these materials.

Sample CA1005 was PLS-ed at 1800°C for 4h while samples CA1005F and CA1005C were first PLS-ed at 1800°C for 3h and 8h, respectively, and followed by HP at 1700°C for 1h. While the microstructure of the three samples exhibited similar features (Figs. 4.5(a) and 4.6(a) and (b)), i.e. consisting of almost equiaxed α-sialon grains with small amounts of grain boundary glass, detailed image analysis revealed some variations in grain size, grain morphology and the amount of intergranular glass. As can be seen from Table 4.4, among the three samples, CA1005 exhibits the smallest grain size and highest intergranular glass content and CA1005C has the largest grain size and lowest glass content. In addition, CA1005F and CA1005C possess a higher grain aspect ratio in comparison to CA1005.

Samples CA1005F and CA1005C were both PLS-ed first and then HP-ed, except the dwell time at the PLS stage was much longer for CA1005C (8h) than for CA1005F (3h). The long dwell time at the sintering temperature has two effects on the microstructure of α-sialon ceramics. Firstly, the longer dwell time can increase the solubility of Ca^{2+} in the α-sialon unit cell and thus decrease the amount of intergranular glass in the final product. The argument that the solubility of Ca^{2+} increases with the increasing dwell time is consistent with the measured unit cell dimensions of the α-sialon phase in these materials. As shown in Table 4.3, sample CA1005C exhibits slightly larger cell dimensions over CA1005F in both *a-* and *c-* axes, indicating that the α-sialon lattice in sample CA1005C has accommodated more Al^{3+} and Ca^{2+} than that in CA1005F. The consequence is that sample CA1005C contains less grain boundary glass than CA1005F (Table 4.4). Secondly, the longer dwell time at the sintering temperature can alter the size and aspect ratio of the α-sialon grains due to the Ostwald ripening effect. As discussed above, grain growth in α-sialon ceramics at the sintering temperature is a process of Ostwald ripening involving dissolution of the small diameter α-sialon grains. Hence the longer sintering time results in a larger grain size.

Samples CA1005 and CA1005F were both held at the sintering temperature for 4 h, except that CA1005 was PLS-ed while CA1005F was PLS-ed for 3 h followed by HP for 1 h. The post-sintering HP resulted in a noticeable grain growth coupled with a reduced amount of grain boundary glass in CA1005F in comparison to CA1005. The densification process in the presence of a liquid phase has been described by Kingery (1959) as being caused by compressive forces, arising from capillary action, acting between contacting particles. These compressive forces result in an increase in chemical potential at the contact points, which gives rise to the higher solubility of the solid at these points (Kingery 1959). The solute diffuses away from contact points allowing the approach of the particle centers and thus densification takes place.

The post-sintering uniaxial HP of sample CA1005F introduces an external compressive force in the sample. Therefore, the grain/liquid/grain interfaces whose plane is perpendicular to the HP direction are exposed to an enhanced compressive stress. The enhanced compressive stress results in an increased solubility of the solid at these interfaces. The solute diffuses away from the high compressive stress regions through the oxynitride melt to deposit in grain boundaries whose plane is perpendicular to the tensile stress (Burke 1990), thus preferential grain growth in the plane perpendicular to the HP direction occurred. The solute also diffuses through the oxynitride melt to deposit at multi-grain junctions where the concentration of the tensile stress is relatively high (Chen and Hwang 1992), thus a reduction in grain boundary glass is observed. In addition, HP can result in grain rotation (Zhan et al. 2000) and redistribution of the grain boundary glass, which are also responsible for the preferential grain growth and reduction in the triple junction glass content observed in HP-ed samples.

Although α-sialon grains, as discussed above, can intrinsically develop into an elongated grain morphology, the preferential grain growth in the HP-ed samples CA1005F and CA1005C only result in a small increase in grain aspect ratio compared to their PLS-ed counterpart CA1005. This is because the small amounts of oxynitride melt in composition CA1005 at sintering temperature results in the overabundance of α-sialon nuclei, which consequently hinders the development of

elongated α-sialon grains. It is interesting to note that a large fraction of grains in composition CA1005 were irregular in shape and such phenomenon became more pronounced in the HP-ed samples CA1005F and CA1005C. This is because that α-sialon grains undergo contact flattening during Ostwald ripening due to the overabundant nuclei in composition CA1005. This phenomenon has been described by Petzow (1990) as Ostwald ripening occurring in a shape accommodation way.

Contact flattening resulting from Ostwald ripening in composition CA2613 is found to be less significant than that in composition CA1005. The relatively high liquid content in composition CA2613 facilitates the dissolution of fine α-sialon grains, which allows the coarser grains to develop into a large elongated morphology and gives a way to further densification by rearrangement of α-sialon grains. While the general microstructural features are very similar in the PLS-ed sample CA2613 and the PLS-ed followed by HP-ed sample CA2613C, the post-sintering HP has resulted in some microstructural variations. Compared to sample CA2613 (Fig. 4.5(b)), sample CA2613C exhibits a larger grain size (in both width and length) coupled with less grain boundary glass and lower porosity (Fig. 4.7(c)). Such differences can be attributed to the mechanism proposed above, Ostwald ripening under an external compressive stress. In addition, two important findings are also worthwhile to mention. First, a textured structure was observed in sample CA2613C (Figs. 4.2(b) and 4.3(b)), suggesting that HP at 1700°C/1h has to some degree resulted in the rotation and directional growth of elongated α-sialon grains. Second, image analysis showed that CA2613C exhibited a lower apparent aspect ratio than CA2613 (Table 4.4), indicating that dissolution of the small diameter α-sialon grains might begin with significant reductions in grain lengths while the grain diameters retain almost unchanged (Hoffmann 1994a).

Microstructural examinations of samples CA2613F and CA2613C, fabricated from the same design composition but under various processing conditions, provide some clues to understanding the effect of sintering temperature on the microstructure of these materials. Sample CA2613F possesses a fine, slightly elongated grain morphology with a relatively high intergranular glass content and a minor unreacted AlN phase while sample CA2613C exhibits a coarser and longer grain morphology

coupled with less grain boundary glass and an additional minor 33R phase. At 1600°C, the conversion from α-Si_3N_4 to α-sialon through the solution/precipitation process was just completed, but other reactions, such as dissolution of AlN, were still in progress. As a result, the abundance and homogeneity of the tiny elongated α-sialon grains with a small amount of AlN raw powder were observed. Lattice parameters measurement revealed that the low temperature fabricated sample CA2613F had a smaller unit cell dimension compared to its high temperature counterparts CA2613 and CA2613C. The smaller unit cell dimension associates with a lower substitution number of Al-N bonds for Si-N bonds and thus results in a lower solubility of Ca^{2+} in the α-sialon lattice and a higher intergranular glass content. Therefore, the higher sintering temperature has at least two effects on the microstructure of Ca α-sialon ceramics: (1) increases the solubility of Ca^{2+} in the α-sialon lattice and hence reduces the intergranular glass content; and (2) facilitates the development of large, elongated α-sialon grains through Ostwald ripening.

4.8 Relationship between Microstructure and Mechanical Properties

It has long been recognized for Si_3N_4-based materials that there exists a close relationship between microstructural parameters and mechanical properties (Becher et al. 1993; Hoffmann 1994a; Chen and Rosenflanz 1997; Zhao et al. 1997; Becher et al. 1998; Ellen et al. 1998; Kleebe et al. 1999). From microstructural observations and mechanical property evaluations in this study, hardness in Ca α-sialons is dependent on a combination of α-sialon content, grain size, porosity and the amount of glass phase in the material. Similarly, fracture toughness is also associated with a number of microstructural parameters, such as grain aspect ratio, grain size and grain boundary secondary phases.

A high α-sialon content with coarse grain size coupled with low intergranular glass and pore contents gives an optimized hardness. In contrast, the apparent aspect ratio of the α-sialon grains is found to have little influence on the hardness value of these materials. As tabulated in Tables 4.4 and 4.5, despite a dramatic difference in the

grain aspect ratio between the HP-ed samples CA1005F and CA2613C, the hardness values of the two materials are virtually the same. It may be argued that the relatively high porosity in sample CA1005F can result in a decline in hardness, however the higher glass content in sample CA2613C is also known to reduce hardness. As the porosity and glass content in these materials are quite low, being less than 2 and 3 vol%, respectively. It is reasonable to conclude that the grain aspect ratio in α-sialon ceramics has little impact on their hardness values. The present finding is consistent with previous observations where α-sialons containing various amounts of elongated grains with very different aspect ratios possessed almost identical hardness values (Chen and Rosenflanz 1997; Kim et al. 2000).

On the other hand, a coarse grain size and a high aspect ratio may both give rise to improvements in the fracture toughness of the materials. The effect of grain size on the fracture toughness is clearly demonstrated in HP-ed samples CA1005F and CA1005C where fracture toughness increases as the grain size increases. The effect of grain aspect ratio on the fracture toughness is evident in the three PLS-ed samples CA1005, CA2613 and CA3618 as well as in HP-ed samples CA2613F and CA2613C where fracture toughness increases as the grain aspect ratio increases. The toughening effect observed in this study is mainly attributed to the crack bridging mechanism. While increasing the grain size and grain aspect ratio can increase the incidence of crack bridging, to further improve the toughness, cracks must propagate along grain interfaces rather than through the grains. This interface debonding process appears to be modified by the chemistry of the oxynitride glass at the grain boundaries (Becher et al. 1994; Hoffmann 1994a; Kleebe et al. 1999).

The chemistry of the grain boundary glass probably holds the key to understanding why the fracture toughness of α-sialon ceramics is significantly lower than that of silicon nitride. Current best room-temperature values of fracture toughness for α-sialon and Si_3N_4 ceramics were ~6 MPa m$^{1/2}$ (Chen and Rosenflanz 1997; Zhao et al. 1997) and >10 MPa m$^{1/2}$ (Becher et al. 1998; Sun et al. 1998), respectively. The Nd and Y stabilized α-sialon ceramics fabricated by Chen and Rosenflanz (1997) and later Kim et al. (2000) exhibited microstructures consisting of large elongated α-sialon grains imbedded in a matrix of fine-grained α-sialon. This microstructure is

very similar to that of Si_3N_4 which was described to have the best properties where large elongated β-sialon grains were evenly dispersed in a matrix of fine-grained β-Si_3N_4 and an amorphous grain boundary phase. However, the fracture toughness of these α-sialons only attained half the fracture toughness value of silicon nitride ceramics. One possible reason for this is that in α-sialon, unlike in β-sialon and β-Si_3N_4, both grain boundary glass and α-sialon grains contain identical elements, resulting in strong interfacial bonding between α-sialon grains and the glassy matrix. Therefore to further improve the fracture toughness of α-sialon ceramics, investigations into compositional design of the intergranular glass that can lead to a weakened interfacial bonding strength between α-sialon grains and the glassy matrix are necessary.

4.9 Grain Boundary Devitrification

It is well established, both theoretically and experimentally, that the amorphous phase in silicon nitride based materials exists as intergranular thin films present at two-grain interfaces and as excess glass located at multi-grain junctions (Clarke and Thomas 1977; Clarke 1987; Clarke et al. 1993). The intergranular films usually have a partially ordered structure with a typical equilibrium thickness of 0.5-2.0 nm depending on the composition of the materials (Kleebe et al. 1992; Hoffmann 1994b; Tanaka et al. 1994). Therefore, these thin films are energetically stable and cannot be further crystallized. Crystallization of the grain boundary amorphous phase mainly takes place at multi-grain junctions. However, high-resolution electron microscopy examination of devitrified silicon nitride ceramics showed that even at those multi-grain junctions, complete crystallization of the amorphous phase could not be achieved. A thin amorphous film remains between the crystalline grain boundary phases and the silicon nitride grains (Vetrano et al. 1992). There are two reasons for the existence of this film. First, the change in composition of the residual amorphous phase resulting from the crystallization process could have reduced the crystallization rate (Bernard-Granger et al. 1995). Second, the volume reduction induced by crystallization process could have created a tensile hydrostatic stress at the multi-grain junctions, which hinders the further devitrification process (Bernard-Granger et al. 1995).

In Ca α-sialon ceramics, the grain boundary glassy phase is oxynitride glass that contains calcium. Previous quantitative measurements (Wang et al. 1999a) showed that, when CaO was used as the calcium source, the solubility of Ca^{2+} in α-sialon structure was approximately 70% of the nominal value for compositions ranging in x = 0.3–1.4, indicating that around 30% of Ca^{2+} remained in the grain boundary glassy phase. More significantly, the above solubility level was found to continuously decrease as the nominal x value further increased (see section 4.3.4 and Wang et al. 1999a).

In the present study, XRD analysis showed that the post-sintering heat treatment of Ca α-sialons produced a crystalline gehlenite phase (Fig. 4.4). This is consistent with the previous reports in the literature where research into oxynitride glasses with various nitrogen contents revealed that the main devitrification product in Ca-SiAlON glasses, at all nitrogen concentrations, was gehlenite or a solid solution of gehlenite with nitrogen (Drew et al. 1981; Hampshire et al. 1985). The gehlenite solid solution is postulated to extend from $Ca_2SiAl_2O_7$ to $Ca_2Si_3O_5N_2$ (Drew et al. 1981) with a general formula $Ca_2Si_{1+x}Al_{2-x}O_{7-x}N_x$ (van Rutten et al. 1996), and has a melilite based structure (Wyckoff 1968).

Devitrification of intergranular Ca oxynitride glass may not be completed under the current heat-treatment condition (1300°C for 12 h). One possible reason is that the radial tensile stress resulting from the crystallization of the excess glass at the multi-grain junctions. Crystallization of the Ca-containing oxynitride glass is combined with a volume reduction due to the higher density of crystalline gehlenite phase than that of the glass. The volume change, of approximately 10 vol% (Deckwerth and Rüssel 1997a and b), leads to the generation of radial tensile stresses in the triple junctions at the interface between α-sialon and the gehlenite phase. In addition, the formation of the gehlenite phase can result in an internal stress at the interface between the gehlenite and α-sialon grains due to thermal expansion mismatch. Because of the higher thermal expansion coefficient of gehlenite relative to α-sialons (Hampshire et al. 1994), this internal stress is also tensile in nature.

These tensile stresses resulting from both volume reduction and thermal expansion mismatch may be relaxed by two possible mechanisms: (1) viscous flow of the amorphous phase at two-grain interfaces into crystallizing multi-grain junctions; and (2) solution of primary grains into the amorphous film at two-grain interfaces, which diffuses into and reprecipitates at crystallizing multi-grain junctions (Kessler et al. 1992). Stress relaxation via viscous flow of the amorphous phase into crystallizing multi-grain junctions will result in a reduction of the intergranular film thickness. However, the viscous thinning of the amorphous film may not be kinetically favoured since the amorphous film is in an equilibrium state with an equilibrium thickness as proposed by Clarke (1987). This leaves solution-reprecipitation of the primary grains as the main stress relaxation mechanism. However, the annealing temperature of 1300°C may be too low to cause a significant solution and reprecipitation of α-sialon. Thus tensile stresses persist at the annealing temperature and the strain energy associated with these stresses acts as a thermodynamic barrier which opposes the further devitrification process (Kessler et al. 1992; Pompe and Kessler 1994). This scenario is supported by the previous study of crystallization behaviour of bulk glasses (Deckwerth and Rüssel 1997a). It was found that for the Mg-Ca-Al-Si-O-N system, a complete crystallized glass-ceramic could not be prepared even after heat treatment at 1350°C for 20 h (Deckwerth and Rüssel 1997a).

The above analysis suggests that the post-sintering heat treatment may have two effects on the Ca α-sialon materials. First, the partial crystallization of the excess glass located at three-grain edges (Hoffmann 1994b), which can result in up to 10% volume reduction in the Ca α-sialon system (Malecki et al. 1997) and thus produce a radial tensile stress in the triple junctions at the interface between the α-sialon grains and the gehlenite phase (Hoffmann 1994b). Second, the creation of thermal stresses at the three-grain edges due to thermal expansion mismatch between the α-sialon grains and devitrified phases. This thermal stress is also a tensile stress owing to the higher thermal expansion coefficient of gehlenite compared to α-sialons (Hampshire et al. 1994).

4.10 Summary

This chapter has examined the densification behaviour and the prospects of microstructural design of Ca α-sialon ceramics as well as the correlation between the microstructure and mechanical properties. It has also examined the possible effects of the crystallization of intergranular glass on the properties of Ca α-sialon ceramics. The following conclusions can be drawn from the results of this study:

- The reaction sequence and densification behaviour of Ca α-sialons seemed, in general, to agree with the reaction densification mechanism proposed by Menon and Chen (1995a and b). In addition, CaO was found to be a very effective sintering aid and PLS-ed Ca α-sialon samples with a bulk density 95-99% of their true density could be prepared for compositions located both inside and outside the single-phase α-sialon forming region.

- The microstructure of Ca α-sialon ceramics is strongly influenced by the quantity and properties of the intergranular glass, which are in turn determined by the starting powder composition. Compositions inside the single-phase α-sialon forming region, in general, produce a microstructure consisting of almost equiaxed grain morphology coupled with a small amount of intergranular glass, while those outside the single-phase region on the Al rich side give microstructures containing mainly elongated α-sialon grains with minor secondary phases and relatively high glass contents.

- The microstructural design of Ca α-sialon ceramics can also be achieved by various sintering techniques and conditions. Post-sintering HP gives a higher grain growth rate and density and also redistributes the intergranular glass. The longer dwell time results in a coarser grain size and larger cell dimensions for the α-sialon phase and thus reduces the amount of intergranular glass. The higher sintering temperature assigns a higher grain aspect ratio and a larger cell dimension.

- The mechanical properties of Ca α-sialon ceramics were found to be closely associated with their microstructures. It was observed that the fracture toughness increased with the increasing grain size and grain aspect ratio. However, to further improve the toughness of these materials, a weakened interface between the α-sialon grains and intergranular glass is necessary.

- Crystallization of the intergranular glass can introduce residual tensile stresses at the multi-grain junctions of Ca α-sialon ceramics.

Chapter 5

EROSION BEHAVIOUR OF Ca α-SIALON CERAMICS

5.1 Introduction

Based on the results obtained in chapter 4, which demonstrated the viability of using various starting compositions and processing conditions to fabricate Ca α-sialon ceramics with well-tailored microstructures, the present chapter investigates the erosion behaviour of Ca α-sialon ceramics. It examines a number of aspects including the effect of impact angles, erodent particle properties and ceramic microstructures on the erosion mechanisms of Ca α-sialon ceramics.

Section 5.2 describes the experimental details involved in the erosion tests and the characterisation of eroded surfaces. Section 5.3 presents the results of erosion tests on various Ca α-sialon ceramics, while section 5.4 highlights the differences in the damage sustained by these materials. Sections 5.5-5.7 form a comprehensive discussion on erosion mechanisms and the effects of erodent properties and ceramic microstructures on mechanisms of material removal.

5.2 Experimental Program

5.2.1 Target materials

The target materials in this investigation were the in-house prepared Ca α-sialon ceramics including the three pressureless-sintered (PLS-ed) compositions, CA1005, CA2613 and CA3618, and their heat-treated (HT-ed) counterparts, as well as the two-stage sintered samples: CA1005F, CA1005C, CA2613F and CA2613C. The compositional, microstructural and mechanical properties of these materials are given

in chapter 4.

5.2.2 Erodent materials

The erodent particles used were commercial grade SiC and garnet abrasive grits (refer to section 3.3.1). Briefly, both grits were angular in shape although the corners of the garnet particles were slightly rounded. The SiC particles had a size distribution between 210-500 µm (mean 388 µm), while the garnet grits exhibited a size range between 200-600 µm (mean 400 µm). The chemical compositions and the mechanical properties of the erodent particles are given in Table 3.3.

5.2.3 Erosion tests

Erosion tests were performed in a gas-blast type erosion test rig which has been described in detail in section 3.3.2.1. Mild steel was employed as the control material in each test. The Ca α-sialon specimens were approximately 20 mm in diameter and 5 mm in thickness in the case of the PLS-ed and HT-ed samples and 24 mm in diameter and 5 mm in thickness in the case of the HP-ed samples. The mild steel sample was 20 mm wide, 50 mm long and 1 mm thick.

The effects of the angle of impact and the erodent particle properties on the erosion behaviour of Ca α-sialon ceramics were investigated. The three PLS-ed compositions, CA1005, CA2613 and CA3618, were selected as the target materials. The test conditions were as follows:

sample to nozzle distance:	13.8 mm;
particle velocity:	20 m/s;
impact angles:	30°, 45°, 60° and 90° for SiC erosion, and
	30° and 90° for garnet erosion.

In the case of erosion using SiC grits, each sample was eroded with a fixed amount of erodent for six exposures. The dose of erodent particles for each exposure was approximately 200 g for 30° and 45° impacts and 100 g for 60° and 90° impacts. The dosage selected for the shallow angles of impact resulted in a sufficient mass loss which could be detected by the weighing balance. However, using the same dosage

for the high angles of impact caused deep erosion craters which effectively changed the test conditions, particularly, the nozzle-sample distance and the impact angle. Thus, a lower dose was used for high angles of impact.

In the case of erosion using garnet particles, the duration of the tests was prolonged and the dosage was increased to over 2500 g for both 30° and 90° impacts in order to produce a detectable mass loss.

The effects of a number of microstructural parameters on the erosion behaviour of Ca α-sialon ceramics were also investigated (Table 5.1). In particular, the effect of porosity was studied by comparing the erosion behaviour between the PLS-ed and HP-ed samples, while the effect of intergranular glass was examined using the three PLS-ed compositions and their HT-ed counterparts. The effects of grain size and grain morphology were explored using the two-stage sintered samples CA1005F, CA1005C, CA2613F and CA2613C.

Table 5.1 Investigated microstructural parameters and corresponding samples

Sample ID	Porosity	Intergranular glass	Grain size	Grain morphology
CA1005	✓	✓		
CA2613	✓	✓		
CA3618		✓		
CA1005(HT)		✓		
CA2613(HT)		✓		
CA3618(HT)		✓		
CA1005F	✓		✓	
CA1005C			✓	
CA2613F				✓
CA2613C	✓			✓

The test conditions were as follows:

sample to nozzle distance:	13.8 mm;
particle velocity:	20 m/s;
Erodent particles:	SiC;
impact angles:	30° and 90°;
dosage:	~200 g for 30° impact and ~100 g for 90° impact.

In all cases, mass loss was measured using an analytical balance with an accuracy of ±0.1 mg. Wear volume was calculated from the mass loss and the bulk density of each material. Cumulative volume loss was plotted as a function of the amount of erodent impacting on the surface. The steady state erosion rate (ΔE), defined as the volume loss from the specimen per unit mass of erodent used, was determined from the slope of the linear part of the volume loss-mass of erodent plot.

5.2.4 Microscopic analysis

The eroded surfaces of all target materials were examined using a JEOL FE6300 scanning electron microscope (SEM) equipped with a field emission gun. Prior to examination, the specimens were ultrasonically cleaned in ethanol for 5 minutes, then dried and sputter coated with carbon to prevent charge accumulation on the samples during examination. The accelerating voltage used was 10 kV.

5.3 Results of Erosion tests

5.3.1 Effect of eroding conditions

The eroding conditions examined in the present study are the angle of impact and the properties of erodent particles. Fig. 5.1 presents the cumulative volume loss of three Ca α-sialon samples as a function of the amount of SiC erodent impinging on the material surface for various incidence angles. In all cases, the cumulative volume loss increased linearly with the amount of erodent after an incubation period. The slope of this linear portion was used to obtain the steady state erosion rate, ΔE. The linear

relationship between the volume loss and the amount of the erodent indicates that each consecutive dose has removed approximately the same amount of material from the target surface.

The cumulative volume loss due to erosion by garnet particles is plotted as a function of the amount of erodent used for both 30° and 90° impacts in Fig. 5.2. As can be seen, all materials experienced a volume/mass increase at the early erosion stages, indicating that the deformed or smeared erodent material has attached onto the surface of the target material. After an exposure of over 2 kg garnet erodent, both samples CA1005 and CA3618 started to show a consecutive volume loss corresponding to each successive dosage, which allowed the erosion rate to be determined. However, sample CA2613 exhibited no detectable volume loss even after an exposure of over 10 kg garnet erodent. It is important to note that the volume loss observed in samples CA1005 and CA3618 includes losses of both target material and the attached erodent material. Nevertheless, after the incubation period, a steady state erosion rate is still observed.
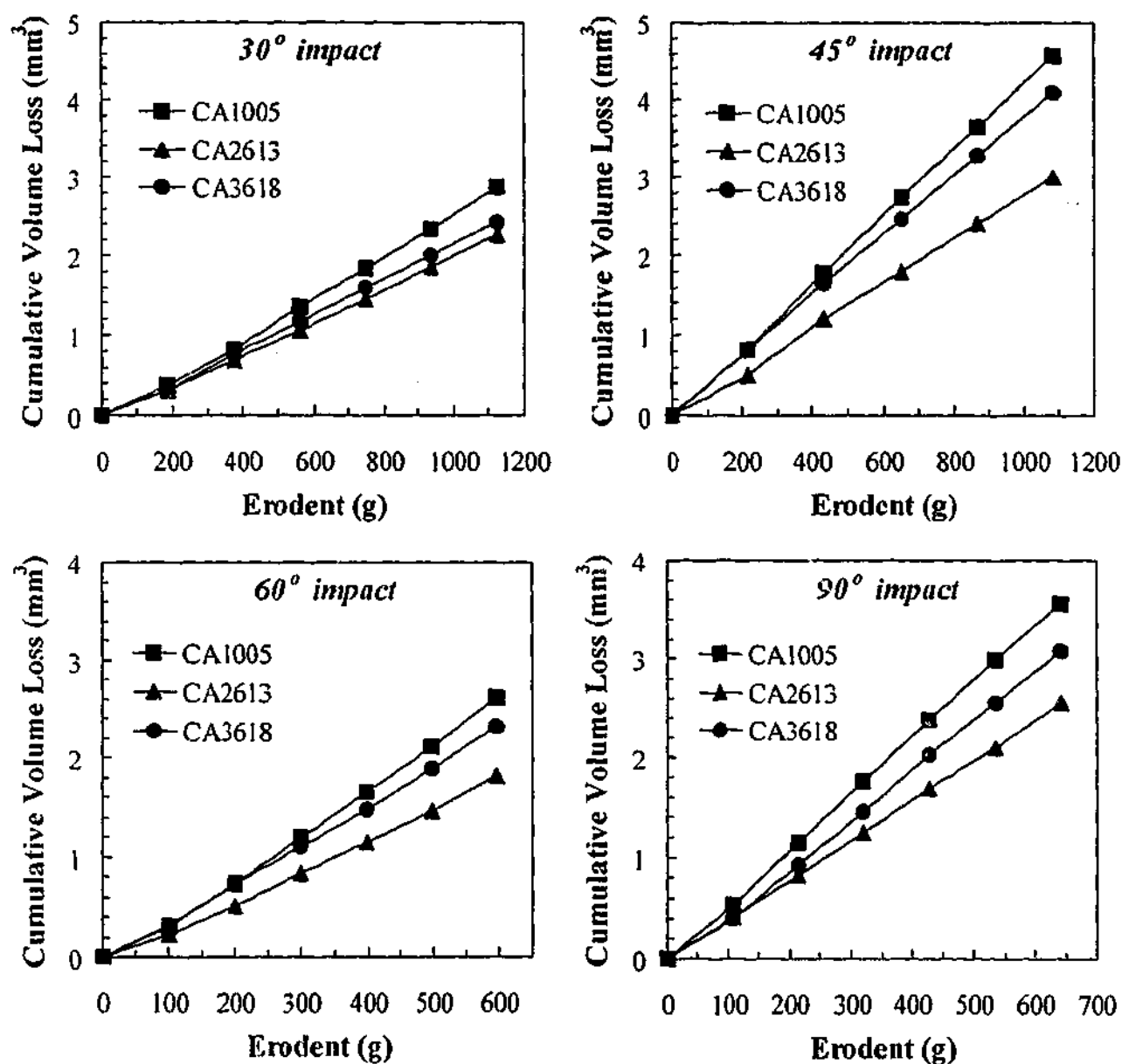
Fig. 5.1. Cumulative volume loss of Ca α-sialon ceramics as a function of the amount of SiC erodent impinging on the target surface for various impact angles.
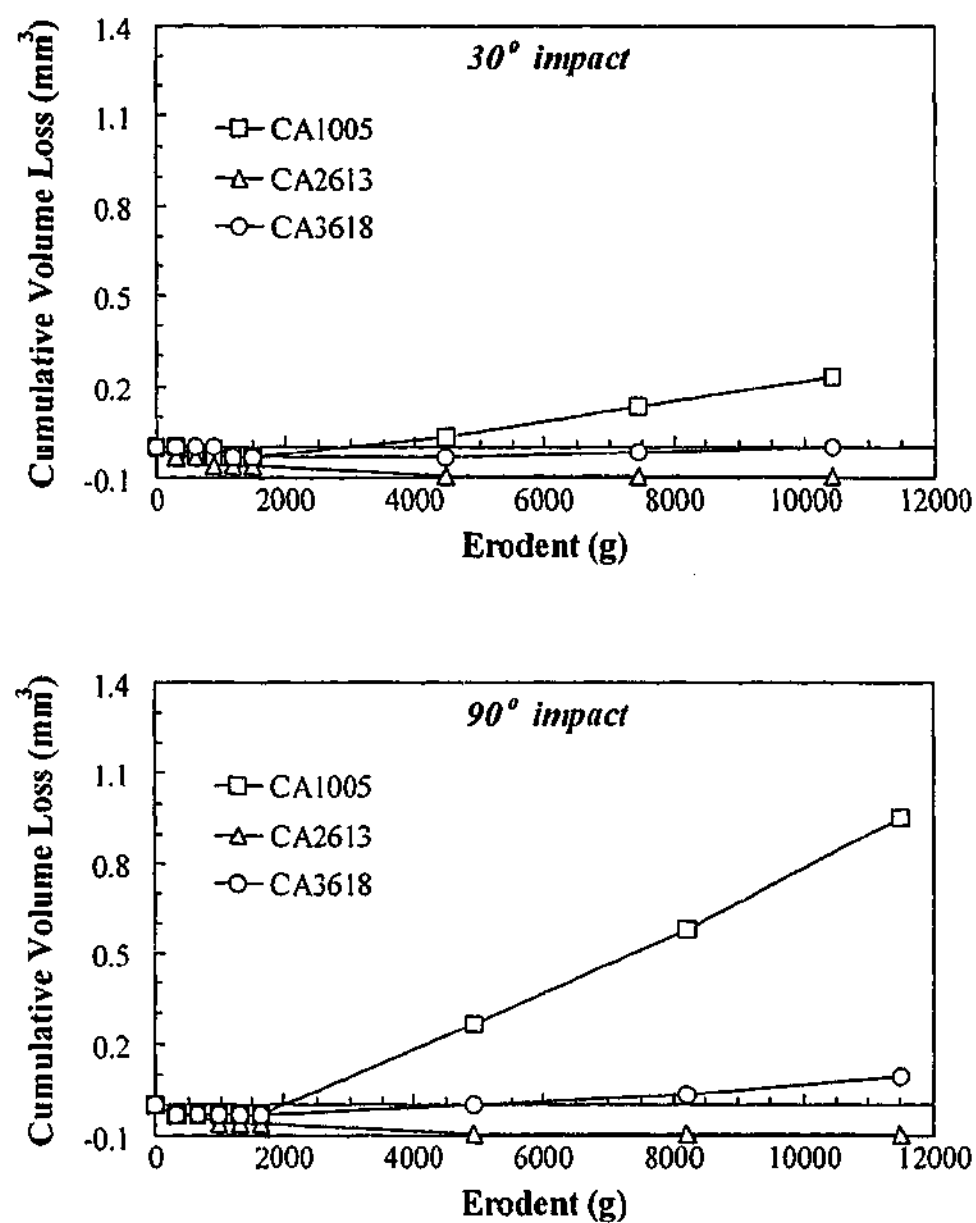
Fig. 5.2. Cumulative volume loss of Ca α-sialon ceramics as a function of the amount of garnet erodent impinging on the target surface for impact angles of 30° and 90°.

Considering the brittle nature of ceramic materials, the maximum erosion rate should occur at normal impact (Sheldon and Finnie 1966a). This is indeed the case observed in the present study. The dependence of the steady state erosion rate on the impact angle for the three PLS-ed Ca α-sialon ceramics eroded by SiC particles is shown in Fig. 5.3. The erosion rate increased monotonically with increasing impact angle and reached a maximum at normal impact. For all samples, the erosion rate at 90° impact angle was approximately twice as great as that at 30° incidence angle. Further, sample CA1005 showed a higher rate of material loss than samples CA3618 and CA2613 at all impact angles. However, the differences in erosion rate among the three materials were not dramatic; the erosion rate of sample CA1005 was only 1.1 and 1.4 times higher than those of samples CA3618 and CA2613, respectively.
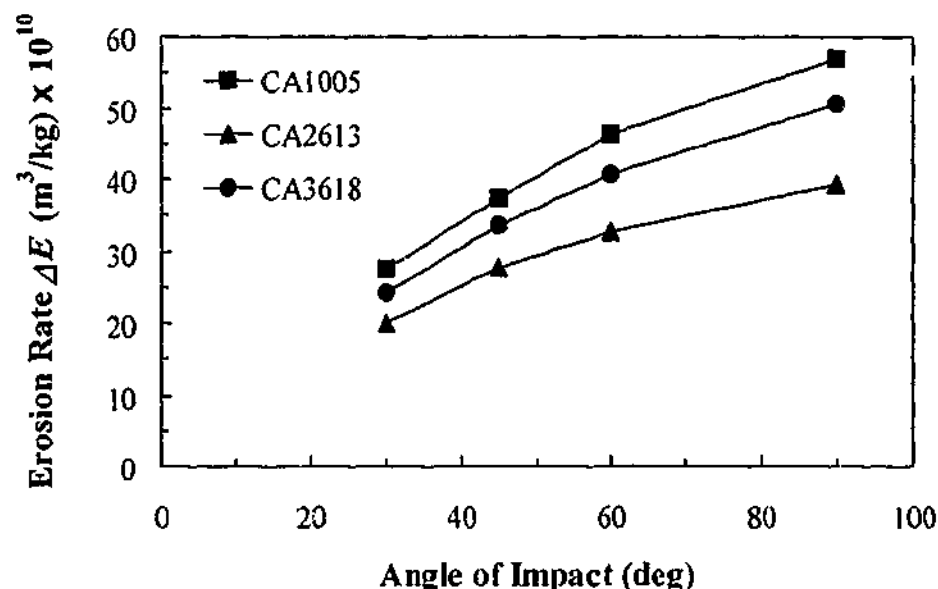
Fig. 5.3. Erosion rate as a function of impact angles for the three PLS-ed Ca α-sialon ceramics after erosion using SiC grits.

The erosion rates of samples CA1005 and CA3618 eroded by garnet particles at impact angles of 30° and 90° are shown in Fig. 5.4. As expected, erosion at 90° resulted in a higher rate of material loss than that at 30° for both materials by approximately a factor of 3. The ranking of the materials from an erosion resistance point of view was essentially the same regardless of the type of erodent. Material CA2613 possessed the best erosion resistance, with material CA3618 next, and material CA1005 showing the lowest erosion resistance. However, two interesting features were revealed:

1. In the case of erosion using garnet erodent, the material removal rate of sample CA1005 was about 6 times higher than that of sample CA3618. However, the difference was significantly reduced when the SiC erodent was used, where the material removal rate of CA1005 was only 1.1 times higher than that of CA3618.

2. In all cases, SiC resulted in significantly higher material removal rates than garnet particles. For material CA1005, the erosion rates at 30° and 90° impingement in SiC crosion were 70 and 50 ⋯⋯ ⋯⋯ ⋯⋯ spectively, than those resulting from garnet erosion. In the ca⋯ ⋯⋯ ⋯⋯ ⋯A⋯18, the differences in wear rates between SiC and garnet ⋯⋯ ⋯⋯ ⋯rther increased by a factor of 6. The erosion rates at 30° and 90° ⋯⋯ pi⋯⋯⋯⋯nt in SiC erosion were about 270 and 400 times greater, respectively, than ⋯⋯se resulting from garnet erosion.
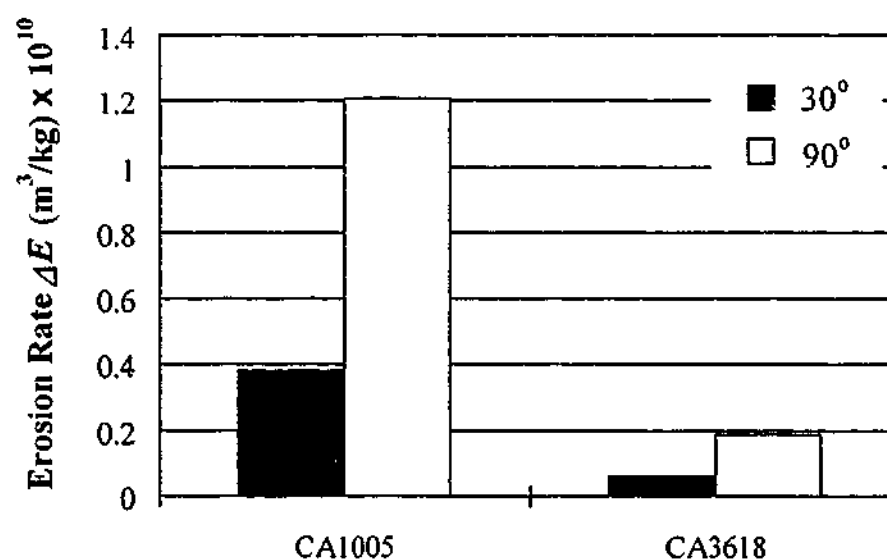
Fig. 5.4. Steady state erosion rates of samples CA1005 and CA3618 eroded by garnet particles at impingement angles of 30° and 90°.

Finally, in order to quantify the effect of erodent particle properties on the rate of material removal for various target materials under different angles of impact, the erosion rates of the three PLS-ed sialon compositions eroded using both SiC and garnet erodents are tabulated in Table 5.2.

Table 5.2 Erosion rates of the three PLS-ed sialon ceramics eroded using both SiC and garnet erodents at 30° and 90° impingement angles

Sample	Impact angle	ΔE_{SiC} $(10^{-10} \, m^3 \, kg^{-1})$	ΔE_{garnet} $(10^{-10} \, m^3 \, kg^{-1})$	$\Delta E_{SiC}/\Delta E_{garnet}$
CA1005	30°	27.6	0.38	~70
	90°	56.9	1.21	~50
CA2613	30°	19.9	—[a]	–
	90°	39.2	—[a]	–
CA3618	30°	24.3	0.06	~400
	90°	50.5	0.19	~270

[a] No detectable volume loss.

5.3.2 Effect of ceramic microstructure

The major microstructural parameters for ceramic materials are the nature of the grain boundary phases, porosity, grain size and grain morphology. It is the primary objective of the present study to examine the influence of these microstructural parameters on the erosion behaviour of Ca α-sialon ceramics.

As mentioned in section 4.2.1, three sialon compositions, i.e. CA1005, CA2613 and CA3618, were PLS-ed at 1800°C for 4 h. Different starting powder compositions resulted in distinctive microstructural features in the final products. Material CA1005 contained mainly fine equiaxed grains and a very small amount of grain boundary glassy material (Fig 4.5(a)). Material CA2613 contained mostly elongated grains and a small amount of glass (Fig. 4.5(b)), and CA3618 contained large elongated grains and a considerable amount of glass (Fig. 4.5(c)). In addition, post-sintering heat treatments (1300°C/12 h in N_2) were carried out on the three materials to devitrify the intergranular glass. Therefore, erosion tests on the three PLS-ed sialon samples and their HT-ed counterparts allow the examination of the effect of the quantity and nature of the intergranular glass on the erosion behaviour of these materials.

The erosion rates of the PLS-ed and HT-ed Ca α-sialon ceramics eroded by SiC particles at 90° impact are presented in Fig. 5.5. Among the three as-sintered samples, material CA1005 showed the highest rate of erosive loss and material CA2613 the lowest. This trend in erosion rates was, however, altered in their heat-treated counterparts where the erosion rate tended to decrease with the increasing m-value, although the erosion rates of the HT-ed CA2613 and CA3618 appeared to be very similar. Note that m-value describes the substitution number of Si^{4+} by Al^{3+} in SiN_4 tetrahedra (see section 2.3.1.2). In all cases, the HT-ed samples displayed higher erosion rates than their as-sintered counterparts and the difference in erosion rate between the HT-ed and the as-sintered samples decreased with increasing m-value.
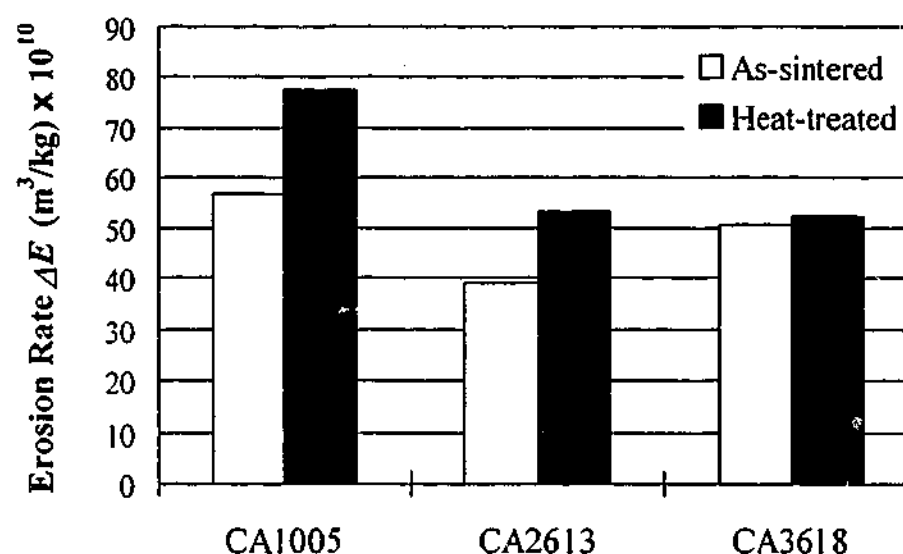
Fig. 5.5. Steady state erosion rates of the three PLS-ed α-sialon ceramics and their HT-ed counterparts eroded by SiC particles at 90° impingement.

As indicated in section 4.2.1, samples CA1005 and CA2613 were PLS-ed at 1800°C for 4 h, while samples CA1005F and CA2613C were PLS-ed at 1800°C for 3 h followed by post-sintering HP at 1700°C for 1 h. The sintering temperature and duration were similar for the PLS-ed and the two-stage fabricated samples. It is therefore expected that samples fabricated from the same starting composition would have similar microstructural features and phase composition. Indeed XRD (section 4.3) and SEM (section 4.4) examinations revealed that samples CA1005 and CA1005F, as well as samples CA2613 and CA2613C consisted of identical

crystalline phases and similar grain morphologies. However, the post-sintering HP resulted in some variations in microstructure in the two-stage sintered materials when compared with their PLS-ed counterparts. The most noticeable difference was in porosity levels. Samples CA1005 and CA1005F exhibited porosity levels of approximately 5.4 and 2.1%, respectively, while CA2613 and CA2613C showed ~2.3 and 0.8% porosity, respectively (Table 4.5). Thus, a comparison of the erosion performances of samples CA1005 and CA2613 with those of CA1005F and CA2613C allows the investigation of the effect of porosity on the erosion behaviour of these materials.

Fig. 5.6 shows the erosion rates of materials CA1005, CA1005F, CA2613 and CA2613C eroded by SiC grits at 30° and 90° impacts. As can be seen, the two PLS-ed samples CA1005 and CA2613 showed a higher erosion rate than their two-stage sintered counterparts CA1005F and CA2613C at both impact angles by approximately a factor of 1.8 and 1.5, respectively.
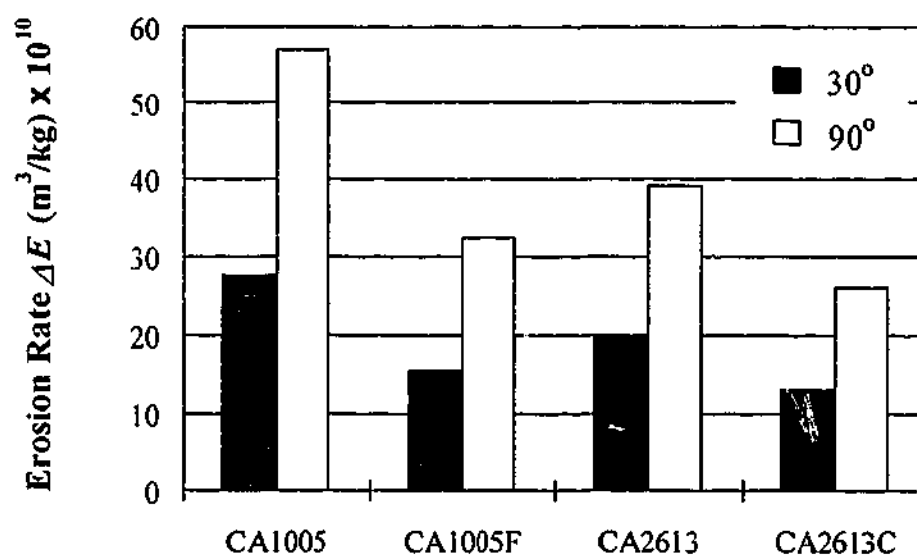
Fig. 5.6. Steady state erosion rates of samples CA1005, CA1005F, CA2613 and CA2613C eroded by SiC particles at 30° and 90° incidence angles.

As stated in section 4.2.1, samples CA1005F and CA1005C were first PLS-ed at 1800°C for 3 and 8 h, respectively, followed by post-sintering HP at 1700°C for 1 h. The longer holding time at 1800°C resulted in a coarser grain size in sample CA1005C compared to CA1005F, but no difference in grain morphology was

revealed between the two samples (Fig. 4.6). In addition, the post-sintering HP at 1700°C for 1 h ensured a comparable porosity level in the two materials (Table 4.5). Hence erosion tests on samples CA1005F and CA1005C allows the evaluation of the effect of grain size on the erosion behaviour of these materials.

On the other hand, sample CA2613F was HP-ed at 1550°C for 0.5 h and then1600°C for 0.5 h and sample CA2613C was PLS-ed at 1800°C for 3 h followed by HP at 1700°C for 1 h. The higher sintering temperature and longer holding time resulted in a coarser grain size with greater aspect ratio in sample CA2613C compared to CA2613F (Fig. 4.7). Thus erosion test on samples CA2613F and CA2613C allows the examination of the effect of grain morphology on the erosion behaviour of these materials.

Fig. 5.7 presents the erosion rates of samples CA1005F, CA1005C, CA2613F and CA2613C eroded by SiC at 30° and 90° impacts. As can be seen, the coarse-grained samples CA1005C showed a higher material removal rate than CA1005F for both impact angles by approximately a factor of 1.2. On the other hand, the fine-grained, lower aspect ratio sample CA2613F exhibited a similar erosion rate as CA2613C at 30° impact. However, for 90° impact, sample CA2613F showed a higher material removal rate than CA2613C by approximately a factor of 1.8.
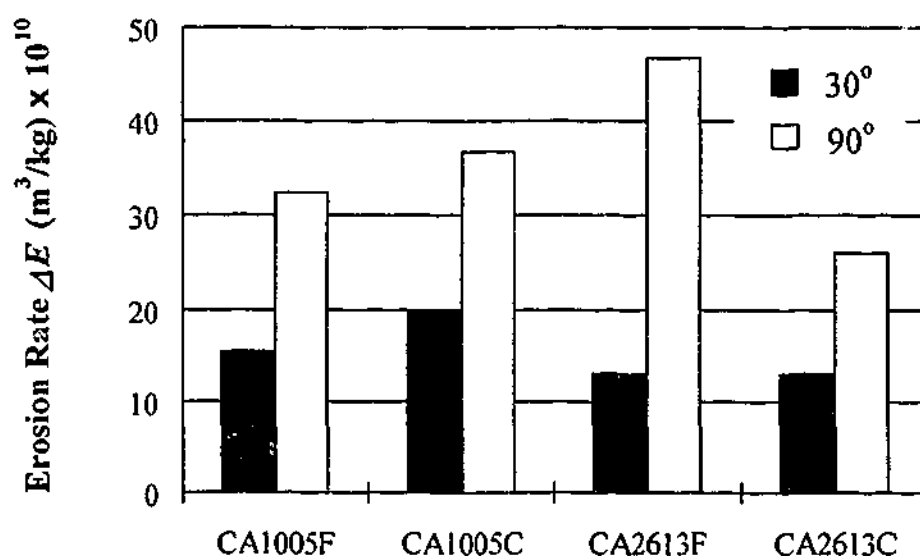
Fig. 5.7. Steady state erosion rates of samples CA1005F (fine-grained), CA1005C (coarse-grained), CA2613F (fine-grained, low aspect ratio) and CA2613C (coarse-grained, high aspect ratio) after erosion using SiC particles at impingement angles of 30° and 90°.

5.4 Examination of Eroded Surfaces

SEM examination of the post-wear surfaces highlights the differences in the damage sustained by the various materials and, therefore, provides a good experimental method for identifying the material removal processes during the wear tests.

5.4.1 Single impact events

In gas-blast erosion, solid particles are accelerated along a parallel walled nozzle, but exit the nozzle as a diverging plume. The distribution of particle trajectories within the plume is well defined (Shipway 1997), and the probability of a particle striking the target becomes smaller as the angle of particle trajectory with respect to nozzle axis increases. Thus the examination of the edge of the erosion crater permits the investigation of the damage induced by single particle impact. Fig. 5.8 presents SEM micrographs of isolated impact craters on the eroded surface of material CA2613F resulting from single impacts of SiC particles at nominal 90° incidence. It can be seen that the nature of impact impression varies according to the size and shape of the erodent particles as well as the particle-target contact condition. The size scale of these impact impressions is of the order of 10-40 μm.
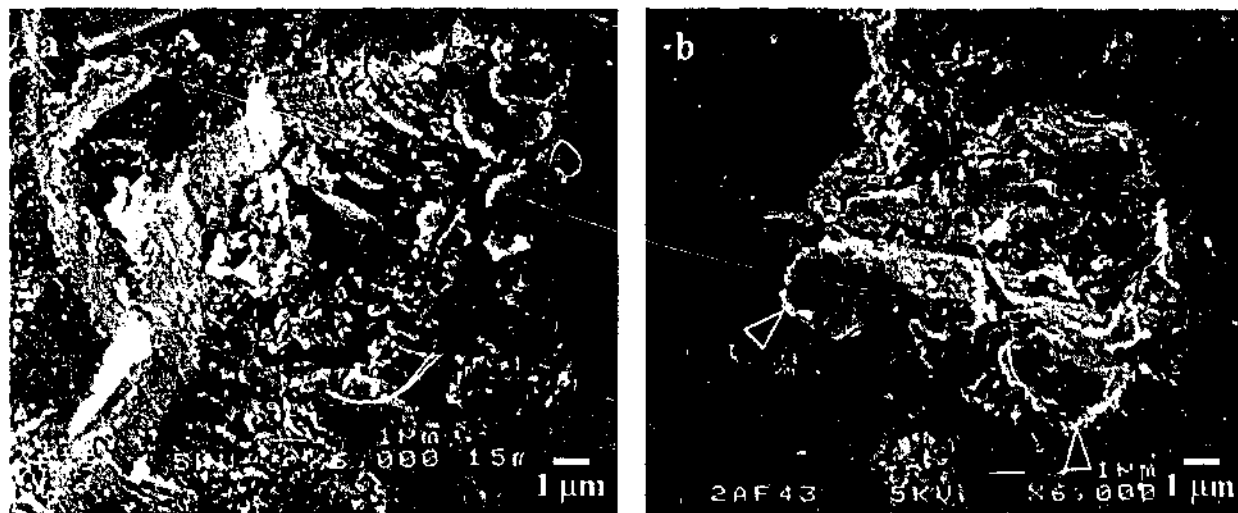
Fig. 5.8. SEM micrographs showing isolated impact crater resulting from erosion of material CA2613F by SiC particles at normal incidence angle.

Fig. 5.8(a) shows a comparatively large impact crater with a relatively flat bed, while Fig. 5.8(b) illustrates an impact crater which is considerably smaller in size and exhibits a pointy valley. However, in both cases, the erodent particles cut deeply into the target surface and produced severe plastic deformation. Plastic deformation is evidenced by the smooth plough marks, the smeared materials, as well as the raised lip of deformed material at the edge of the impact site. In addition, microcracks and small-scale grainy regions were observed, indicating that a brittle-fracture mode also operated. The debris resulting from this brittle-fracture were found scattered in the impact sites. The grainy regions are believed to be caused by the small-scale lateral cracking, marked by arrows in Fig. 5.8(b), leading to chipping of the surface material. The size of the lateral cracks is typically of the order of several micrometers. This is, however, different from the "classical" lateral crack patterns produced by single impact events observed in very brittle materials such as single crystal Si (Routbort et al. 1980a) and glass (Srinivasan and Scattergood 1987) where lateral cracks extend far from the impact sites.

The damage features resulted from single impacts were, in fact, very similar in all sialon target materials under the current erosion condition, suggesting that in erosion of Ca α-sialon ceramics, plastic flow processes contribute in addition to the nominally brittle-fracture mode.

Although the present observation revealed only small-scale lateral cracking from single impact events on incipient surfaces, more severe lateral cracking was evidenced on the fully eroded surfaces, marked by arrow in Fig. 5.9. However, the lateral crack of this kind (Fig. 5.9) is seldom observed on the fully worn surfaces due to the linking up of numerous lateral cracks. Indeed, even in erosion of single crystal and glass materials, the "classical" lateral cracks are not often revealed (Lathabai and Pender 1995; Shipway and Hutchings 1996).

Fig. 5.9. Single impact damage revealed on the fully eroded surface of material CA2613F using SiC particles at 30° incidence angle. Note: lateral crack indicated by arrow.

5.4.2 Effect of eroding conditions

The erosion craters formed by gas-blast erosion were circular in shape for normal impact and elliptical for oblique impact. The elliptical erosion crater had its major axes lying along the direction of particle impact and its ellipticity (ratio of major to minor axes) increased as the impact angle became more oblique. Also in these gas-blast erosion craters, a halo effect was observed. The halo zone, a ring surrounding the actual circular/elliptical erosion crater, was formed by the particles which left the nozzle orifice with a large divergence angle to the nozzle axis (Lapides and Levy 1980; Shipway 1997).

The representative features of the eroded surface of the three PLS-ed α-sialon ceramics after erosion using SiC particles at shallow and normal impingement angles are presented in the SEM micrographs of Fig. 5.10. To facilitate comparison of damage sustained by the three test materials under various impingement angles, all micrographs were taken at or near the centre of the erosion crater, at the same magnification.

In all cases, the erosion damages were characterized by both brittle-fracture and plastic deformation of the materials. However, a comparison of the morphological features on the surfaces of these materials subjected to 30° and 90° impacts, as shown

in Figs. 5.10(a), (c) and (e) and Figs. 5.10(b), (d) and (f), respectively, revealed the following differences.

In the case of 30° impingement, the damaged surface contained a high area fraction of plastically deformed zones with high incidence of long-trailed plough marks or grooves lying along the particle colliding direction.
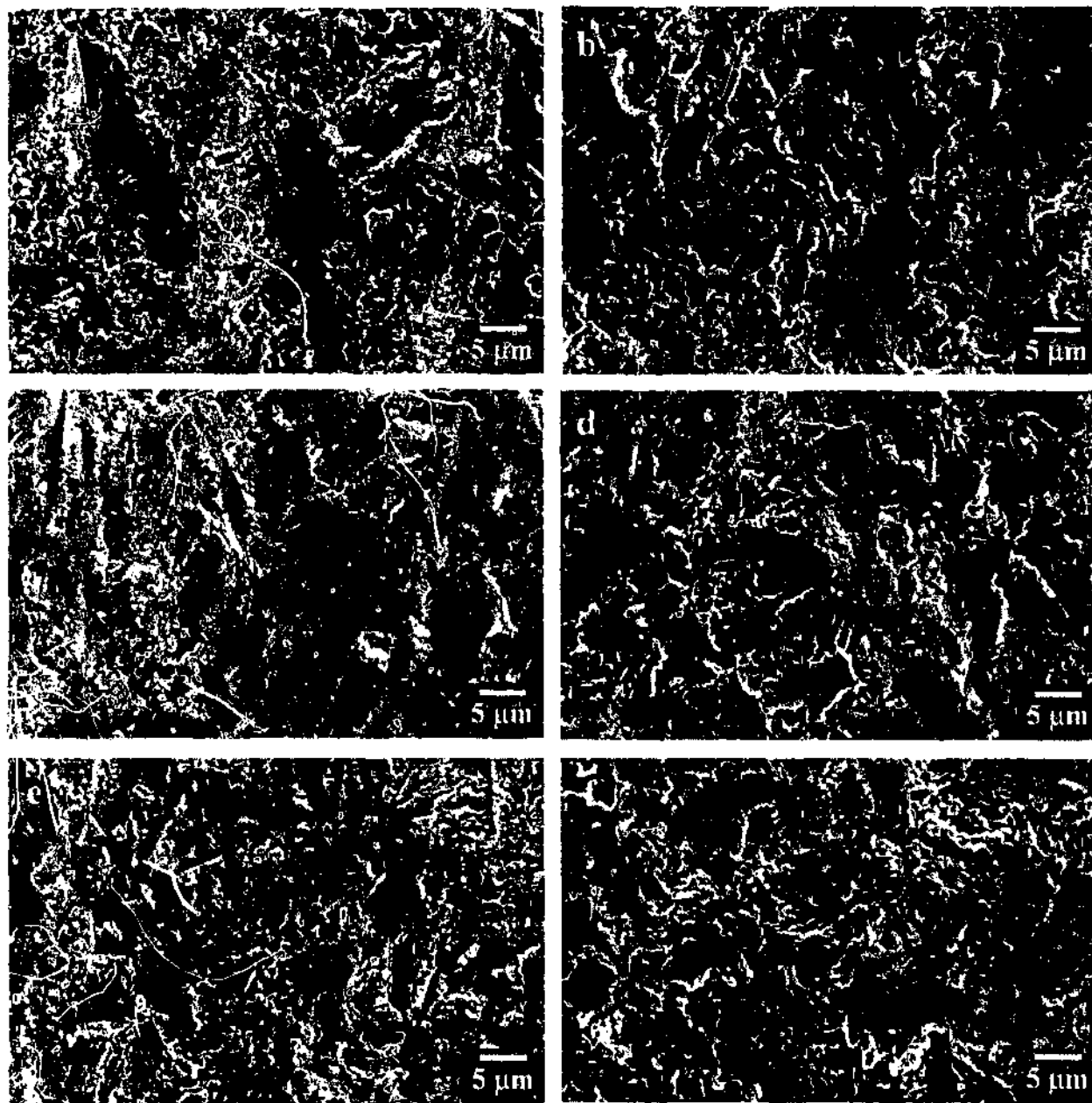
Fig. 5.10. Steady state erosion surfaces of the three PLS-ed α-sialon ceramics after 30° and 90° impingement. (a and b) CA1005 at 30° and 90° impact; (c and d) CA2613 at 30° and 90° impact; (e and f) CA3618 at 30° and 90° impact. The particle impact direction for 30° impact is from top to bottom of the micrographs.

118

The plastic grooves, as shown at a higher magnification in Fig. 5.11, were similar to scratches produced on ceramic surfaces by a diamond stylus (Zhou and Bahadur 1995) and contained many smooth stringers extruding along the groove, indicating that the target material underwent localized plastic shear deformation. However, the edges of the groove, and in some instances even the bottom of the groove, showed evidence of brittle-fracture. Microcracks, wear debris and smeared materials were found along the sides of the groove, suggesting that cracks of grain facet dimension had propagated from near the edge of the plastic zone.

Fig. 5.11. Higher magnification SEM micrograph showing the plough mark produced by SiC particles on material CA1005 at 30° impact.

In the case of high angle impingement, however, the damaged surface contained an increased area fraction of brittle-fracture zones. The brittle-fracture zones are characterized by a facetted morphology, indicating that large amounts of material have been removed from the target surface through fracture. In addition, the trails of plough marks were much shorter compared to those observed in 30° eroded surfaces.

The eroded areas of material CA1005 after erosion using garnet and SiC particles at 30° impact were examined by SEM. Micrographs of the eroded surfaces are presented in Fig. 5.12.
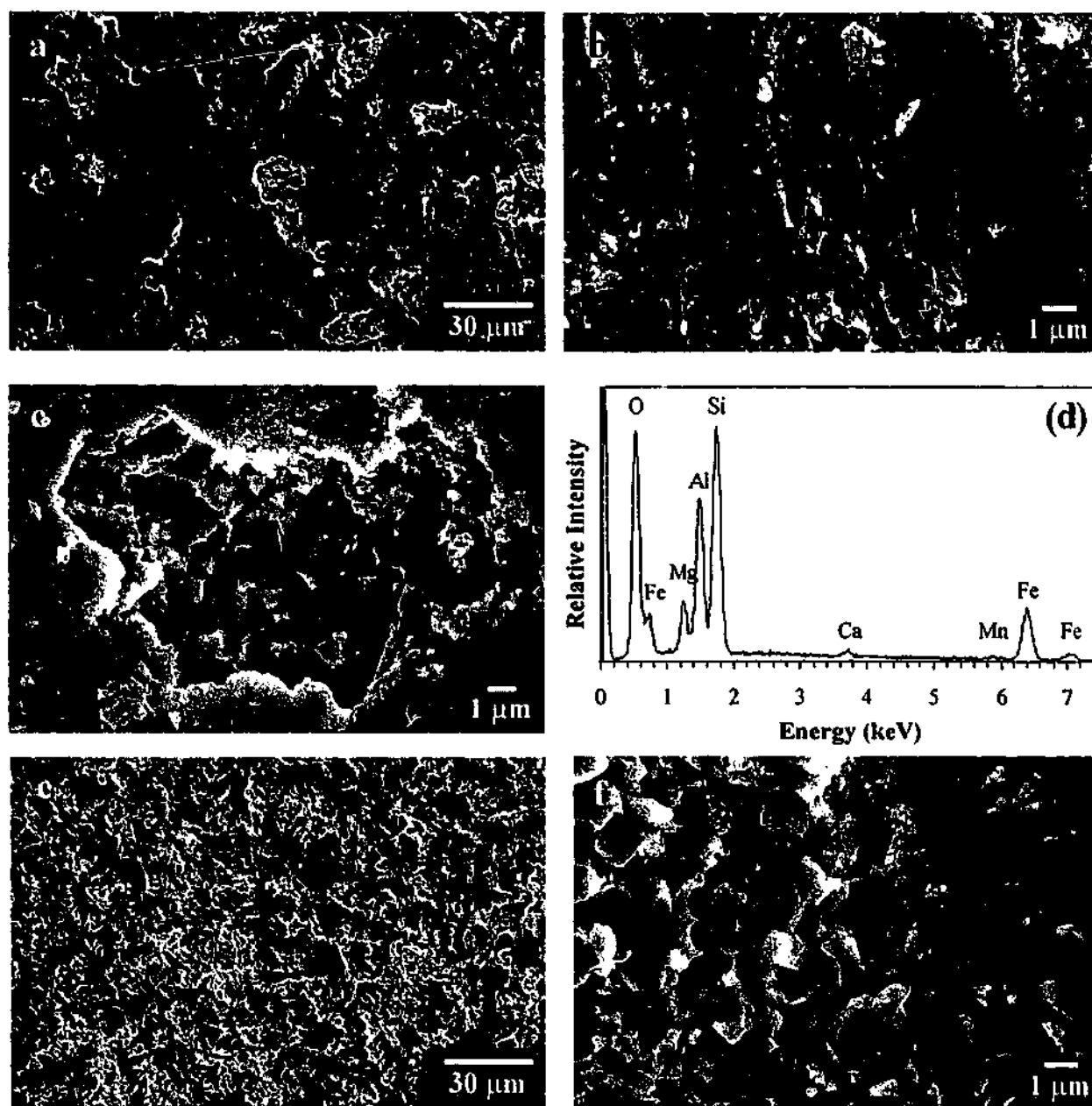
Fig. 5.12. SEM micrographs of the eroded surfaces of sample CA1005 after erosion using (a)-(c) garnet and (e) and (f) SiC erodent particles at 30° angle of impingement. (d) EDX spectrum of deformed and melted materials shown in (b). Note: (a) and (e) are low magnification images of the eroded surfaces. (b) is a higher magnification image of the plastically deformed areas shown in (a). (c) and (f) are higher magnification images of damaged surfaces inside the pits shown in (a) and (e), respectively.

Fig. 5.12(a) shows that the damaged surface due to erosion by garnet erodent was relatively smooth and contained a few isolated pits. These pits were generally 15-30 μm in size, which is much bigger than the sintering pores, typically several microns or less, in this material. Higher magnification SEM view of the plastically deformed regions, shown in Fig. 5.12(b), revealed that fine debris, deformed materials and locally melted materials were present. Energy dispersive X-ray (EDX) analysis of

these deformed and melted materials showed a high level of Fe (Fig. 5.12(d)), indicating that they derived or partially derived from the garnet erodent which contained 30 wt% of FeO. A higher magnification picture of the damaged surface inside the pits, presented in Fig. 5.12(c), revealed clear grain facets, indicating that grain ejection is the main material removal mechanism. On the other hand, the damaged surface due to erosion by SiC erodent, shown in Fig. 12(e), appeared to be much rougher than that eroded by garnet particles due to large-scale fracture of the surface material. A higher magnification view of the eroded area, illustrated in Fig. 12(f), showed that the damage features included grain facets, plastically deformed materials and small-scale chipping, with grain ejection apparently the main material removal mechanism.

5.4.3 Effect of ceramic microstructure

SEM examination of eroded areas of various α-sialon compositions as well as their devitrified counterparts provides some insights to identify the influence of intergranular glass on the erosion behaviour of these materials. Fig. 5.13(a) shows a general view of the eroded surface of as-sintered sample CA2613, while Fig. 5.13(b) shows the centre-right region outlined by the frame in Fig. 5.13(a) at a higher magnification. Similarly, Fig. 5.13(c) presents a general view of the eroded surface of the heat-treated sample CA2613 and Fig. 5.13(d) is a higher magnification micrograph of the centre-left region outlined in Fig. 5.13(c).

It can be seen that the morphology of the eroded surface was quite different for the as-sintered and heat-treated samples. For as-sintered material CA2613 (Fig. 5.13(a)), the damaged surface appeared to be relatively smooth and contained some small-scale facetted regions. The higher magnification micrograph (Fig. 5.13(b)) revealed that the damage features for the as-sintered sample were mainly transgranular fracture and smearing of the deformed materials coupled with limited intergranular fracture. Transgranular fracture was even observed in the elongated grains which were oriented virtually parallel to the target surface, as indicated by arrows in Fig. 5.13(b), suggesting that the intergranular calcium oxynitride glass provided strong bonding between the grains. Further, in many cases, the skeletons of the underlying grains were observed in the plastically deformed regions, indicating the preferential

removal of the softer glassy phase. In contrast, for the post-sintering heat-treated material CA2613 (Fig. 5.13(c)), the erosion damage was clearly more severe. Higher magnification SEM examination (Fig. 5.13(d)) showed that erosion damage involved predominantly transgranular and intergranular fractures with very limited plastic deformation. Intergranular fracture, evidenced as grain pull-outs, is caused by substantial grain boundary microcracking and was often observed for equiaxed grains as well as some elongated grains that were oriented parallel to the surface.
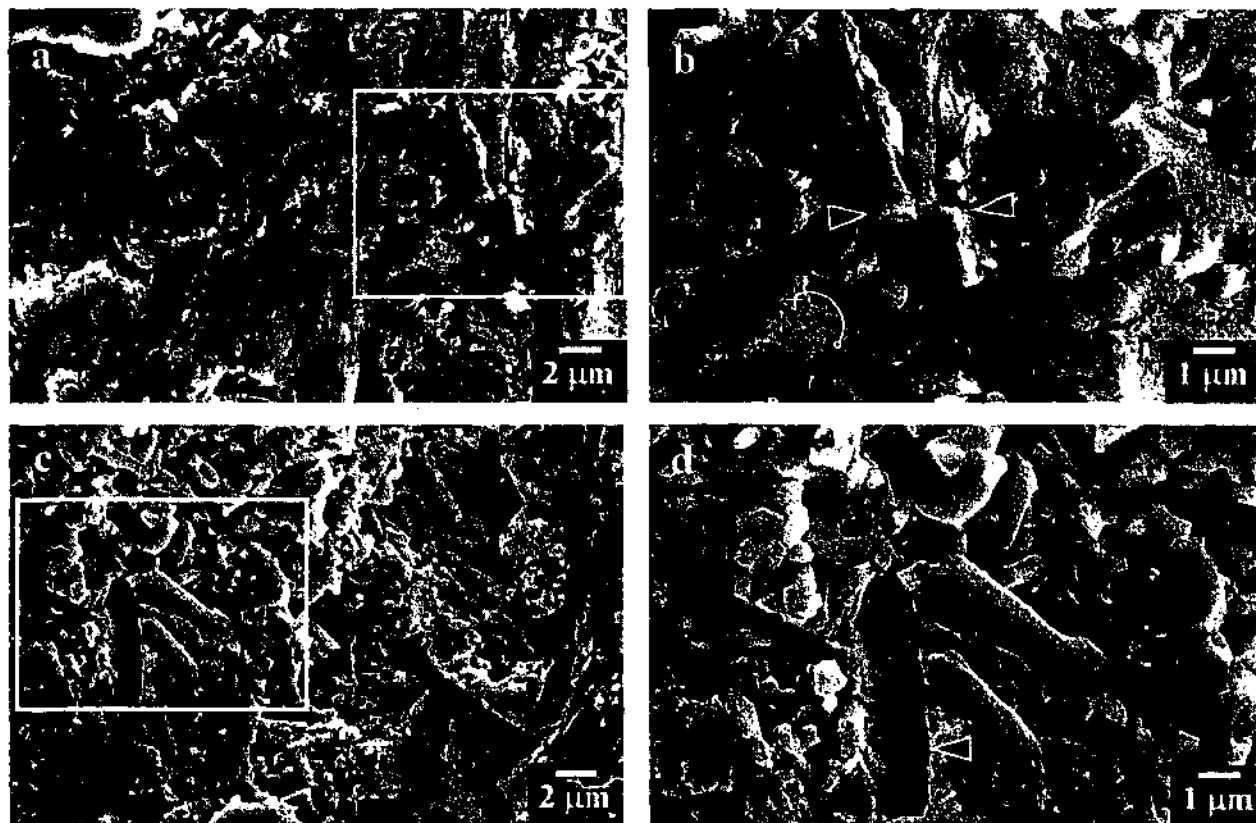
Fig. 5.13. SEM micrographs of steady state erosion surfaces of material CA2613 after erosion using SiC particles at 90° impact: (a) and (b) as-sintered sample; (c) and (d) heat-treated sample. Note: arrows in (b) and (d) indicate the transgranular fracture and dislodgment, respectively, of the elongated grains which are oriented virtually parallel to the eroding surface.

When as-sintered material CA3618 was exposed to SiC erosion at normal impact, as shown in Fig. 5.14(a), the damage patterns were again dominated by transgranular fracture and plastically deformed regions. On the other hand, when the heat-treated CA3618 sample was eroded by SiC particles, as shown in Fig. 5.14(b), profuse grain boundary microcracking occurred. The higher magnification SEM examination (Fig.

5.14(c)) showed that the main material removal mechanisms were transgranular fracture and grain dislodgment.
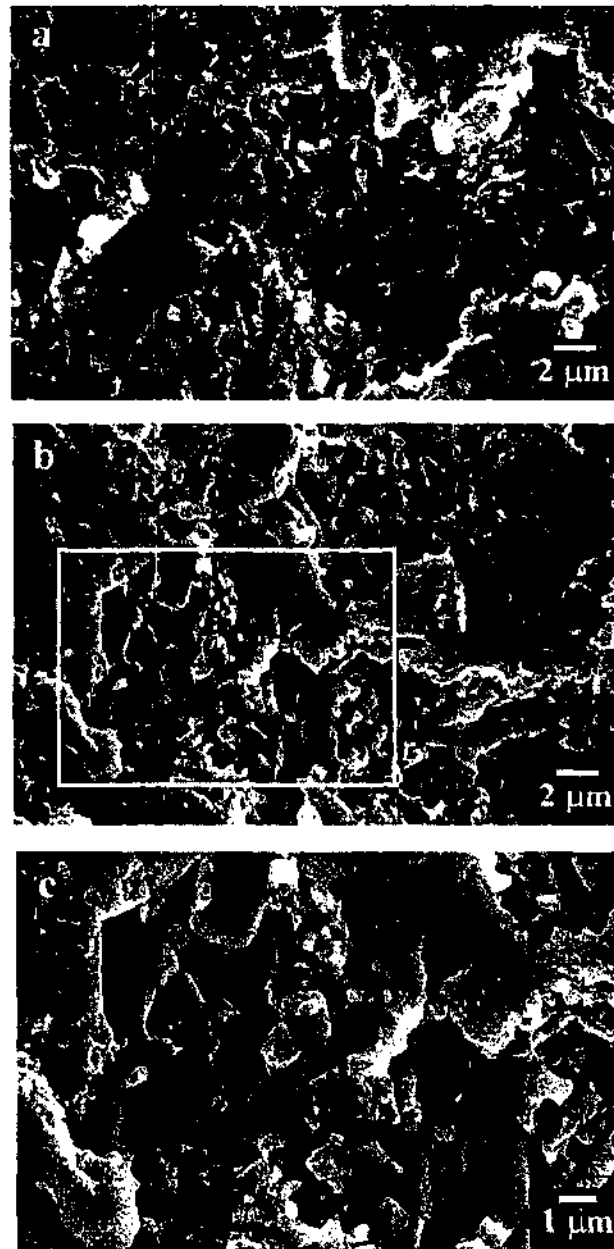
Fig. 5.14. SEM micrographs of steady state erosion surfaces of material CA3618 after erosion using SiC at 90° impact: (a) as-sintered sample; (b) and (c) heat-treated sample.

The eroded surfaces of material CA1005, both as-sintered and heat-treated, are presented in Fig. 5.15(a) and (b), respectively. As can be seen, in both cases, the damage features were governed by grain ejection and plastically deformed materials coupled with small-scale chipping. This is, however, quite different from the damage features observed in as-sintered materials CA2613 and CA3618 where transgranular fracture was the dominant material removal mechanism.
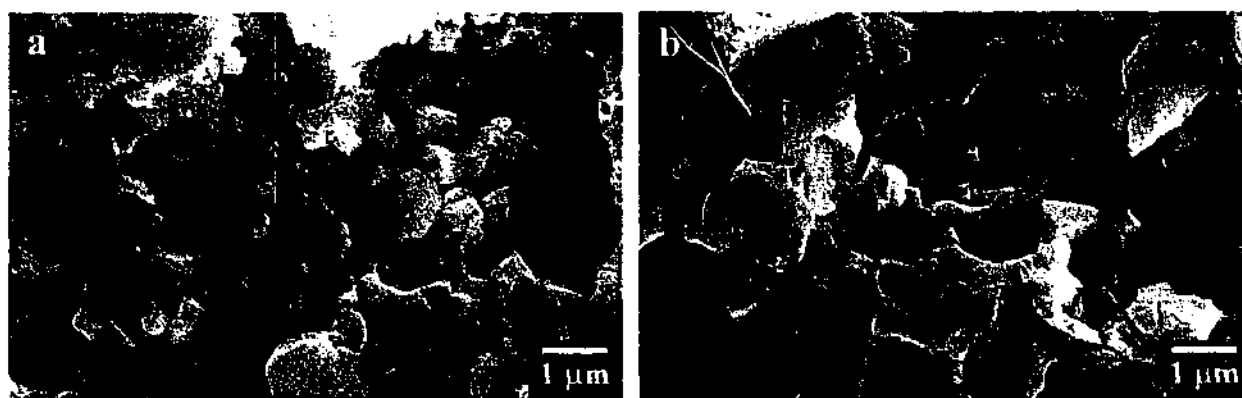
Fig. 5.15. SEM micrographs of steady state erosion surfaces of sample CA1005 after erosion with SiC at normal impact: (a) as-sintered sample and (b) heat-treated sample.

The damaged surfaces of samples CA1005F and CA1005C generated by erosion using SiC erodent at normal impact are presented in Figs. 5.16(a) and (b), respectively. The damage patterns were found to be similar to those observed in as-sintered and heat-treated composition CA1005 samples consisting of grain ejection and plastically deformed materials, indicating that the dominant mechanism of material removal in these materials involved intergranular microfracture leading to dislodgment of individual grains.
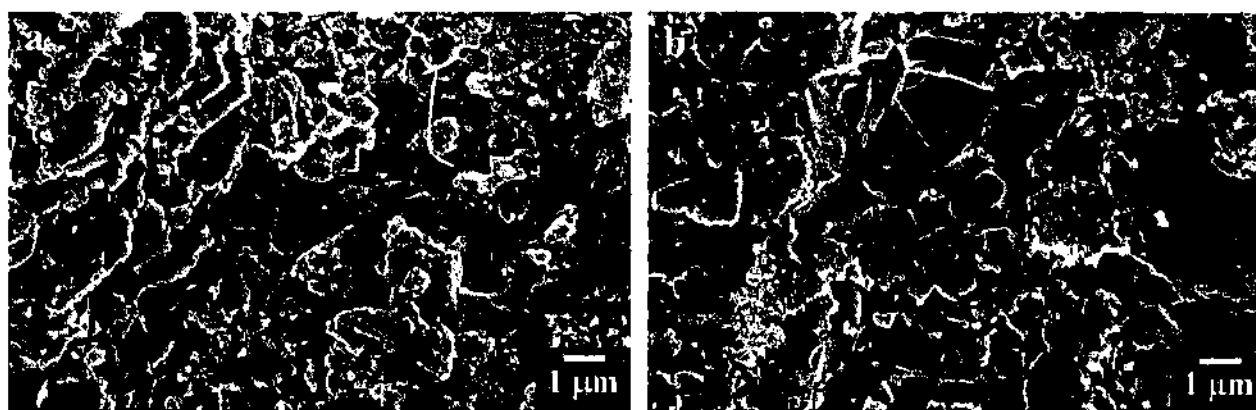
Fig. 5.16. SEM micrographs of steady state erosion surfaces of samples (a) CA1005F and (b) CA1005C after erosion with SiC at normal impact.

The micrographs in Fig. 5.17 show the types of damage produced by erosion using SiC erodent at normal impact in samples CA2613F and CA2613C. Figs. 5.17(a) and (b) depict the general view of eroded surfaces of samples CA2613F and CA2613C,

while Figs. 5.17(c) and (d) are the higher magnification views of regions containing facetted grain morphology.
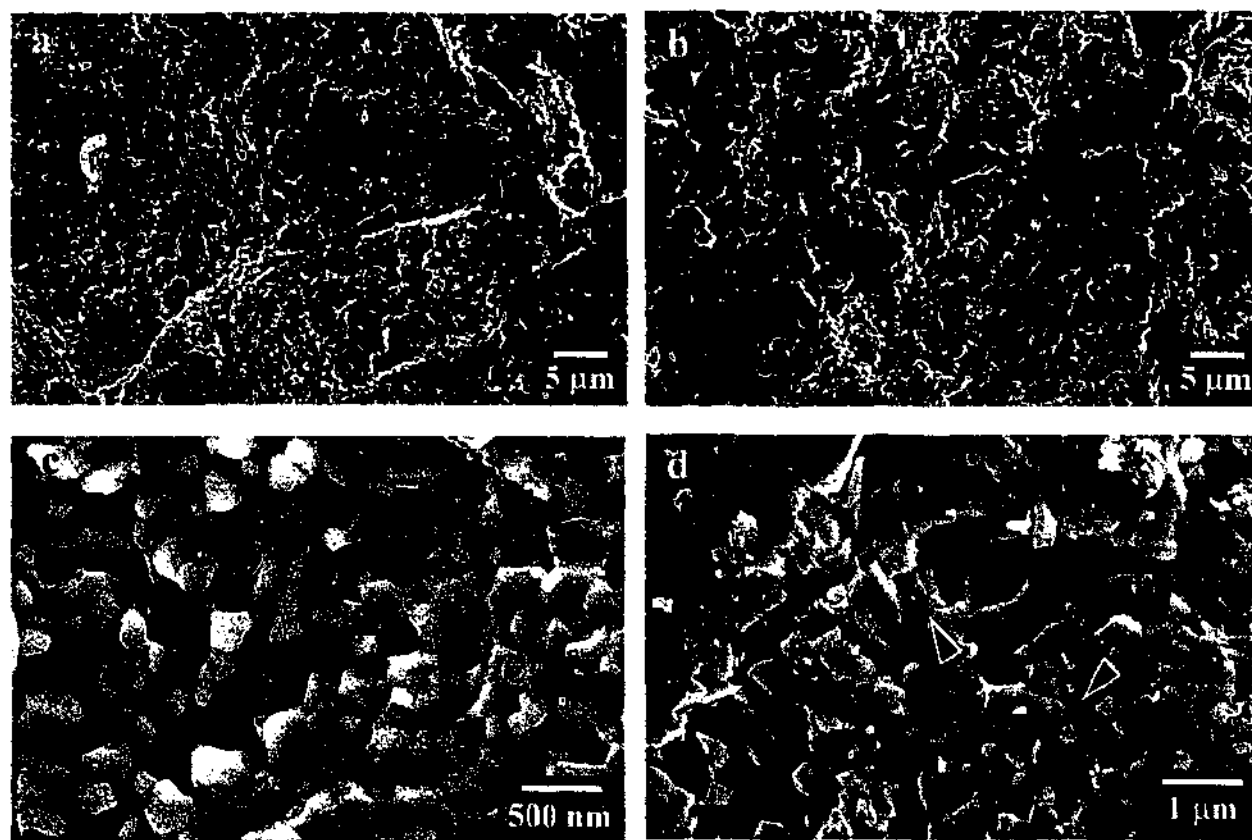
Fig. 5.17. Surface morphology of samples (a) and (c) CA2613F and (b) and (d) CA2613C following erosion using SiC particles at 90° impact angle. Note: (a) and (b) are low magnification general microstructures of the eroded surfaces, while (c) and (d) are the higher magnification images of regions with grainy morphology.

It can be seen that the damaged surface of sample CA2613F appeared to be very rough with a distinct grainy nature and contained large deep craters, suggesting that the process of material removal involved the formation and propagation of large cracks originating from the deep subsurface (Fig. 5.17(a)). High-resolution SEM examination revealed that the propagation of these macroscopic cracks in sample CA2613F was predominantly intergranular in nature (Fig. 5.17(c)). In contrast, the eroded surface of sample CA2613C seemed to be relative flat, containing mainly plastically smeared materials with some small-scale grainy regions (Fig. 5.17(b)). High-resolution SEM observation revealed that the process of material removal in sample CA2613C involved the propagation and intersection of microcracks of grain-facet dimensions, marked by solid arrows in Fig. 5.17(d), in the fashion of both transgranular and intergranular fractures.

The micrographs in Fig. 5.18 show the types of damage produced by erosion using SiC erodent at 30° impact in samples CA2613F and CA2613C. In both cases, damage features consisted mainly of plastically deformed materials originating from the cutting and ploughing actions of the hard, sharp SiC particles. Isolated brittle-fracture regions, characterized by facetted grainy morphology, were also observed. Again, these brittle-fracture regions in material CA2613F were larger and deeper in size compared to those observed in material CA2613C, suggesting material CA2613F experienced a greater rate of material removal in comparison to material CA2613C.
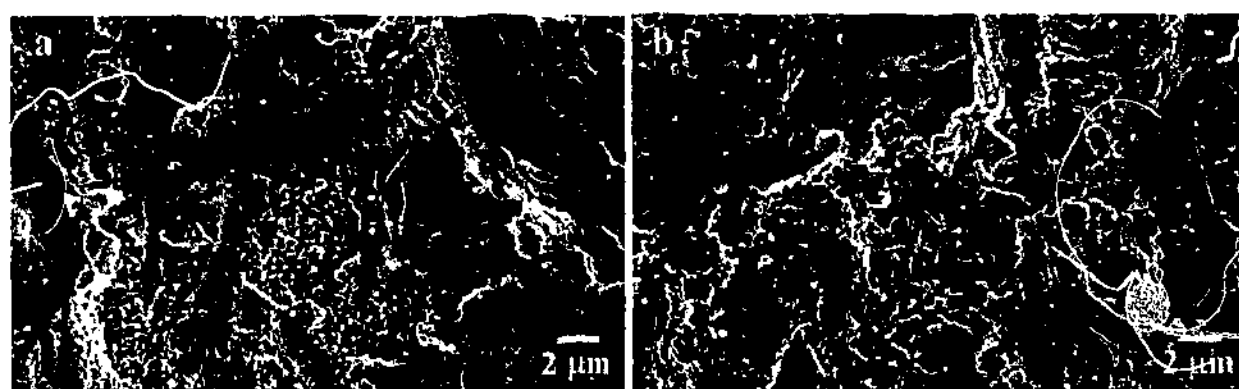
Fig. 5.18. Surface morphology of samples (a) CA2613F and (b) CA2613C following erosion using SiC particles at 30° impact angle.

5.5 Erosion Mechanisms

5.5.1 Initial damage

When hard, angular particles impinge on a ceramic surface at normal incidence, they penetrate into the target surface and produce severely plastically deformed zones (Fig. 5.8). The resulting damage patterns show some degree of similarity to those produced by a sharp indenter such as a Vickers diamond pyramid indenter. Accordingly, a quasi-static indentation theory has been developed to model the erosion event (Wiederhorn and Lawn 1979). Such an attempt appears to be appropriate since although impact speeds of some tens of meters per second do not seem quasi-static, they are still much smaller than the velocity of elastic and plastic deformation in brittle materials (Slikkerveer et al. 1998).

In Vickers indentation on strong ceramics such as Si_3N_4 and sialons, the sharp indenter penetrates into the solid and results in material deformed plastically in an outward mode, su_ _esting that the original stress field fades rapidly with the distance away from the surface (Rowcliffe 1992). When the peak load is sufficiently high, a sharp indenter can induce both plastic flow and elastic damage in the form of a variety of well-defined cracks such as radial and lateral cracks (Lawn 1993).

The single impact damage observed in the present study in Figs. 5.8(a) and (b) is characterized by a zone of intense plastic deformation surrounded by microcracks extending into the material and on the surface, with associated small-scale lateral cracking. The absence of well-developed lateral cracks may be explained in terms of the relatively low stress level induced by the single particle impact under the current conditions.

An estimation of the average load for individual erodent particles during erosion can be obtained using the concept of the quasi-static indentation model. Following the analysis by Ritter et al. (1991), the relationship between the impinging particle kinetic energy (U_k) and equivalent indentation load, P, can be expressed as

$$P = \alpha \, \xi \, H^{1/3} \, U_k^{2/3} \tag{5.1}$$

where α is a constant related to the fraction of energy transferred to the target material, ξ is an indenter constant equal to 4.8 for the Vickers geometry, and H is the hardness of the target material.

The geometric irregularity of the impacting particle can cause it to hit on an edge or face rather than a sharp point. This would result in less energy being transferred to the target surface and also change the indenter constant ξ. Take the most extreme case for an example, i.e. assume 100% of the impinging particle energy is transferred to the target and the particle-target conta t made on the sharp point of the particle. This results in an estimated maximum load ranging between 8-10 N being exerted by individual particles on the sialon materials. The minimum threshold load, P^*, for lateral crack initiation can be calculated using indentation fracture mechanics (Evans et al. 1980)

$$P^* = \zeta \, (K_c^4 / H^3) \, f(E/H) \tag{5.2}$$

where H, K_c and E are the hardness, fracture toughness and elastic modulus of the material, respectively. ζ is the dimensionless constant, depending upon the type of crack, and $\zeta f(E/H) \approx 2 \times 10^5$ (Evans et al. 1980).

By using the measured hardness an' fracture toughness values of Ca α-sialon materials (Table 4.5), eq. 5.2 predicts that the minimum load required for initiation of a lateral crack in these materials varies $\sqsubset_{\omega}$. 10-30 N. Therefore the load on individual particles under the present erosion conditions is in the same order to that required for lateral crack initiation. Hence, only small-scale lateral cracking is expected.

Indeed, in a previous study (Gulden 1981b) of single-impact damage on HP-ed and PLS-ed Si_3N_4 materials using 300 μm SiC grits at a much higher velocity, 176 m/s, and thus a much higher load, it was seen that in all cases, well-developed radial and lateral cracks were produced.

Erosive wear is a cumulative process. Once steady state erosion is reached, the target surface is covered by a layer of severely damaged material. This damaged layer contains a high density of cracks and exhibits much poorer mechanical properties than the undamaged bulk material. Hence the subsequent impacts may generate more severe damage involving lateral cracking and large-scale chipping. This must be borne in mind when using the single impact event to evaluate the erosion mechanism.

5.5.2 Transient erosion regime

At low erodent dosage, during the initial stages of the erosion test, the rate of material removal from the surface of the target was not linear with erodent dose. Typical plots of cumulative volume loss as a function of the mass of impacting particles, Figs. 5.1 and 5.2, displayed an initial transient of increasing slope followed by linear steady state behaviour. The duration of the transient, also known as the incubation period, appeared to increase as the angle of impact decreased. Furthermore, erosion using softer garnet particles also yielded a longer incubation period than that by hard SiC grits.

The earliest report on transients of the kind shown in Figs. 5.1 and 5.2, for erosion of ceramic materials appeared in 1980 (Routbort et al. 1980b). However, despite the large volume of literature concerning the erosion behaviour of ceramic materials during the past twenty years, little experimental or theoretical work on this topic exists (Routbort 1996). Based on the erosion mechanism proposed above, a better understanding of the transient effect on erosion of ceramic materials can be obtained.

When si⋅' ⋅n ceramics are exposed to erosive wear by SiC particles at normal incidence, the erodent particles cut into the target surface and leave a zone of irreversible deformation surrounded by microcracks. Repeated impacts are therefore necessary to accumulate the requisite levels of stress in order to extent the cracks to form a crack network. Up to this stage, the material loss from the target surface is mainly via small-scale chipping. The subsequent impacts can, however, result in relatively severe wear, particularly when the cracks propagate back to the free surface. A damage-free surface will thus experience a delay period before wear starts, after which a steady state erosion rate should become established, proportional to the rate of propagation and linking of microcracks in the material (Davidge and Riley 1995). The duration of such a delay is therefore largely dependent on the residual stress level induced from the impact of abrasive particles.

The longer incubation period observed in oblique impacts compared to normal impacts, as shown in Fig. 5.1, can be rationalized in terms of the erosion efficiency. In the case of high angle impact, the kinetic energy of an impinging particle is mainly dissipated in the penetration of the particle into the target. As a result, a relatively deep plastic zone would be generated which could produce a comparatively high residual stress level leading to high crack driving forces. On the other hand, in the case of shallow angle impact, the kinetic energy of the impinging particle contributes mainly to the ploughing mechanism and very little to normal repeated impact. This would simply result in a low penetration of the impinging particle on the target surface and consequently low crack driving forces. Therefore, more impacts would be required to additively produce a residual crack driving force which is equivalent to that produced by normal impacts. This would lead to a lower efficiency of erosion and an extended incubation period in oblique impacts compared to normal impacts.

The longer incubation period observed in erosion by garnet particles compared to that by SiC grits, as shown in Figs. 5.1 and 5.2, can also be rationalized in terms of the erosion efficiency. Compared to SiC grits, garnet particles are much softer and contain approximately 80 wt% of relatively soft phases including SiO_2, FeO, MgO, Fe_2O_3, etc (Table 3.3). When the soft garnet particles impact on the harder ceramic surface, they undergo severe plastic deformation that effectively diminishes the load transfer characteristics and thus reduces the penetration depth of the impacting particle into the target. The small penetration depth produces a small stress field associated with a low driving force for crack extension. As a result, erosion by garnet erodent is less efficient, in accordance with the much longer incubation period observed in erosion using garnet erodent compared to that using SiC grits.

5.5.3 Steady state erosion

In spite of the wealth of literature in the field of erosive wear of ceramic materials (Ritter 1992; Routbort and Scattergood 1992; Finnie 1995), the detailed mechanisms of material removal in erosion of sialon ceramics have been only cursorily explored (Park et al. 1997). Yet good understanding of mechanisms is an essential prerequisite to the development of optimum wear characteristics, especially for complex processes such as erosive wear. The intent of this section is to examine possible mechanisms of material removal in steady state erosion of sialon ceramics.

Investigation of the dependence of erosion behaviour on impact angles is probably the most sensitive way to study the material removal mechanism. SEM micrographs of the eroded surfaces of sialon ceramics, shown in Fig. 5.10, indicated that although the predominant mechanism of material removal, for both 30° and 90° impacts, involved brittle fracture with limited plastic deformation, clear evidence of the effect of impact angle on the mechanism and rate of material removal was also seen. For instance, the high angle impact produced a more severely damaged surface, evidenced by an increased area fraction of zones with facetted morphology and a higher material removal rate, while the low angle impact generated a relatively smooth surface with an increased area fraction of plastically deformed regions and a higher incidence of ploughing trajectories lying along the particle colliding direction.

The facetted morphology is a result of the indentation-induced fracture due to the repeated impact of the erodent particles on the sample surface, while the plastic deformation is caused by the repeated sliding and impact of the particles on the target surface (Lathabai and Pender 1995). The above combined damage features observed in erosion of Ca α-sialon ceramics suggest that impact stresses are accommodated by both plastic deformation and brittle fracture.

In order to identify more clearly the dominance of one or other set of mechanisms controlling the wear mode and rate, it is helpful to examine the erosive wear process at opposite extremes: the shallow angle impingement and the normal impact.

When hard, angular particles impinge on the ceramic surface at a very small angle, θ, the kinetic energy of the eroding particles contributes mainly to ploughing (horizontal component of the energy, proportional to $\cos^2\theta$) and very little to normal repeated impact (normal component proportional to $\sin^2\theta$). This process is therefore very similar to the scratching test on a ceramic surface using a sharp indenter under an ultra low load.

In a typical scratching test, two major processes take place. The first process involves the formation of grooves in which material is deformed to the sides of the grooves. This plastic cutting process for groove formation may result in direct material removal, and the rate of material removal is determined by the plastic penetration and should thus be related to the material hardness (Evans and Marshall 1980). The second process involves the formation of microcracks in the vicinity of the groove. The propagating and intersecting of these microcracks can result in material removal from the surface in the form of wear debris and microchips via microfracture. It is this microfracture process which dominates the material removal process in sliding wear of ceramic materials (Mukhopadhyay and Mai 1993 and 1997). It is, however, important to note that there also exists a critical load for the onset of microcracking during scratching. This is because only when this critical load is reached, the quasi-static tensile stress developed behind the moving particle and the shear stress beneath the sliding particle become sufficient to cause cracks to initiate and propagate from the plastic zone surrounding the groove (Moore 1980; Xu et al. 1995).

In view of the above discussion, it is a natural step to assume that at very low impact angles, the abrasive particles are virtually sliding on the target surface with ultra low external load, suggesting that material is mainly removed by a plastic cutting process. Ceramics have high hardness, and thus they are not easily plastically deformed. Hence the material removal rate caused by erosion at shallow impact angles is low.

When abrasive particles attack the ceramic surface at a high angle of impingement, a vast majority of the kinetic energy of the eroding particles is devoted to initiate and propagate microcracks in the target material. Erosive wear is a dynamic process and the subsequent impacts could land on the vicinity of the existing damaged zones to produce a new plastic zone with associated microcracks. Cumulative stresses induced by the repeated impacts then force these microcracks to propagate and intersect each other to form crack networks. Ceramics generally have low resistance to crack propagation, and the rapid interactions between microcracks along with the intersection of these cracks with the free surface can result in high volumes of material removal via chipping and/or grain dislodgment processes during multiple impacts. Hence the wear rate caused by erosion at high impact angles is high.

It is important to note that the process of propagation and linking of microcracks involved in erosion of ceramic materials is cumulative in nature and advances in a microscopic scale. Therefore the crack propagation paths are less predictable compared to those resulting from the quasi-static indentation using sharp diamond indenters. Consequently, the fractured surfaces produced by the impact of abrasive particles do not always display characteristic features such as saucer-shaped lateral cracks. It is also worthwhile to note that the cumulative process of crack propagation and intersection alternatively provides time for surface materials to be crushed and smeared by the repeated impact of abrasive particles, resulting in flakes of plastically smeared material with isolated plough marks on the surface. Further impacts result in material removal by spalling of the smeared flakes, leaving a surface with exposed grain facets.

A comparison of the morphological features in eroded surfaces of sample CA1005 (Figs. 5.10(a-b)) and samples CA2613 and CA3618 (Fig. 5.10(c-f)) revealed some

distinctive differences. The eroded surfaces of samples CA2613 and CA3618 were considerably smoother and contained more plastically deformed or smeared regions than those of sample CA1005 after erosion at 30° and 90° incidence angles. Higher magnification SEM micrographs of the centre of the erosion craters after erosion at normal impact showed that the dominant material removal mechanism for samples CA2613 and CA3618 was transgranular fracture (Figs. 5.13(a) and 5.14(a)), while for sample CA1005 it was intergranular fracture (Fig. 5.15(a)).

The major difference between samples CA2613 and CA3618 and sample CA1005 was their microstructure. As mentioned in section 4.4.1, samples CA2613 and CA3618 consisted mainly of randomly oriented elongated α-sialon grains and large AlN-polytypoid laths, while sample CA1005 contained almost equiaxed α-sialon grains coupled with a small amount of intergranular glass. Upon impact, interlocking of the elongated grains and large laths in samples CA2613 and CA3618 effectively hindered the dislodgment of the grains. Thus, more energy was required to remove the interlocked elongated grains from the target surface than to dislodge equiaxed grains. In addition, although in general the grain boundaries are weaker in comparison to the grains, the cracks may propagate either along grain boundaries or as intracrystalline cleavage through grains, largely depending upon the morphology and size of the grains and the chemistry of the intergranular phases. Therefore microstructure has a controlling influence on the fracture mode and thus the erosion behaviour of the ceramic materials. The effects of a number of microstructural parameters on the mechanism of material removal will be further discussed in section 5.7.

Finally, the above analysis clearly demonstrates that in erosion of Si_3N_4-based ceramics using hard, sharp particles such as SiC, the mechanism of material removal could change depending on the erosion efficiency. The erosion efficiency is governed by a number of factors including the angle of impact, the particle type, size and velocity. A large particle with high velocity impacting at a high angle is likely to penetrate deeply into the target and to produce lateral cracks. Hence material can be removed by *each* impact. However, at low impact velocities, the erodent particle is only capable of producing a zone of irreversible deformation surrounded by

microcracks with the absence of "classical" lateral cracking, suggesting that many *more* impacts are required to accumulate the damage before material eventually becomes detached.

5.6 Effect of Erodent Properties

The role of erodent properties in determining the erosion behaviour of brittle materials has been studied by numerous investigators (Srinivasan and Scattergood 1988a; Shipway and Hutchings 1991; Murugesh and Scattergood 1991; Routbort and Scattergood 1992; Shipway and Hutchings 1996). It appears that various properties of the erodent particles, such as size, shape, hardness, toughness etc, can all affect, although probably to different degrees, the erosion efficiency and thus the material removal mechanism and rate.

Impact damage models for erosion, such as those of Evans et al. (1978) and Wiederhorn and Lawn (1979) take account of several me. nical and physical properties of the target and erodent particles, respectively (eq. 2.5), but mechanical properties, such as hardness and fracture toughness, of the erodent particles are not considered. This is because the implicit assumption in these models is that the erodent particles are infinitely hard and strong and suffer negligible deformation (Srinivasan and Scattergood 1988a). However, the most commonly encountered abrasive particles in practical situations are silica-based minerals, exhibiting a hardness value ranging between 8-12 GPa (Shipway and Hutchings 1991). This value is much lower than the hardness of the ideally strong diamond indenter and the rigid SiC particles (30-35 GPa). Therefore, investigation of the role of the mechanical properties of erodent particles on erosion of ceramic materials has significant practical importance.

In the current research, garnet particles (hardness, 13.8 GPa) and SiC grits (hardness, 30.4 GPa) with similar shape and size distribution were selected as the erodent materials. The erosion tests were carried out on the three PLS-ed sialon ceramics under similar experimental conditions including the angle of impact, the velocity and flux of the particle stream. This set of experiments enables the evaluation of the

134

effect of the mechanical and chemical properties of the particles on the erosion behaviour of ceramic materials.

As noted in section 5.3.1, two significant effects of erodent properties on erosion rate of sialon ceramics are apparent: (1) SiC erodent resulted in a significantly higher material removal rate than garnet particle in all sialon materials; and (2) the ratio of erosion rates, as determined by the $\Delta E_{SiC}/\Delta E_{garnet}$ ratio in Table 5.2, is larger for low angles of impact and for material CA3618 in comparison to material CA1005. The difference in erosion rates between garnet and SiC erodents can be attributed to the variations in the properties of erodent materials.

SEM observations of steady state erosion surfaces of material CA1005 generated by garnet (Figs. 5.12(a-c)) and SiC (Figs. 5.12(d and e)) erodent particles revealed some distinctive differences. The damaged surface generated by the comparatively soft garnet erodent appeared to be relatively smooth and contained a few isolated pits. Between these pits, the target surface seemed to be covered by a layer of smeared material. Random EDX analysis of this smeared layer showed that it contained mainly deformed erodent and target materials as well as melted erodent material. In addition, the incidence of the melted erodent material was found to increase as the angle of impact decreased. The damaged surface generated by SiC erodent, however, exhibited indentation-induced fracture, associated with a much rougher morphology.

It is evident from these observations that when the softer garnet erodent particles impinge on the harder sialon target, they undergo severe deformation leading to particle fragmentation and crushing. In addition, the particles also undergo local melting, with the melted material being drawn into stringers in the direction of particle impact. The localized melting of garnet erodent has also been observed in a recent study of erosion of alumina ceramics using garnet particles (Zhang et al. 2000b) and was ascribed to a combined effect of the local adiabatic heating to high temperatures when particles with high kinetic energy impact the target and the relatively low melting point of the garnet particle (Table 3.3).

The fragmentation of the impinging particle can have two effects on the ability of the erodent to remove material from the target surface: (1) the fragmentation can lead to

the crushing and blunting of sharp particle tips, diminishing the load transfer characteristics and reducing the efficiency of crack generation (Murugesh and Scattergood 1991); and (2) the fragmentation can lead to a drop in the impulse delivered to the target surface due to the fact that the energy transferred to the fragments might be as much as 20-30% of the original kinetic energy of the particle (Anand and Conrad 1988), and thus lead to a reduction in the erosivity. Both effects suggest that severe deformation and consequently fragmentation of the erodent particles resulting from the use of *softer* erodent materials, such as garnet on sialon ceramics, reduce the efficiency of erosion. Therefore, the rate of material removal is much lower for erosion using garnet particles compared to erosion using SiC grits.

The difference in erosion rates resulting from SiC and garnet impacts, as described by the $\Delta E_{SiC}/\Delta E_{garnet}$ ratio in Table 5.2, becomes greater as the impingement angle becomes more oblique. This can be rationalized in terms of the effect of angle of impact on erosion mechanism. As suggested in section 5.5.2, at very low incidence angles, the kinetic energy of the impacting particles contributes mainly to ploughing and very little to normal repeated impact, suggesting that material is mainly removed by a plastic cutting process. Therefore, the use of the *softer* garnet particles to cut relatively *harder* sialon ceramics is much less effective than the case of *harder* SiC cutting relatively *softer* sialons. In addition, the frictional heat generated from the plough action associated with the low angle impacts promotes the melting of the garnet particles and thus further reduces the wear efficiency.

Another interesting feature about the present erosion data is that although the ranking of the erosion resistance of the target materials is essentially same for SiC and garnet erodents, the difference in erosion rates between materials CA1005 and CA3618 has increased by a factor of six when the erodent particles changed from SiC to garnet (Table 5.2). As already noted in section 5.5.2, the difference in the erosion rates of materials CA2613 and CA3618 and material CA1005 is mainly attributed to the different mechanisms of material removal which is a consequence of the different microstructures of the three materials. Upon erosion, the elongated grain morphology in materials CA2613 and CA3618 exhibits a greater resistance to crack extension, compared to equiaxed material CA1005, owing to a number of toughening mechanisms such as crack bridging and deflecting. Thus, more energy is required to

form a crack network in materials CA2613 and CA3618 than in material CA1005. Furthermore, the elongated grains and large laths result in an interlocking effect in samples CA2613 and CA3618 which effectively hinders the dislodgment of the grains. Although the interlocking effect may not be significant in erosion using SiC erodent where the hard SiC particles can effectively chip the surface material once the crack network is established, such an effect can be significant in erosion using softer garnet particles where material removal by the chipping process is suppressed.

The results from the current research clearly demonstrate that when laboratory testing methods are used for material selection, one has to be aware that any accelerated erosion test using erodent particles which are not representative of the proposed service environment may not give true information.

5.7 Effect of Ceramic Microstructure

As discussed in section 2.6, the two widely used erosion models, the dynamic (Evans et al. 1978) and the quasi-static (Wiederhorn and Lawn 1979) models, predicted that the erosion rate has a strong inverse dependence on the fracture toughness, but has a much weaker dependence on the hardness of the target material. The validity of these two models has been tested on a wide range of ceramic materials (Routbort et al. 1980a; Wiederhorn and Hockey 1983; Routbort and Scattergood 1992; Wada 1992). The results, however, vary from one system to another. For example, for erosion of alumina ceramics, it was well established that the erosion rate does not simply depend on the hardness and fracture toughness of the target materials. In fact, the microstructure of the target materials has been shown to have a controlling effect on the material removal mechanism (Heath et al. 1990; Lathabai 1995; Lathabai and Pender 1995; Zhang et al. 2000b). On the other hand, for erosion of sialon ceramics, the only two published systematic studies showed a qualitative agreement between the experimental results and the two theoretical models: the erosion rate decreases markedly with the increasing fracture toughness, but less sensitively with the increasing hardness (Wada 1992; Liu et al. 1998). However, such qualitative agreements are not supported by the results of the current research. While the most erosion resistant Ca α-sialon composition, CA2613, possesses moderat hardness and

toughness values, the other two compositions, having either higher hardness (CA1005) or higher toughness (CA3618) than CA2613, are less erosion resistant than sample CA2613. In addition, sample CA1005C exhibits higher hardness and toughness values compared to sample CA1005F (Table 4.5), yet its erosion resistance is poorer than that of sample CA1005F (Fig. 5.7). The discrepancies between the present experimental observations and the two theoretical models may be explained in terms of the microstructural characteristics of the target materials.

As noted earlier, the major microstructural parameters for ceramic materials are porosity, crystalline phases, grain size and morphology and the nature of the grain boundary phases. It is the primary interest of the present study to examine the effects of these microstructural parameters on the erosion behaviour of α-sialon ceramics.

5.7.1 Effect of grain boundary glassy material

The dominant material removal mechanism for the as-sintered CA2613 and CA3618 samples is transgranular fracture (Figs. 5.13(a) and 5.14(a)), but for CA1005 it is intergranular fracture (Fig. 5.15(a)). Samples CA2613 and CA3618 consist mainly of randomly oriented elongated α-sialon grains and large AlN-polytypoid laths, while sample CA1005 contains mostly equiaxed α-sialon grains. The elongated grain morphology can affect the erosion mechanism in two ways: (1) increase the resistance to crack propagation owing to toughening mechanisms such as crack deflecting and bridging; and (2) hinder the grain dislodgment mechanism due to the interlocking effect of the elongated grains. Both effects suggest that more energy is required to remove the interlocked elongated grains from the target surface than to dislodge equiaxed grains as in the case of material CA1005. As a result, samples CA2613 and CA3618 exhibit a better erosion resistance than sample CA1005.

The interlocking effect hypothesis is further supported by SEM observations of the eroded surfaces of the heat-treated materials CA2613 and CA3618. As shown in Figs. 5.13(d) and 5.14(c), despite the substantial intergranular cracking, transgranular fracture of the interlocked long α-sialon grains still remains as one of the dominant material removal mechanisms.

The difference in erosion rates between materials CA2613 and CA3618 can also be rationalized in terms of the microstructural variations in these materials. The major microstructural difference between the pair is that CA2613 possesses a fine elongated grain morphology with relatively less grain boundary glass and higher porosity while CA3618 exhibits a coarser and longer grain morphology coupled with a higher amount of grain boundary glass and an additional minor AlN' phase.

It is well known that porosity has a deleterious effect on erosion resistance because the pores, especially those at grain boundary triple junctions, can be regarded as a stress-concentrating flaw system (Miranda-Martinez et al. 1994) and consequently become preferred sites for microcrack initiation (Lawn 1993). Thus, from a porosity point of view, the more porous material CA2613 should have inferior erosion resistance than CA3618. However, experimental results showed a lower erosion rate for CA2613 compared to CA3618 (Fig. 5.5).

It is, therefore, thought that the excessive amount of intergranular glass in sample CA3618 is primarily responsible for its poorer erosion performance, as the glassy phase is expected to be much less resistant to erosion than the α-sialon grains. On the other hand, an optimum amount of grain boundary glass may improve the erosion resistance of these ceramics. Grain boundary glass fills the pores, facilitates the particle rearrangement during sintering and enhances bonding between grains and also has the potential to absorb or cushion the stress induced from solid particle impact via viscous flow.

The Ca oxynitride glass present in the Ca α-sialon ceramics has a relatively low T_g point (800-900°C) (Hampshire et al. 1985). Thus, the glass in the vicinity of the impact site could be softened due to local adiabatic heating caused by the impact of the fast-moving particles (Yust et al. 1978; Lawn et al. 1980; Zhang et al 2000b). In a previous study of erosion of these materials by garnet particles under similar conditions, it was observed that the local adiabatic heating effect resulted in the melting of the garnet erodent particles whose melting point is 1250°C (Zhang et al. 2001b). Moreover, if the grain boundary glass has strong bonding with the elongated ceramic grains, it would make intergranular fracture and grain ejection more difficult

upon erosion. This effect could be especially significant in α-sialon ceramics because in α-sialon, unlike in β-sialon and β-Si_3N_4, both grain boundary glass and α-sialon grains contain identical elements. Thus, the bonding between α-sialon grains and the glassy matrix could be strong. The contribution of intergranular phases to the erosion process can be further illustrated by comparing the α-sialon samples before and after post-sintering heat treatment.

The erosion test results showed that the as-sintered material CA2613 possessed significantly higher erosion resistance than its heat-treated counterpart (Fig. 5.5). As discussed in section 4.9, the post-sintering heat treatment can have two effects on α-sialon materials: (1) the partial crystallization of the excess glass located at three-grain edges (Hoffmann 1994b), which can result in up to 10% volume reduction in the Ca α-sialon system (Malecki et al. 1997) and thus produce a radial tensile stress in the triple junctions at the interface between the α-sialon grains and the gehlenite phase (Hoffmann 1994b); and (2) the creation of thermal stresses at the three-grain edges due to thermal expansion mismatch between the α-sialon grains and devitrified phases. This thermal stress is also a tensile stress owing to the higher thermal expansion coefficient of gehlenite compared to α-sialons (Hampshire et al. 1994).

The volume reduction and the creation of thermal stresses can generate microcracks or even pores at the grain boundary triple junctions and consequently weaken the bonding strength between the α-sialon grains and the gehlenite phase. The weakened grain boundary triple junctions can be regarded as preferred sites for microcrack initiation upon erosion and thus degrade the erosion resistance of the α-sialon ceramics. Indeed, SEM observations of the eroded surfaces revealed a more distinctive grainy nature in heat-treated samples CA2613 and CA3618, as shown in Figs. 5.13(d) and 5.14(c) respectively, compared to their as-sintered counterparts. This is because, upon erosion, the weakened bonding strength between the α-sialon grains and the intergranular gehlenite phase in the heat-treated samples can result in the dislodgment of gehlenite phase from the grain boundary triple junctions and thus leave a facetted morphology of interlocked elongated grains.

In addition, the partial crystallization of the intergranular glass results in significant reduction in the amount of grain boundary glass in the α-sialon ceramics, which in turn degrades the erosion resistance of these materials owing to the reduction in the ability of grain boundary to viscoplastically absorb or cushion the impact stress (Stough et al. 1994). This scenario is supported by the SEM study on the eroded surfaces of material CA2613. As shown in Fig. 5.13(b), the material removal mechanism for the as-sintered sample is predominantly transgranular fracture, indicating strong bonding between the grains. In contrast, the eroded surface of heat-treated sample CA2613 (Fig. 5.13(d)) revealed substantial grain boundary microcracking and grain dislodgment.

Comments may be made on the erosion behaviour of material CA1005. It has been shown that the dominant material removal mechanism, for both as-sintered and heat-treated samples, was grain ejection coupled with small-scale chipping. This is because material CA1005 contains approximately equiaxed grains and a very small amount of intergranular glass, which is mainly responsible for a relatively large number of pores in the sample. The linkage of the preexisting flaws and the substantial grain boundary microcracks (see Fig. 5.15(a)) induced from the severe impact result in the ejection of the equiaxed grains. Thus, material CA1005 has the highest erosion rate of the three compositions. Furthermore, small-scale chipping is evidence of the severity of the damage produced by SiC erosion owing to its extremely high hardness. Finally, heat treatment has further weakened the intergranular bonding strength of the material, resulting in poor performance in the erosion tests (Fig. 5.5).

5.7.2 Effect of grain size

Erosion tests showed that sample CA1005C exhibited a higher material removal rate than sample CA1005F at both 30° and 90° impacts (Fig. 5.7). However, SEM examination of surfaces of the two samples generated by erosion using SiC erodent at 90° incidence revealed that the dominant mechanism of material removal, in both cases, was grain ejection caused by grain boundary microcracking (Fig. 5.16).

Samples CA1005F and CA1005C were fabricated from the same batch and were both PLS-ed first and then HP-ed at the high temperatures, except that the dwell time of the PLS stage was much longer for CA1005C (8 h) than CA1005F (3 h) (Table 4.1). Therefore the microstructural features of the two samples were similar: both contained mainly equiaxed α-sialon grains coupled with a very low amount of intergranular glass, except that the grains were coarser in sample CA1005C compared to CA1005F (Fig. 4.6).

The low content of the intergranular glassy phase or the liquid phase when it is above the eutectic temperature could hinder the densification process of these materials during sintering. As a result, samples CA1005F and CA1005C possessed higher porosity, by approximately a factor of 3, than sample CA2613C which was also two-stage sintered under the similar conditions but from a composition containing a considerably higher amount of intergranular glass. The high porosity can result in a weakened bonding between grains in materials CA1005F and CA1005C.

In addition, as discussed in section 5.7.1, the pores, especially sintering pores at grain boundary triple points, are preferred sites for microcrack initiation. Therefore, upon impact, microcracks are readily initiated at the multi-grain junctions and consequently propagate along the two-grain boundaries and link up to from crack networks due to the weak grain boundaries and the equiaxed grain morphology of these materials. As a result, material is removed from the target surface via grain dislodgment. This scenario is in accordance with SEM observations of worn surfaces of materials CA1005F and CA1005C (Fig. 5.16).

As foreshadowed in section 5.7, theoretical treatments based on contact fracture mechanics (Evans et al. 1978; Wiederhorn and Lawn 1979) indicate that the associated erosion rates should be greatest for materials with the least toughness. The experimental erosion evidence shows that material CA1005C exhibits a higher erosion rate than material CA1005F (Fig. 5.7), suggesting that the erosion rate increases with the toughness, at least with the toughness determined using the traditional indentation technique (Table 4.5). The discrepancy between the theoretical predictions and the erosion results may be accounted for by the crack-size dependent toughness or T-curve behaviour which depends strongly on the microstructural

makeup of these materials. Although no T-curve measurements have been made on the present materials, the dominant role of microstructure in T-curve behaviour of ceramic materials is well established (Lawn 1993).

SEM observations of the polished and etched surfaces of materials CA1005 and CA1005F revealed an approximately equiaxed grain morphology (Fig. 4.6), while examinations of the eroded surfaces showed that material removal was primarily by grain ejection, suggesting that fracture took place mainly along the grain boundaries. It is generally accepted that ceramics with equiaxed grain morphology coupled with a weak grain boundary, such as alumina, exhibit rising crack resistance with crack extension as a result of grain-localized crack bridging (Chantikul et al. 1990; Lawn 1993).

The role of grain size in T-curve properties of alumina ceramics has been extensively investigated by Steinbrech et al. (1990), Chantikul et al. (1990) and Lawn (1993). It is seen that T-curves of alumina ceramics with different grain sizes cross each other with coarse-grained materials displaying lower crack-growth resistance in the short crack region but rising to higher large-crack toughness (Steinbrech et al. 1990; Chantikul et al. 1990; Lathabai and Pender 1995). The T-curve response of the two CA1005 materials are expected to follow the general trend where the finer grained material CA1005F exhibits a higher short-crack toughness while the coarser grained CA1005C possesses a better large-crack toughness.

In erosion of ceramic materials, although the size of the damage zone produced by an individual particle impact is related to the hardness of the material, the microcrack density associated with the impact zone is related to the toughness from the T-curve that is operative in the crack size scale of erosion impact events. SEM observations showed that the dominant material removal process in erosion of composition CA1005 involved grain dislodgment due to grain boundary microfracture with cracks in the order of several micrometers. Therefore, the higher toughness of material CA1005F over CA1005C in the T-curve region of greatest pertinence to erosion process, i.e. short-crack region, leads to a greater erosion resistance of material CA1005F compared to CA1005C.

5.7.3 Effect of grain morphology

Unfortunately, the above grain size-erosion rate scenario failed to predict the wear behaviour of ceramic materials with an elongated grain morphology where the interlocking effect of the elongated grains could change the fracture mode, upon particle impact, from intergranular to intracrystalline cleavage through grains. One extreme example is a comparison of the erosion behaviours of materials CA2613F and CA2613C using SiC erodent at 90° impact where erosion tests showed that sample CA2613F exhibited a much higher rate of material removal than sample CA2613C (Fig. 5.7).

The major differences in microstructural features between the two materials are that CA2613F consists of predominately fine α-sialon grains with relatively low aspect ratios (Fig. 4.7(a)) together with a small amount of unreacted AlN and a relatively high amount of intergranular glass (Table 4.4), while CA2613C contains mainly coarse elongated α-sialon grains (although the grains are ranged widely in sizes and aspect ratios) coupled with a small amount of AlN-polytypoid (Fig. 4.7(c)). These differences in microstructural features have reflected different mechanical properties of these materials. Material CA2613F possesses a relatively low hardness (owing to the higher amount of intergranular glass and a small amount of unreacted AlN) and toughness (due to the lack of toughening mechanism such as crack bridging and deflection) compared to material CA2613C (Table 4.5).

SEM observations of surfaces produced by SiC erosion at 90° impact revealed that the dominant mechanism of material removal in material CA2613F was macroscopic chipping that resulted from lateral cracks that were generated deep in the subsurface and propagated back to the surface (Fig. 5.17(a)). However, for material CA2613C, the primary material removal was by microfracture operating at the grain-facet scale leading to dislodgment of fine grains with low aspect ratios and coarse elongated grains orientated virtually parallel to the surface, as well as by transgranular chipping of large interlocking grains (Fig. 5.17(b) and (d)).

As discussed in section 5.7.1, the elongated grain morphology can have two beneficial effects on erosion resistance of ceramic materials: (1) it enhances crack

deflection and bridging by blocking the crack path, forcing it to detour; and (2) it hinders the grain dislodgment mechanism due to the interlocking effect, resulting in material removal via microfracture at the grain-facet scale (Fig. 5.17(d)). Both effects suggest that more energy is required to propagate and link up cracks between the neighborhood impact sites to form a crack network, as well as to remove the interlocked grains from the target surface. This also suggests that material CA2613C exhibits higher toughness than material CA2613F in the crack size scale associated with erosion impact events, resulting in a much lower erosion rate of CA2613C compared to CA2613F at normal impact.

On the other hand, hardness of the ceramic material can also influence the erosion resistance. In theory, hardness determines both the maximum load during impact and the depth of particle penetration into the target surface (Wiederhorn and Hockey 1983). In an expression for the maximum load upon solid particle erosion (eq. 5.1), hardness of the target material enters the equation with a positive exponent, 1/3. Hence, for a fixed impact energy the maximum impact load increases as the target hardness increases. The higher impact load may cause a greater amount of chipping leading to a higher rate of material removal. On the other hand, hardness also determines the penetration depth of particle into the target surface which in turn decides the depth of the formation of lateral cracks. Hence, the lower the hardness the deeper the particle penetration and consequently the higher the material removal rate. Therefore, there exists a two-fold effect of target hardness on the erosion rate in which the penetration term opposes the impact load term.

As a worst case, assuming that a surface is impacted with one or more sharp particles and the kinetic energy of an impinging particle is consumed entirely as work of penetration (Lawn 1993). The impact load can be calculated using eq. 5.1. Under the current condition, the estimated impact loads, according to eq. 5.1, are 8.8 and 9.2 N for materials CA2613F and CA2613C, respectively. Furthermore, according to indentation fracture mechanics, the contact area, A, is related to the indentation load, P, and the target hardness, H, as (Lawn 1993):

$$A = P/H \qquad\qquad (5.3)$$

For illustration, Vickers indentation was used to estimate the radius of the damage zone for materials CA2613F and CA2613C under the loads of 8.8 and 9.2 N, respectively. Using the relevant hardness values of 16 and 18.4 GPa (determined at a load of 9.8 N) for materials CA2613F and CA2613C, respectively, the indentation half diagonal value, a, of materials CA2613F and CA2613C was 16.6 and 15.8 μm, respectively. In addition, the indenter penetration depth, d, is related to its diagonal, a, by the expression:

$$d = k_0 \, a \tag{5.4}$$

where k_0 is a geometric constant of the indenter. The above calculation showed that upon impact, although the higher hardness could result in a higher impulsive load, the erodent particles still penetrated deeper in sample CA2613F in comparison to sample CA2613C under the current conditions.

The deeper penetration in material CA2613F induces a larger irreversible (plastic) deformation zone and thus results in higher residual stresses leading to higher crack driving forces. Prior to removal of the impinging particle, lateral cracks are initiated near the base of the deformation zone and consequently spread sideways (Lawn 1993). Although SEM examination revealed that crack propagation in material CA2613F was predominately intergranular in nature (Fig. 5.17(c)), the fine, slightly elongated grain morphology of this material offers limited scope for toughening mechanisms to dissipate the energy of the advancing crack tip. Therefore, cracks readily link up between the neighboring impact sites and eventually propagate back to the surface. Subsequent impacts result in macroscopic chipping. The above scenario is supported by experimental observations where large cracks which propagated in straight paths were observed on the worn surface of material CA2613F (Fig. 5.17(a)).

It is, therefore, thought that the elongated grain morphology combined with a relatively high hardness gave material CA2613C a better erosion resistance over material CA2613F.

Although material CA2613C still exhibited a better erosion resistance than material CA2613F under 30° impact, the difference in erosion rate between these materials was found to decrease substantially compared to that of the normal impact (Fig. 5.7).

One possible reason is that erosive wear is a dynamic process, which involves numerous experimental variables. Therefore it may not be a sensitive technique to reveal the small difference in erosion rate.

Another possible reason is that, as discussed earlier, in brittle ceramics lateral cracks from sharp contacts are the most potent agents of material removal in erosive wear and the scale of these crack systems is largely dependent on the kinetic energy of the impinging particle. As the impact angle decreases, the proportion of the kinetic energy devoted to the normal impact reduces dramatically. Consider the most extreme case as an example. When the impact angle approaches zero, there should be no difference in particle penetration between materials CA2613F and CA2613C. Therefore, the difference in erosion resistance between these two materials is expected to reduce as the impact angle decreases. This is in accordance with experimental observations where damaged surfaces of materials CA2613F and CA2613C generated by 30° SiC erosion contained mainly plastically deformed materials with limited grainy regions (Fig. 5.18).

5.8 Summary

It appears more convenient to specify the mechanical properties, such as fracture toughness and hardness, that determine the erosive wear behaviour of ceramic materials (Evans et al. 1978; Wiederhorn and Lawn 1979). The current research has shown, however, that the microstructure may have more significant influence on the mechanism and rate of material removal, although quantitative prediction of erosion rate using microstructural parameters may not be feasible. The following conclusions can be drawn from the results of this study:

• Ca α-sialon ceramics exhibit excellent erosion resistance when subjected to erosion using soft garnet particles, especially at low angles of impact.

• An optimum amount of intergranular glass may improve the erosion resistance of α-sialon ceramics due to its strong bonds with the α-sialon grains, while an

excess amount of grain boundary glass will result in poorer erosion performance owing to the lower erosion resistance of the glass phase compared to α-sialon.

- Post-sintering heat treatment increases the erosion rate of Ca α-sialon materials. Such differences can be attributed to (1) the weakening of the bond strength between the α-sialon grains and devitrified glass at the three-grain edges; (2) the creation of the intergranular stresses due to thermal expansion mismatch between the α-sialon grains and devitrified phases; and (3) the inability of devitrified glass to viscoplastically absorb or cushion the stresses during erosion.

- For material consisting of fine approximately equiaxed grains (CA1005), the dominant material removal mechanism is grain ejection, while for materials containing mostly elongated grains (CA2613 and CA3618), it is combined transgranular and intergranular fracture. This is because the interlocking effect of the elongated grains hinders the grain ejection mechanism.

- For material consisting of fine approximately equiaxed grains (CA1005), a microstructure with a finer grain size exhibits a better erosion resistance, while for materials containing elongated grains, a coarse elongated microstructure possesses a better erosion resistance than a fine slightly elongated microstructure, especially at high angles of impact.

- Although single impact events may provide some insights into mechanisms by which particles remove material, care must be taken when such information is used to predict mechanisms of material removal during the steady state erosion.

Chapter 6

EROSION BEHAVIOUR OF ENGINEERING CERAMICS

6.1 Introduction

In Chapter 5, the role of various microstructural features, such as grain boundary glass, grain size and grain morphology, in the erosion of sialon ceramics has been independently examined. The next natural step is to extend the knowledge obtained to various advanced ceramics with a wide range of properties. To achieve this, erosion tests were carried out on a number of engineering ceramic materials including alumina, zirconia, silicon nitrides and silicon carbides using garnet and SiC erodents at 30° and 90° impact. A direct comparison of the erosion resistance of these materials will be provided. Finally, using detailed SEM examination of the eroded surfaces of all target materials, a qualitative model, based on fracture mechanics using the energy dissipation/energy balance approach, will be proposed to account for the erosion behaviour of ceramic materials.

6.2 Experimental Program

6.2.1 Selection of target materials

Four commercial ceramic materials and two laboratory grade gas pressure sintered silicon nitride ceramics from four generic groups, alumina, zirconia, silicon nitride and silicon carbide, were selected for erosion tests. These were a high-purity alumina ceramic (AD998), an MgO partially stabilized zirconia (Mg-PSZ), two self-reinforced silicon nitride ceramics (SN-F and SN-C) and two siliconised silicon carbides (SiC-C and SiC-S). In addition, two in-house prepared Ca α-sialon ceramics (CA2613 and CA2613C) were also tested.

These different ceramic materials were selected because they exhibit a wide range of properties. For example, the alumina ceramic has a moderate hardness and relatively low toughness among the four ceramic materials. The zirconia ceramic has the highest toughness but the lowest hardness, while the silicon nitride and sialon ceramics possess a combination of high hardness and toughness. The silicon carbide ceramics exhibit the highest hardness, but relatively low toughness among the test materials.

6.2.2 Selection of erodent materials

The erodent particles used were commercial grade garnet and SiC abrasive grits (refer to section 3.3.1). Garnet erodent was selected because its properties are similar to those of the most encountered mineral materials in the mining industry, while SiC erodent was chosen because it is the most commonly used abrasive particle in accelerated laboratory tests. Both erodents used here have similar size distributions and morphologies, but exhibit very different hardness values. This permits a direct comparison of the effect of erodent particle hardness on the erosion mechanism of ceramic materials.

SiC erodent was used to erode all the target materials, but garnet particles were used to erode only selected materials, namely alumina, zirconia and pressureless-sintered (PLS-ed) sialon, due to the limited supply of the siliconised silicon carbides (SiSiC) and the gas-pressure-sintered (GPS-ed) silicon nitride samples.

6.2.3 Erosion tests

Samples for erosion tests were cut and machined to dimensions approximately $20 \times 20 \times 3$ mm^3 (AD998), $\phi 24$ mm $\times 5$ mm (Mg-PSZ), $\phi 20$ mm $\times 5$ mm (CA2613), $\phi 24$ mm$\times 5$ mm (CA2613C), $25 \times 25 \times 5$ mm^3 (SN-F and SN-C) and $25 \times 25 \times 10$ mm^3 (SiC-C and SiC-S). The surfaces to be eroded were prepared by finish grinding with 800-mesh SiC abrasive paper.

Erosion tests were performed at room temperature in a gas-blast type erosion test rig described in detail in section 3.3.2.1. Mild steel was employed as the control material in each test. The testing procedures and the method used to determine the erosion rate were described in section 5.2.2. The test conditions used are as follows:

sample to nozzle distance: 13.8 mm;

particle velocity: 20 m/s;

impact angles:

    SiC erosion: 30°, 45°, 60°and 90° for alumina, zirconia and PLS-ed sialon; 30° and 90° for silicon carbides, silicon nitrides and HP-ed sialon;

    Garnet erosion: 30° and 90° for alumina, zirconia and PLS-ed sialon.

6.2.4 Microscopic analysis

The eroded surfaces of all target materials were examined using a JEOL FE6300 scanning electron microscope (SEM) equipped with a field emission gun. A JEOL JSM-840A SEM equipped with an energy dispersive X-ray (EDX) spectrometer was also used when qualitative chemical analysis was required. Prior to examination, the specimens were ultrasonically cleaned in ethanol for 5 minutes and then sputter coated with gold or carbon to prevent charge accumulation on the samples during examination. The accelerating voltage used was 10 and 20 kV for the FE6300 and JSM-840A SEM, respectively.

6.3 Microstructural Analysis of Target Materials

6.3.1 Oxide ceramics

Material AD998 is a high-purity alumina ceramic supplied by Ceramic Oxide Fabricators (Eaglehawk, Victoria, Australia). It contains 99.8 wt% of alumina and 0.2 wt% total of $Na_2O + SiO_2 + MgO$ which is exhibited as a glassy phase that surrounds the grains of Al_2O_3. The size of the Al_2O_3 grains varies widely from 2 μm to over 50 μm with an average diameter of 12.7 μm (Fig. 6.1).
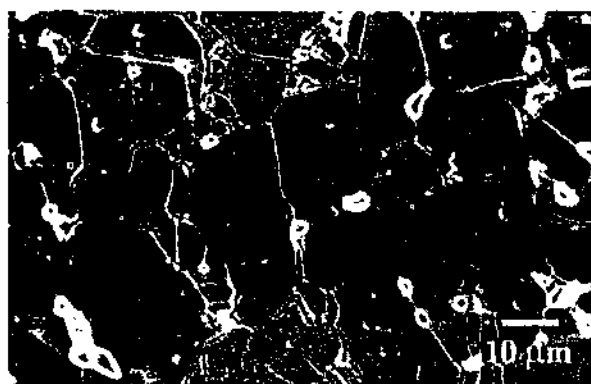
Fig. 6.1. SEM micrograph of polished and thermally etched surface (1500°C/20min) of alumina sample.

The as-fired Mg-PSZ material, supplied by Carpenter Advanced Ceramics (Clayton, Victoria, Australia), contains approximately 70 vol% tetragonal precipitates, 20 vol% cubic matrix phase and 10 vol% monoclinic phase distributed at the grain boundaries (manufacturer's data sheet). SEM observation of a polished and thermally etched surface, as shown in Fig. 6.2, revealed large equiaxed cubic grains with a mean size of 45 μm, as measured by the linear intercept technique. Also as shown in Fig. 6.2, this material contains small isolated pores distributed both in the grains and at the grain boundaries, and the total porosity, as determined using an image analysis technique, is approximately 1 vol%.
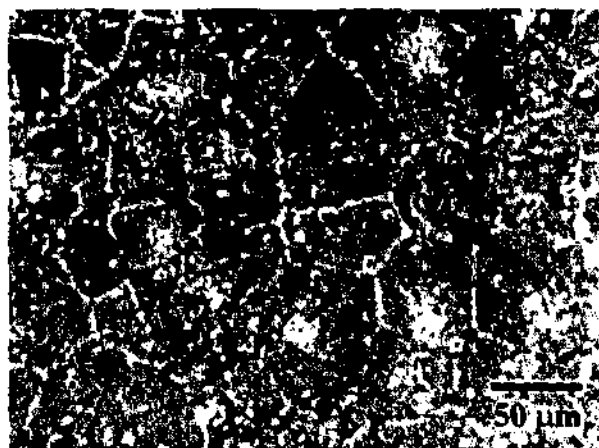
Fig. 6.2. SEM micrograph of polished and thermally etched (1500°C/30min) Mg-PSZ showing the grain morphology and porosity distribution.

6.3.2 Silicon nitride and sialons

The two GPS-ed Si_3N_4 ceramics were supplied by the National Industrial Research Institute, Nagoya, Japan. The starting powders were Si_3N_4 (E-10 grade, ≥95% α-phase, Ube Industries, Japan), Y_2O_3 (purity >99.9%, Shinetsu Chemicals, Japan) and Al_2O_3 (purity >99.9%, Taimei Chemicals, Japan). The composition of the densification additives was 5 wt% Y_2O_3 + 2 wt% Al_2O_3. Material SN-F was prepared by cold isostatic pressing the powder mixture followed by gas pressure sintering, while material SN-C was fabricated using the same powder mixture with an additional 5 vol% of elongated β-Si_3N_4 seeds and was prepared by tape casting, stacking, debinding and gas pressure sintering. The β-Si_3N_4 seeds were rod-like single crystal particles with a typical diameter of ~0.5 μm and a length of ~2 μm. Both samples were densified at 1850°C for 6 h under a nitrogen gas pressure of 0.9 MPa. The processing procedures employed are described in greater detail in a paper by Hirao et al. (1995).
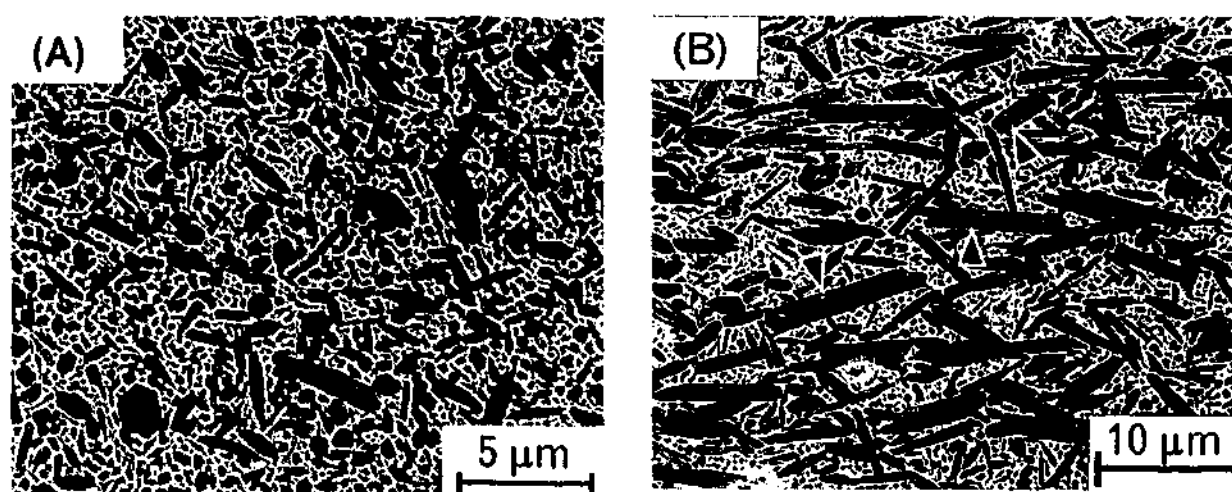
Fig. 6.3. Microstructures of the two GSP-ed silicon nitride materials: (a) SN-F (not seeded, cold pressed) and (b) SN-C (seeded, tape cast), micrograph was taken on the surface parallel to the tape casting plane (tape casting direction: ↔). Plasma etching highlights the epitaxial growth of β-sialon on β-Si_3N_4 cores (indicated by the arrows).

Microstructures of the two GSP-ed Si_3N_4 ceramics are shown in Fig. 6.3. As can be seen, both materials contain elongated reinforcing β-Si_3N_4 grains. However, the unseeded sample SN-F displays a fine-grained microstructure containing randomly

oriented fine elongated grains. The distribution of its grain diameter appears to lie in a transition region between the distinctly bimodal and the broad monomodal distribution. The average grain diameters of the coarse and fine grains are approximately 0.3 and 0.6 μm, respectively.

On the other hand, the seeded sample SN-C exhibits a distinct bimodal distribution of grain diameter in which large elongated β-grains are evenly distributed in a matrix of finer β-grains and an amorphous grain boundary phase. More significantly, these large elongated β-grains, or whiskers, appear to lie mainly in the tape casting plane and are oriented in the casting direction. The average diameters of the large elongated grains and fine matrix grains are approximately 2 and 0.3 μm, respectively.

The two selected Ca α-sialon samples, namely CA2613 and CA2613C, were fabricated from the same batch of starting powder, i.e. composition CA2613. However, sample CA2613 was PLS-ed at 1800°C for 4 h, while sample CA2613C was first PLS-ed at 1800°C for 3 h followed by HP at 1700°C for 1 h. Detailed descriptions of composition and microstructural properties of these materials are given in Chapter 4.

6.3.3 Siliconised silicon carbides

The two SiSiC materials, namely SiC-C and SiC-S (supplied by Concord Engineering, Australia and Schunk, Germany, respectively) are two-phase ceramics which consist of high-purity SiC and Si. Fig. 6.4 shows details of the microstructures of polished sections of the as-received materials imaged in an optical microscope using reflected light. The light Si phase in Fig. 6.4 is due to the higher reflectivity of Si in comparison to that of SiC (Lee and Rainforth 1994). As can be seen, both materials possess a duplex microstructure with angular shaped SiC grains of a bimodal size distribution evenly dispersed in a matrix of fine β-SiC, formed from reaction of the carbon with liquid Si, and free silicon. The average grain size is approximately 50 μm and 6-10 μm for large and small SiC grains, respectively, in material SiC-C. The corresponding data for material SiC-S are 30 μm and 3-4 μm. The volume fractions of large SiC grains, small SiC grains and free Si, as determined

using image analysis, are approximately 49%, 35% and 16%, respectively, for material SiC-C and 58%, 31% and 11%, respectively, for material SiC-S. Note that the volume fraction of small SiC grains includes the original fine-grained α-SiC particles as well as newly reacted elongated β-SiC grains.
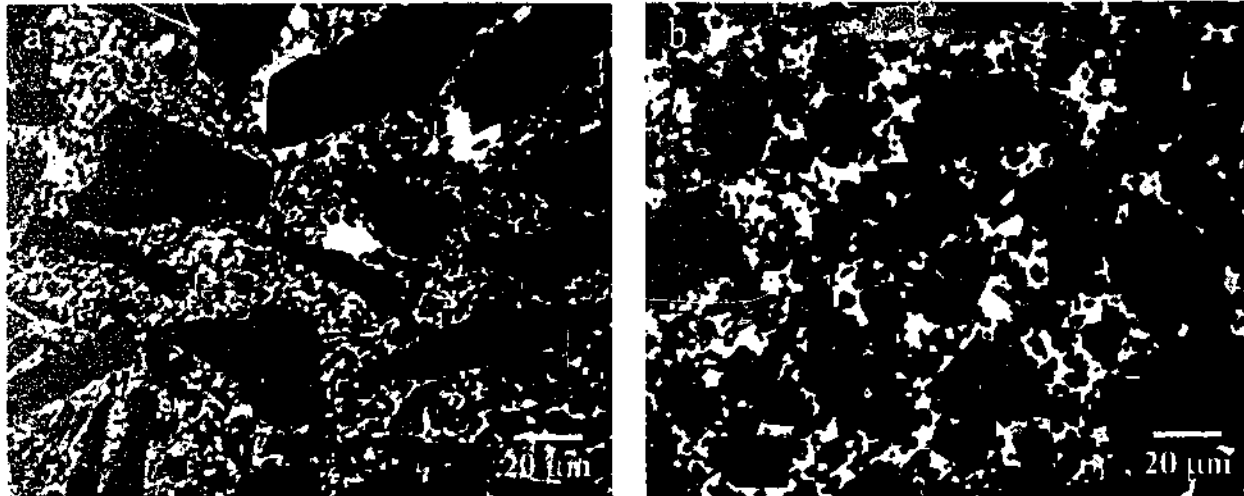
Fig. 6.4. Microstructures of the two siliconised silicon carbide materials observed with reflected light under an optical microscope, showing different reflective indexes between Si (light) and SiC (dark). (a) SiC-C and (b) SiC-S.

The microstructure of the SiSiC material reflects an interesting processing history. It involved the mixing of α-SiC particles, usually with a bimodal size distribution, with carbon and a thermosetting resin to form a green body. The green compact was then charred to carbonize the resin binder and to drive off the volatiles. Finally, the resulting porous body was infiltrated with molten Si at temperatures greater than 1500°C under either vacuum or an inert atmosphere. Liquid Si penetrated the porous body by capillary force and reacted with the carbon to form fine-grained β-SiC grains, epitaxial β-SiC deposits on the α-SiC grains as well as large β-SiC grains (Lee and Rainforth 1994). The reacted SiC along with the residual Si bonded the body together to from a final product with good strength.

6.3.4 Property evaluation

The bulk densities of all the materials were determined using Archimede's method (AS 1774.5, 1979). The Vickers indentation technique was used to measure the hardness in each case. The applied load in the Vickers hardness tests was 10 kg for zirconia, silicon nitrides and sialons. However, using the same load produced irregular intergranular cracking in the alumina and severe lateral cracking in silicon carbides around indents, both of which prevented the accurate measurement of the diagonals of indents. Therefore the load was reduced to 0.1 and 0.3 kg for the alumina and silicon carbide samples, respectively. For illustration, Fig. 6.5 shows the typical indents of siliconised silicon carbide material SiC-S (Fig. 6.5(a)) and Ca α-sialon sample CA2613 (Fig. 6.5(b)) produced by Vickers indentation using 10 kg load.
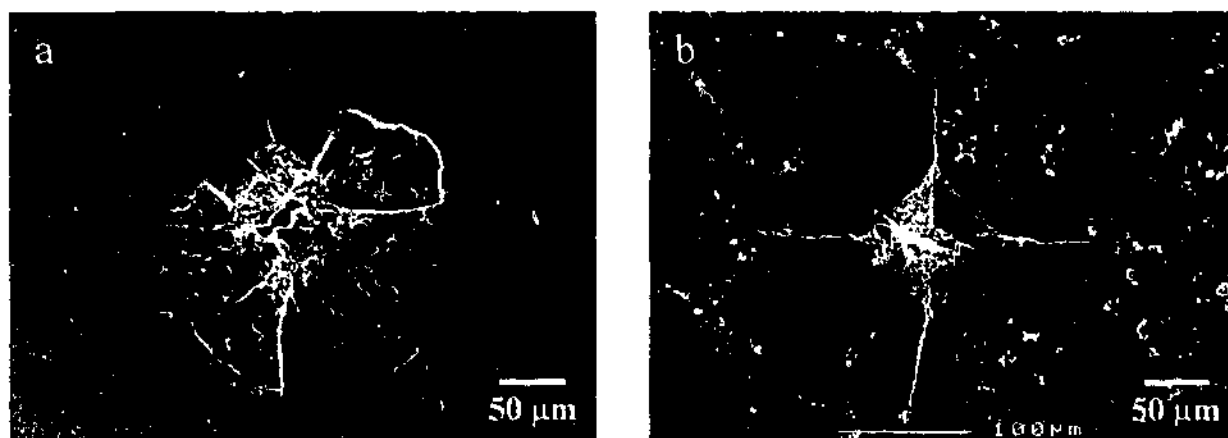
Fig. 6.5. SEM micrographs of the indentation using a 10 kg load on polished surfaces of samples (a) SiC-S, siliconised silicon carbide material; and (b) CA2613, PLS-ed Ca α-sialon material.

Fracture toughness of these materials was also estimated using the Vickers indentation technique by measuring the well-developed radial cracks emanating from the four corners of the indent. The indentation load was 0.3 kg for silicon carbides, 10 kg for sialons, 20 kg for silicon nitrides, and 30 kg for zirconia. The reason for using different loads for the different materials was to produce well-developed radial cracks of length $2c$ (Fig. 3.8) which were twice as long as the diagonal length, $2a$, of the indent (Anstis et al. 1981). However, the fracture toughness of the high-purity

alumina ceramic, AD998, could not be measured by this method because severe grain boundary cracking occurred even at a load as low as 0.1 kg. In addition, since the orientation of the large elongated β-grains, or whiskers, in sample SN-C is highly directional, approximately aligned in the tape casting direction (Fig. 6.6), toughness measurements were carried out in directions both parallel and perpendicular to the orientation of the whiskers.
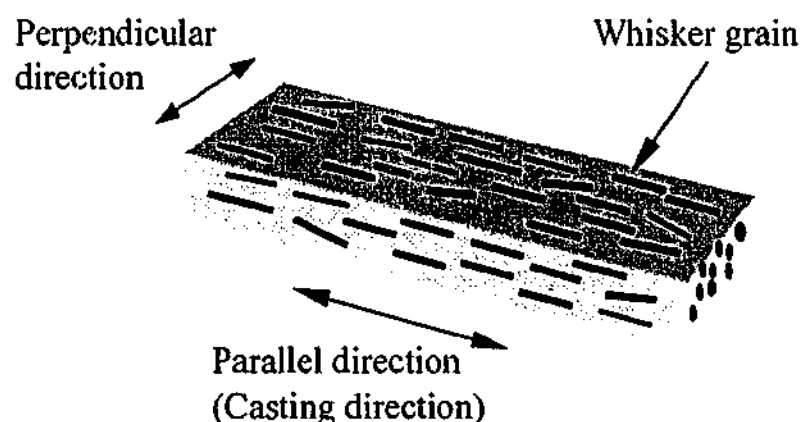
Fig. 6.6. Schematic diagram showing perpendicular and parallel directions in toughness determination and erosion tests of sample SN-C.

It is important to note that in many of the test materials, fracture toughness is not unique, but rather displays a strong dependence on the crack size, the so-called T-curve or R-curve behaviour (Lawn 1993). The values reported here thus correspond to the plateau toughness of the T-curve. The physical and mechanical properties of the materials studied in this work are presented in Tables 6.1 and 6.2.

Table 6.1 Physical and microstructural properties of target materials

Materials	Density[a] (kg/m³)	Porosity[b] (vol%)	Grain diameter (μm)
AD998, High-purity alumina	3740	~4	12.7
Mg-PSZ, Partially stabilized zirconia	5740	~1	45
CA2613, Ca α-sialon, PLS-ed	3160	~2	0.46
CA2613C, Ca α-sialon, PLS-ed+HP-ed	3208	1<	0.51
SN-F, Silicon nitride without seeds	3247	1<	0.3/0.6, nearly bimodal
SN-C, Silicon nitride with seeds	3238	1<	0.3/2, bimodal
SiC-C, Reaction bonded silicon carbide	3020	0	8/45, bimodal
SiC-S, Reaction bonded silicon carbide	3101	0	4/30, bimodal

[a] The bulk density of target materials was measured using the water immersion method.

[b] The porosity of the alumina and sialon ceramics was determined using a combination of water immersion method and the image analysis technique. The porosity of the rest of the materials was obtained either from the manufacture's data sheet (Mg-PSZ, SiC-C and SiC-S) or quoted from literature (SN-F and SN-C) (Becher et al. 1998).

Table 6.2 Mechanical properties of target materials

Samples	Hardness[a] (GPa)	Toughness[b] (MPa m$^{1/2}$)	Young's modulus[c] (GPa)	Four-point flexure strength, σ_f^c, (MPa)	Comments
AD998	17.2 ± 0.2	–	390-400	200-400	Almost equiaxed grains
Mg-PSZ	10.1 ± 0.1	9.1 ± 0.9	175-235	620-820	Equiaxed grains, MgO partially stabilized
CA2613	15.0 ± 0.3	5.4 ± 0.5	235-245	510-590	Elongated grains
CA2613C	18.3 ± 0.2	5.6 ± 0.4	235-245	–	Elongated grains
SN-F	16.4 ± 0.3	5.9 ± 0.1	304	~1000	Elongated grains
SN-C	16.7 ± 0.2	7.9 ± 0.5[¶] 5.9 ± 0.2[§]	312	~1400 MPa[†] ~700 MPa[‡]	12 MPa m$^{1/2}$(K_{IC}, SEPB method)[¶] 7 MPa m$^{1/2}$(K_{IC}, SEPB method)[§]
SiC-C	20.5 ± 0.3	2.4 ± 0.6	350-400	230-300	Mainly equiaxed grains
SiC-S	22.7 ± 0.1	2.4 ± 0.3	300-390	200-300	Mainly equiaxed grains

[a] The applied load in Vickers hardness tests was 0.1 kg for alumina, 0.3 kg for silicon carbides, 10 kg for zirconia, silicon nitrides and sialons.

[b] The applied load in fracture toughness determination was 0.3 kg for silicon carbides, 10 kg for sialons, 20 kg for silicon nitrides, and 30 kg for zirconia.

[c] The values of Young's modulus and four-point flexure strength of target materials were obtained from literature and suppliers.

[¶] Toughness in the direction perpendicular to the orientation of the large elongated β-grains (whiskers).

[§] Toughness in the direction parallel to the orientation of the large elongated β-grains (whiskers).

[†] When tensile stress was applied parallel to the tape casting direction (whisker orientation).

[‡] When tensile stress was applied perpendicular to the tape casting direction (whisker orientation).

6.4 Erosion Performance

6.4.1 Erosion by silicon carbide particles

The cumulative volume loss of all target materials as a function of the amount of SiC erodent impinging on the surface at 90° incidence angle is presented in Fig. 6.7. For all materials, the cumulative volume loss increased linearly as the amount of the erodent increased and the linear portion of the plot was used to determine the steady state erosion rate.

Fig. 6.7. Cumulative volume loss of all target ceramics as a function of the amount of SiC erodent impinging on the surface at 90° incidence angle.

The steady state erosion rates of the target materials followed by SiC erosion at 30° and 90° impact are shown in Fig. 6.8. Erosion rates for all samples were higher for 90° impact compared with 30°. This is consistent with the expected trend for brittle materials (Sheldon and Finnie 1966a). The ranking of the materials, in descending order of erosion resistance, was the Ca α-sialon ceramics, the two types of self-reinforced silicon nitride materials, MgO partially stabilized zirconia, the two SiSiC materials, and alumina, irrespective of the impact angle. Note that, for the two self-reinforced Si_3N_4 materials, SN-C exhibited a higher erosion rate than SN-F, while

for the two sialon ceramics, material CA2613 possessed a higher erosion rate than CA2613C. In addition, for the Mg-PSZ material, the erosion rates were determined for both as-fired (AF) and ground (G) surfaces in the case of 90° impact, while for 30° impact, only the erosion rate of the ground surface was measured.
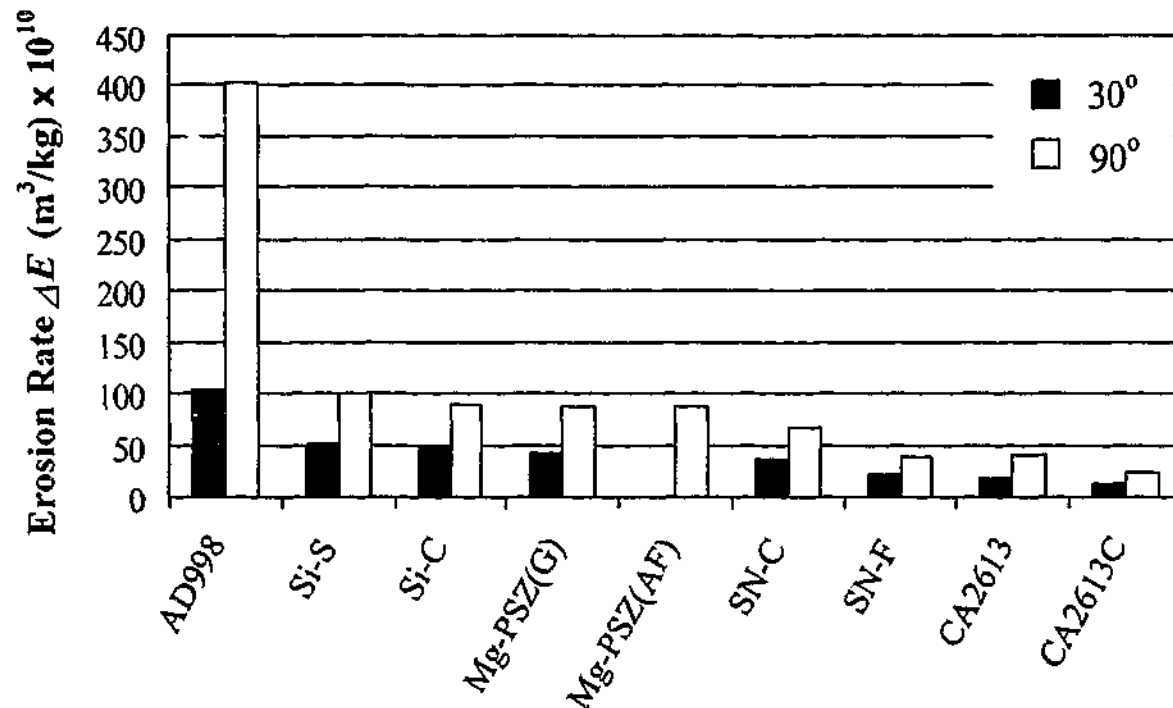
Fig. 6.8. Steady state erosion rates of all target materials eroded by SiC particles at impingement angles of 30° and 90°. Note: the erosion rate of the as-fired (AF) surface of Mg-PSZ was not measured at 30° impingement.

The dependence of the steady state erosion rate on the angle of impact for three selected target materials, namely AD998 (high-purity alumina), Mg-PSZ (MgO partially stabilized zirconia) and CA2613 (PLS-ed sialon composition $m = 2.6$, $n = 1.3$), eroded by SiC particles, is shown in Fig. 6.9. In all cases, the erosion rate increased steadily as the impact angle increased, with the maximum rate appearing at 90° impact. This indicates that despite the large differences in fracture toughness (Table 6.2), the three target materials all behaved as conventional brittle materials when subjected to solid particle erosion. The alumina material showed a higher erosion rate than zirconia and α-sialon ceramics for all angles of impact. At 90° impact, the erosion rate of alumina was higher than that of the zirconia and α-sialon ceramics by a factor of 4 and 10, respectively.
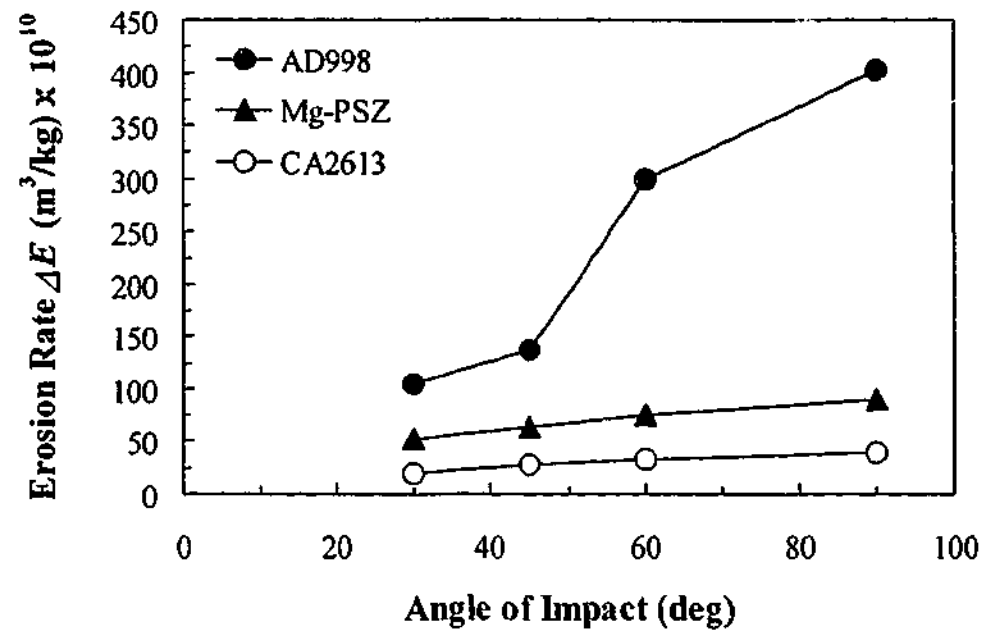
Fig. 6.9. Erosion rate as a function of impact angle for the selective target materials after erosion using SiC grits.

In order to clarify the effect of the surface treatment on the erosion behaviour of Mg-PSZ material, the cumulative volume losses from both as-fired and ground surfaces were plotted as a function of the erodent dosage (Fig. 6.10). It is evident that after the initial 100 g dose, the ground surface experienced a volume loss approximately 1.5 times greater than that of the as-fired surface. Remarkably, the subsequent doses produced almost identical amount of volume loss from the two surfaces, resulting in an identical steady state erosion rate of the two cases. These findings suggest that surface treatments, such as grinding, do not benefit the erosion resistance of Mg-PSZ materials. In addition, the thin surface transformation layer has little influence on the bulk properties of these materials, which govern the steady state erosion rate.

In order to elucidate the effect of the whisker orientation on the erosion behaviour of material SN-C, the cumulative volume losses due to erosion in directions both parallel and perpendicular to the whisker orientation were plotted as a function of the amount of SiC erodent used (Fig. 6.11). It is apparent that in the highly directional whisker-reinforced silicon nitride material, solid particle erosion in the direction

parallel to the whisker orientation resulted in a faster rate of material removal compared to that in the perpendicular direction.
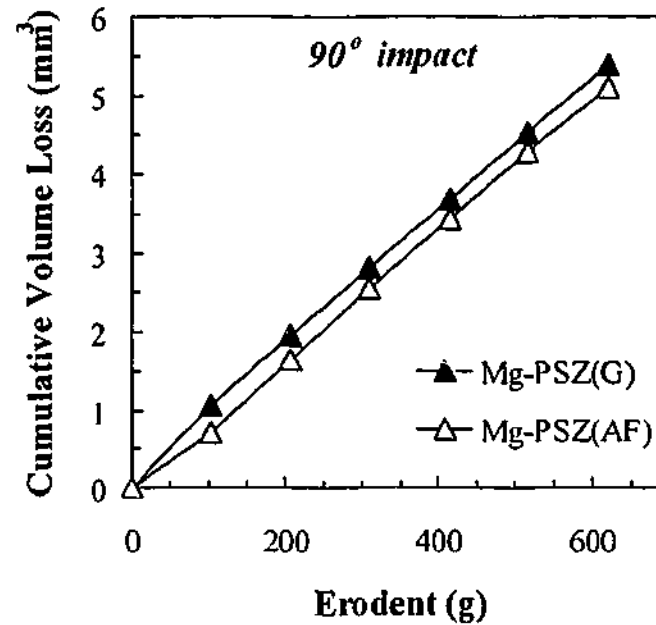
Fig. 6.10. Cumulative volume loss from Mg-PSZ surfaces with (G) and without (AF) grinding as a function of the amount of SiC erodent impinging on the surface at 90° incidence angle.
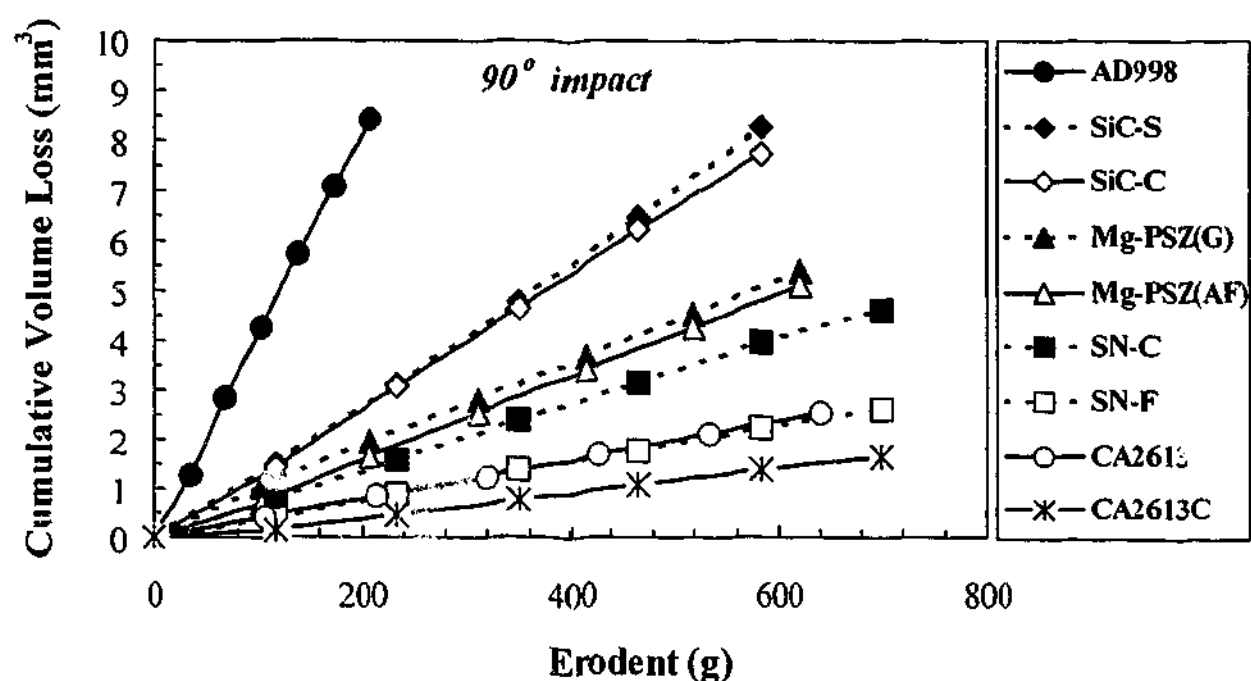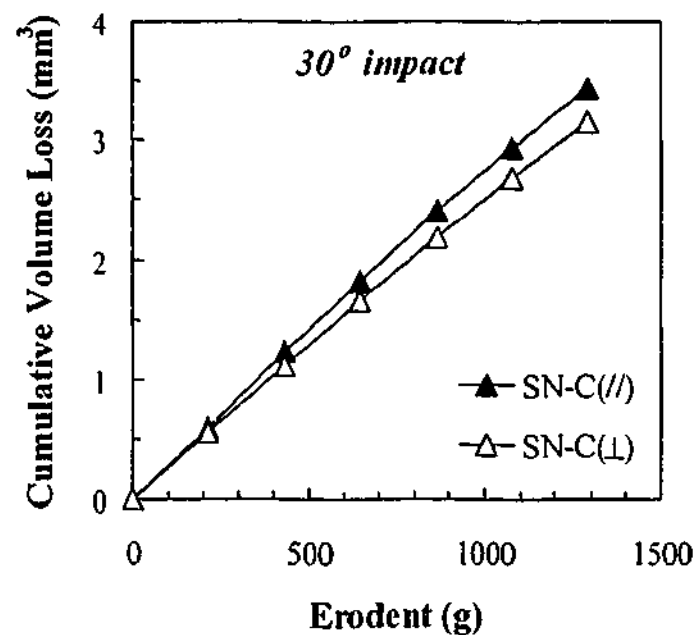

Fig. 6.11. Cumulative volume loss of material SN-C as a function of the amount of SiC erodent impinging on the surface at 30° incidence angle in the directions both parallel (//) and perpendicular (⊥) to the whisker orientation or the tape casting direction (see Fig. 6.6).

6.4.2 Erosion by garnet particles

The cumulative volume loss of alumina (AD998), zirconia (Mg-PSZ) and PLS-ed sialon (CA2613) as a function of the amount of garnet erodent impinging on the surface at 90° incidence angle is presented in Fig. 6.12. For the alumina and zirconia ceramics, the cumulative volume loss increased linearly as the amount of the erodent increased and the linear portion of the plot was used to derive the steady state erosion rate. However, the sialon composition CA2613 displayed an initial weight gain and then remained no detectable volume loss even after exposure to over 10 kg of garnet particles. Therefore, no erosion rate can be determined for this condition.
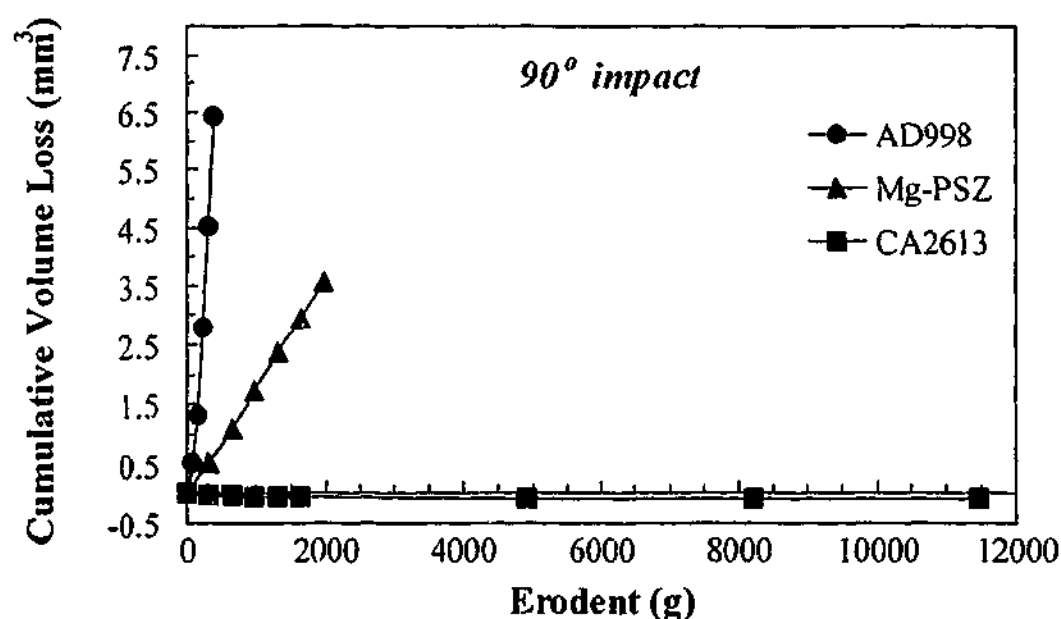
Fig. 6.12. Cumulative volume loss of materials AD998 (alumina), Mg-PSZ (zirconia) and CA2613 (sialon) as a function of the amount of garnet erodent impinging on the surface at 90° incidence angle.

The erosion rates of alumina (AD998), zirconia (Mg-PSZ) and PLS-ed sialon (CA2613) after erosion using garnet particles at impingement angles of 30° and 90° are shown in Fig. 6.13. Again, the erosion rates for all samples were higher for 90° impact compared to 30° impact, and the alumina ceramic showed a much higher erosion rate than the zirconia, by approximately a factor of 13, and the α-sialon ceramic.
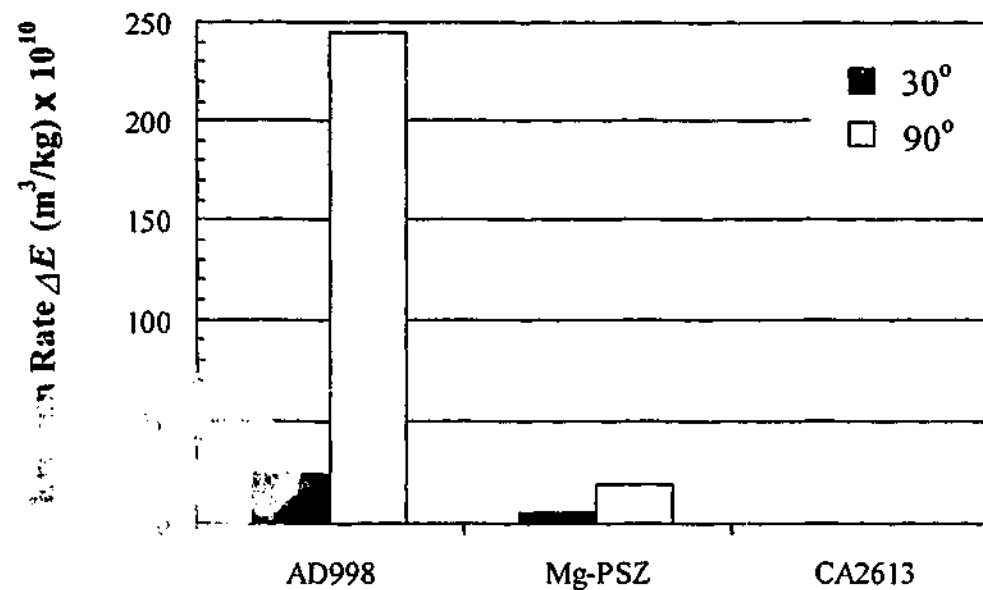
Fig. 6.13. Steady state erosion rates of materials AD998, Mg-PSZ and CA2613 eroded by garnet particles at impingement angles of 30° and 90°.

6.5 Microstructures and Erosion Mechanisms

6.5.1 Alumina ceramic

6.5.1.1 Examination of eroded surfaces

Damage induced on ceramic surfaces due to erosion by solid particle impact was examined using scanning electron microscopy (SEM). Qualitative chemical information was obtained using energy dispersive X-ray (EDX) analysis.

SEM micrographs of the steady state erosion surfaces of high-purity alumina, AD998, after garnet erosion at 30° and 90° impact are shown in Figs. 6.14(a) and (b), respectively, while the damage sustained by the same material subjected to SiC erosion at 30° and 90° impact is presented in Figs. 6.14(c) and (d).
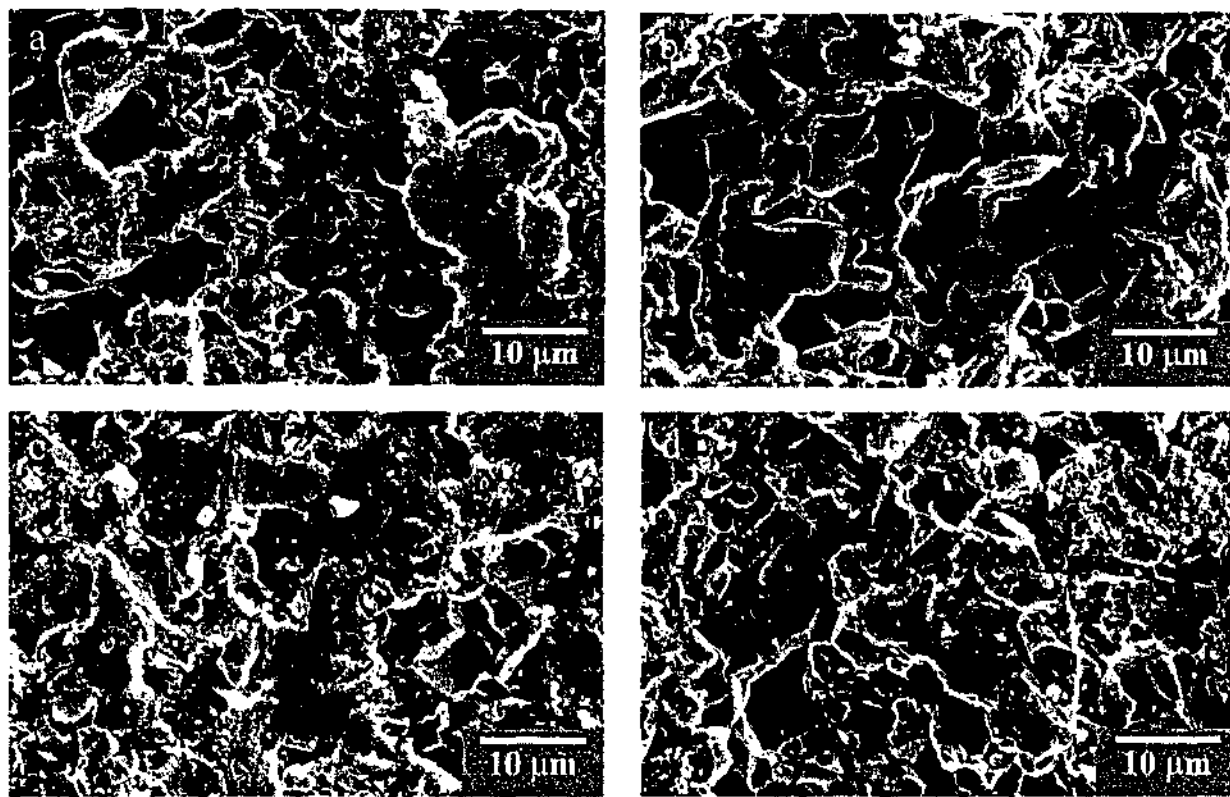
Fig. 6.14. Surface morphology of high-purity alumina ceramic, AD998, following erosion using garnet erodent at 30° (a) and 90° (b) impact, and SiC erodent at 30° (c) and 90° (d) impact. Note: the particle impact direction for 30° impact is from top to bottom of the micrographs.

The effect of impingement angle on the mechanisms of material removal is clearly demonstrated. It is evident that in both garnet and SiC erosion, damage produced by shallow angle impacts is dominated by exposed grain facets and plastic deformation of the materials. The highly deformed regions formed as a result of repeated particle impact as well as plastic cutting, while freshly exposed grain facets are caused by grain dislodgment (ejection) and delamination of the deformed material. Under normal impact, on the other hand, grain ejection appears to be the predominant mechanism of material removal and there are much fewer and smaller plastically deformed regions present.

Although the damage features appear remarkably similar for erosion using garnet and SiC erodents (Fig. 6.14), closer examination of worn surfaces from the two cases revealed some interesting differences. In the case of shallow angle impact, the garnet eroded surface contains large flakes of deformed material (Fig. 6.14(a)). These flakes

are often composed of smeared fine particles, indicating that they resulted from the crushing of wear debris and smearing of exposed alumina grains by repeated particle impact. Random EDX analysis of these deformed materials revealed various levels of Fe and Si contents (see Figs. 7.8 and 7.10), suggesting that they consist of a mixture of smeared target alumina and garnet erodent materials. The worn surface due to erosion by SiC, on the other hand, displayed a high incidence of alumina grains with a flattened surface in addition to the deformed flaky material (Fig. 6.14(c)). Further, ploughing marks, oriented in the direction of particle impact, were frequently observed on these flattened grains, suggesting that the flattened surface feature is a result of plastic deformation of the alumina grains induced by the cutting of the hard, sharp SiC particles.

In the case of normal impact, the worn surface produced by SiC erosion exhibited a high incidence of grain boundary microcracking, transgranular cracking, and chipping and fragmentation of grains (Fig. 6.14(d)), indicating that the SiC erodent induced more severe damage on the target surface compared to garnet particles.

6.5.1.2 Mechanisms of material removal

The above results indicate that several material removal mechanisms operate during the erosion of high-purity alumina ceramics. These include grain dislodgment, deformation of exposed surface grains by repeated particle impact, plastic cutting, and spalling or delamination of the deformed material. However, the dominant mechanism of material removal is grain ejection due to grain boundary cracking. Note that spalling or delamination of the deformed material can also be attributed to the grain ejection process. As will be shown in section 7.4.1, in many of the deformed regions, there is clear evidence of grain boundary microcracking of the underlying alumina grains, and the subsequent impacts will result in spalling of the deformed material.

The formation of grain boundary microcracks during erosion of high-purity alumina ceramics is largely determined by the microstructure of these materials. It is well documented that in high-purity alumina ceramics, the thermal expansion anisotropy

between individual alumina grains creates internal tensile stresses at the grain boundaries (Blendell and Coble 1982; Doğan and Hawk 1999). These residual tensile stresses result in local degradation in resistance of the grain boundaries to fracture. In addition, the equiaxed grain morphology provides little additional resistance to the crack propagation. Therefore, upon external stresses induced by solid particle impact, cracks readily initiate at and propagate along the grain boundaries, leading to material removal from the target surface in an intergranular mode of fracture.

6.5.2 Zirconia ceramic

6.5.2.1 Mechanisms of transformation toughening

ZrO_2 occurs in three polymorphs: cubic (c), tetragonal (t) and monoclinic (m). The tetragonal phase can be partially stabilized by the addition of oxides such as MgO, CaO, Y_2O_3 and CeO_2. The Mg-PSZ material contains a cubic matrix in which there are a large number of fine, partially stabilized tetragonal zirconia precipitates. Under a high stress, the $t \rightarrow m$ phase transformation of the metastable tetragonal precipitates occurs. This stress-activated transformation is accompanied by a shear strain of ~0.16 and a volume expansion of ~4% (Hannink et al. 2000). The shear strain and the volume change induce residual stresses and microcracks around the transformed particles in the matrix, which effectively oppose the opening of cracks and increase the resistance of the ceramic to crack propagation (Garvie et al. 1975). This is the so-called transformation toughening mechanism, and its consequences are that a marked improvement in resistance to erosive wear was ob ~ ed in MgO-partially stabilized ¬irconia ceramics compared to their non-toughened counterparts (Srinivasan and Scattergood 1988b).

The $t \rightarrow m$ transformation can be triggered by surface treatments such as sawing, grinding, polishing or wear. These surface treatments can affect the properties of the material, such as fracture toughness and strength, by introducing residual compressive stress, plastic deformation and microfracture. However, these influences are usually restricted to a thin layer of the material located within tens of micrometers from the surface (van den Berg and de With 1993; Conoci et al. 1999).

In this study, the erosion response of both as-fired and ground surfaces was examined. Grinding induces a compressive residual stress at the surface of zirconia ceramics containing tetragonal precipitates, which can effectively improve the apparent surface toughness and hence the resistance to contact damage. It is, therefore, interesting to see whether this improvement in contact damage resistance affects the erosion resistance of these materials.

The extent of transformation toughening is proportional to the amount of transformable t-ZrO_2 phase present in a ceramic since it is this phase which, upon transformation, produces the toughening and strengthening mechanism. It is therefore expected that various surface treatments could lead to different amounts of t-ZrO_2 remaining on the surface of the material. The remainder of this section intends to quantify the amount of the tetragonal phase on the ground and eroded surfaces of Mg-PSZ ceramics.

Quantitative analysis of t and m phases using X-ray diffraction data was proposed by Whitney (1965). It was suggested that the volume fraction of t-ZrO_2, f_t, in a mixture of a two-phase (t and m) ZrO_2 system could be calculated using the following relationship (Whitney 1965):

$$f_t = I_{t(111)}/[I_{m(11\bar{1})}+I_{t(111)}+I_{m(111)}] \qquad (6.1)$$

where $I_{m(11\bar{1})}$, $I_{m(111)}$ and $I_{t(111)}$ are the intensity of monoclinic ($11\bar{1}$), (111) and tetragonal (111) peaks, respectively. For the present Mg-PSZ material, the manufacturer's data sheet showed that the as-fired material consists of approximately 70 vol% t-ZrO_2 precipitates, 20 vol% c-ZrO_2 matrix phase and 10 vol% m-ZrO_2. Using the as-fired material as a reference and assuming that the amount of c-ZrO_2 remains the same before and after the $t \rightarrow m$ transformation, the amount of t-ZrO_2 precipitates on the ground and eroded surfaces can be calculated using eq. 6.1. The XRD spectra of the as-fired, ground, and eroded surfaces are shown in Fig. 6.15, where the eroded surfaces were obtained from both as-fired and ground surfaces. The results showed that the ground surface contained approximately 46% tetragonal particles, while the eroded surface had about 43% t-ZrO_2. As expected, in both cases considerable amounts of transformation has taken place.
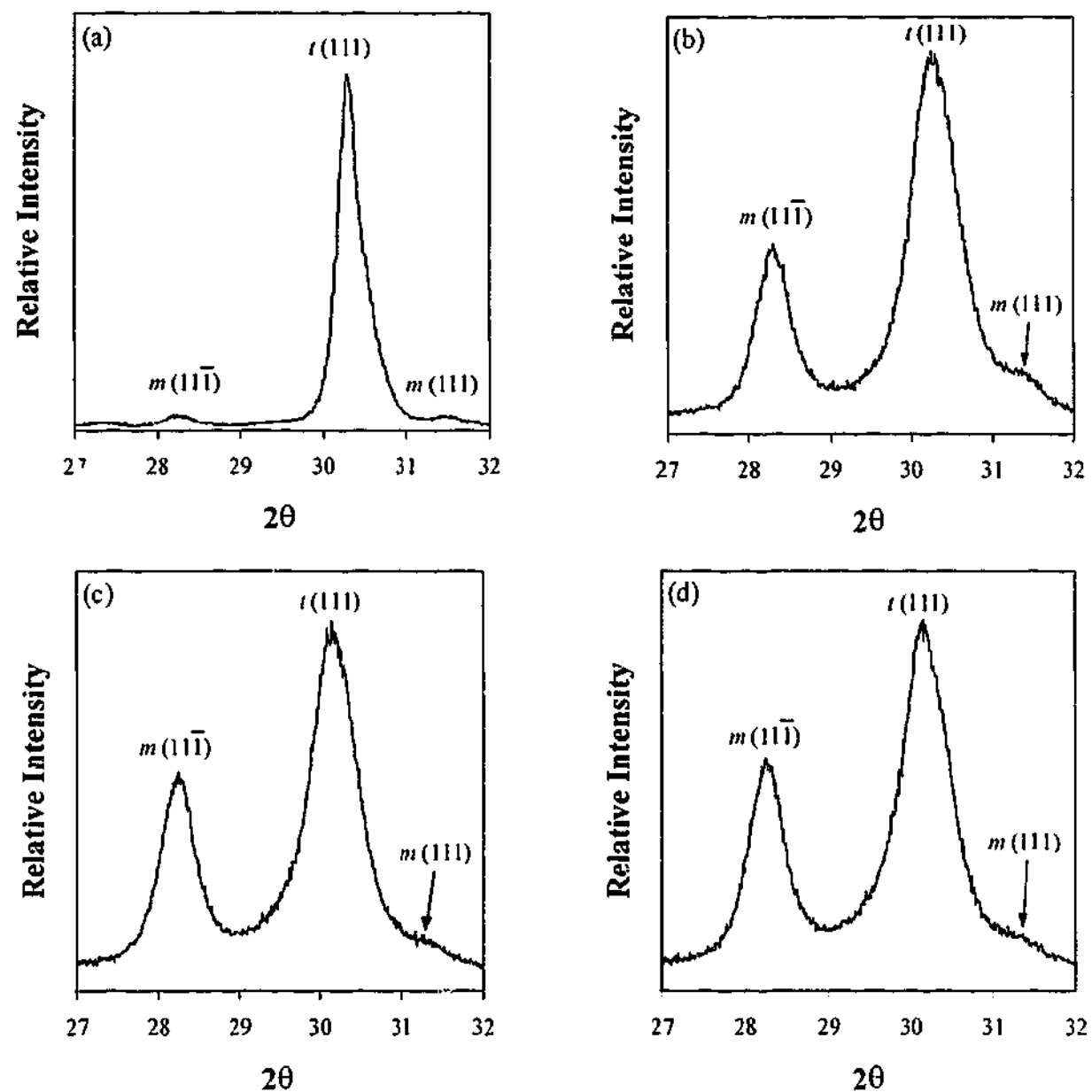
Fig. 6.15. Low angle ($2\theta = 27\text{-}32°$) X-ray diffraction data showing the relative intensity of monoclinic (*m*) peaks (11$\bar{1}$) and (111), and tetragonal (*t*) peak (111) obtained from Mg-PSZ surfaces with and without treatments: (a) as-fired; (b) ground; (c) eroded from the as-fired surface; and (d) eroded from the ground surface.

6.5.2.2 Examination of eroded surfaces

SEM micrographs of the steady state eroded surfaces of Mg-PSZ ceramic after garnet erosion at 30° and 90° impact are shown in Figs. 6.16(a) and (b), respectively, while the damage sustained by the same material following SiC erosion at 30° and 90° impact are presented in Figs. 6.16(c) and (d).
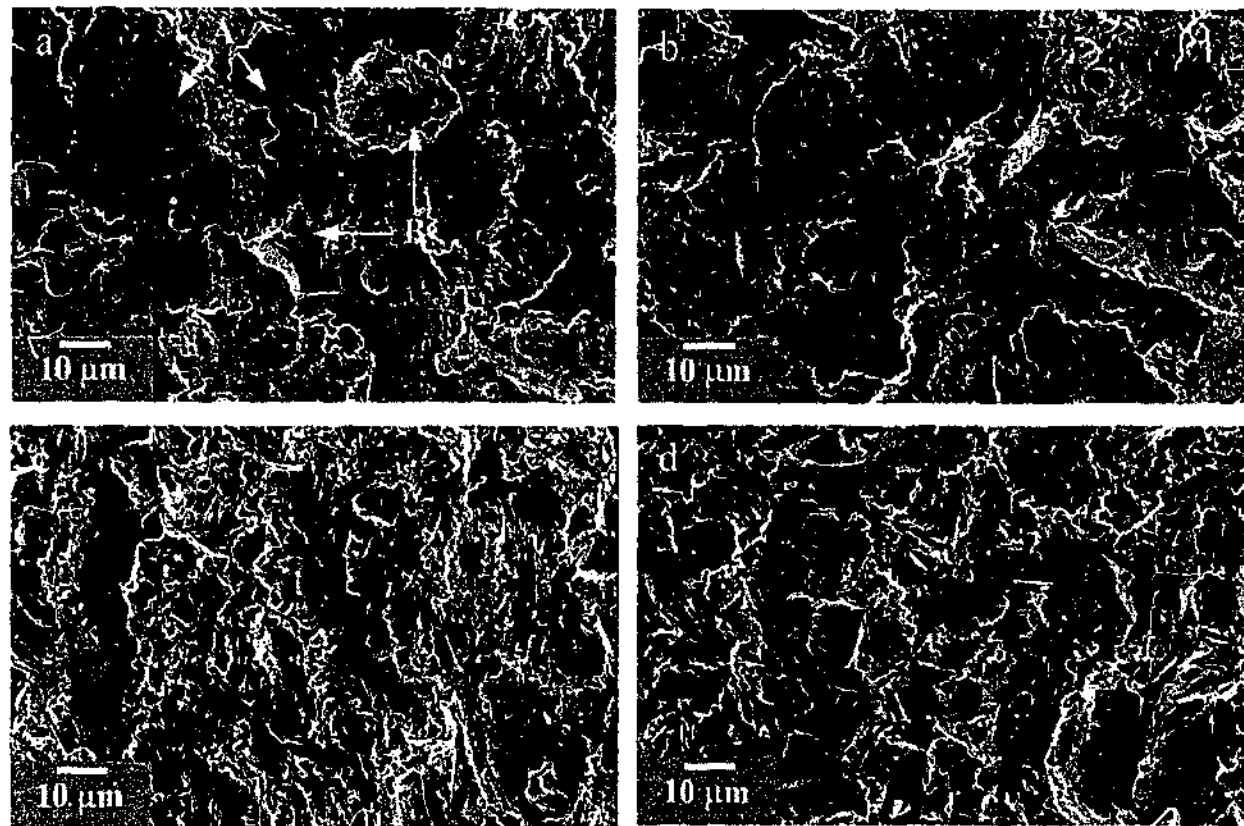
Fig. 6.16. Steady state erosion surfaces of partially stabilized zirconia, Mg-PSZ, generated by garnet erodent at 30° (a) and 90° (b) impact, and SiC particles at 30° (c) and 90° (d) impact. Note: the particle impact direction for 30° impact is from top to bottom of the micrographs.

A comparison of the morphological features of the worn surfaces generated by erosion using garnet and SiC erodent reveals the following differences. In the case of garnet erosion, as shown in Figs. 6.16(a) and (b), the damaged surfaces appeared to be covered by large flakes of deformed material (indicated by the arrows labelled 'A') and displayed a relatively smooth morphology. Some isolated pits resulting from brittle fracture were also apparent (indicated by the arrows labelled 'B'). Interestingly, the 30° impact produced a surface resembling that of the normal

impact, although the scale of damage is reduced. This is indicated by fewer and smaller pits exhibited on the surface produced by the 30° impact compared to that following the normal impact. In addition, there were very few plough marks or grooves present on the shallow angle eroded surface.

In the case of SiC erosion, as shown in Figs. 6.16(c) and (d), the damaged surfaces appeared to be much rougher than those eroded by garnet particles. A flakelike morphology coupled with a high incidence of transgranular chipping was apparent on the surface following normal impact. A higher magnification SEM micrograph, Fig. 6.17, showed deep indentations associated with chipping of the material from the highly deformed surface. On the other hand, the 30° impacts produced a surface that showed substantial grooving and transgranular chipping associated primarily with the scooping mechanism. Small-scale fracture associated with particle indentations was also present. However, the incidence of such fracture was significantly lower on surfaces produced by 30° impact than normal impact.
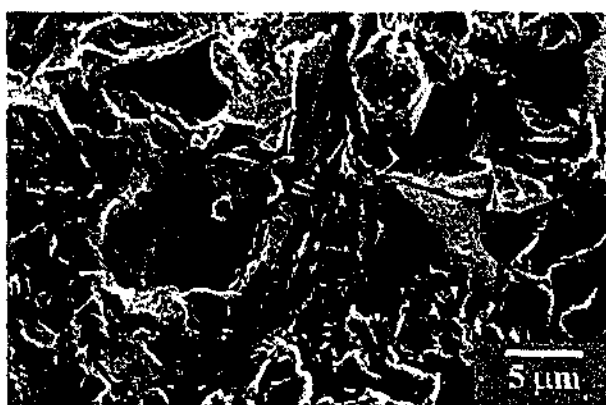
Fig. 6.17. Higher magnification view showing deep indentation impressions produced by SiC particles at normal impact.

6.5.2.3 Mechanisms of material removal

The above analysis suggests that the erosion mechanism of Mg-PSZ materials is associated with indentation-induced transgranular chipping, plastic cutting and scooping, deformation of the exposed surface grains by repeated particle impact, and spalling or delamination of the deformed materials. The dominant mechanism of material removal is transgranular chipping caused by deep indentations and the

scooping mechanism. However, some degree of grain dislodgment is also evident. This is in sharp contrast to erosion of high-purity alumina ceramics where grain boundary cracking and grain ejection govern the rate of material removal. The current result is consistent with that of Srinivasan and Scattergood (1988b), who also found that lateral cracking and scooping mechanism were the dominant mechanisms of material removal in erosion of Mg-PSZ materials.

The plot of erosion rate versus impact angle showed that the erosion rate of the Mg-PSZ ceramic increased steadily as the impact angle increased and reached a maximum at normal impact (Fig. 6.9). The phenomenon of maximum erosion rate at normal impact is usually used as a signature for the erosion behaviour of brittle materials (Sheldon and Finnie 1966a; Srinivasan and Scattergood 1988b). In this sense, Mg-PSZ ceramic exhibits a brittle nature, as do other ceramic materials. However, the stress-activated transformation toughening mechanism of this material has to some degree suppressed the indentation-induced cracking as observed in other brittle materials, where "classical" radial and lateral cracks are often seen to extend far from the impact site. Unfortunately, the relatively low hardness of the zirconia made this material deform substantially when exposed to impact by hard, sharp particles. Thus material removal has still taken place efficiently in part by indentation-induced chipping and in part by plastic cutting and scooping mechanisms.

6.5.2.4 Effects of the surface phase transformation and residual stress on erosion behaviour

It has long been recognized that transformation toughening could significantly improve the resistance to erosive wear, by as much as an order of magnitude, when toughened Mg-PSZ materials were compared to their non-toughened counterparts (Srinivasan and Scattergood 1988b). The consequent question is whether the presence of a transformation layer at the surface can further improve the erosion resistance of these materials.

Experimental results showed that the steady state erosion rates of Mg-PSZ materials with and without the surface transformation layer, i.e. ground and as-fired surfaces, respectively, were essentially the same under the current conditions (Figs. 6.7 and 6.8). However, a closer examination of the volume loss-erodent plot (Fig. 6.10) revealed some differences between the two cases in the early stage of erosion. After an initial dosage of 100 g, the surface with a transformation layer experienced a higher volume loss compared to that without the transformation layer. The measured mass loss was 6.0 and 4.0 mg for surfaces with and without the transformation layer, respectively. Taking into account of errors from the erosion test (~5%) and the analytical balance (± 0.1 mg), there still exists a significant difference in mass loss, and consequently volume loss, between the two cases.

The higher rate of material removal observed from the surface with a transformation layer compared to that without the transformation layer in the initial stage of erosion may be explained as follows. The surface transformed layer contained a higher volume fraction of m-ZrO_2 compared to the untreated surface (section 6.5.2.1). This m-ZrO_2 is assumed to be weakly bonded to the cubic matrix because of microcracking produced by the transformation and possesses a relatively low hardness compared to t-ZrO_2. Therefore, upon solid particle impact, the surface m-ZrO_2 can be removed more easily, resulting in a fast removal rate of the transformed surface layer. However, as erosion proceeds, a surface transformed layer is regenerated, which is then removed. This process occurs continuously. As can be seen from Figs. 6.15(c) and (d), the amount of m-ZrO_2 is virtually the same irrespective of whether the initial surface was as-fired or ground. This leads to a similar steady state erosion rate between the as-fired and ground surfaces.

6.5.3 Silicon nitrides

6.5.3.1 Examination of eroded surfaces

SEM micrographs of the steady state erosion surfaces of material SN-F generated by SiC erosion are presented in Fig. 6.18. Fig. 6.18(a) shows a general view of the damaged surface following 30° impact, while Fig. 6.18(b) shows the central region outlined by the frame in Fig. 6.18(a) at a higher magnification. Similarly, Fig. 6.18(c)

presents a general view of the worn surface following 90° impact and Fig. 6.18(d) is a higher magnification micrograph of the region outlined in Fig. 6.18(c).
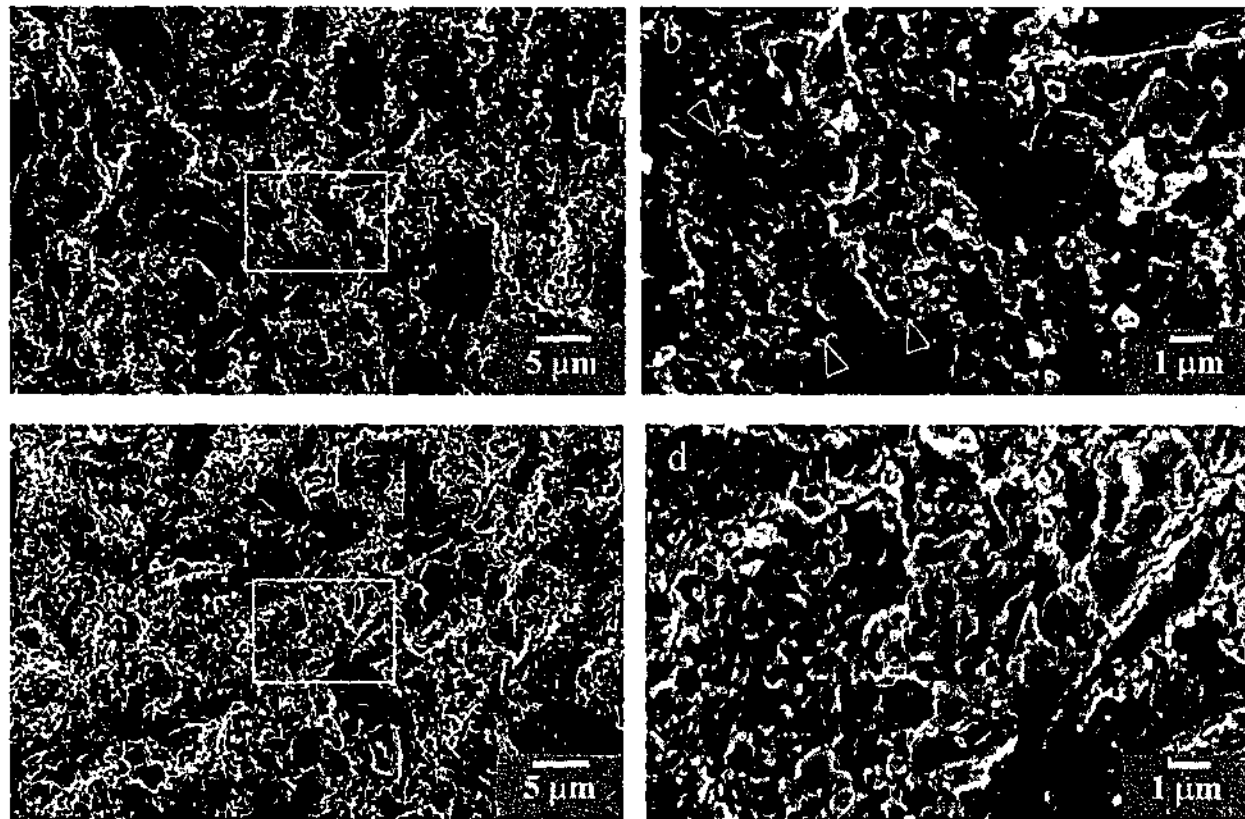
Fig. 6.18. Worn surfaces of material SN-F after SiC erosion at different impact angles. (a) 30° impact, low magnification general view. (b) Higher magnification image showing the central region outlined by the frame in (a). Note: arrows in (b) indicate the fragmentation of the deformed flakes. (c) 90° impact, low magnification general view. (d) Higher magnification image showing the brittle-fracture region outlined by the frame in (c). Note: the particle impact direction for 30° impact is from top to bottom of the micrographs.

The damage features induced by 30° and 90° impact were similar; both indicated brittle-fracture and plastic deformation of the materials, except that the 30° impacts produced a higher area fraction of plastically deformed zones with long ploughing trajectories. Higher magnification SEM examination of the brittle-fracture region showed that erosion damage involved intergranular fracture, transgranular fracture as well as the smearing of exposed surface grains (Fig. 6.18(d)). In addition, some wear debris, typically submicrometer in size and irregular in shape, were seen on the worn surface, suggesting that they were derived either from the fine, more equiaxed grains or from the fragmentation of the large, more elongated grains (Fig. 6.3 and Table

6.1). Upon repeated impacts, the surface grains along with some loosely bonded wear debris were crushed and smeared to form highly deformed flakes (Fig. 6.18(b)). At the same time, crack networks also developed in the target material. Subsequent impacts resulted in fracture of the underlying silicon nitride grains as well as the spalling or fragmentation of the smeared flakes (marked by arrows in Fig. 6.18(b)).

SEM micrographs of the steady state erosion surfaces of material SN-C generated by SiC erosion at 30° and 90° impact are presented in Figs. 6.19 and 6.20, respectively. The damage surface produced by 30° impact in the direction parallel to the tape casting direction displayed combined features of brittle-fracture and plastic deformation (Fig. 6.19(a)). The tape casting direction in Figs. 6.19(a) and (b) is indicated by the arrow shown in Fig. 6.19(a), while the particle impact direction is from top to bottom of the micrographs. Fig. 6.19(b) which is a higher magnification view of the brittle-fracture region outlined in Fig. 6.19(a) revealed that damage sustained by the reinforcing whiskers was mainly intergranular fracture with a few incidences of transgranular fracture, resulting in pullout of the whiskers, or, at least large portions of the whiskers. In addition, microfracture of the fine matrix grains was also seen.

The worn surface generated by 30° impact in the direction perpendicular to the tape casting direction again displayed a mixture of brittle-fracture and plastic deformation features (Fig. 6.19(c)). Note that the tape casting direction in Figs. 6.19(c) and (d) is parallel to the horizontal direction, indicated by the arrow in Fig. 6.19(c), while the erosion direction is from top to bottom of the micrographs. However, more wear debris were observed on this surface at high magnification (Fig. 6.19(d)) compared to that resulting from erosion in the parallel direction (Fig. 6.19(b)). Although pullout still remained one of the dominant damage features sustained by the reinforcing whiskers, an increased incidence of microchipping of the whiskers as a result of the impact was clearly evident (Fig. 6.19(d)). In some cases, several parallel whiskers were fractured into a number of sections in the area of contact with the impinging particles, exhibiting a severely crushed morphology consisting of many fragments as seen in the area highlighted by the elliptical frame in Fig. 6.19(d).
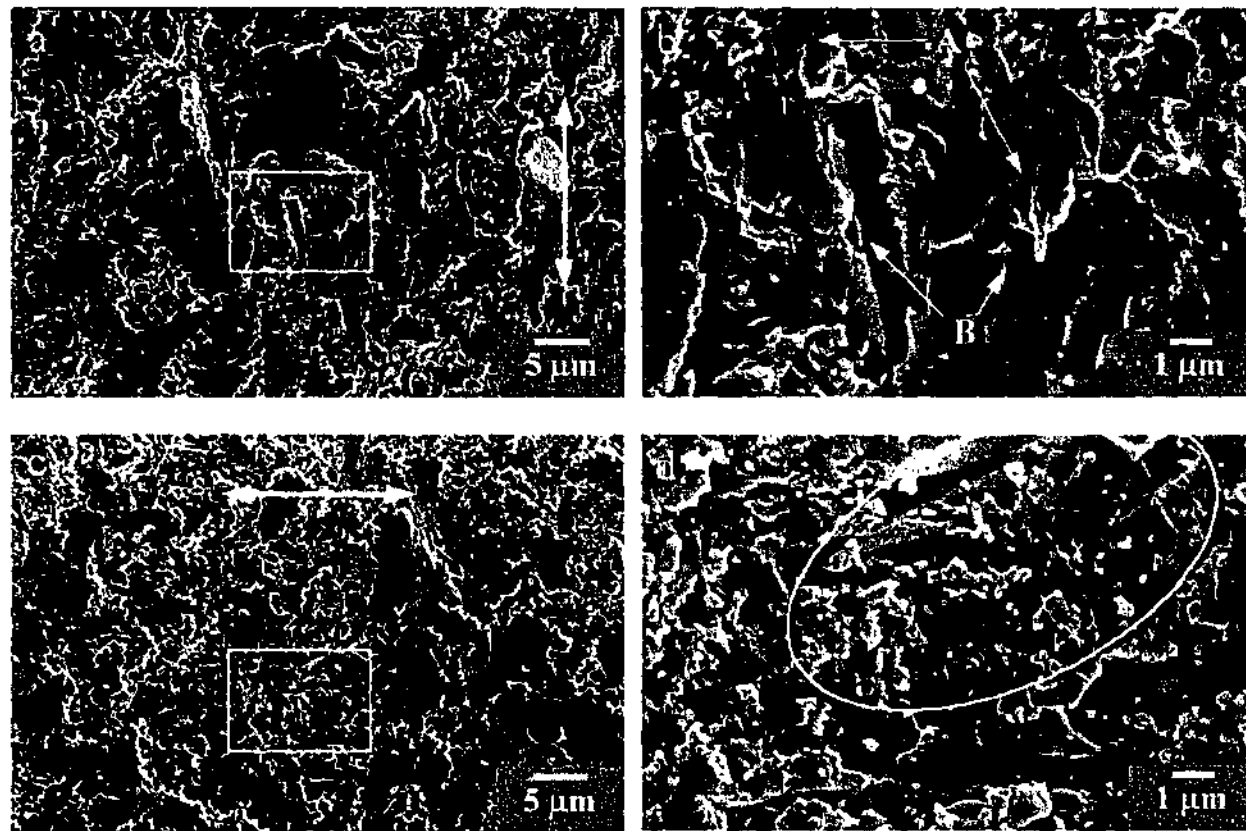
Fig. 6.19. Worn surfaces of material SN-C after 30° SiC erosion with different impact directions. Arrows indicate the tape casting direction, while the particle impact direction is from top to bottom of the micrographs. (a) Parallel to the tape casting direction (Fig. 6.6). (b) Higher magnification view of the brittle-fracture region of (a), outlined by the frame. (c) Perpendicular to the tape casting direction. (d) Higher magnification view of the brittle-fracture region of (c), highlighted by the frame. Note: arrows labelled 'A' show the transgranular fracture, while arrows labelled 'B' indicate the intergranular fracture.

The eroded surface resulting from 90° impact (Fig. 6.20(a)) exhibited a higher area fraction of brittle-fracture zones compared to that produced by 30° impacts (Figs. 6.19(a) and (c)). Pullout and transgranular chipping of the whiskers as well as microfracture of the fine matrix grains were observed at high magnification (Fig. 6.20(b)).
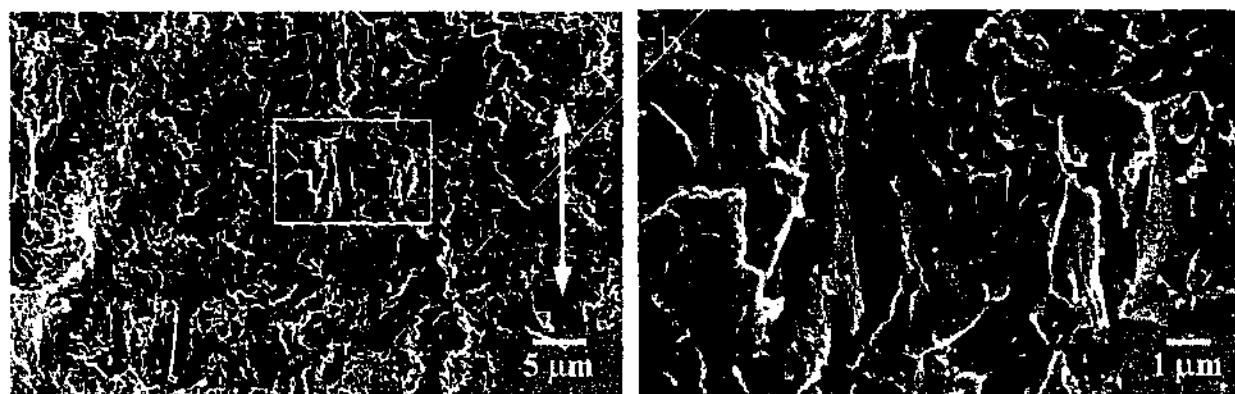
Fig. 6.20. Worn surfaces of material SN-C after 90° SiC erosion. (a) Low magnification general view of the eroded surface. (b) Higher magnification microstructure of a brittle-fracture region outlined by the frame in (a). Note: arrow in (a) indicates the tape casting direction.

6.5.3.2 Mechanisms of material removal

The above observations suggest that the erosion mechanism in self-reinforced or *in-situ* reinforced silicon nitride ceramics apparently involves grain pullout, transgranular chipping, and plastic deformation of the exposed surface grains as well as the fragmentation of deformed materials. The dominant mechanisms of material removal are, however, grain dislodgment and transgranular chipping.

In the erosion of silicon nitride with a preferred orientation of large elongated grains, the reinforcing whiskers are seen to suffer pullout and fragmentation. More significantly, the material removal mechanism of the whiskers was found to vary with the solid particle impacting direction, i.e. in a direction parallel or perpendicular to the tape casting direction. From Fig. 6.6, it is seen that the tape casting direction is in fact the growth direction of the elongated grains. When solid particles attack the surface in the direction parallel to the casting direction, the whiskers are removed primarily by debonding, pullout, or fracture of a large portion of the whisker (Fig. 6.19(b)). On the other hand, when erodent particles strike the surface in the direction perpendicular to the casting direction, the whiskers experience an increased incidence of multiple fractures in addition to pullout (Fig. 6.19(d)). In many cases, the multiple fractured sections are chipped away or crushed by the impacting particles.

6.5.3.3 Effects of microstructure on erosion behaviour

Traditionally, hardness and toughness are often used to model the erosion behaviour of ceramic materials (Evans et al. 1978; Wiederhorn and Lawn 1979). The models indicate that the erosion rate of ceramic materials should have a strong inverse dependence on the fracture toughness, but have a much weaker dependence on the hardness of the material (eq. 2.5). However, such prediction seems to be contrary to the present findings. Mechanical property evaluations showed that material SN-C exhibited a significantly higher toughness, in the direction perpendicular to the tape casting direction, than material SN-F, while the hardness of the two materials was almost identical (Table 6.2). According to the theoretical models (eq. 2.5), material SN-C should have a better erosion resistance, especially when eroded in a direction perpendicular to the tape casting direction, than material SN-F. Nevertheless, erosion tests showed that material SN-F exhibited better erosion resistance than material SN-C under both 30° and 90° impacts (Fig. 6.8).

It is well established that the self-reinforced silicon nitride materials exhibit significant R-curve behaviour where the fracture resistance, K_R, increases as the crack propagates (Li et al. 1992; Ohji et al. 1995; Becher et al. 1998). Becher and colleagues (1998) studied the R-curve behaviour of materials SN-F and SN-C using an applied moment double cantilever beam (AMDCB) geometry. For illustration, the R-curves published by Becher et al. (1998) are shown in Fig. 6.21. As can be seen, material SN-C (curve 6.21(a)) exhibited both high steady-state toughness and the rapidly rising fracture resistance with the extension of the short cracks, while material SN-F (curve 6.21(b)) displayed a much lower steady-state toughness compared to sample SN-C. In addition, the fracture resistance of material SN-F quickly reached its steady-state value at crack lengths <500 µm. Note that curves 6.21(c) and (d) are derived from two commercial self-reinforced silicon nitride materials which are not examined in the present study.
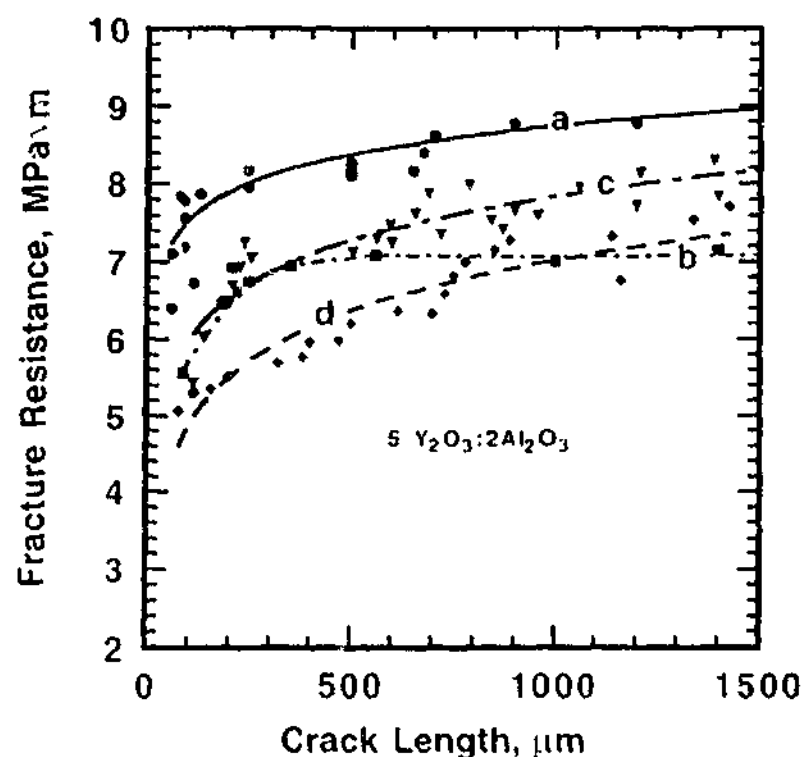
Fig. 6.21. Rising fracture resistance behaviour for silicon nitrides densified using an additive mixture of 5 wt% yttria + 2 wt% alumina. *R*-curves labelled 'a' and 'b' are derived from materials SN-C and SN-F, respectively, while 'c' and 'd' correspond to two commercial materials which are not investigated in the present study. (After Becher et al. 1998.)

The present erosion results showed that self-reinforced silicon nitride ceramics displaying a high steady-state toughness might not exhibit good erosion resistance (Fig. 6.8). This finding may be explained by the following reasons. In a fracture toughness test, when the propagating crack tip interacts with the reinforcing whiskers, the weak interface between the whiskers and the matrix promotes crack bridging, resulting in a crack-size dependent toughness. This is particularly the case of material SN-C where highly directional, large elongated grains are well dispersed in a fine, submicrometer grain sized matrix. Such a microstructure ensures a high steady-state fracture toughness owing to the large number of reinforcements and the large length of the debonded interfaces between the whiskers and the matrix.

In an erosion test, the situation where a crack grows at equilibrium over a long distance and involves a number of bridging grains does not exist. Rather, multiple microcracks develop simultaneously in the vicinity of the impact site and the linking up of microcracks between the neighborhood impact sites forms a network of short

cracks, leading to material loss from the target surface. The weak interface, which is essential for the *R*-curve behaviour, can facilitate the formation of interfacial microcracking and thus result in the dislodgment of the large reinforcing whiskers, leading to a high rate of material removal. More significantly, the reinforcing whiskers in material SN-C are well dispersed and oriented parallel to the eroding surface. During erosion, these whiskers tend to get plucked out or sheared out of the matrix, rather than undergoing the partial pullout which leads to crack bridging. On the other hand, the randomly oriented reinforcing grains in material SN-F provide an interlocking effect. Upon erosion, the interlocking effect hinders the dislodgment of the large reinforcing grains, resulting in a relatively low material removal rate.

It has been reported in the literature (Srinivasan and Scattergood 1991; Marrero et al. 1993) that when fracture toughness values corresponding to short cracks relevant to the erosion phenomenon are used, better correlation between the fracture toughness and the erosion results can be obtained. As discussed in section 5.7.2, erosive wear involves cracks typically of the order of tens of micrometers, e.g. under the current experimental conditions, the typical crack sizes due to single particle impacts ranged between 10-40 μm (Fig. 5.8). Unfortunately, determination of fracture resistance for crack lengths well below 50 μm is not straight forward (Becher et al. 1998; Zenotchkine et al. 2001). Therefore, no direct comparison of the operative toughness values involved in erosion process of materials SN-F and SN-C can be made.

There are indications in the literature that material SN-C should have higher or at least comparable fracture toughness with material SN-F even in the short crack region. For example, an early study on *R*-curve behaviour of self-reinforced silicon nitride materials (Ohji et al. 1995) showed that material SN-C exhibited a substantially higher fracture resistance at the beginning of the crack extension (~30 μm) compared to the conventional self-reinforced silicon nitride with a broad grain diameter distribution involving larger, randomly oriented reinforcing grains. Their findings are consistent with the observed higher fracture strength of material SN-C (when the tensile stress was applied parallel to the whisker orientation) compared to material SN-F (Table 6.2). It is known that the typical fracture defect size in high-strength silicon nitride materials is smaller than 50 μm, which suggests that material

SN-C should have a higher fracture resistance than material SN-F even at the crack size smaller than ⁵0 μm (Ohji et al. 1995). Nevertheless, the actual fracture toughness of the two materials in the crack regions between 10-30 μm, which is most relevant to the erosion damage in the present study, still remain elusive.

While the R-curve behaviour or the operative short-crack toughness may give some indications of the erosion response of materials SN-F and SN-C, the use of short-crack toughness to quantitatively predict the erosion resistance must be made with caution, due to the following reasons. Firstly, as mentioned above, the key features for a pronounced R-curve behaviour are large directional reinforcing whiskers coupled with weak interfaces. The present results clearly pointed out that both directional whiskers and a weak interface could deteriorate the erosion resistance owing to the substantial dislodgment of the large reinforcing grains (Figs. 6.19 and 6.20). Secondly, R-curve measurement determines the plane strain fracture toughness, K_{IC}, which corresponds to the Mode I fracture. Erosive wear could, however, involve Mode I, II and/or III fractures and thus may not be solely described by K_{IC}.

Erosion tests showed that for material SN-C, the erosion rate generated by 30° impact in the direction parallel to the tape casting direction is noticeably higher than that in the direction perpendicular to the casting direction (Fig. 6.11). Such a discrepancy can be again rationalized by the microstructural characteristics in terms of the highly aligned reinforcing whiskers of this material.

SEM observations of the damage surfaces produced by erosion in directions parallel and perpendicular to the orientation of the whiskers showed that whisker-dislodgment is a dominant mechanism of material removal in both cases (Figs. 6.19). However, detailed examinations revealed a higher incidence of whisker-dislodgment during erosion in a direction parallel to the whisker orientation (Fig. 6.19(b)), whereas a higher amount of fine debris formed during erosion in the perpendicular direction due to the higher incidence of multiple fractures suffered by the whiskers in this mode (Fig. 6.19(d)). Since erosion in the direction perpendicular to the whisker orientation entails multiple fracture, which requires higher energy compared to the

whisker-dislodgment in the parallel direction, for the same incident energy the erosion loss should be less in the direction perpendicular to the whisker orientation than that parallel to the whisker orientation.

6.5.4 Silicon carbides

6.5.4.1 Examination of eroded surfaces

The eroded surfaces were examined using SEM. Investigations were carried out in damaged areas located both in the centre and on the edge of the erosion crater. As discussed in section 5.4, the examination of the edge of the erosion crater provides useful insights into the early stage erosion process, while the investigation of the center of the erosion crater reveals the damage sustained during steady state erosion.

The early stage erosion surface of material SiC-C resulting from SiC erosion at 90° impact is shown in Fig. 6.22. A few isolated pits similar to those shown in Fig. 6.22(a), marked by arrows, were found in these regions. Interestingly, detailed examination revealed that damage features associated with individual impact sites were quite different. In the impact crater marked by the arrow labelled 'A', classical chipping or conchoidal fracture resulting from lateral cracking was evident. In contrast, in the nearby crater labelled 'B', dislodgment of fine SiC grains was observed.

A back scattered electron (BSE) image of the same area in (a) is shown in Fig. 6.22(b) where the bright phase indicates the regions rich in Si. The light grey phase presents the two-phase SiC-Si region while the dark grey phase, highlighted by the frame, shows the large SiC grains. As can be seen from Fig. 6.22(b), conchoidal fracture from lateral crack chipping occurred within individual coarse SiC grains, while the grain dislodgment took place in the two-phase region. In addition, small-scale chipping damage was also observed on the surface of large SiC grains, suggesting that not every impacting particle could effectively produce a significant lateral crack. As discussed in section 5.5.1, this is probably due to the threshold effect on lateral crack initiation where only those particles with high kinetic energy

are capable of producing lateral cracking or even multiple impacts are necessary to accumulate the requisite levels of stress to generate lateral cracking.
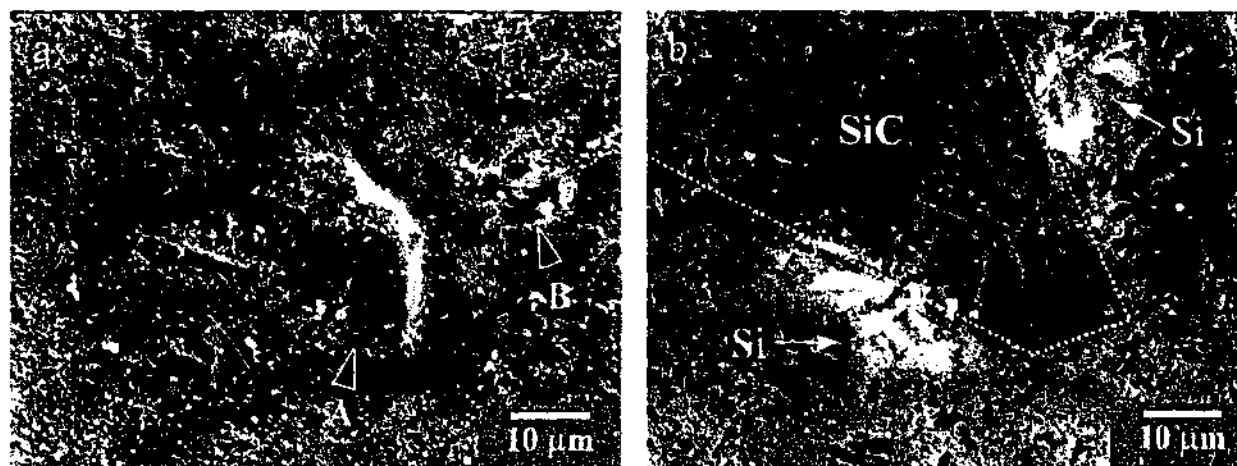
Fig. 6.22. SEM micrographs showing surface morphology of isolated particle impacts on material SiC-C following 90° SiC erosion. (a) Secondary electron (SE) image, and (b) Back scattered electron (BSE) image where atomic number contrast between Si (light) and SiC is perceived. Note: images are taken near the edge of the erosion crater.

The steady state erosion surface of material SiC-C produced by SiC erosion at 90° impact is shown in Fig. 6.23. The worn surface was much rougher than that resulting from early stage erosion. Areas of smeared-looking or deformed material were also observed in addition to the brittle-fracture regions (Fig. 6.23(a)). Furthermore, in the brittle-fracture zones, two distinct types of damage were present: (1) large-scale transgranular chipping resulting from the link-up of lateral cracks; and (2) dislodgment of the fine SiC grains and occasional small-scale transgranular chipping of the elongated β-SiC grains, highlighted by elliptical frames in Fig. 6.23.

The BSE image of the same area in Fig. 6.23(a) is shown in Fig. 6.23(b). The effect of microstructure on erosion damage is immediately evident. The erosion damage of large SiC grains was predominately transgranular chipping of lateral cracks, see the dark grey regions, indicated by the frame with dashed lines, in Fig. 6.23(b). On the other hand, the damage features observed in the two-phase region were grain dislodgment, limited small-scale transgranular chipping as well as highly plastically deformed materials, as seen in regions containing the scattered bright Si phase in Fig.

6.23(b). The deformed material is believed to contain free Si as well as fine SiC debris and thus should have a bright appearance relative to SiC grains under the BSE mode. However, such differences are often diminished due to the rough erosion surface and the non-uniform distribution in thickness of the surface deformed materials.
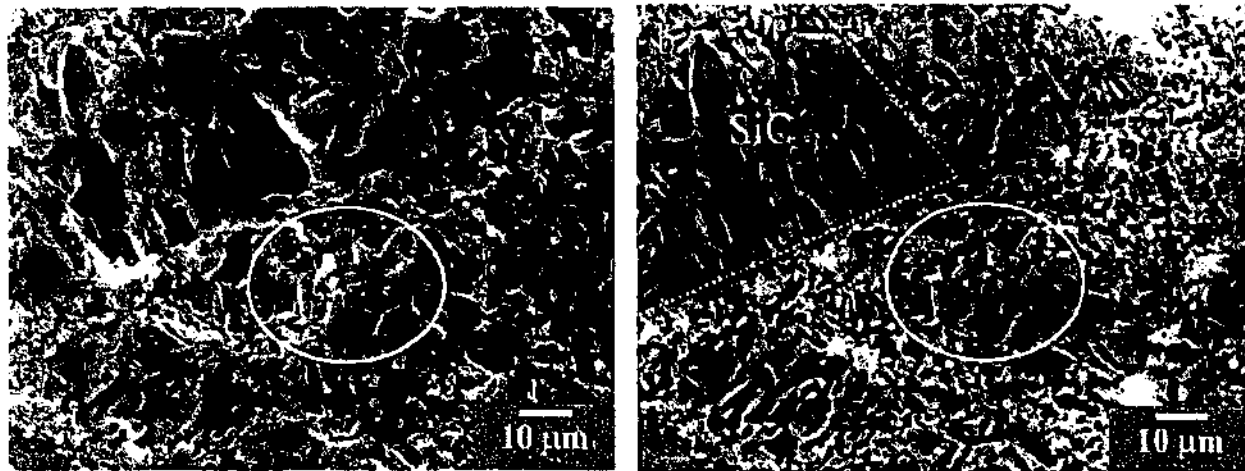
Fig. 6.23. SEM micrographs showing surface morphology of material SiC-C following 90° SiC erosion. (a) SE image, and (b) BSE image. Note: images are taken near the center of the erosion crater, where steady state erosion occurred.

Steady state erosion surfaces of material SiC-S generated by SiC particles at 30° and 90° impact are shown in Figs. 6.24(a) and (b), respectively. Remarkably, damage features were very similar in the two cases, both involving transgranular chipping associated with lateral cracks and intergranular fracture of fine SiC grains as well as plastic smearing of the deformed materials. Additionally, there was a noticeable lack of ploughing marks on the 30° eroded surface, suggesting that the plastic cutting mechanism was suppressed even when the hard, sharp SiC erodent was used.

As already shown in Fig. 6.5(a), the Vickers indentation impressions of the two SiSiC materials, at least at 10 kg load or greater, were surrounded by regions of widespread lateral cracking and associated surface chipping. Fig. 6.25(a) is a BSE image showing the damaged surface located at the edge of an indentation impression in material SiC-S, while Fig. 6.25(b) is a higher magnification view of Fig. 6.25(a) illustrating a typical trajectory of the indentation induced crack. As can be seen, the

advancing crack tip propagates through the SiC grains with no sign of deflection or bridging, resulting in a low fracture toughness of these materials (Table 6.2).
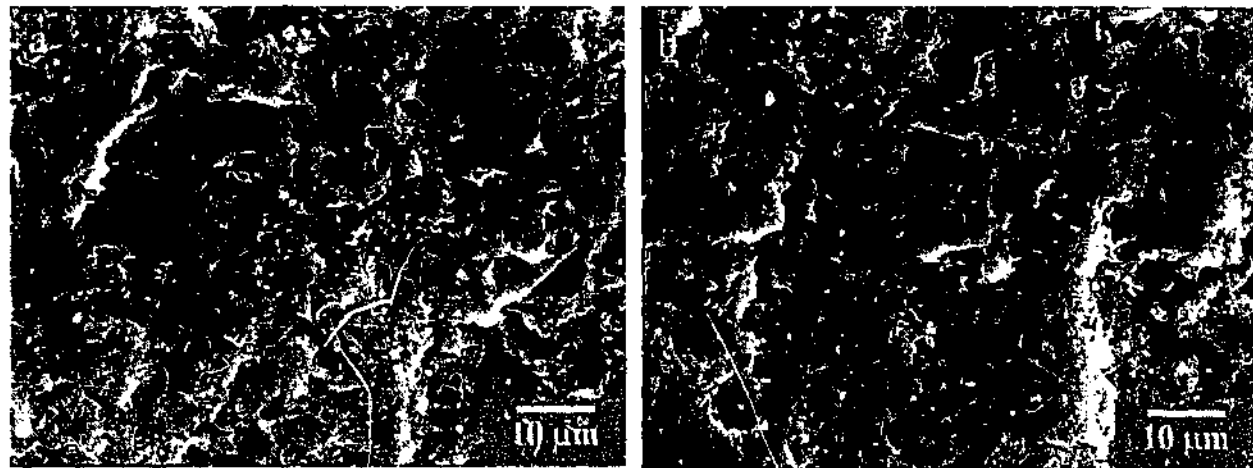
Fig. 6.24. Steady state erosion surfaces of material SiC-S following SiC erosion at (a) 30° impact, and (b) 90° impact. Note: the particle impact direction for 30° impact is from top to bottom of the micrographs.
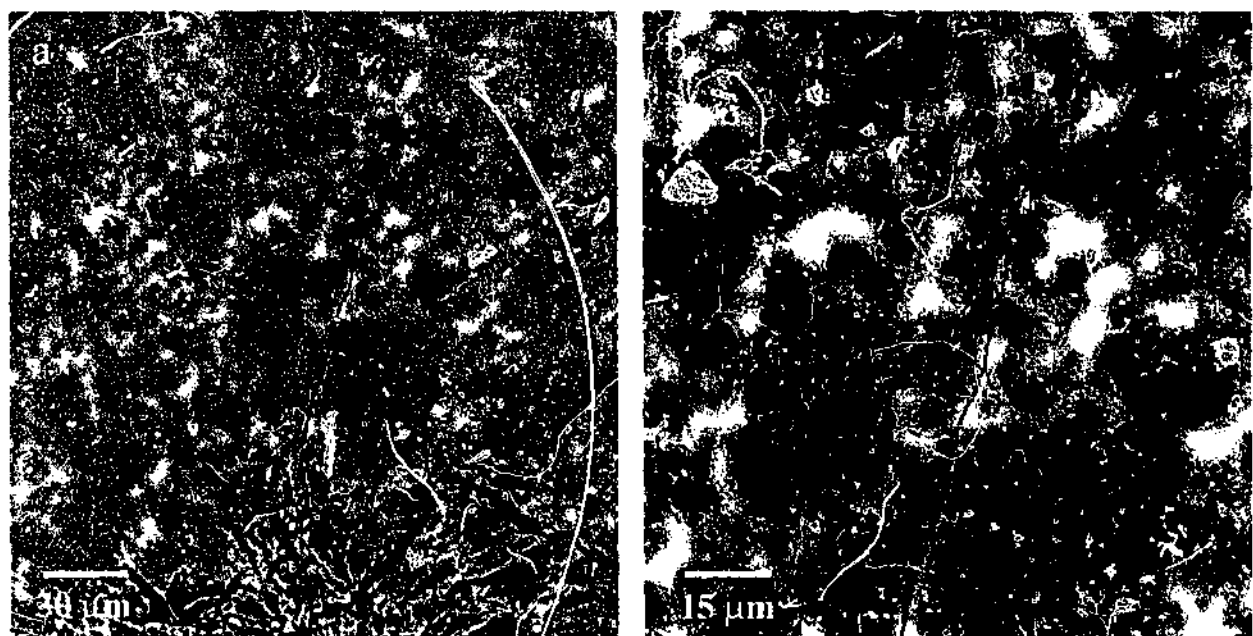
Fig. 6.25. SEM observations of (a) indentation induced damage, and (b) interaction between a propagating crack and SiC grains of material SiC-S. Note: images are taken using BSE mode.

6.5.4.2 Mechanisms of material removal

From the above discussion, it can be concluded that the erosion mechanism in SiSiC materials apparently involves the linking up of lateral cracks, dislodgment of the fine SiC grains, occasional small-scale transgranular fracture of the fine, elongated β-SiC grains, and plastic smearing of the free Si phase and fine debris. The dominant mechanisms of material removal are, however, conchoidal fracture within individual large SiC grains and dislodgment of the fine-grained SiC particles in the two-phase region.

Despite the considerable differences in microstructure of the two SiSiC materials, e.g. the size and volume fraction of the bimodal SiC grains as well as the amount of the free Si phase (Table 6.1 and Fig. 6.4), the erosion rates of the two materials vary by less than 10% for both 30° and 90° impacts (Figs. 6.7 and 6.8). The lack of a microstructural effect on erosion rate under the current experimental conditions suggests that although there exists a distinct difference in mechanisms of material removal between the large SiC grains and the two-phase regions, the actual rate of material removal may be very similar. Indeed, SEM observations of the eroded surfaces showed an uniform type of surface morphology; there is no noticeable preferential wear of particular regions (Figs. 6.23 and 6.24).

A previous study reported in the literature showed that pure Si erodes much faster, by approximately two orders of magnitude, than single-phase SiC (Routbort et al. 1980b). However, preferential erosion of the two-phase SiC-Si region was not observed in the current investigation. This can be attributed in part to the fact that the fine SiC particles and the newly reacted elongated β-SiC grains act as reinforcement to the residual silicon phase, which has effectively improved the erosion resistance of the two-phase regions, and in part to the severity of the SiC erosion which can effectively cause lateral chipping of the large SiC grains. In fact, previous studies of erosion of SiSiC materials using fine Al_2O_3 erodent particles (Routbort et al. 1980b) and coal slurry (Shetty et al. 1982) have observed the preferential erosion of the two-phase region resulting in a surface morphology exhibiting mesa-like protrusions of the large SiC grains. This is because both Al_2O_3 and coal are much softer than SiC

and therefore are not capable of causing significant fragmentation of the large SiC grains. As a result, the two-phase SiC-Si region between the large SiC grains erodes relatively fast, leaving the flat-topped mesa-like protrusions of the large grains separated by valleys of the two-phase region (Routbort et al. 1980b).

Finally, no clear evidence of dislodgment of the large SiC grains was revealed in the two SiSiC materials under the current experimental conditions, suggesting strong bonding exists between the large SiC grains and the mixed SiC-Si phase. This scenario is further supported by SEM observations of the interaction between a propagating crack and SiC grains of these materials, where the advancing crack tip cuts through the large SiC grains with no sign of deflection or bridging (Fig. 6.25(b)).

6.6 Erosion Performance of Engineering Ceramics

6.6.1 Erosion response

The Ca α-sialon and silicon nitride ceramics in the current study best illustrate the effect of microstructural features, such as grain size, grain morphology and grain boundary glass, on the erosion response of ceramic materials. The present results showed that materials consisting of randomly oriented, elongated grains coupled with a small amount of intergranular glass, i.e. CA2613, CA2613C and SN-F, exhibited the best erosion resistance. This is mainly due to the fact that the elongated grain morphology gives rise to a better resistance to crack propagation/networking and has an interlocking effect that prevents material removal via grain dislodgment. On the other hand, an optimum amount of grain boundary glass can also improve the erosion resistance of ceramic materials by absorbing the impact stress via viscous flow as well as by enhancing the bonding strength between the grains and the matrix. The effect of intergranular glass on bonding strength is particularly significant in α-sialon ceramics since both intergranular glass and α-sialon grains contain identical elements.

Despite the fact that material CA2613 displayed a higher porosity (Table 6.1) and lower hardness and fracture toughness (Table 6.2) in comparison to sample SN-F, the erosion rates of the two materials were very similar (Figs. 6.7 and 6.8). This is because the microstructures of the two materials are very similar, both consisting of fine, randomly oriented, elongated grains, leading to a similar erosion mode and thus a similar erosion rate. SEM observations of the worn surfaces revealed a combined intergranular and transgranular modes of fracture in both materials ((Figs. 5.13(a) and (b) and 6.18).

The highly directional whisker-reinforced silicon nitride material, SN-C, showed a lower erosion resistance than the finer grained self-reinforced silicon nitride material, SN-F, and the Ca α-sialon material, CA2613. This can be attributed to substantial pullout of the reinforcing whiskers during the erosion of material SN-C (Figs. 6.19 and 6.20) in comparison to erosion of materials SN-F (Fig. 6.18) and CA2613 (Figs. 5.13(a) and (b)). The significant pullout of the whiskers is a direct consequence of the highly directional orientation of the whiskers, which is practically parallel to the erosion surface, and a weak interface between the whiskers and the matrix.

As discussed in Chapter 5, the equiaxed sialon materials, i.e. CA1005, CA1005F and CA1005C, displayed a predominantly intergranular mode of fracture (Figs. 5.12(c) and (f), 5.15(a) and 5.16), associated with a relatively high erosion rate compared to composition CA2613 (Figs. 5.5 and 5.7). This is because composition CA1005 contains a very small amount of intergranular glass (Table 4.4), leading to higher porosity and consequently a weak grain boundary in these materials (Table 4.5). The weak grain boundary promotes grain boundary cracking under the external stress. In addition, the almost equiaxed grain morphology of these materials has little resistance to grain dislodgment. As a result, the dominant erosion mechanism of composition CA1005 is grain ejection.

The grain dislodgment mechanism becomes more pronounced in erosion of high-purity alumina material (Figs. 6.14(b) and (d)). As in most liquid-phase sintered ceramics, the weakening of the grain boundaries in alumina is partly due to the segregation of the sintering additives and other defects, such as pores, at the grain

boundaries. More significantly, the anisotropy of thermal expansion and elastic properties of the hexagonal alumina grains can further weaken the grain boundaries. In silicon nitride and sialon ceramics, which also have a hexagonal structure, the difference in thermal expansion coefficient between the two crystal axes is very small. For example, in β-Si_3N_4, the thermal expansion coefficients are 3.2×10^{-6} °C^{-1} and 3.3×10^{-6} °C^{-1} for the directions perpendicular and parallel to the c-axis, respectively (Wada and Watanabe 1987a). In contrast, in alumina ceramics, the values are 8.3×10^{-6} °C^{-1} and 9.0×10^{-6} °C^{-1} for the directions perpendicular and parallel to the c-axis, respectively (Wada and Watanabe 1987a). The highly anisotropic thermal contraction of the hexagonal alumina grains upon cooling from the sintering temperature produces a residual tensile stress at the grain boundaries, which contributes to extensive grain boundary failure during erosion, leading to severe grain dislodgment and a high material removal rate.

Although the two SiSiC materials, namely SiC-S and SiC-C, show sharp edged worn surfaces as did the high-purity alumina ceramic, the surface of SiSiC is characterized by combined lateral chipping of the large SiC grains and grain dislodgment in the SiC-Si two-phase region, while the surface of alumina is dominated by grain ejection. In the SiSiC materials, the average size of the large SiC grains (Table 6.1) is greater than that of the impact crater (Fig. 5.8). Fig. 6.26 schematically shows the possible impact situations in these materials: particles impact the large SiC grains (A), the two-phase region (B) and the composite of large SiC grains and two-phase region (C).
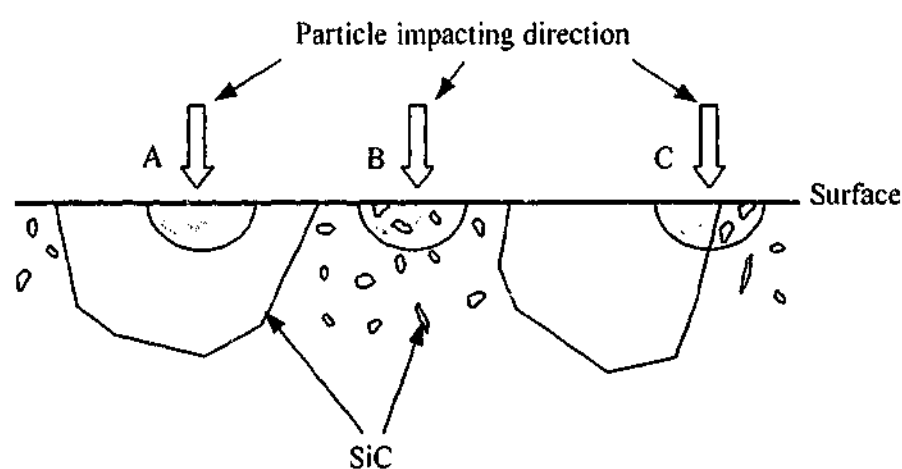
Fig. 6.26. Schematic illustration of various impact situations discussed in the text.

It is well established that the strain energy associated with imposed stresses in a material can be relieved by either plastic flow or fracture (Ajayi and Ludema 1991). Which of the two processes dominates is largely dependent on the stress level needed to initiate each of these processes. In scenario A, the high hardness and brittleness of the SiC grains has made them resistant to plastic deformation and vulnerable to brittle fracture. Upon impact, the fracture path occurs in the trajectory of the maximum tensile stress and the fracture mode is transgranular, leading to lateral chipping. In scenario B, the relatively softer Si phase and weaker grain boundaries have to some degree promoted plastic smearing of the Si phase and grain boundary cracking, resulting in dislodgment of the fine SiC grains in the two-phase region (Figs. 6.23, 6.24 and 6.25). In scenario C, a combined fracture mode is expected.

The relatively low erosion resistance of the two SiSiC materials in comparison to silicon nitride and sialon ceramics is due in part to the lateral chipping of the large SiC grains and in part to the relatively low erosion resistance of the soft Si phase. Lateral cracking, as discussed in section 5.7.3, is the most potent agent of material removal in erosive wear, while a previous study has shown that pure silicon erodes approximately 200 times faster than single-phase SiC (Routbort et al. 1980b).

The present results clearly demonstrate that the grain size of ceramic materials has a significant effect on the fracture mode in response to solid particle erosion. In the coarse-grained material, i.e. the grain size is larger than the impact crater, the fracture mode is transgranular. On the other hand, in the fine-grained material, especially when the grain boundary is relatively weak and the grain morphology is approximately equiaxed, the fracture mode is mainly intergranular.

6.6.2 Energy balance approach

The current investigation has indicated that the most pronounced damage mechanism in polycrystalline ceramics, when subjected to solid particle erosion, is brittle fracture. Evidence of plastic flow was also observed. It is believed that the impacting particle produces plastic flow at the contact zone which is surrounded by crack

networks. This network-like cracking can be either intergranular or transgranular in nature, depending on the grain size, grain morphology, and grain boundary bonding strength.

The above process can be better understood using the energy dissipation/energy balance approach where the kinetic energy of the impacting particle is in part transferred to the target material and in part dissipated as residual energy in the form of particle rebounding and fragmentation. The total energy absorbed by the target during impact can be expressed in terms of the plastic deformation energy and stress wave energy (Zeng and Kim 1996a). The plastic deformation energy is dissipated in plastic work converted into heat and stored energy in the form of residual strain (Zeng and Kim 1996a and 1996b). The stress wave energy is transmitted through the target material and is dissipated by fracture and internal friction (Zeng and Kim 1996a and 1996b).

As discussed earlier, in erosion of ceramic materials, the most influential process of material removal is brittle fracture resulting from crack networking. Assuming all the stress wave energy, W, is converted into fracture energy, E_f, and the fracture energy required for the formation of the crack network can be expressed as:

$$E_f = 2A_f \gamma \tag{6.2}$$

where $2A_f$ is the total surface area of the crack network and γ is the fracture energy per unit area (Zeng and Kim 1996b).

The propagation of stress waves in an isotropic elastic half space due to a point load was investigated by Lamb (1904), Miller and Pursey (1954 and 1956), Hunter (1957) and Hutchings (1959). One possible form of the stress wave transmission is a circular disc of finite radius vibrating normal to the free surface (Miller and Pursey 1954 and 1956). Thus, the relationship between the fracture surface, $2A_f$, and the fracture volume, V_f, can be expressed as:

$$2A_f = k V_f \tag{6.3}$$

where k is a geometric factor.

By substituting eq. 6.3 into eq. 6.2, the fracture volume, V_f, can be related to the stress wave energy, W, by:

$$V_f = W / (k\,\gamma) \qquad\qquad (6.4)$$

Therefore, for a fixed amount of stress wave energy, W, the higher the fracture energy per unit area, γ, the smaller the fracture volume, V_f, leading to a lower material removal rate.

The two Ca α-sialon materials CA2613F and CA2613C best illustrate the effect of grain morphology on fracture energy of these materials. SEM observations of the eroded surfaces revealed ample evidence of grain boundary microcracking (Fig 5.17), indicating that microcracks are preferentially initiated and propagated along the grain boundaries. However, the randomly oriented elongated grains in material CA2613C can deflect and bridge the cracks by blocking their paths and forcing them to detour. On the other hand, the fine, low aspect ratioed grains in material CA2613F offer little toughening mechanism such as crack bridging and deflection. Therefore, more fracture energy is required to form crack networks in material CA2613C than material CA2613F.

In addition, the subsequent impacts can readily detach the highly fractured volume in material CA2613F, as shown schematically in Fig. 6.27, resulting in macroscopic lateral chipping. In contrast, the dislodgment of the fracture volume in material CA2613C is to some degree more difficult due to the interlocking effect of the large elongated grains (Fig. 6.28). Again, more energy is required to remove the fractured zone in material CA2613C than material CA2613F. Therefore, under the same erosion conditions, materials containing interlocked elongated grains exhibit higher fracture energy associated with a smaller fracture volume, leading to a lower material removal rate in comparison to materials consisting of an equiaxed grain morphology.
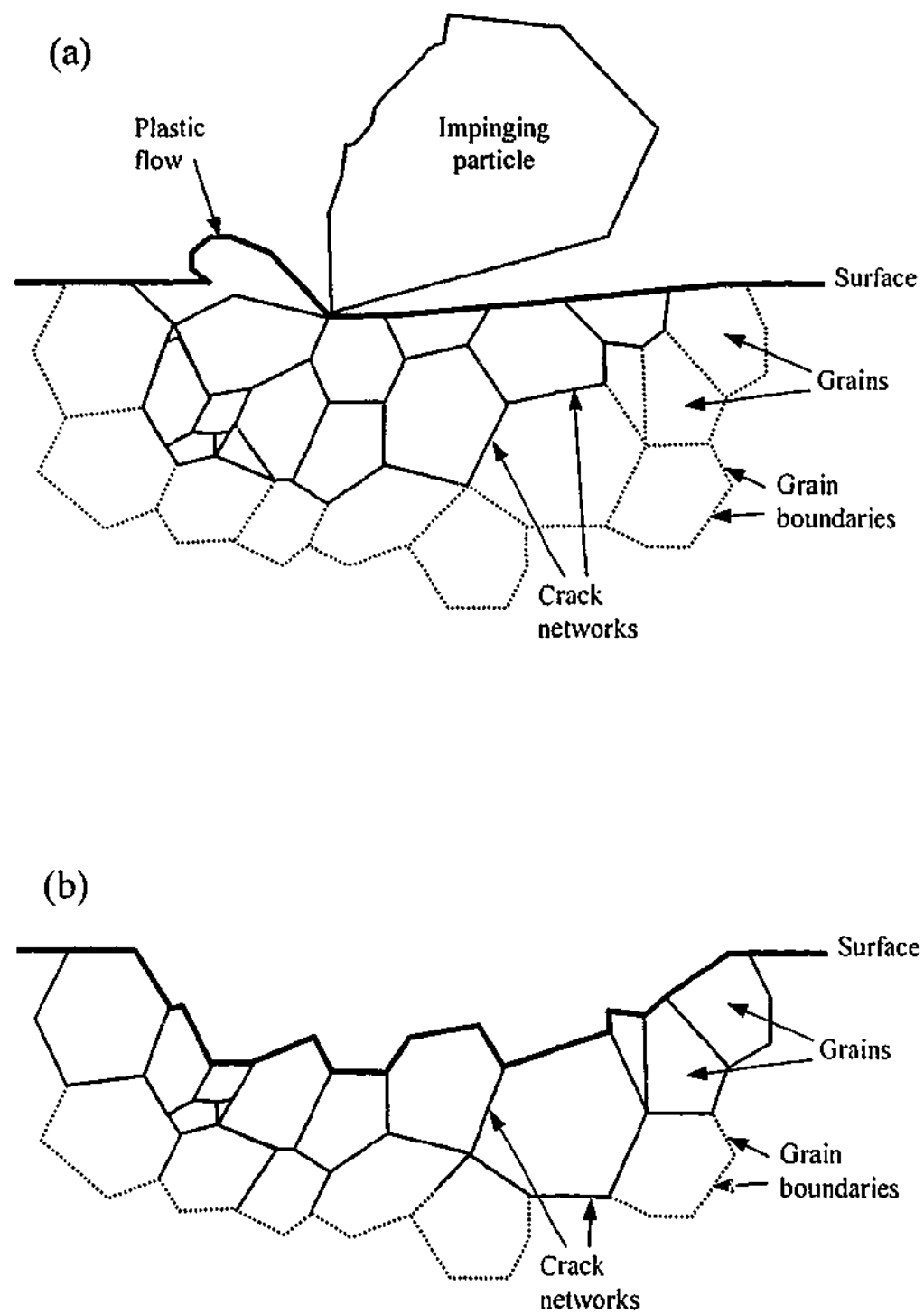
Fig. 6.27. Schematic illustration of the material removal process of a target material containing equiaxed grain morphology. Note: material removal is mainly due to the dislodgment of the equiaxed grains.
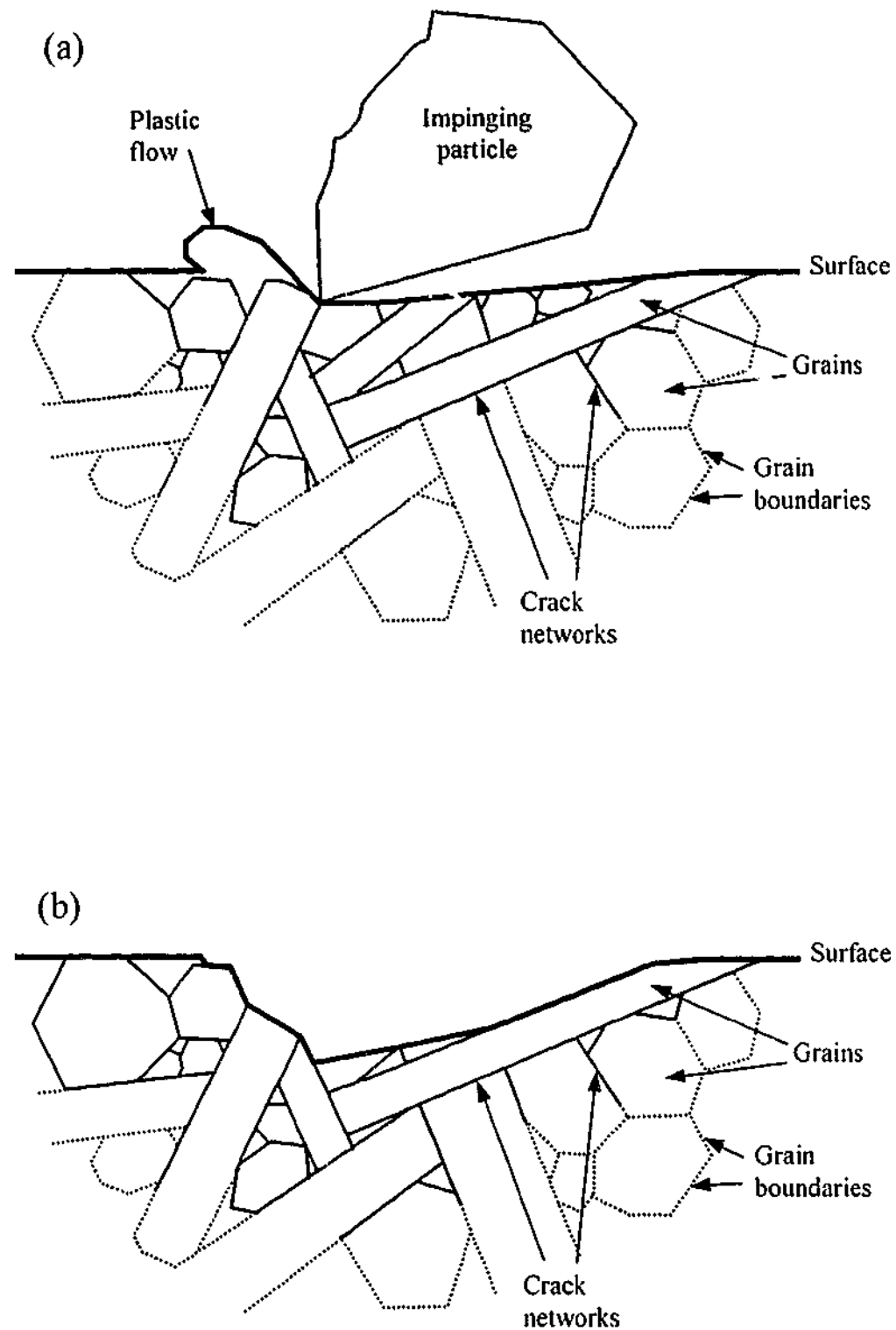
Fig. 6.28. Schematic illustration of the material removal process of a target material containing interlocked elongated grain morphology. Note: material removal is achieved by combined intergranular fracture of the equiaxed grains and transgranular fracture of the interlocked elongated grains.

Finally, when the average grain size of the target material is greater than the impact crater, as shown in scenario A of Fig. 6.26, the impact damage is confined to the single crystal grains. In single crystals, fracture energy approaches the surface free energy, and the fracture surface energy, γ_{IC}, is related to the fracture toughness, K_{IC}, and Young's modulus, E, of the material by (Becher 1991):

$$\gamma_{IC} = K^2_{IC} / 2E \qquad\qquad (6.5)$$

Single crystal ceramics generally have extremely low fracture toughness, e.g. 0.5-2 MPa m$^{1/2}$ (Kelly and Macmillan 1986), due to the absence of toughening mechanisms, and high modulus owing to strong covalent bonding. This is particularly the case for SiC. Therefore the fracture energy of the single crystal SiC grains is very low. Upon impact, the low fracture energy results in a large fracture volume, leading to a high material removal rate.

6.6.3 Effect of erodent properties

It is clear that the properties of the erodent particles, particularly their hardness, have a profound influence on erosion rates. In all materials, the erosion rate increased as the hardness of the erodent particles increased. This is consistent with the well-recognized effect of target-particle hardness ratio, H_t/H_p, in erosion of ceramics, where the severity of erosion damage increases as the hardness ratio decreases (Gulden 1979 and 1981b; Wada and Watanabe 1987b; Wada 1992; Shipway and Hutchings 1996).

The garnet erodent is softer than most of the target materials investigated in this study, except for zirconia. As discussed in section 5.6, when the *softer* erodent particles impinge on the *harder* target surface, they undergo severe deformation and fragmentation, resulting in less energy transferred to the target surface and thus low efficiency of erosion. Therefore, the material removal rate is much lower for erosion using the soft garnet particles compared to the hard SiC grits.

Significant differences were also found in erosion response among various ceramic materials when different erodent particles were used (Fig. 6.8 vs Fig. 6.13). For

example, in erosion of alumina ceramic, the erosion rate increased by a factor of 1.6 and 4.4 for 90° and 30° impacts, respectively, when the erodent particles changed from garnet to SiC. However, the corresponding margins were increased to a factor of 4.5 and 9 for zirconia, and to a factor of over 50 and two orders of magnitude for materials CA1005 and CA3618, respectively.

As noted earlier, the low erosion efficiency using soft erodent particles compared to hard particles is mainly due to the deformation and fragmentation of the soft particles leading to less energy being transferred to the target material. However, this effect is not significant in erosion of high-purity alumina ceramics, since these materials possess exceptionally weak grain boundaries owing to the anisotropy of thermal expansion and elastic properties of non-cubic alumina grains. Thus, less fracture energy is required to produce grain boundary crack networks. As a result, the difference in material removal rate between erosion using the soft garnet particles and the hard SiC grits is relatively small, being a factor of 1.6 and 4.4 for 90° and 30° impacts, respectively.

In the case of erosion of zirconia ceramics, although garnet particles are much softer than SiC grits, they are still harder than the zirconias (Tables 3.3 and 6.2). Hence, erosion using garnet erodent can still result in material removal from the zirconia surface by cutting and scooping mechanisms, although the efficiency is lower for garnet erosion than SiC erosion owing to the fact that garnet particles deform and fragment more easily in comparison to SiC grits.

The effect of erodent properties on erosion rate becomes more significant in erosion of Ca α-sialon ceramics, especially for compositions comprised of interlocked elongated grains (Table 5.2). As discussed in Chapter 5, though grain boundary microcracking is still the dominant fracture mode in erosion of sialon ceramics composed of elongated grains, more fracture energy is required to form crack networks in these materials compared to the equiaxed microstructure, due to toughening mechanisms such as crack bridging and deflection. In addition, the removal of the fracture volume again requires more energy for materials with an elongated microstructure than an equiaxed one owing to the interlocking effect of the

elongated grains. Garnet erosion is much less effective than SiC erosion, therefore more impacts are required to accumulate the equivalent fracture energy to that produced by SiC erosion. Finally, garnet particles are much softer than sialon ceramics (Tables 3.3 and 4.5), which effectively suppresses material removal by a chipping process.

6.7 Summary

Erosion studies were carried out on five major engineering ceramics, namely alumina, zirconia, silicon nitrides, sialons, and silicon carbides. In terms of material loss, the Ca α-sialon ceramics are the most erosion resistant materials, while the high-purity alumina is the worst. The two types of self-reinforced silicon nitride materials have better erosion resistance than the MgO partially stabilized zirconia and the two SiSiC materials. It was found that mechanical properties were not the only factor that governed the erosion performance of ceramic materials. In fact, microstructure was found to have a very strong influence on the mechanism and rate of material removal in these materials. The following conclusions can be drawn from the results of this study:

- Ceramics with a very coarse-grained microstructure, i.e. those with grain size larger than the impact crater, exhibit poor erosion resistance under harsh erosion conditions due to the low fracture energy of the single crystal relative to that of polycrystalline materials, leading to large lateral chipping.

- Ceramics with randomly oriented elongated microstructures appear to be favored in applications requiring erosive wear.

- The effect of microstructure on erosion of ceramic materials can be explained using an energy balance approach. Materials with higher fracture energy, in general, exhibit a better erosion resistance. However, the fracture energy described here involves stress in various directions, a case which can not be solely described by K_{IC} which is for the Mode I fracture condition.

- Garnet particles are less efficient in erosion of ceramic materials compared to SiC grits. This is mainly due to the relatively low hardness of garnet erodent in comparison to most ceramic materials, which results in significant deformation and fragmentation of the garnet particles, leading to less energy transferred to the target surface. However, garnet particles are more representative of the type of erodent particles found in practical situations such as mining, and hence more relevant than the very hard SiC grits.

- Different ceramic materials had different responses to erosion by garnet and by SiC. The microstructure of these ceramics was found to have a strong influence on this behaviour.

Chapter 7

EROSION OF ALUMINA CERAMICS BY AIR AND WATER SUSPENDED GARNET PARTICLES

7.1 Introduction

Chapter 6 compared the erosion behaviour of a number of engineering ceramics. It was found that α-sialon ceramic possessed the best erosion resistance, while alumina showed the worst. However, among the engineering ceramics, alumina and alumina-based ceramics are probably the most commonly used materials in applications requiring wear resistance (Esposito and Tucci 1997). Therefore, the erosion behaviour of alumina and alumina-based ceramics has been extensively studied over the past years and was found to be influenced by several parameters such as the properties of the erodent materials (Murugesh and Scattergood 1991; Shipway and Hutchings 1996), fluid flow conditions (Finnie 1995; Oka et al. 1997) and the properties of the target alumina materials (Wiederhorn and Hockey 1983; Ritter et al. 1984; Lathabai and Pender 1995).

Most previous studies on solid particle erosion have been conducted using silicon carbide, alumina or rounded silica particles as the erodent materials. These are either harder or smoother than the particles most commonly encountered in practical situations such as mining which tend to be silica-based, irregular in shape and typically have a Vickers hardness value of 8~12 GPa (Shipway and Hutchings 1991).

More significantly, much of the work reported in the literature on solid particle erosion tends to concentrate on airborne erosion and there is much less work reported on slurry erosion of ceramics. Compared to airborne erosion, slurry erosion is further

complicated by the presence of water which is known to have a deleterious effect on crack propagation in ceramics (Lawn 1993; Lathabai and Pender 1995) and by the influence of the carrier fluid viscosity on particle trajectories (Levy et al. 1987; Clark 1995) and possible lubrication effects (Levy and Hickey 1987). Therefore, there is a need to establish a better understanding of the response of ceramics to slurry erosion.

Furthermore, alumina ceramics, in general, have complicated microstructures and there exists a close relationship between the microstructure and the mechanical properties of these materials. However, there is not yet a common model which accounts for the effects of the complex microstructure on wear performance of alumina ceramics.

The objectives of this investigation are:

(1) To study the role of microstructure on the erosion behaviour of alumina ceramics.

(2) To clarify the mechanisms by which garnet erodent removes target alumna material.

(3) To provide a comparison between airborne and slurry jet erosion behaviours of alumina materials.

7.2 Experiments

7.2.1 Materials

The target materials in this investigation were commercial alumina ceramics AD998 and AD92 (supplied by Ceramic Oxide Fabricators and Norton Pakco Industrial Ceramics, respectively). AD998 was a high purity material with an alumina content of 99.8 wt% and was supplied with two different grain sizes, the fine grained AD998-F, and the coarse grained AD998-C. AD92 contained 92 wt% aluminium oxide with the balance consisting of a small amount of $MgAl_2O_4$ (spinel) and grain boundary silicate glassy material. All the target materials displayed a bimodal distribution of grain sizes (Figs. 7.1(a)-(c)). The average grain size of each material was measured using the lineal intercept technique (Wurst and Nelson 1972). AD998-F and AD998-C had average grain sizes of 3.1 μm and 12.7 μm, respectively, although each

contained some grains as large as 15 μm and 50 μm, respectively. Similarly, AD92 had an average grain size of 7.5 μm with some coarse grains as large as 40 μm.
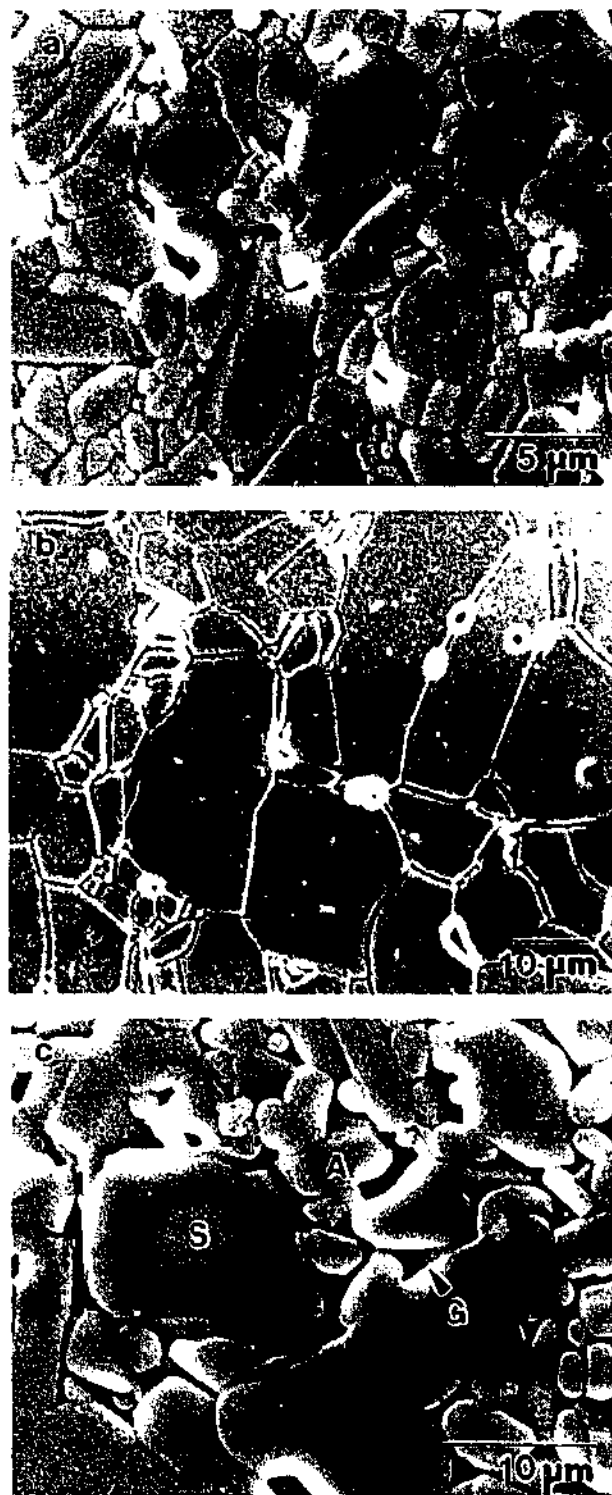

Fig. 7.1. SEM micrographs of polished and thermally etched surfaces of alumina samples: (a) AD998-F, (b) AD998-C, and (c) AD92. Note: in (c) the presence in sample AD92, of a spinel grain (S) surrounded by alumina grains, one of which is identified by 'A' and an intergranular glassy phase (G).

The erodent particles used were commercial grade garnet abrasive grits (supplied by Australian Mining). The garnet grits were angular in shape (although the corners were slightly rounded) and had a size range between 200-600 μm (Fig. 3.1(a)). Particle size distribution analysis by a laser diffraction technique showed that the median diameter, d_{50}, of the erodent particles was ~400 μm.

The chemical compositions and the mechanical properties of the erodent particles and the target materials are shown in Tables 7.1 and 7.2, respectively. The specific density of the erodent particles was determined using an AccuPyc 1330 Micromeritics densitometer. The bulk density of the target materials was determined using the boiling water method, while the true density of these materials was measured on finely powdered samples using the Micromeritics densitometer. The total porosity of each target material was calculated from its respective bulk density and true density. It is important to note that the density values of the two grades of AD998, though of high purity, are only 96% of their true densities, due to the presence of large flaws and poorly sintered agglomerates in the microstructure. Material AD92 shows a lower absolute density value because of the presence of low density spinel and grain boundary glassy materials. However, its porosity content is lower than those of the AD998 materials.

The hardness and, where possible, the fracture toughness of the target and erodent materials were determined by micro-indentation tests at a load of 0.98 N. The phase compositions of the target materials were examined using X-ray diffraction (XRD). The XRD analysis revealed the presence of α-Al_2O_3 (corundum) alone in samples AD998-F and AD998-C, and the presence of α-Al_2O_3 and $MgAl_2O_4$ in sample AD92. SEM examinations of polished and thermally etched samples of AD92 confirmed the presence of α-Al_2O_3 grains, spinel grains and glassy material distributed at grain boundaries and triple points in this material (Fig. 7.1(c)). Thermal etching was carried out in air at temperatures 50°C lower than the sintering temperature of individual alumina materials. The heating and cooling rates were 500°C/h. The volume fraction of the intergranular glassy phase was estimated using image analysis to be approximately 6%.

Table 7.1 Properties of garnet erodent

Property	Range
Chemical Composition[a] (wt%)	36 SiO_2, 30 FeO, 20 Al_2O_3, 6 MgO, 2 Fe_2O_3, 1 MnO, 1 CaO, and 1 Ti O_2
Specific Density (kg/m^3)	4100
Hardness[b] (GPa)	13.8
Toughness[b] (MPa m$^{1/2}$)	1.10
Melting Point[a] (°C)	1250
Particle Size, d_{50} (μm)	400

[a] Manufacturer's data sheet.

[b] Measured by Vickers Indentation at 0.98 N load.

Table 7.2 Properties of target materials

Property	AD998-F	AD998-C	AD92
Chemical Composition[a]	99.8 wt% Al_2O_3, 0.2 wt% (Na_2O+SiO_2+MgO)	99.8 wt% Al_2O_3, 0.2 wt% (Na_2O+SiO_2+MgO)	92 wt% Al_2O_3, 8 wt% ($MgAl_2O_4$+silicate glass)
Mean Grain Size (μm)	3.1	12.7	7.5
True Density (kg/m^3)	3899	3883	3609
Bulk Density (kg/m^3)	3740	3740	3560
Total Porosity (%)	~4.1	~3.7	~1.4
Hardness[b] (GPa)	17.2	17.2	13.4
Toughness[b] (MPa m$^{1/2}$)	–	–	2.75

[a] Manufacturer's data sheet.

[b] Measured by Vickers Indentation at 0.98 N load.

7.2.2 Erosion measurements

7.2.2.1 Airborne erosion test

Airborne erosion tests were performed using the gas-blast type erosion test rig described in section 3.3.2.1. The erodent particles were entrained in a stream of compressed air and accelerated through a 125 mm long, 5.4 mm inner diameter steel nozzle to impact on the stationary target. The particle velocity was controlled by means of the compressed air pressure and measured using the rotating double disk technique (Ruff and Ives 1975).

Airborne erosion tests were carried out on all three alumina materials as well as on mild steel which served as the control material. The dimensions of the specimens were $20 \times 20 \times 3$ mm^3 (AD998-F and AD998-C), $20 \times 20 \times 6$ mm^3 (AD92) and $20 \times 50 \times 1$ mm^3 (mild steel). In all tests, the specimens were located 13.8 mm from the nozzle orifice for all impingement angles. The impact angles used were 15°, 30°, 45°, 60° and 90° for AD998-C and AD92, and 30°, 60° and 90° for AD998-F.

Each sample was eroded with a fixed amount of erodent at a velocity of 37 m/s in six exposures. For shallow impact angles (15°, 30° and 45°), the dose of erodent particles for each exposure was 200 g, while for higher angles (60° and 90°), this was reduced to 100 g. Mass loss was measured using an analytical balance with an accuracy of ±0.1 mg. As discussed in section 5.2.3, the dosage selected for the shallow angles of impact allowed a sufficient mass loss to occur, which could be detected by the weighing balance. However, using the same dosage for the higher angles of impact resulted in deep erosion craters which would effectively change the test conditions, specifically, the nozzle-sample distance and the impact angle. Hence, a lower dose was used in these cases.

As described in section 3.3.2.3, wear volume was calculated from the mass loss and the bulk density of each material. Cumulative volume loss was plotted as a function of the amount of erodent impacting on the surface. It was observed that for all impact angles, the cumulative volume loss increased linearly with the amount of erodent after an incubation period. The steady state airborne erosion rate (ΔE_A), defined as the

volume loss from the specimen per unit mass of erodent used, was determined from the slope of the linear part of the volume loss-mass of erodent plot.

In order to directly compare the erosion rate between the dry and wet erosions, airborne erosion test was also carried out at 20 m/s at 30° impact angle for material AD998-C. As will be shown in section 7.2.2.2, the maximum velocity of the slurry erosion tests carried out in the present study was 20.5 m/s. However, due to the design of the present dry erosion apparatus (section 3.3.2.1), the flux of the erodent beam varies with the velocity of the air stream and can not be independently controlled. At an erodent velocity of 20 m/s, the beam flux was estimated to be 100 kg/m^2s, which is significantly lower than that of the slurry jet erosion at a comparable impact velocity. According to eqs. 3.8 and 3.9, the estimated beam flux of a slurry jet travelling at 20.5 m/s would be 1500 kg/m^2s.

7.2.2.2 Slurry erosion test

Slurry erosion tests were carried out with a custom designed slurry jet apparatus, the details of which were described in section 3.3.3.1. Briefly, the equipment utilised a slurry holding tank, an agitator, a diaphragm pump, compressed air, an ejector nozzle (inner diameter of 4 mm), and a sample holder. The slurry, a mixture of tap water and garnet grits, was pumped from the holding tank to the ejector nozzle through which it emerged as a high velocity jet to strike the target surface. The loading of solids and the velocity of this slurry stream were varied by adjusting the agitator speed and the compressed air pressure, respectively. The angle of impingement was varied by tilting the specimen holder via a mechanical lever.

The major variables examined were angle of impingement, particle loading (i.e. mass fraction of erodent particles in the slurry) and velocity of the slurry jet. The specimens, with the same dimensions as described in the airborne tests, were mounted directly under the ejector nozzle, approximately 13.8 mm below the nozzle exit, for all tests. The effect of the angle of impact was determined for AD998-C, AD92 and mild steel control at 15°, 30°, 45°, 60°, 75° and 90°. In this series of tests, the particle loading was held at 7.7 wt% and the slurry velocity was 16.5 m/s. The

207

effect of slurry velocity was determined for a fixed particle loading at an angle of impact of 30°. The velocities tested were 12.7 m/s, 14.5 m/s, 16.5 m/s, 18.6 m/s, and 20.5 m/s. The effect of particle loading was measured at a fixed slurry velocity of 16.5 m/s, again at a fixed angle of impact, 30°. The different particle loadings used were 3.1 wt%, 7.7 wt% and 11 wt%. Because only a limited quantity of AD998-F was available, no slurry erosion tests were carried out using this material.

Each sample was eroded with a fixed amount of erodent in five exposures. The amount of erodent used in a single exposure was controlled by timing the release of the slurry as determined by careful pre-calibration. As in the case of airborne erosion, the dosage per exposure had to be varied for the various angles of impact. For shallow impact angles (15° and 30°), the erodent dose was approximately 920 g, while for higher angles (45°, 60° and 90°), it was 480 g. The specimens were ultrasonically cleaned, oven dried at 150°C to eliminate moisture trapped in pores, and weighed before and immediately after the erosion test. As in the case of airborne erosion testing, the cumulative erosive volume loss was plotted as a function of the mass of erodent particles used. The steady state slurry erosion rate (ΔE_S) was determined as the ratio of the volume loss from the specimen to the mass of the erodent particles used, again from the slope of the linear part of the cumulative volume loss-erodent mass plot.

7.2.2.3 Characterisation of eroded surfaces

The eroded surfaces of all target materials were examined with a JEOL JSM-840A scanning electron microscope equipped with an energy dispersive X-ray (EDX) spectrometer. EDX analysis was used to obtain qualitative chemical information from the worn surfaces. Prior to examination, the specimens were ultrasonically cleaned in ethanol for 5 minutes and then sputter coated with gold or carbon to prevent charge accumulation on the samples during examination. The accelerating voltage used was 20 kV.

7.3 Results of Erosion Tests

7.3.1 Airborne erosion tests

Fig. 7.2 illustrates the dependence of the erosion rate on the impact angle for the three alumina ceramics and the mild steel eroded by airborne garnet particles at 37 m/s. As can be seen, the erosion rates of alumina ceramics increase with increasing impact angle and the maximum erosion rate occurs at 90° impact angle. For samples AD998-C and AD92, the erosion rates at 90° impact angle are approximately 4 and 5 times greater, respectively, than those at 15° incidence angle. Further, sample AD998-C shows a higher rate of material loss than samples AD998-F and AD92 at all impact angles by approximately a factor of 2 and 3, respectively. In contrast, the erosion rate of mild steel increases with increasing impact angle at low angles, with a peak rate occurring at about 45°, and slowly declines at higher angles of incidence. However, the difference between the maximum erosion rate at 45° and the minimum erosion rate which occurs at 90° is less than a factor of 2. Fig. 7.2 also reveals that mild steel has the lowest erosive volume loss in airborne erosion for all impingement angles.
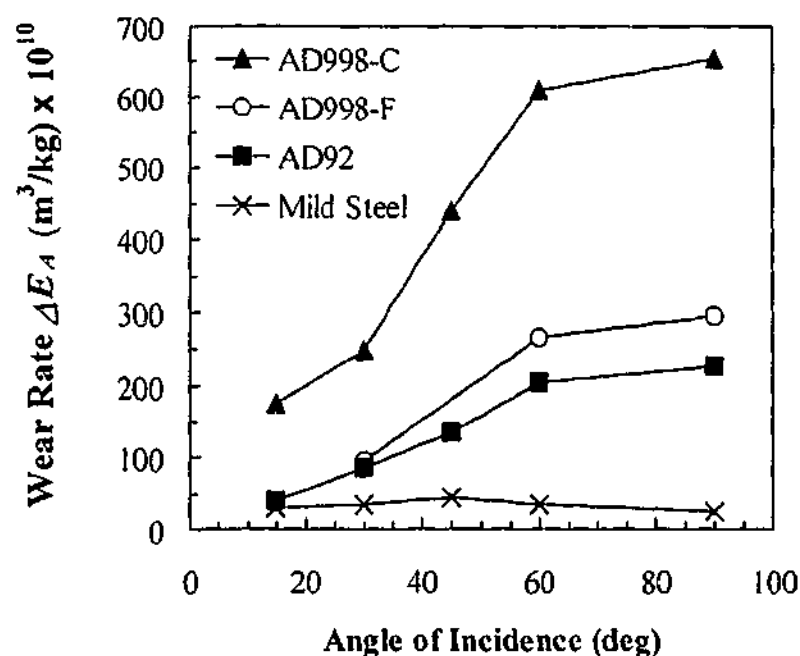
Fig. 7.2. Airborne erosion rate as a function of impact angle for three alumina ceramics and the control mild steel.

7.3.2 Slurry jet tests

Fig. 7.3 presents the dependence of the steady state slurry erosion rate on impact angle for materials AD998-C, AD92 and the mild steel, eroded by a slurry jet with 7.7 wt% solid loading at 16.5 m/s. The trends observed here are very similar to those obtained from airborne erosion (see Fig. 7.2). For alumina ceramics, the erosion rate reaches maximum at normal impact and decreases steadily as the impingement angle becomes more oblique. In addition, material AD92 shows a lower erosion rate than AD998-C at all impact angles. Again, it is interesting to note that, for materials AD998-C and AD92, the erosion rates at 15° impingement angle are almost 22 and 17 times lower, respectively, than those at normal impact. For mild steel, the peak erosion rate occurs at 60°, a higher angle than that observed in airborne erosion, and the minimum erosion rate which is approximately 4 times lower than the peak rate, occurs at 15°. Again, mild steel shows the lowest erosive loss among all test materials.
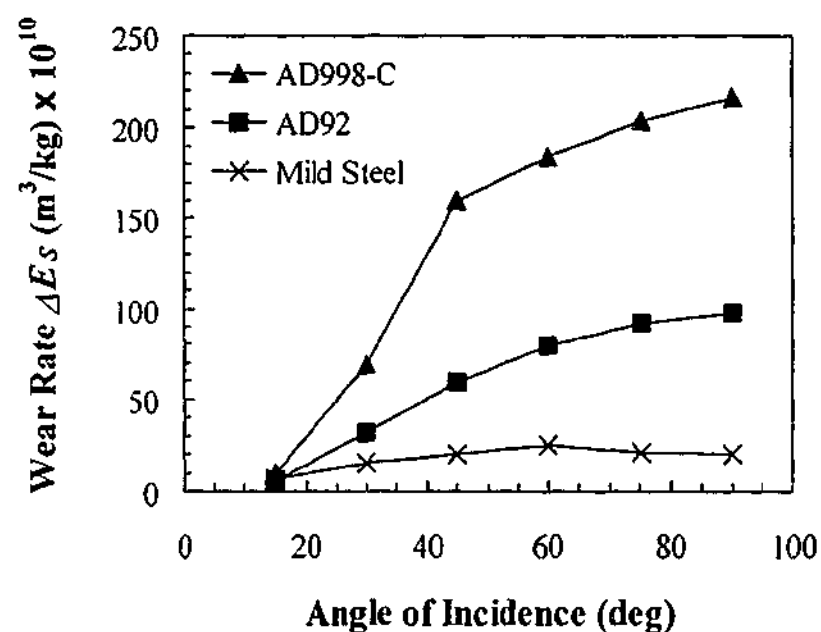
Fig. 7.3. Slurry erosion rate as a function of impact angle for materials AD998-C and AD92 and the control mild steel.

Fig. 7.4 shows the effect of particle velocity on the erosion rates of materials AD998-C and AD92, eroded by a 7.7 wt% slurry jet at 30° impact. Tests were performed at five different slurry jet velocities. In each case, the erosion rate increases with the

particle impact velocity. Regression analysis shows that a power-law provides the best empirical fit to this data. This indicates that the variation of erosion rate with particle velocity is of the form, $\Delta E_S \propto V^n$. The velocity exponent, n, is different for the different materials, being 2.8 for AD998-C and 2.1 for AD92. These values of n are similar to those reported in the literature for various ceramics for both airborne and slurry erosion (Wiederhorn and Hockey 1983; Murugesh and Scattergood 1991; Srinivasan and Scattergood 1991; Routbort and Scattergood 1992; Wada 1996).
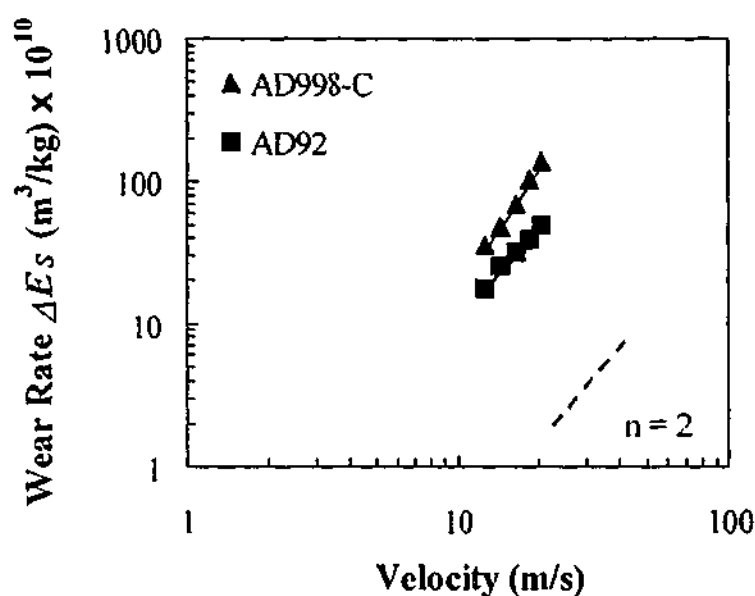
Fig. 7.4. Slurry erosion rates of materials AD998-C and AD92 as a function of particle velocity. The solid lines are power-law fits to the data, while the dash line represents where $n=2$ in equation $\Delta E_S \propto V^n$. The angle of incidence was 30°; the slurry loading was 7.7 wt%.

Fig. 7.5 presents the effect of slurry loading on the erosion rates of materials AD998-C and AD92, eroded at 16.5 m/s at 30° impact. The erosion rate is found to decrease with increasing slurry concentration. In order to facilitate comparison with data obtained using different apparatuses or from different laboratories, the data has been plotted as a function of the erodent particle flux rather than the solid concentration. The erodent beam fluxes was calculated using eqs. 3.8 and 3.9.
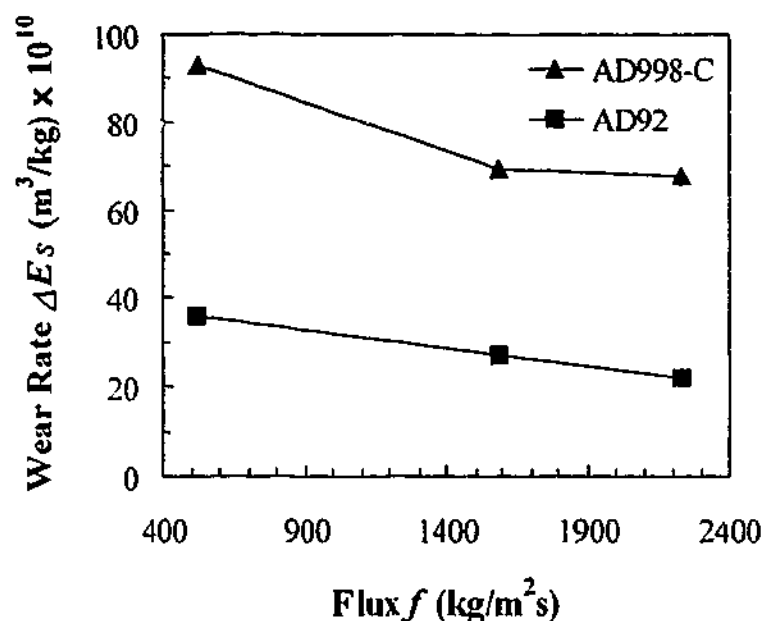
Fig. 7.5. Slurry erosion rates of materials AD998-C and AD92 as a function of particle flux.

Fig. 7.6 shows the erosion rates of material AD998-C eroded by garnet particles at 30° impact at impact velocities of 20 and 20.5 m/s for dry and wet erosions, respectively. Note that the particle fluxes are quite different between the two cases; being 100 and 1500 kg/m²s for dry and wet erosions, respectively. As can be seen the material removal rate due to slurry jet erosion is much higher than that produced by airborne erosion.
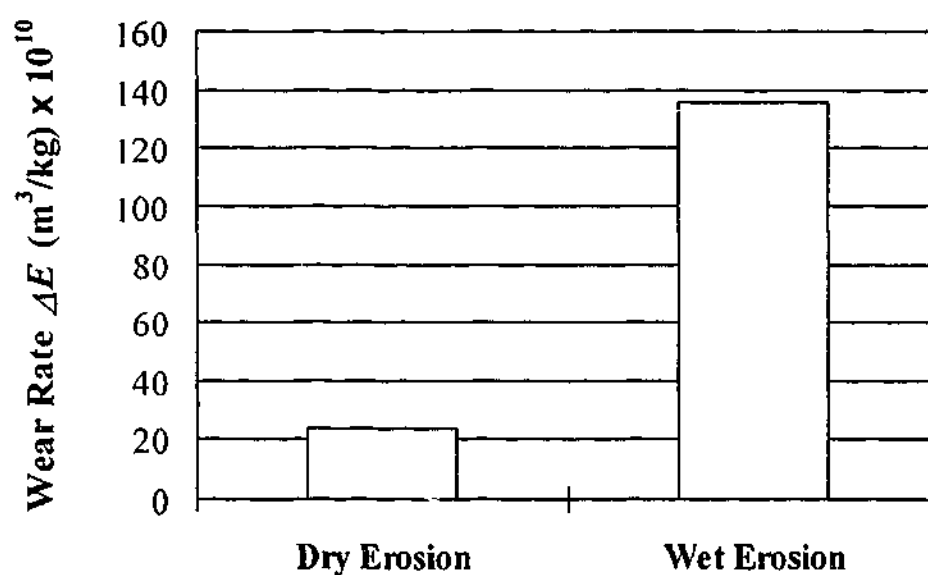
Fig. 7.6. Erosion rates of material AD998-C eroded by garnet particles at 30° impact under airborne and slurry erosions. Note: the impact velocities are 20 m/s and 20.5 m/s, for dry and wet erosions, respectively.

7.4 SEM Observations

7.4.1 Airborne eroded surfaces

The representative features of the eroded surfaces of all three alumina ceramics after airborne erosion at shallow and normal impingement angles are presented in the SEM micrographs of Fig. 7.7. To facilitate comparison of damage sustained by different test materials under different impingement angles, all micrographs were taken at or near the centre of the erosion crater. It is important to note that in these airborne erosion craters, the halo effect (see section 5.4.2) was observed.

Figs. 7.7(a), (c) and (e) show the completely eroded areas of samples AD998-C, AD92 and AD998-F, respectively, eroded at an impingement angle of 30°. Figs. 7.7(b), (d) and (f) show the corresponding areas of the same materials eroded at 90° impact. The effect of the impingement angle on the material removal mechanisms is clearly demonstrated. It is evident that at shallow impingement angles, erosion damage is dominated by both grain ejection and plastic deformation of the materials. Further, in the plastically deformed areas, grooves or plough marks are often observed. The plastic grooves, in many instances, are similar to scratches produced on alumina surfaces by a sharp diamond indentor (Wang and Hsu 1996) and tend to lie along the particle colliding direction. Localised melting, as shown in Fig. 7.7(e), is observed at all impingement angles, but becomes more conspicuous at lower angles. The locally melted materials tend to draw in the direction of the impinging particles and to form elongated stringers with roun￢ed ends. EDX analysis of these melted materials shows high levels of Fe and Si (Fig. 7.8), indicating that they derive from the garnet erodent which contains SiO_2 and FeO (Table 7.1). Under normal impact, grain ejection is the main material removal mechanism and there are much fewer and smaller plastically deformed regions present. However, in those few plastically smeared areas, the grain boundary cracks of the underlying alumina grains are well developed as can be seen in Fig. 7.7(f). In the case of the coarse grained alumina, AD998-C, there is evidence of cleavage and conchoidal fracture within individual grains.
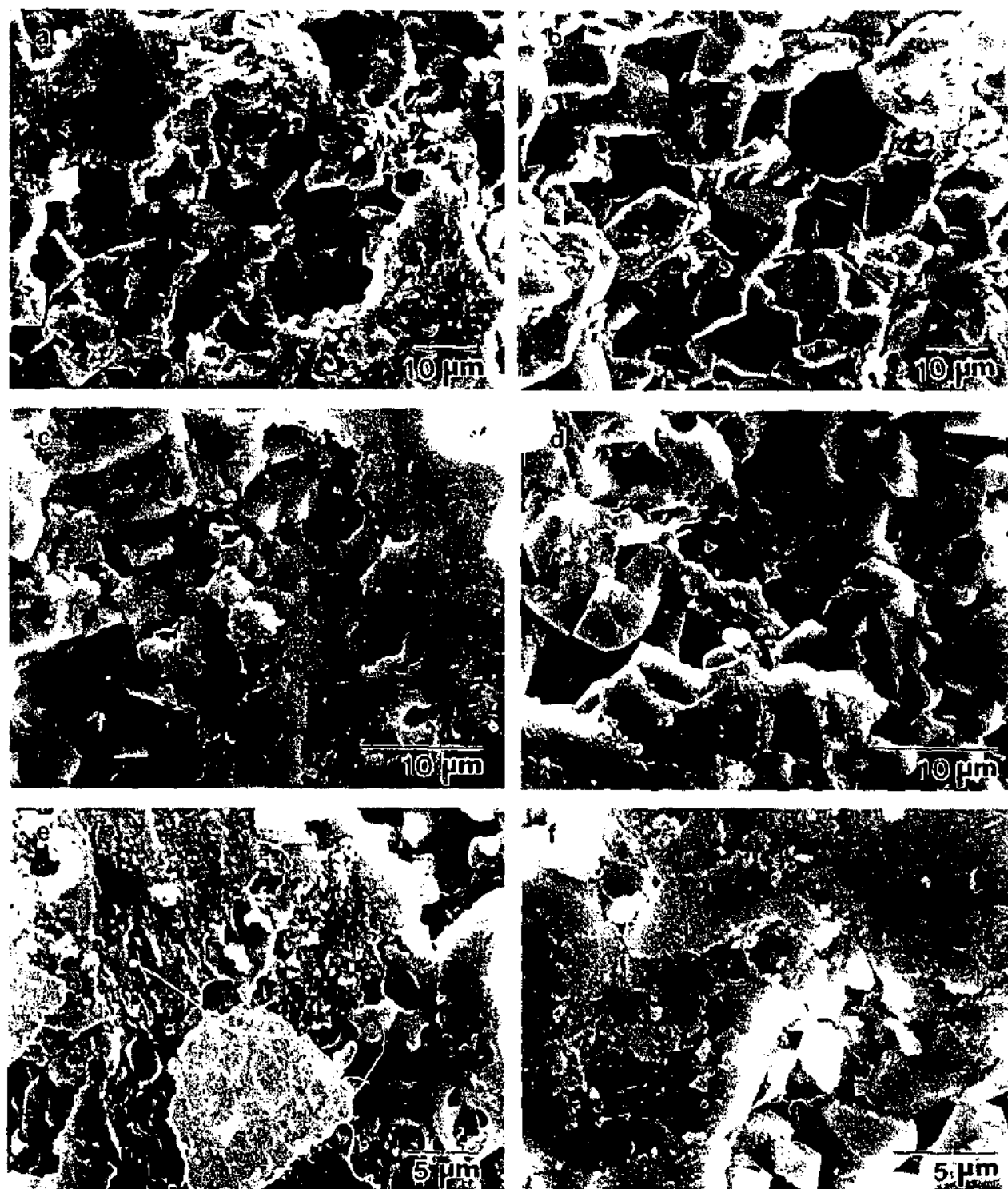
Fig. 7.7. SEM micrographs of steady state airborne erosion surfaces of alumina samples after 30° and 90° impingement. (a) and (b): AD998-C at 30° and 90° impact; (c) and (d): AD92 at 30° and 90° impact; (e) and (f): AD998-F at 30° and 90° impact. The particle impact direction for 30° impact is from top to bottom of the micrographs.
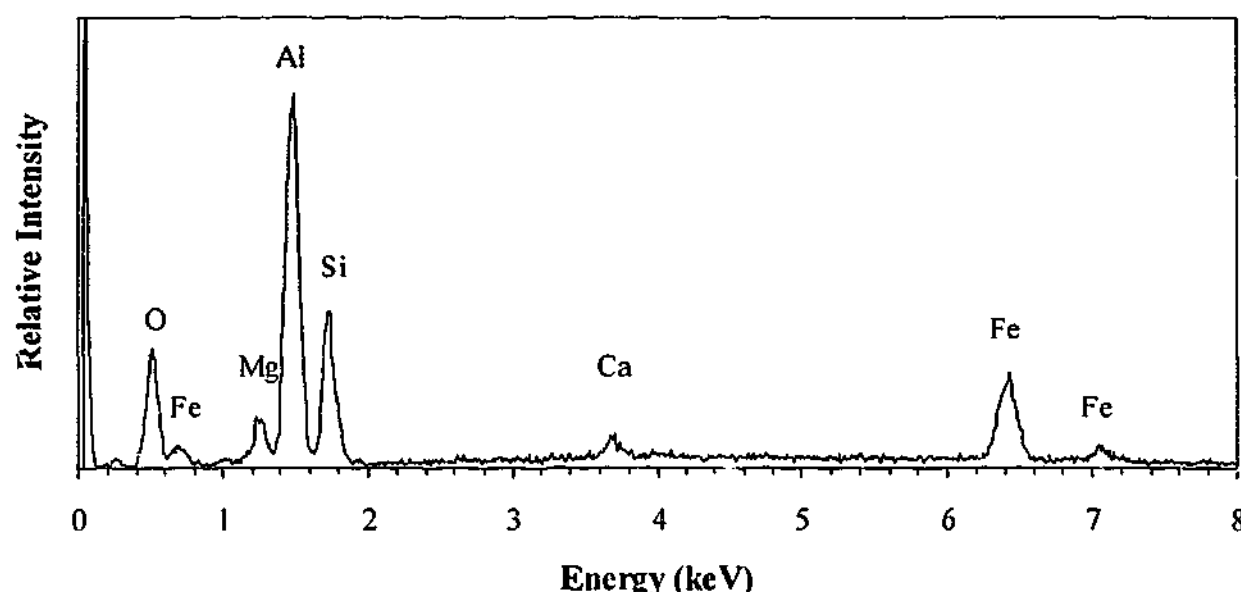
Fig. 7.8. EDX spectrum of deformed and melted materials shown in Fig. 7.7(e).

To clarify the interaction between the erodent particles and target surface and to understand the erosion mechanisms by which particles remove material, ideally one should study the damage features corresponding to different stages of erosion. Examination of an erosion crater reveals that the edge of the crater is much less eroded than its centre. Thus, examining the various areas of the erosion crater obtained from a single test should give some indication of the wear processes occurring at various stages of erosion. It is important to note that the angle of impact at the crater edge would be slightly different from that at the centre of the erodent beam because of the divergence associated with jets carrying particles. However, for a nominal angle of impact of 45°, under the present experimental conditions, the angle of impact at the crater edge (closer to the nozzle side) is estimated to be less than 55°.

Fig. 7.9 shows SEM micrographs of different locations on the worn surface of sample AD998-F after airborne erosion by a single dose of 1000 g of garnet erodent particles at an angle of impingement of 45°. The particle impact direction is from top to bottom of the micrographs. Fig. 7.9(a) is a low magnification secondary electron (SE) micrograph of the region of the elliptical erosion crater that corresponds to particles emerging from near the nozzle wall. Fig. 7.9(b), a higher magnification view of the

central area in Fig. 7.9(a), reveals the presence of wear tracks in the direction of particle impact at the top fringe of the crater. Fig. 7.9(c) is a SE image which shows the damage features in the wear track and Fig. 7.9(d), a back scattered electron (BSE) image of the same area. Figs. 7.9(e) and (f) are the SE and BSE images which show the damage features at the centre of the wear crater.
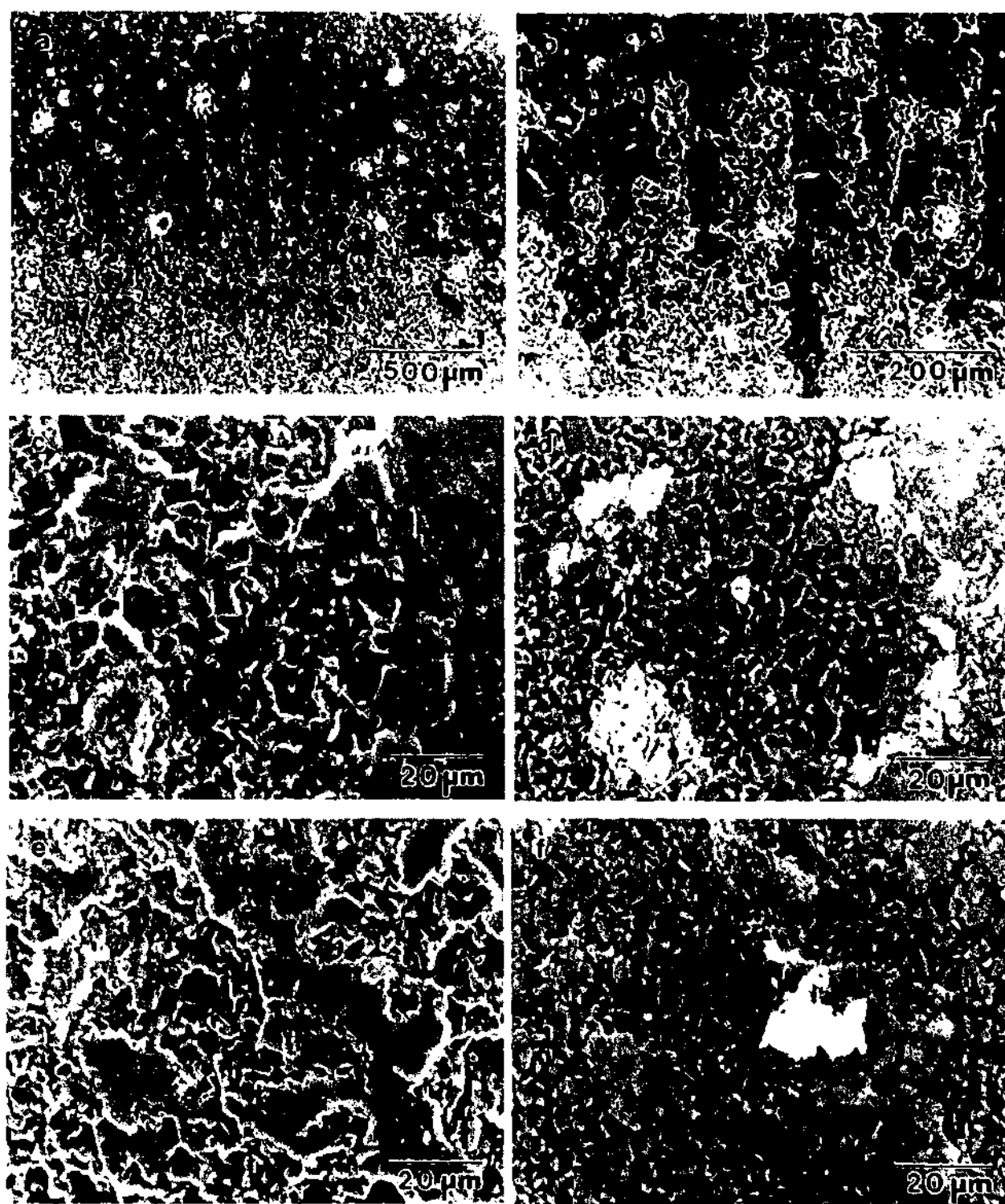
Fig. 7.9. SEM micrographs of different locations on the eroded surface of sample AD998-F after airborne erosion at an angle of impingement of 45°. Note: (a), (b), (c) and (e) are secondary electron (SE) images. (d) and (f) are back scattered electron (BSE) images of the areas shown in (c) and (e), respectively. The particle impact direction is from top to bottom of the micrographs.

The wear tracks shown in Figs. 7.9(a) and (b) are the result of the ploughing of the erodent particles on the sample surface. The damage patterns observed in the wear tracks, as shown in Fig. 7.9(c), are mainly grain dislodgment and some isolated plastically deformed regions. The BSE image of the same area in Fig. 7.9(d) shows that the deformed material seen in Fig. 7.9(c) contains materials with higher atomic number than Al, resulting in the lighter contrast. EDX analysis confirmed that the regions with bright contrast contain high levels of Fe (Fig. 7.10), confirming that they derive from the garnet erodent which contains a high proportion of FeO. The surface features of the centre of the wear crater are also dominated by grain ejection and some larger scaled flakes of deformed materials as seen in Fig. 7.9(e). It is evident from the BSE image in Fig. 7(f) that these flakes consist primarily of deformed target alumina with traces of smeared erodent material in some regions.
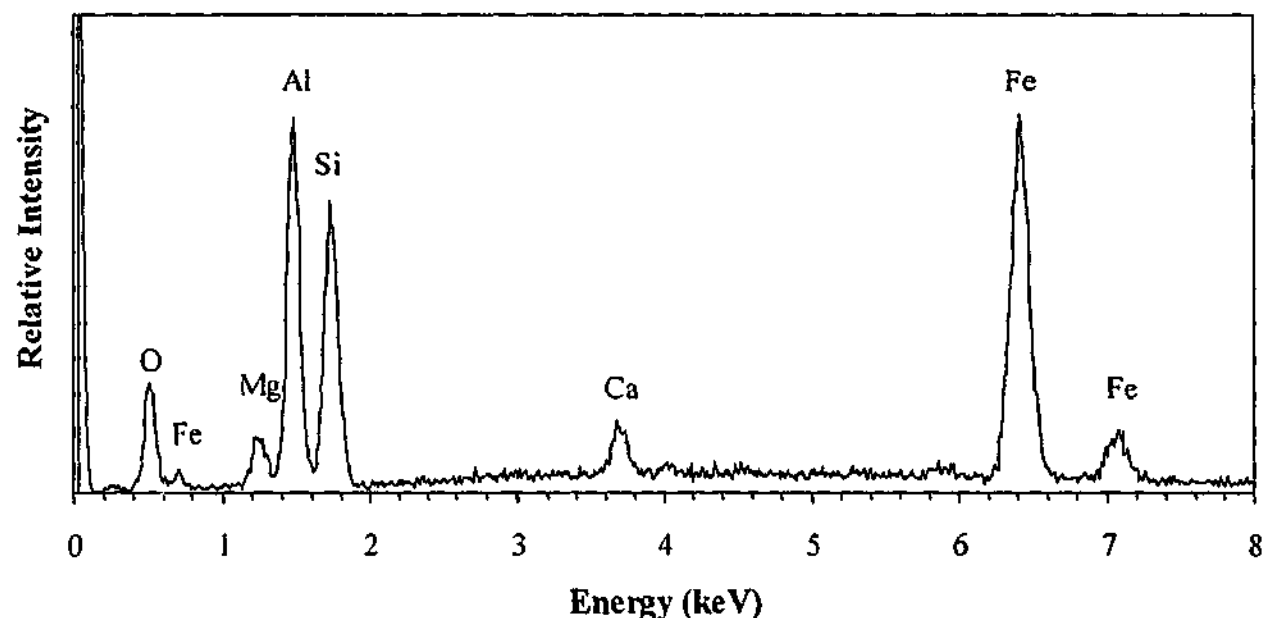
Fig. 7.10. EDX spectrum of regions with bright contrast, as shown in Figs. 7.9(d) and (f).

7.4.2 Slurry jet eroded surfaces

As in the case of the airborne erosion, the erosion craters in the slurry jet tests are circular in shape for normal impact and become more elliptical as the impact angle decreases. There is, however, a distinct difference in the morphology of the erosion craters for the two cases. The edge of the erosion crater in the slurry jet test is much

sharper than that in the airborne erosion test and no halo effect is observed under all impact conditions.
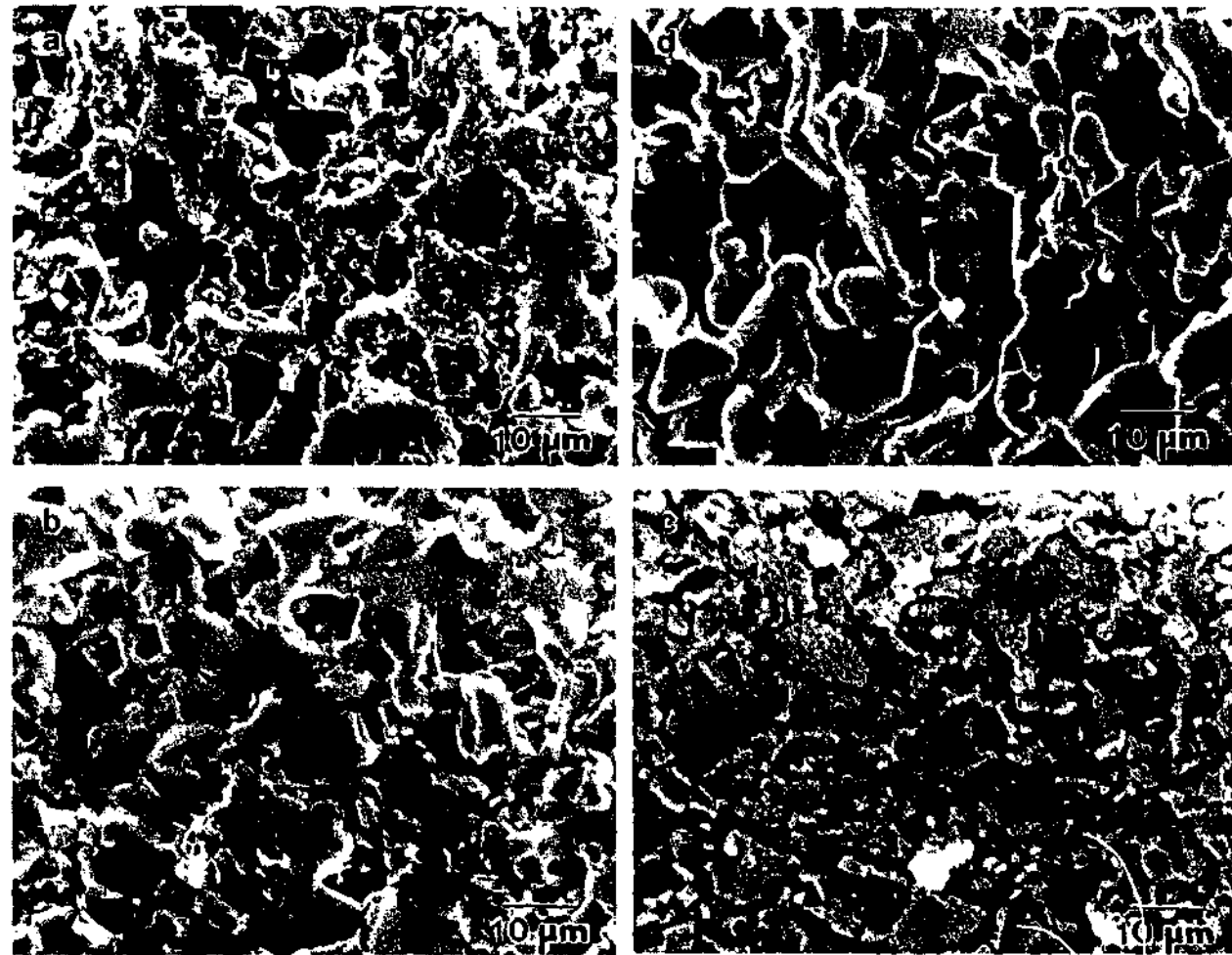
Fig. 7.11. SEM micrographs of steady state slurry erosion surfaces of sample AD998-C at various angles of impingement: (a) 15°, (b) and (c) 30°, and (d) 90°. Note: (a), (b) and (d) are SE images and (c) is a BSE image of the area in (b). The particle impact direction, for oblique impacts, is from top to bottom of the micrographs.

Figs. 7.11(a)-(d) are SEM micrographs which show the surface damage features at the centre of the wear crater of AD998-C after slurry jet erosion at both shallow and normal impingement angles. Figs. 7.11(a), (b) and (d) present SE images of the areas at the crater centre of sample AD998-C after slurry erosion at impingement angles of 15°, 30° and 90°, respectively, while Fig. 7.11(c) is a BSE image which shows the same area as in Fig. 7.11(b). As can be seen in Fig. 7.11(a), when the impingement angle is 15°, the damage occurs by both grain dislodgment and plastic deformation and smearing of the materials. However, when the impingement angle is increased to 30°, the plastically smeared regions become much smaller and fewer in number, as

218

seen in Fig. 7.11(b). The BSE mode reveals that there is only a trace of deformed erodent material in those few smeared regions (Fig. 7.11(c)). EDX analysis of the smeared area showed high levels of Al and no traces Si and Fe, confirming that this is indeed deformed alumina. This is in contrast to the damage patterns on airborne eroded surfaces, where much of the deformed material on the surface was found to derive from the erodent (Fig. 7.7(a)). When the impingement angle is increased to 90°, grain ejection becomes the main material removal mechanism and there are very few plastically deformed regions present (Fig. 7.11(d)). Furthermore, no melted material similar to that seen on airborne eroded surfaces (see Fig. 7.7(e)) was evident on the slurry jet eroded surfaces.

7.5 Erosion Mechanisms

An advantage of the jet impingement test is that it enables the study of the effect of varying the particle jet impact angle on the erosion behaviour of a material. By relating this to a detailed SEM examination of the eroded surfaces, it is possible to identify the various material removal processes.

When ceramics are eroded by sharp, hard particles, such as silicon carbide and alumina grits, both airborne (Sheldon and Finnie 1966a; Hutchings 1992) and slurry-entrained (Franco and Roberts 1998), it is well established that the erosion rate tends to peak at normal impact and decreases steadily as the impingement angle becomes more oblique. When ceramics are eroded by angular garnet particles with somewhat rounded edges, carried by either air or water, under the conditions used in this study, similar trends are observed. As shown in Figs. 7.2 and 7.3, the erosion rate-impact angle curves are well defined for all three alumina samples and exhibit a maximum erosion rate at 90°. Further, the erosion rate at 15° impingement angle is almost 5 times lower for airborne erosion and 20 times lower for slurry erosion than that at 90° impingement angle.

A comparison of the morphological features on the eroded surfaces of the high purity aluminas, AD998-C and AD998-F, subjected to low impact angles (15° and 30°) and

normal impact angle (90°), after both airborne and slurry erosion, reveals some interesting differences in the material removal mechanisms. In the case of shallow angle eroded surfaces, shown in Figs. 7.7(a), 7.7(e) and 7.11(a), the dominant material removal mechanisms are grain ejection, which is caused by grain boundary microcracking, and plastic deformation followed by smearing of the deformed materials. On the other hand, in the case of the 90° eroded surfaces, shown in Figs. 7.7(b), 7.7(f) and 7.11(d), the material removal mechanism is mainly grain ejection and ᵃᵗ ᵗᵗᶜantly lower degree of plastic smearing than in the case of the oblique iᵣ ᵃᵗ

ᵗᵒ ᵤₙₐₑᵣₛₜₐₙᵈ these differences, it is helpful to examine in more detail the damage feaᵤᵣₑ ᵗᵒᵣ the various impact angles at different stages of the erosion test. As discussed earlier, Figs. 7.9(a)-(f) show the appearance of the eroded surfaces of the high purity alumina, AD998-F, exposed to 45° impact. Note that the erosion damage for oblique impact is a result of two actions; vertical repeated impact and horizontal ploughing (Oka et al. 1997; Routbort and Scattergood 1992). Based on the SEM examination of the eroded surfaces, the erosion process can be divided into stages. At the early stage of erosion, wear tracks are formed (Fig. 7.9(b)). In these wear tracks, the material is mainly removed by grain ejection which results in a surface showing exposed grain facets. EDX analysis of this surface shows no detectable silicon and iron confirming the absence of influence from the garnet erodent. However, some isolated plastically smeared regions contain deformed erodent as well as the target alumina. It is also seen that, in some instances, the garnet particles have melted and splashed onto the target surface with the melted material being drawn into stringers in the direction of particle impact (Fig. 7.7(e)). Between the wear tracks, shown on the right side of Fig. 7.9(c), the target surface seems to be largely covered by a thin smeared layer. This smeared layer, as revealed by BSE mode (Fig. 7.9(d)) and random EDX analysis, mainly contains deformed and melted erodent material. The distribution of the smeared layer is not uniform, in agreement with the randomness of the impacts of the erodent particles.

It is evident from these observations that when the softer garnet erodent particles impinge on the harder alumina target (Tables 7.1 and 7.2), they undergo deformation

and fragmentation. In addition, the particles also undergo local melting, with the melted material drawn into stringers. This is in contrast to observations of localised melting of soda lime glass, alumina and mullite *targets* when impacted by silicon carbide erodent (Yust and Crouse 1978; Lawn et al. 1980). Lawn et al. (1980) have shown that this melting of the target material was due to local adiabatic heating to high temperatures when particles with high kinetic energy impact the target. However, in the present case, the localised heating has caused the melting of the lower melting garnet particle rather than the alumina target.

As the erosion progresses, the damaged surface becomes very rough. Grain ejection is still the main material removal mechanism. However, the plastically deformed features, shown as flakes in Fig. 7.9(e), have also become more pronounced. Further impacts result in material removal by spalling of the smeared flakes.

From these observations, the following picture emerges: when alumina ceramics are exposed to erosive wear by garnet particles, both airborne and slurry-entrained, the horizontal component of the kinetic energy of the impinging particles is mainly dissipated in plastic deformation of the erodent and target materials by means of a ploughing mechanism. In addition, local adiabatic heating caused by the impact of the fast moving particles may result in melting of the lower melting erodent. Melting is not observed in the case of slurry erosion because of the presence of water, a natural coolant. The vertical component of the kinetic energy is dissipated partially in the initiation and propagation of grain boundary microcracks in the target material resulting in grain dislodgment and partially in the fragmentation of the erodent particles. Grain ejection, as demonstrated by the present results, has a controlling effect on the material removal rate.

The distinctive differences in erosion rates, as well as the morphological features for shallow and normal impact angles, can be explained in terms of the above scenario. For example, at 15° impact, the kinetic energy of the impinging particles contributes mainly to ploughing (horizontal component of the energy, proportional to cos15°, ~97%) and very little (normal component proportional to sin15°, ~3%) to normal repeated impact. There is, therefore, much less energy available for initiating and

propagating the grain boundary microcracks, resulting in grain ejection, compared to 90° impact where a vast majority of the kinetic energy is devoted to this process. As a result, the material removal rate at shallow impact angle is much lower than that at normal impact.

7.6 Effect of Microstructure

Distinct differences in the erosive wear behaviours of the three aluminas have been seen. As shown in Figs. 7.2 and 7.3, material AD998-C has the highest wear rate under all impact conditions, being 2 and 3 times greater than those of materials AD998-F and AD92, respectively. The two widely quoted theoretical models for erosion of brittle materials, describing the elastic-plastic damage caused by sharp particle contact (Evans et al. 1978; Wiederhorn and Lawn 1979) indicate an inverse dependence of erosion rate on the fracture toughness of the target material. However, as has been previously demonstrated (Heath et al. 1990; Lathabai and Pender 1995; Lathabai 1995), the use of mechanical properties such as hardness and fracture toughness to explain the erosion behaviour of alumina ceramics has not always been satisfactory. In recent years, it has been increasingly appreciated by various investigators that the microstructures of ceramics have a controlling effect on their wear behaviour (Wiederhorn and Hockey 1983; Ajayi and Ludema 1991; Miranda-Martinez et al. 1994; Lathabai and Pender 1995; Lathabai 1995; Wada 1996). This hypothesis is further examined in the light of the present experimental results.

In the present study, the major microstructural parameters of interest are grain size, porosity and the nature of the grain boundary phase. The two high purity (99.8%) alumina materials, AD998-C and AD998-F, with similar hardness and porosity but different grain size, exposed to erosive wear under the same set of experimental conditions, enable the evaluation of the effect of grain size. It was not possible to measure the fracture toughness of these materials by the indentation method, since indentation produced cracking along grain boundaries rather than well-developed radial cracks. However, it is now well recognised that many alumina materials do not have single-valued fracture toughness, but exhibit an R-curve behaviour (Lawn

1993). The mechanism responsible for this crack size dependent toughness has been unequivocally established as grain-localised crack bridging, brought about by the presence of internal (thermal expansion mismatch) stresses in the non-cubic alumina matrix (Bennison and Lawn 1989). As such, the R-curve behaviour in alumina is strongly dependent on the microstructure, becoming more pronounced with increasing grain size (Knehans and Steinbrech 1984; Chantikul et al. 1990). It has been observed that as the grain size increases, the steady state or long-crack fracture toughness, measured in traditional fracture mechanics tests, increases, but the short-crack toughness decreases (Chantikul et al. 1990). A similar trend can be expected for the two high purity aluminas in this study.

As shown in Fig. 7.2, the erosive loss increases strongly with the grain size. As stated earlier, the dominant mechanism of material removal in erosive wear of aluminas is grain boundary microfracture resulting in grain ejection. In a study on the effect of grain size in the *sliding* wear of alumina (which also occurs by grain boundary microfracture), Cho et al. (1989) showed that refining the grain size and eliminating internal stresses would lead to higher fracture toughness in the short crack region which is of the greatest pertinence to wear processes. This also explains the higher erosion resistance of the finer grained AD998-F.

The mean grain size of material AD92 is over twice as large as that of AD998-F; yet its erosion resistance is better than that of AD998-F at all impact angles. As noted earlier, the other major microstructural difference in the two materials is that AD998-F is a high purity alumina with relatively high porosity while AD92 is a denser material consisting of approximately six volume percent grain boundary glassy phase. It is well known that porosity influences the erosion performance. For example, an extensive investigation of solid-particle erosion of several commercial aluminas with various physical and mechanical properties showed that the erosion rate increases as the porosity increases (Wada and Watanabe 1987a). On the other hand, it has also been suggested that the presence of the grain boundary glassy phase, which is capable of viscous flow, can accommodate the anisotropic nature of alumina deformation, reduce the residual stresses at the grain boundaries (Ajayi and Ludema 1991), as well as improve the bonding between alumina grains (Zhou and Bahadur

1991 and 1993). Both these effects are consistent with the superior erosive wear resistance observed for AD92 in this study.

The SEM micrographs of the eroded surfaces of samples AD998-F and AD92, impacted at 90°, Figs. 7.7(d) and (f) respectively, show that grain ejection is the dominant material removal mechanism in the former case while significant amounts of plastically deformed material are observed in the latter. The lower porosity, coupled with the energy absorption capacity and the stronger bonding between alumina grains provided by the grain boundary glass in sample AD92, has made grain ejection more difficult. As a result, the repeated impact by particles causes plastic smearing of the grains before they are ejected.

7.7 Effect of Erosion Test Variables

It is generally accepted that for most ceramic materials, the erosion rate, ΔE, exhibits a power law relationship with the particle velocity, with the value of the velocity exponent, n, being between 1.8 to 4 for both dry and wet erosion (Murugesh and Scattergood 1991; Srinivasan and Scattergood 1991; Routbort and Scattergood 1992; Wada 1996; Franco and Roberts 1998). In the present investigation, the n values for the two alumina ceramics, AD998-C and AD92, were determined under the same set of slurry erosion conditions and were found to be 2.8 and 2.1, respectively. These results are consistent with a study reported in literature, where the velocity exponents for a group of aluminas with a wide variety of grain sizes, densities and purity, subjected to identical erosion conditions, showed a variation in the range 2.5-3.2 (Routbort and Scattergood 1992).

The difference in n values observed in the present study could be attributed to the different Al_2O_3 contents of these two aluminas. Zhou and Bahadur (1995) observed that when an alumina with 4 wt% silicate glassy phase was eroded by airborne silicon carbide grits, the n value decreased with increasing operating temperature. It was argued that this was due to the increase in plasticity of the intergranular glassy phase with temperature which effectively absorbed more impact energy (Zhou and Bahadur

1995). The same argument may be used to explain the present observation. The relatively lower *n* value for material AD92 could be due to the presence of the 6 vol% grain boundary glassy phase, absent in AD998-C, which significantly contributes to the dissipation of the impact energy.

In the case of jet impingement erosion, it is known that the erosion rate decreases as the erodent particle flux increases (Anand et al. 1987; Zu et al. 1991). The data in Fig. 7.5 confirms this relationship. This flux effect has been described by Anand et al. (1987) by a first-order particle collision model in which a shielding of the target surface from the incident particles occurs by particles rebounding from the surface. They assumed that upon collision, the particles are removed from the flux beam and do not contribute to the erosion process. When the erodent particle flux is low, the mean free path of the erodent particles is quite long and thus the probability of collision between the rebounding particles and the incident particles is very low. As the flux increases, the probability of collision increases exponentially and hence the erosion rate would be expected to decrease (Anand et al. 1987).

The effect of particle flux on the erosion rate may also arise from the dependence of the incident particle velocity on the particle flux. According to the analysis by Anand et al. (1987), in an airborne erosion apparatus, when the particle flux value reaches about 100-200 kg/m^{2}s, hydrodynamic particle interactions occur in the nozzle and become more noticeable as the particle flux increases further. The particle fluxes examined in this work are typically in the region of 500-2500 kg/m^{2}s which are well beyond that value and thus hydrodynamic interaction is highly likely. It has been proposed (Anand et al. 1987) that the interactions between particles could result in a decrease in the incident particle velocity. In fact, a slight decrease in particle velocity with increasing flux was observed during the calibration of the slurry jet apparatus. Given the power law relationship between the erosion rate and particle velocity, a small decrease in particle velocity will, therefore, result in an amplified reduction of the erosion rate.

7.8 Comparison of Dry Erosion and Wet Erosion

To directly compare the erosive wear behaviour of alumina ceramics under airborne and slurry jet erosion, the test conditions of the two processes must be similar. However, the erosion rate data of material AD998-C presented in this work (Fig. 7.6) for dry and wet erosion were obtained for similar particle velocities but different particle fluxes; being 100 and 1500 kg/m^2s for airborne and slurry jet erosions, respectively. The higher flux rate in the latter case, as discussed in section 7.7, would be expected to significantly reduce the erosion rate. Nevertheless, erosion tests showed that the wet erosion rate of material AD998-C was significantly higher than that for dry erosion by approximately a factor of 6 (Fig. 7.6). The enhanced slurry erosion rate over airborne erosion rate could be attributed to the presence of water as a carrier fluid. Water can influence the erosive wear behaviour of alumina ceramics in two different ways – by enabling moisture-accelerated crack growth and by a hydrodynamic lubrication effect.

It has been shown that the erosive wear of alumina ceramics is primarily controlled by grain boundary microfracture. It is well-established that crack tips in ceramics may experience a stress-corrosion process in the presence of water, which will accelerate crack growth (Lancaster et al. 1992; Lawn 1993). Such an enhancement of crack growth in the presence of water has been observed in the case of high purity alumina (Lathabai and Lawn 1989). The other intergranular oxide phases are suspected to behave in the same fashion as the alumina phase (Michalske and Bunker 1986). The enhancement of grain boundary microfracture in water would account for the increased slurry erosion rate of alumina ceramics, extrapolated from the results obtained in this study.

Hydrodynamic lubrication is a result of the viscosity of the carrier fluid and is a purely physical reaction (Levy and Hickey 1987). A thin viscous film of the carrier fluid can be formed between impinging particles and the eroding surface which effectively acts as an energy barrier to reduce their kinetic energy and hence, their erosivity (Levy et al. 1987; Levy and Yau 1984). At low impact angles, the vertical component of the kinetic energy of the impinging particle which enables the

penetration of the barrier film is small, resulting in the lubrication effect becoming more pronounced. Thus the erosion rate may be further reduced. As the impact angle increases, the impinging particles are less affected by the lubrication effect due to the increasing penetration energy (Levy and Yau 1984). This agrees well with the present experimental observations. As shown in Figs. 7.2 and 7.3, in the case of slurry erosion, the erosion rates for both aluminas at 90° impingement angle are almost 20 times greater than those at 15° incidence angle. This difference reduces to a factor of 4 for airborne erosion due to the absence of the lubrication effect.

Finally, it has been observed that the halo effect was absent around the slurry jet erosion craters. This may be explained by the fact that the viscosity of water is sufficiently high to force the erodent particles to follow the streamline, resulting in less deviation of the particles which causes the halo effect in airborne erosion.

7.9 Summary

Based on the results obtained from this study, the following conclusions may be reached:

- In both airborne and slurry erosion, the erosion rate of the polycrystalline aluminas peaks at normal impact and decreases steadily as the impingement angle becomes more shallow. The erosion rates for the aluminas at 15° impingement angle are almost 5 times lower for airborne erosion and 20 times lower for slurry erosion than those at 90° incidence angle. The much lower erosion rate at 15° slurry erosion compared to that at 90° may be explained by the hydrodynamic lubrication effect which is more pronounced when the vertical component of the velocity of the impinging particle is low.

- The material removal mechanisms in both airborne and slurry erosion were found to be strongly dependent on the erodent stream impact angle. For low angle impact, the damage occurs by a ploughing mechanism, characterised by both grain ejection and spalling of plastically deformed materials, while for 90°

impact, the dominant mechanism is grain ejection. In both types of erosion, deformed garnet was found on the eroded surfaces. In the case of airborne erosion, there was evidence of melting and splashing of the garnet erodent on the target surface as a result of the locally high temperatures generated by adiabatic heating due to particles impacting at high energy. Such localised melting of the erodent was not seen during slurry erosion because of the cooling effect of water.

- The microstructures of alumina ceramics were found to have a controlling effect on their erosion behaviour. Dense, fine-grained alumina materials containing an intergranular glassy phase would be good candidates for use in applications requiring erosion resistance.

- The erosion rates of alumina ceramics increase with increasing velocity and decreasing flux of the erodent particles.

- Extrapolation of slurry erosion data to experimental conditions used in airborne tests suggests that the former type of erosion is much more severe. The deleterious effect of water on the crack propagation of alumina ceramics can account for this behaviour.

Chapter 8

CONCLUSIONS AND FUTURE WORK

8.1 Conclusions

This thesis has examined the relationship between the microstructure and the erosion behaviour of engineering ceramics. The major finding resulting from this research is that while mechanical properties, such as hardness and fracture toughness, influence the erosion performance of ceramic materials, the microstructure is also found play an important role. A number of microstructural parameters, namely the porosity, composition, grain size, grain morphology and the amount of intergranular glass phase, all have an important role in determining the erosion behaviour of ceramic materials.

A detailed investigation of the effects of microstructural parameters on erosion performance of ceramics was carried out using Ca α-sialon ceramics as a modeling system. Sialon ceramics have shown to be suitable candidates for an investigation of the effects of microstructure on the mechanical and tribological properties of engineering ceramics. This is mainly due to the fact that these materials, compared to the other engineering ceramics, have greater phase complexity and more degrees of freedom for tailoring of microstructures.

Tailoring of the microstructure of Ca α-sialon ceramics was accomplished by altering the starting powder composition as well as the sintering techniques and conditions. It was shown that compositions inside the single-phase α-sialon forming region produced mainly equiaxed grain morphologies coupled with small amounts of intergranular glass, while those outside the single-phase region on the Al rich side generated elongated α-sialon grains and minor secondary phases with a relatively high glass content. Furthermore, for the same starting composition, the longer dwell

time resulted in a coarser grain size and larger unit cell dimensions of α-sialon and thus reduced the amount of intergranular glass, while the higher sintering temperature gave rise to a higher grain aspect ratio with less intergranular glass. Moreover, a post-sintering heat treatment could partially crystallize the intergranular glass and introduce residual stresses at the multi-grain junctions.

A solid understanding of the effect of various microstructural parameters on the erosion behaviour of ceramic materials has been developed. This understanding should result in the design of better performing and long lasting ceramic materials for use in applications involving erosive wear. As far as erosion resistance is concerned, dense ceramics with an optimum amount of intergranular glass are recommended. Additionally, fine-grained materials outperform coarse-grained materials, while the elongated microstructure outperforms the equiaxed microstructure. The optimum amount of intergranular glass can increase the bonding strength and also absorb the energy of impacting particles via viscoplastic flow, while the interlocked elongated grains provide some toughening mechanisms as well as hinder grain dislodgment.

The erosion behaviour of a number of engineering ceramics, namely alumina, partially stabilized zirconia, silicon nitrides, sialons, and silicon carbides, was examined. In terms of material loss, the Ca α-sialon ceramics are the most erosion resistant materials, while the high-purity alumina is the least. The two types of self-reinforced silicon nitride materials have better erosion resistance than the MgO partially stabilized zirconia and the two siliconised silicon carbide materials. In the light of detailed SEM examinations of the eroded surfaces, a relationship between the microstructure of the ceramic materials and their erosion performance has been established. This relationship can be explained using the energy dissipation/energy balance analysis based on the experimental evidence that the impacting particle produces plastic flow at the contact zone and its surrounding crack networks.

It was found that hardness and fracture toughness were not the only factors which determined the erosion behaviour of ceramic materials. This is because hardness determines both the maximum load and the depth of particle penetration during solid particle erosion. An expression for the maximum load (eq. 5.1) showed that for a

230

fixed impact energy the maximum impact load increased as the target hardness increased. A higher impact load could result in a greater amount of chipping leading to a higher rate of material removal. On the other hand, the high hardness can impede the particle penetration into the target surface (eqs. 5.3 and 5.4), which may reduce the depth of the formation of lateral cracks. Furthermore, in erosion of polycrystalline ceramics, the size of the fractured region in the vicinity of the contact zone is largely dependent on the microstructure of the materials. Therefore, no simple relationship between the erosion rate and the hardness can be established.

Many previous studies claimed that a better relation between the erosion rate and the fracture toughness, especially the short-crack toughness or the operative fracture toughness, was observed. However, the results presented in this thesis clearly indicated that even the short-crack toughness might not be directly used to quantitatively predict the erosion performance of ceramic materials. This is because the fracture toughness, K_{IC}, used here is the plane strain fracture toughness which corresponds to Mode I fracture while the fracture involved in erosive wear may comprise Mode I, II and/or III fractures.

The results presented in this thesis also indicate that the erosion rate of ceramic materials is markedly influenced by the erodent properties. An erodent that is softer than target materials produces a low rate of material removal, especially for the target materials containing an interlocked elongated grain morphology. This finding has practical importance as from an engineering point of view, the particles encountered in practice are often significantly softer than ceramics. Therefore, the use of ceramic materials with an optimized microstructure could be very beneficial if other design criteria, such as cost-benefit ratio, are permitted.

Damage produced by wet erosion was found to be much more severe for alumina ceramics compared to that induced by dry erosion under similar conditions. The deleterious effect of water on crack propagation of alumina ceramics can account for this behaviour.

8.2 Suggestions for Future Work

Several aspects of this study have suggested the following areas that could be enhanced by future work.

- It appears that in order to further improve the fracture toughness of Ca α-sialon ceramics, an investigation into compositional design of the intergranular glass which can lead to a weakened interfacial bonding strength between α-sialon grains and the glassy matrix is necessary.

- There is a need for further investigation into erosive wear under carefully controlled conditions to clarify the effects of phenomena related to erodent properties, such as erodent fragmentation and deformation, on the erosion behaviour of ceramic materials.

- A clear understanding of the effects of particle size and velocity on the erosion performance of ceramics with various microstructures is also vital in selecting the best material for a particular use.

- In order to design better ceramic materials for erosive environments, extension of the existing theoretical models to include effects of microstructural variables and erodent particle properties is highly desirable.

References

Ajayi, O. O., Ludema, K. C., (1991) "The effect of microstructure on wear modes of ceramic materials", in *Wear of Materials*, ed. K. C. Ludema, *The American Society of Mechanical Engineers*, New York, pp. 307-318.

Anand, K., Hovis, S. K., Conrad, H., Scattergood, R.O., (1987) "Flux effects in solid particle erosion", *Wear*, **118**, 243-257.

Anand, K., Conrad, H., (1988) "Microstructure and scaling effects in the damage of WC-Co alloys by single impacts of hard particles", *J. Mater. Sci.*, **23**, 2931-2942.

Anstis, G. R., Chantikul, P., Lawn, B. R., Marshell, D. B., (1981) "A critical evaluation of indentation techniques for measuring fracture toughness: I, Direct crack measurements", *J. Am. Ceram. Soc.*, **64**(9), 533-538.

AS 1774.5, (1979) "The determination of density, porosity and water absorption", *Standards Association of Australia*, 1-3.

Bando, Y., Mitomo, M., Kitami, Y., Izumi, F., (1986) "Structural and composition analysis of silicon aluminium oxynitride polytypes by combined use of structure imaging and microanalysis", *J. Microsc.*, **142**, 235-246.

Becher, P. F., Lin, H. T., Hwang, S. L., Hoffmann, M. J., Chen, I.-W., (1993) "The influence of microstructure on the mechanical behaviour of silicon nitride ceramics", in *Silicon Nitride-Scientific and Technological Advances*, ed. I.-W. Chen, *MRS Symposium Proceedings*, **287**, MRS Pittsburgh, USA, pp. 147.

Becher, P. F., Hwang, S. L., Lin, H. T., Tiegs, T. N., (1994) "Microstructural contribution to the fracture resistance of silicon nitride ceramics", in *Tailoring of Mechanical Properties of Si₃N₄ Ceramics*, ed. M. J. Hoffmann, G. Petzow, *NATO ASI Series, Series E: Applied Science*, **276**, Kluwer Academic Publishers, Dordrecht, The Netherlands, pp. 87-100.

Becher, P. F., Hsueh, C. H., Alexander K. B., Sun, E. Y., (1996) "Influence of reinforcement content and diameter on the R-curve response in SiC-whisker-reinforced alumina", *J. Am. Ceram. Soc.*, **79**(2), 298-304.

Becher, P. F., Sun, E. Y., Plucknett, K. P., Alexander, K., B., Hsueh, C.-H., Lin, H.-T., Waters, S. B., Westmoreland, C. G., Kang, E.-S., Hirao, K., Brito, M. E., (1998) "Microstructural design of silicon nitride with improved fracture toughness: I, Effects of grain shape and size", *J. Am. Ceram. Soc.*, **81**(11), 2821-2830.

Bennison, S. J., Lawn, B. R., (1989) "Role of interfacial grain-bridging sliding friction in crack-resistance and strength properties of non-transforming ceramics", *Acta Metall. Mater.*, **37**(10), 2659-2671.

Bernard-Granger, G., Crampon, J., Duclos, R., (1995) "Glassy grain-boundary phase crystallization of silicon nitride: Kinetics and phase development", *J. Mater. Sci. Lett.*, **14**, 1362-1365.

Blendell, J. E., Coble, R. L., (1982) "Measurement of stress due to thermal expansion anisotropy in Al_2O_3", *J. Am. Ceram. Soc.*, **65**, 174-178.

Breder, K., Ritter, J. E., Jakus, K., (1988) "Strength degradation in polycrystalline alumina due to sharp-particle impact damage", *J. Am. Ceram. Soc.*, **71**(12), 1154-1158.

Briscoe, B. J., Rough, S. L., (1998) "The effects of wall friction in powder compaction", *Colloids and Surfaces. A: Physicochemical and Engineering Aspects*, **137**, 103-116.

Burke, J. E., (1990) "Recrystallization and sintering in ceramics", in *Sintering key papers*, ed. S. Somiya, Y. Moriyoshi, Elsevier Science Publishers, Essex, England, pp. 17-37.

Cao, G. Z., Metselaar, R., (1991) "α'-sialon ceramics: A review", *Chem. Mater.*, **3**, 242-252.

Carborundom Co., (1952) "Silicon nitride bonded articles", U.S. Pat. No. 2 618 565, Nov. 18.

Carborundom Co., (1953) "Silicon nitride bonded refractory oxide bodies and method of making", U.S. Pat. No. 2 636 828, Apr. 18.

Carborundom Co., (1954) "Improvements in or relating to shaped silicon nitride bodies and their manufacture", British Pat. No. 717 555, Oct. 27.

Chantikul, P., Bennison, S. J., Lawn, B. R., (1990) "Role of grain size in the strength and *R*-curve properties of alumina", *J. Am. Ceram. Soc.*, **73**(8), 2419-2427.

Chatfield, C., Ekström, T., Nikus, M., (1986) "Microstructural investigation of alpha-beta yttrium sialon materials", *J. Mater. Sci.*, **21**, 2297-2307.

Chen, I-W., Hwang, S.-L., (1992) "Shear thickening creep in superplastic silicon nitride", *J. Am. Ceram. Soc.*, **75**(5), 1073-1079.

Chen, I-W., Rosenflanz, A., (1997) "A tough SiALON ceramic based on α-Si_3N_4 with a whisker-like microstructure", *Nature*, **389**, 701-704.

Chen, I-W., Engineer, M., (1999) "Model for fatigue crack growth in grain-bridging ceramics", *J. Am. Ceram. Soc.*, **82**(12), 3549-3560.

Cheng, Y.-B., Thompson, D. P., (1994) "Preparation and grain boundary devitrification of samarium α-sialon ceramics" *J. Euro. Ceram. Soc.*, **14**, 13-21.

Cho, S-J., Hockey, B. J., Lawn, B. R., Bennison, S. J., (1989) "Grain-size and R-curve effects in the abrasive wear of alumina", *J. Am. Ceram. Soc.*, **72**(7), 1249-1252.

Clarke, D. R., Thomas, G., (1977) "Grain boundary phase in a hot-pressed MgO fluxed silicon nitride", *J. Am. Ceram. Soc.*, **60**(11-12), 491-495.

Clarke, D. R., (1987) "On the equilibrium thickness of intergranular glass phases in ceramic materials", *J. Am. Ceram. Soc.*, **70**(1), 15-22.

Clarke, D. R., Shaw, T. M., Philipse, A. P., Horn, R. G., (1993) "Possible electrical double-layer contribution to the equilibrium thickness of intergranular glass films in polycrystalline ceramics", *J. Am. Ceram. Soc.*, **76**(5), 1201-1204.

Conoci, S., Melandri, C., De Portu, G., (1999) "Wear of 3Y-TZP containing compressive residual stresses at the surface", *J. Mat. Sci.*, **34**, 1009-1015.

Davidge, R. W., Riley, F. L., (1995) "Grain-size dependence of the wear of alumina", *Wear*, **186-187**, 45-49.

Deeley, G. G., Herbert, J. M., Moore, N. C., (1960) "Dense silicon nitride", *Powder Metall.*, **8**, 145-156.

Deckwerth, M., Rüssel, C., (1997a) "Crystallization of oxynitride glasses in the system Mg-Ca-Al-Si-O-N prepared with the aid of a polymeric precursor", *J. Non-Cryst. Solids*, **217**, 55-65.

Deckwerth, M., Rüssel, C., (1997b) "Oxynitride glasses in the system Mg-Ca-Al-Si-O-N prepared with the aid of a polymeric precursor: preparation and properties", *J. Non-Cryst. Solids*, **217**, 66-71.

Deville, S.-C., Wöhler, F., (1859) "On the direct compound silicon nitride", *Liebigs Ann. Chem. Pharm.*, **110**, 248-250.

Dimond, C., Kirk, J. N., Briggs, J., (1983) "The evaluation of existing models for impact erosion and abrasive wear of ceramic materials", in *Proc. Int. Conf. Wear of Materials*, ed. K. C. Ludema. ASME, New York, pp. 333-339.

Doğan, C. P., Hawk, J. A., (1999) "Role of composition and microstructure in the abrasive wear of high-alumina ceramics", *Wear*, **225-229**, 1050-1058.

Drew, R. A. L., Hampshire, S., Jack, K. H., (1981) "Nitrogen ceramics", *Proc. Brit. Ceram. Soc.*, **31**, 119-132.

Ekström, T., Kall, P.-O., Nygren, M., Olsson, P.-O., (1989) "Dense single-phase β-sialon ceramics by glass-encapsulated hot isostatic pressing", *J. Mater. Sci.*, **24**, 1853-1861.

Ekström, T., (1989) "Effect of composition, phase content and microstructure on the performance of yttrium sialon ceramics", *Mater. Sci. Eng.*, **A109**, 341-349.

Ekström, T., Nygren, M., (1992) "Sialon ceramics", *J. Am. Ceram. Soc.*, **75**(2), 259-276.

Ekström, T., (1994) "Sialon composite ceramics", in *Tailoring of Mechanical Properties of Si₃N₄ Ceramics*, ed. M. J. Hoffmann, G. Petzow, *NATO ASI Series, Series E: Applied Science*, **276**, Kluwer Academic Publishers, Dordrecht, The Netherlands, pp. 149-161.

Ekström, T., Shen, Z.-J., (1995) "Temperature stability of rare-earth doped α-sialon ceramics", in *5th International Symposium on Ceramic Materials and Components for Engines*, eds D.-S. Yan, X.-R. Fu, S.-X. Shi, World Scientific, Singapore, pp. 206-210.

Ekström, T., Shen, Z.-J., Falk, L., (1997) "Duplex α-β sialon ceramics stabilised by Dysprosium and Samarium", *J. Am. Ceram. Soc.*, **80**(2), 301-312.

Ellen, Y. S., Becher, P. F., Plucknett, K. P., Hsueh, C.-H., Alexander, K. B., Waters, S. B., Hirao, K., Brito, M. E., (1998) "Microstructural design of silicon nitride with improved fracture toughness: II, effects of yttria and alumina additives", *J. Am. Ceram. Soc.*, **81**(11), 2831-2840.

Esposito, L., Tucci, A., (1997) "Microstructural dependence of friction and wear behaviours in low purity alumina ceramics", *Wear*, **205**, 88-96.

Evans, A. G., Gulden, M. E., Rosenblatt, M., (1978) "Impact damage in brittle materials in the elastic-plastic response regime", *Proc. R. Soc. London, Ser. A*, **361**, 343-365.

Evans, A. G., Marshall, D. B., (1980) "Wear mechanisms in ceramics", in *Fundamentals of Friction and Wear of Materials*, ed. D. A. Rigney, *American Society for Metals*, Metals Park, Ohio 44073, pp. 439-452.

Evans, P. A., Stevens, R., Binner, J. G. P., (1984) "Quantitative X-ray diffraction analysis of polymorphic mixes of pure zirconia", *Br. Ceram. Trans. J.*, **83**, 39-43.

Fairbanks, C. J., Lawn, B. R., Swanson, P. L., (1987) "Crack-interface grain bridging as a fracture resistance mechanism in ceramics", *J. Am. Ceram. Soc.*, **70**, 279-294.

Finnie, I., (1960) "Erosion of surfaces by solid particles", *Wear*, **3**, 87-103.

Finnie, I., (1995) "Some reflections on the past and future of erosion", *Wear*, **186-187**, 1-10.

Franco, A., Roberts, S. G., (1996) "Controlled wet erosive wear of polycrystalline alumina", *J. Euro. Ceram. Soc.*, **16**, 1365-1375.

Franco, A., Roberts, S. G., (1998) "The effect of impact angle on the erosion rate of polycrystalline α-Al₂O₃", *J. Euro. Ceram. Soc.*, **18**, 269-274.

Garvie, R. C., Hannink, R. H. J., Pascoe, R. T., (1975) "Ceramic steel?", *Nature*, **258**, 703-704.

Gauckler, L. J., Petzow, G., (1983) "Representation of multicomponent silicon nitride- based systems", in *Progress in Nitrogen Ceramics*, ed. F. L. Riley, Martinus Nijhoff, The Hague, Netherlands, pp. 41-44.

Glass, S. J., Ewsuk, K. G., (1997) "Ceramic powder compaction", *MRS Bulletin*, **Dec.**, 24-28.

Grieveson, P., Jack, K. H., Wild, S., (1968) "The crystal chemistry of ceramic phases in the Silicon-Nitrogen-Oxygen and related systems", Prog. Rep. No. 1, Min. of Def. Contract. N/CP.61/94111/67/48/M.P. 387, July.

Grun, R., (1979) "The crystal structure of β-Si_3N_4: structural and stability considerations between α- and β-Si_3N_4", *Acta Crystallogr.*, **B35**, 800-804.

Gulden, M. E., (1981a) "Correlation of experimental erosion data with elastic-plastic impact models", *J. Am. Ceram. Soc.*, **64**, C59-60.

Gulden, M. E., (1981b) "Solid particle erosion of Si_3N_4 materials", *Wear*, **69** 115-129.

Gulden. M. E., (1979) "Solid particle erosion of high-technology ceramics (Si_3N_4, glass-bonded Al_2O_3 and MgF_2)", in *Erosion: Prevention and Useful Applications, ASTM STP 664*, ed. W. F. Adler, Philadelphia, PA, 101-122.

Hampshire, S., Park, H. K., Thompson, D. P., Jack, K. H., (1978) "α-sialon ceramics", *Nature*, **274**, 880-882.

Hampshire, S., Drew, R. A. L., Jack. K. H., (1985) "Oxynitride glasses", *Phys. Chem. Glasses*, **26**(5), 182-186.

Hampshire, S., (1993) "Nitride ceramics", in *Materials Science and Technology: A comprehensive treatment*, eds. R. W. Cation *et al.*, **11**, ch.3, VCH, Germany.

Hampshire, S., Nestor, E., Flynn, R., Besson, J.-L., Rouxel, T., Lemercier, H., Goursat, P., Sebai, M., Thompson, D. P., Liddell, K., (1994) "Yttrium oxynitride glasses: properties and potential for crystallisation to glass-ceramics", *J. Euro. Ceram. Soc.*, **14**, 261-273.

Hannink, R. H. J., Kelly, P. M., Muddle, B. C., (2000) "Transformation toughening in zirconia-containing ceramics", *J. Am. Ceram. Soc.*, **83**(3), 461-487.

Heath. G.R., Johnson. T.D., Parry. M.T., Wall. D.J., (1990) "Solid particle erosion of alumina linings for pulverised fuel transport piping", *Br. Ceram. Trans. J.*, **89**, 17-21.

Hewett, C. L., Cheng, Y.-B., Muddle, B. C., Trigg, M. B., (1994) "Preparation of fine-grained Calcium α-sialon", *J. Mater. Sci. Lett.*, **13**, 1612-1615.

Hewett, C. L., (1998) "The fabrication and characterisation of calcium α-sialon ceramics", PhD thesis, Materials Engineering Department, Monash University, Australia.

Hewett, C. L., Cheng, Y.-B., Muddle, B. C., Trigg, M. B., (1998a) "Phase relationships and related microstructural observations in the Ca-Si-Al-O-N system", *J. Am. Ceram. Soc.*, **81**(8), 1781-1788.

Hewett, C. L., Cheng, Y.-B., Muddle, B. C., Trigg, M. B., (1998b) "Thermal stability of Calcium α-sialon ceramics", *J. Euro. Ceram. Soc.*, **18**, 417-427.

Himsolt, G., Knoch, H., Hueoner, H., Kleinlein, F. W., (1979) "Mechanical properties of hot-pressed silicon nitride with different grain structures", *J. Am. Ceram. Soc.*, **62**(1), 29-32.

Hirao, K., Ohashi, M., Brito, M. E., Kanzaki, S., (1995) "Processing strategy for producing highly anisotropic silicon nitride", *J. Am. Ceram. Soc.*, **78**(6), 1687-1690.

Hockey, B. J., Wiederhorn, S. M., Johnson, H., (1978) "Erosion of brittle materials by solid particle impact", in *Fracture Mechanics of Ceramics*, Vol. **3**, *Flows and Testing*, ed. R. C. Bradt, D. P. H. Hasselman and F. F. Lange, Plenum Press, New York, pp. 379-402.

Hoffmann, M. J., (1994a) "Analysis of microstructural development and mechanical properties of Si_3N_4 ceramics", in *Tailoring of Mechanical Properties of Si_3N_4 Ceramics*, ed. M. J. Hoffmann, G. Petzow, *NATO ASI Series, Series E: Applied Science*, **276**, Kluwer Academic Publishers, Dordrecht, The Netherlands, pp. 59-71.

Hoffmann, M. J., (1994b) "High-temperature properties of Yb-containing Si_3N_4", in *Tailoring of Mechanical Properties of Si_3N_4 Ceramics*, ed. M. J. Hoffmann, G. Petzow, *NATO ASI Series, Series E: Applied Science*, **276**, Kluwer Academic Publishers, Dordrecht, The Netherlands, pp. 233-244.

Huang, Z.-K., Sun, W.-Y., Yan, D.-S., (1985) "Phase relations of the Si_3N_4-AlN-CaO system", *J. Mater. Sci. Lett.*, **4**, 255-259.

Huang, Z.-K., Tien, T.-Y, Yan, T.-S., (1986) "Subsolidus phase relationship in Si_3N_4-AlN-rare earth oxide systems", *J. Am. Ceram. Soc.*, **69**(10), C241-242.

Huang, Z.-K., Yan, D.-S., (1992) "Phase relationships in Si_3N_4-AlN-M_xO_y systems and their implications for sialon fabrication", *J. Mater. Sci.*, **27**, 5640-5644.

Hunter, S. C., (1957) "Energy absorbed by elastic waves during impact", *J. Mech. Phys. Solids*, **5**, 162-171.

Hutchings, I. M., (1979) "Energy absorbed by elastic waves during plastic impact". *J. Phys. D: Appl. Phys.*, **12**, 1819-1824.

Hwang, C. J., Susintzky, D. W., Beaman, D. R., (1995) "Preparation of multication α-sialon containing strontium", *J. Am. Ceram. Soc.*, **78**(3), 588-592.

Jack, K. H., Wilson, W. I., (1972) "Ceramics based on the Si-Al-O-N and related systems", *Nature*, **238**, 28-29.

Jack, K. H., (1976) "Review – Sialons and related nitrogen ceramics", *J. Mater. Sci.*, **11**, 1135-1158.

Jack, K. H., (1983) "The characteristion of α-sialons and the α-β relationships in sialons and silicon nitrides", in *Progress in Nitrogen Ceramics*, ed. F. L. Riley, Martinus Nijhoff, The Hague, Netherlands, pp. 45-49.

Jack, K. H., (1986) "Sialons: a study in materials development", in *Non-oxide Technical and Engineering Ceramics*, ed. S. Hampshire, Elsevier.

Jack, K. H., (1987) "Silicon nitride, sialons and related ceramics", in *Ceramics and Civilization*, Vol. **3**, *High-Technology Ceramics – Past, Present, and Future*, Am. Ceram. Soc., pp.259-288.

Johansson, K. E., Palm, T., Werner, P.-E., (1980) "An automatic microdensitometer for X-ray powder diffraction photographs", *J. Phys. E.: Sci. Instrum.*, **13**, 1289-1291.

Karasek, K. R., Whalen, P. J., Rateick, R. G., Routbort, J. L., Hamilton, A. C., (1996) "Transient and steady-state erosion of in situ-reinforced Si_3N_4", *Tribology Transactions*, **39**, 374-379.

Kato, K., Inoue, Z., Kijimaja, K., Kawada, I., Tanaka, H., Yamane, T., (1975) "Structural approach to the problem of oxygen content in alpha silicon nitride", *J. Am. Ceram. Soc.*, **58**, 90-91.

Kelly, J. F., Lawn, B. R., Rodel, J., (1991) "In situ measurements of bridged crack interfaces in the scanning electron microscope", *J. Am. Ceram. Soc.*, **74**, 3154-3157.

Kessler, H., Kleebe, H.-J., Cannon, R. W., Pompe, W., (1992) "Influence of internal stresses on crystallization of intergranular phases in ceramics", *Acta metall. Mater.*, **40**(9), 2233-2245.

Kim, J., Rosenflanz, A., Chen, I.-W., (2000) "Microstructure control of in-situ-toughened α-sialon ceramics", *J. Am. Ceram. Soc.*, **83**(7), 1819-1821.

Kingery, W. D., (1959) "Densification during sintering in the presence of a liquid phase", *J. Appl. Phys.*, **30**, 301-306.

Kleebe, H.-J., Hoffmann, M. J., Rühle, M., (1992) "Influence of secondary phase chemistry on grain boundary film thickness in silicon nitride", *Z. Metallkd.*, **83**(8), 610-617.

Kleebe, H.-J., Pezzotti, G., Ziegler, G., (1999) "Microstructure and fracture toughness of Si_3N_4 ceramics: combined roles of grain morphology and secondary phase chemistry", *J. Am. Ceram. Soc.*, **82**(7), 1857-1867.

Knehans, R., Steinbrech, R. W., (1984) in *Science of ceramics*, ed. P. Vincenzini, **12**, Ceramurgia, Imoda, Italy, pp. 613-619.

Kosel, T. H., (1992) "Solid particle erosion", in *ASM Handbook*, Vol. **18**, *Friction, Lubrication and Wear Technology*, Mentals Park, Ohio, ASM International, pp. 199-213.

Kuang, S.-F., Huang, Z.-K., Sun, W.-Y., Yen, T.-S., (1990) "Phase relationships in the LiO_2-Si_3N_4-AlN system and the formation of lithium α-sialon", *J. Mater. Sci. Lett.*, **9**, 72-74.

Lamb, H., (1904) "On the propagation of tremors over the surface of an elastic solid", *Phil. Trans. R. Soc. Lond.*, A, **203**, 1-42.

Lancaster, J. K., Mashal, Y. A-H, Atkins, A. G., (1992) "The role of water in the wear of ceramics", *J. Phys. D: Appl. Phys.*, **25**, A205-A211.

Lange, F. F., (1973) "Relation between strength, fracture energy, and microstructure of hot-pressed silicon nitride", *J. Am. Ceram. Soc.*, **56**(10), 518-522.

Lange, F. F., (1979) "Fracture toughness of Si_3N_4 as a function of the initial α-phase content", *J. Am. Ceram. Soc.*, **62**(7-8), 428-430.

Lapides, L., Levy, A., (1980) "The halo effect in jet impingement solid particle erosion testing of ductile metals", *Wear*, **58**, 301-311.

Lathabai, S., Lawn, B., R., (1989) "Fatigue limits in noncyclic loading of ceramics with crack-resistance curves", *J. Mater. Sci.*, **24**, 4298-4306.

Lathabai, S., Pender, D. C., (1995) "Microstructural influence in slurry erosion of ceramics", *Wear*, **189**, 122-135.

Lathabai, S., (1995) "Erosion of ceramics", *Materials Forum*, **19**, 101-116.

Lathabai, S., (2000) "The effect of grain size on the slurry erosive wear of Ce-TZP ceramics", *Scripta mater.*, **43**, 465-470.

Lawn, B. R., Hockey, B. J., Wiederhorn, S. M., (1980) "Thermal effects in sharp-particle contact", *J. Am. Ceram. Soc.*, **63**(5-6), 356-358.

Lawn, B. R., (1993) *Fracture of brittle solids*, Cambridge University Press, Cambridge, UK.

Lee, W. E., Rainforth, W. M., (1994) *Ceramic microstructures, property control by processing*, Chapman & Hall, London, pp. 389-451.

Levin, E. M., Robbins, C. R., McMurdie, H. F., Reser, M. K. (eds.), (1964) *Phase diagrams for ceramists*, American Ceramic Society, Columbus, Ohio, pp. 219.

Levy, A. V., Yau, P., (1984) "Erosion of steels in liquid slurries", *Wear*, **98**, 163-182.

Levy, A. V., Jee, N., Yau, P., (1987) "Erosion of steels in coal-solvent slurries", *Wear*, **117**, 115-127.

Levy, A. V., Hickey, G., (1987) "Liquid-solid particle slurry erosion of steels", *Wear*, **117**, 129-146.

Lewis, M. H., Powell, B. D., Drew, P., Lumby, R. J., North, B., Taylor, A. J., (1977) "The formation of single phase sialon ceramics", *J. Mater. Sci.*, **12**, 61-74.

Lewis, M. H., Batti, A. R., Lumby, R. J., North, B., Taylor, A. J., (1980) "The microstructure of sintered Si-Al-O-N ceramics", *J. Mater. Sci.*, **15**, 103-113.

Lewis, M. H., Fung, R., Taplin, D. M. R., (1981) "Indentation plasticity and fracture of Si_3N_4 ceramic alloys", *J. Mater. Sci.*, **16**, 3437-3446.

Li, C. W., Yamanis, J., (1989) "Super-tough silicon nitride with R-curve behaviour", *Ceram. Eng. Sci. Proc.*, **10**(7-8), 632-645.

Li, C. W., Lee, D. J., Lui, S. C., (1992) "R-curve behavior and strength for in-situ reinforced silicon nitrides with different microstructures", *J. Am. Ceram. Soc.*, **75**(7), 1777-1785.

Li, Y.-W., Wang, P.-L., Chen, W.-W., Cheng, Y.-B., Yan, D.-S., (2000) "Phase formation and microstructural evolution of Ca α-sialon using different Si_3N_4 starting powders", *J. Euro. Ceram. Soc.*, **20**, 1803-1808.

Liu, D.-M, Lin, J.-T., Lee, R. R.-R, (1998) "Erosive wear behaviour in duophase sialon composites", *Ceram. Inter.*, **24**, 217-221.

Malecki, A., Gajerski, R., Labus, S., Prochowska-Klisch, B., Oblakowski, J., (1997) "Kinetics and mechanism of crystallization of gehlenite glass pure and doped with Co^{2+}, Eu^{3+}, Cr^{3+} and Th^{4+}", *J. Non-Cryst. Solids*, **212**, 55-58.

Mandal, H., Thompson, D. P., Ekström, T., (1993) "Reversible α-β sialon transformations in heat treated sialon ceramics", *J. Euro. Ceram. Soc.*, **12**, 421-429.

Mandal, H., Thompson, D. P., (1996) "CeO_2 doped α-sialon ceramics", *J. Mater. Sci. Lett.*, **15**, 1435.

Mandal, H., (1999) "New developments in α-sialon ceramics", *J. Euro. Ceram. Soc.*, **19**, 2349-2357.

Marrero, M., Routbort, J., Whalen, P., Li, C-W., Karasek, K. R., (1993) "Solid-particle erosion of *in situ* reinforced Si_3N_4", *Wear*, **162-164**, 280-284.

Marshall, D. B., Evans, A. G., Gulden, M. E., Routbort, J. L., Scattergood, R. O., (1981) "Particle size distribution effects on the solid particle erosion of brittle materials", *Wear*, **71**, 363-373.

McEntire, B. J., (1991) in *Ceramics and Glasses*, Engineered Materials Handbook, Vol.4 ASM International, pp.141.

Menon, M., Chen, I-W., (1995a) "Reaction densification of α-sialon: I, wetting behaviour and acid-base reactions", *J. Am. Ceram. Soc.*, **78**(3), 545-552.

Menon, M., Chen, I-W., (1995b) "Reaction densification of α-sialon: II, densification behaviour", *J. Am. Ceram. Soc.*, **78**(3), 553-559.

Michalske, T. A., Bunker, B. C., (1986) "Stress corrosion of ionic and mixed ionic/covalent solids", *J. Am. Ceram. Soc.*, **69**(10), 721-724.

Miller, G. F., Pursey, H., (1954) "The field and radiation impedance of mechanical radiators on the free surface of a semi-infinite isotropic solid", *Proc. R. Soc. Lond., Ser. A*, **223**, 521-541.

Miller, G. F., Pursey, H., (1956) "On the partition of energy between elastic waves in a semi-infinite solid", *Proc. R. Soc. Lond., Ser. A*, **223**, 55-69.

Miranda-Martinez, M., Davidge, R. W., Riley, F. L., (1994) "Grain size effects on the wet erosive wear of high-purity polycrystalline alumina", *Wear*, **172**, 41-48.

Mitomo, M., (1991) "Toughening of silicon nitride ceramics by microstructural control", in *Proc. Sci. Eng'g Ceram.*, eds. S. Kimura, K. Niihara, Ceram. Soc. Jpn. Tokyo, pp.101-107.

Moore, M. A., (1980) "Abrasive wear", in *Fundamentals of Friction and Wear of Materials*, ed. D. A. Rigney, *American Society for Metals*, Metals Park, Ohio 44073, pp. 73-118.

Mukhopadhyay, A. K., Mai, Y.-W., (1993) "Grain size effect on abrasive wear mechanisms in alumina ceramics", *Wear*, **162-164**, 258-268.

Mukhopadhyay, A. K., Chakraborty, D., Swain, M. V., Mai, Y.-W., (1997) "Scratch deformation behaviour of alumina under a sharp indenter", *J. Euro. Ceram. Soc.*, **17**, 91-100.

Murugesh, L., Scattergood, R. O., (1991) "Effect of erodent properties on the erosion of alumina", *J. Mater. Sci.*, **26**, 5456-5466.

Murugesh, L., Srinivasan, S., Scattergood, R. O., (1991) "Models and material properties for erosion of ceramics", *J. Mater. Eng.*, **13**, 55-61.

Mutton, P. J., (1988) "Abrasion resistant materials for the Australian Minerals Industry", report number MRL/CI4/88/001, May, BHP Melbourne Research Laboratories.

Niihara, K., (1983) "A fracture mechanics analysis of indentation-induced palmqvist crack in ceramics", *J. Mater. Sci. Lett.*, **2**, 221-223.

North, B., Lumby, R. J., Taylor, A. J., (1980) "A method of forming a ceramic product", British Pat. No. 1 573 299, Aug. 20.

Oka, Y. I., Ohnogi, H., Hosokawa, T., Matsumura, M., (1997) "The impact angle dependence of erosion damage caused by solid particle impact" *Wear*, **203-204**, 573-579.

Oyama, Y., Kamigaito, O., (1971) "Solid solubility of some oxides in Si_3N_4", *Jpn. J. Appl. Phys.* **10**, 1637-1642.

Oyama, Y., (1972) "Solid solution in the ternary system Si_3N_4-AlN-Al_2O_3". *Jpn. J. Appl. Phys.* **11**, 760-761.

Park, D.-S., Han, B.-D., Lim, D.-S., Yeo, I.-W., (1997) "A study on wear and erosion of sialon-Si_3N_4 whisker ceramic composites", *Wear*, **203-204**, 284-290.

Petzow, G., Kaysser, W. A., (1990) "Basic mechanisms of liquid phase sintering", in *Sintering key papers*, ed. S. Somiya, Y. Moriyoshi, Elsevier Science Publishers, Essex, England, pp. 595-614.

Pezzotti, G., Kleebe, H.-J., (1999) "Effect of residual microstresses at crystalline multigrain junctions on the toughness of silicon nitride", *J. Euro. Ceram. Soc.*, **19**, 451-455.

Pompe, W., Kessler, H., (1994) "Internal stress in silicon nitride and their influence on mechanical behaviour", in *Tailoring of Mechanical Properties of Si_3N_4 Ceramics*, ed. M. J. Hoffmann, G. Petzow, *NATO ASI Series, Series E: Applied Science*, **276**, Kluwer Academic Publishers, Dordrecht, The Netherlands, pp. 353-364.

Reed, J. S., Runk, R. B., (1976) "Ceramic fabrication processing", in *Treatise on Materials Science and Technology*, Vol. **9**, ed. F. F. Y. Wang, Academic Press, New York, pp. 71.

Reed, J. S., (1988) in *Introduction to the Principles of Ceramic Processing*. John Wiley & Sons, New York, pp. 329.

Reynolds, O., (1873) "On the action of a blast of sand in cutting hard materials", *Philos. Mag.*, **46**, 337-343.

Riley, F. L., (2000) "Silicon nitride and related materials", *J. Am. Ceram. Soc.*, **83**(2), 245-265.

Ritter, J. E., Strzepa, P., Jakus, K., Rosenfeld, L., Buckman, K. J., (1984) "Erosion damage in glass and alumina", *J. Am. Ceram. Soc.*, **67**, 769-774.

Ritter, J. E., (1985) "Erosion damage in structural ceramics", *Mater. Sci. Eng.*, **71**, 195-201.

Ritter, J. E., Rosenfeld, L., Jakus, K., (1986) "Erosion and strength degradation in alumina", *Wear*, **111**, 335-346.

Ritter, J. E., Choi, S. R., Jakus, K., Whalen, P. J., Rateick, Jr. R. G., (1991) "Effect of microstructure on the erosion and impact damage of sintered silicon nitride", *J. Mater. Sci.*, **26**, 5543-5546.

Roberts, N. F., Hutchings, I. M., (1989) "Erosion of polycrystalline alumina by solid particle impact", in *Proc. 5th Int. Congr. On Tribology, Eurotrib '89*, ed. K. Holmberg and I. Nieminen, **3**, 307-315.

Rowcliffe, D. J., (1992) "Quasi-static indentation of ceramics", in *Erosion of ceramic materials*, ed. J. E. Ritter. Trans. Tech. Publications, Switzerland, pp. 1-22.

Rosenflanz, A., (1999) "Silicon nitride and sialon ceramics", *Current Opinion in Solid State and Materials Science*, **4**, 453-459.

Routbort, J. L., Scattergood, R. O., Kay, E. W., (1980a) "Erosion of silicon single crystals", *J. Am. Ceram. Soc.*, **63**(11-12), 635-640.

Routbort, J. L., Scattergood, R. O., Turner, A. P. L., (1980b) "The erosion of reaction-bonded SiC", *Wear*, **59**, 363-375.

Routbort, J. L., Scattergood, R. O., (1980) "Anomalous solid-particle erosion rate of hot-pressed silicon carbide", *J. Am. Ceram. Soc.*, **63**, 593-595.

Routbort, J. L., Scattergood, R. O., (1992) "Solid particle erosion of ceramics and ceramic composites", in *Erosion of ceramic materials*, ed. J. E. Ritter. Trans. Tech. Publications, Switzerland, pp. 23-50.

Routbort, J. L., (1996) "Degradation of structural ceramics by erosion", *J. Nondestructive Evaluation*, **15**(3/4), 107-112.

Rowcliffe, D. J., (1992) "Quasi-static indentation of ceramics", in *Erosion of ceramic materials*, ed. J. E. Ritter. Trans. Tech. Publications, Switzerland, pp. 1-22.

Ruff, A. W., Ives, L. K., (1975) "Measurement of solid particle velocity in erosive wear", *Wear*, **35**, 195-199.

Scattergood, R. O., Routbort, J. L., (1981) "Velocity and size dependences of the erosion rate in silicon", *Wear*, **67**, 227-232.

Scattergood, R. O., Routbort, J. L., (1983) "Velocity exponent in solid-particle erosion of silicon", *J. Am. Ceram. Soc.*, **66**, C184-C186.

Sheldon, G. L., Finnie, I., (1966a) "On the ductile behaviour of nominally brittle materials during erosive cutting", *Trans. ASME*, **88B**, 387-392.

Sheldon, G. L., Finnie, I., (1966b) "The mechanism of material removal in the erosive cutting of brittle materials", *Trans. ASME*, **88B**, 393.

Shen, Z., Ekström, T., Nygren, M., (1996) "Temperature stability of samarium doped α-sialon ceramics", *J. Euro. Ceram. Soc.*, **16**, 43-53.

Shen, Z. J., Nordberg, L.-O., Nygren, M., Ekström, T., (1997) "α-sialon grains with high aspect ratio - utopia or reality?", in *NATO AST Engineering Ceramics'96 - Higher reliability through processing*, ed. Babini, G. N., Kluwer Academic Publishers, Dordrecht, The Netherlands, pp. 169-178.

Shetty, D. K., Wright, I. G., Clauer, A. H., (1982) "Coal slurry erosion of reaction-bonded SiC", *Wear*, **79**, 275-279.

Sheu, T.-S., (1994) "Microstructure and mechanical properties of the *in situ* β-Si_3N_4/α-sialon composite", *J. Am. Ceram. Soc.*, **77**(9), 2345-2353.

Shipway, P. H., Hutchings, I. M., (1991) "The influence of particle properties on the erosive wear of sintered boron carbide", *Wear*, **149**, 85-98.

Shipway, P. H., Hutchings, I. M., (1996) "The role of particle properties in the erosion of brittle materials", *Wear*, **193**, 105-113.

Shipway, P. H., (1997) "The effect of plume divergence on the spatial distribution and magnitude of wear in gas-blast erosion", *Wear*, **205**, 169-177.

Slasor, S., Thompson, D. P., Ekström, T., (1991) "Comment on phase relations in the Si_3N_4-rich portion of the Si_3N_4-AlN-Al_2O_3-Y_2O_3 system", *J. Am. Ceram. Soc.*, **74**(3), 686-687.

Slikkerveer, P. J., Bouten, P. C. P., in't Veld, F. H., Scholten, H., (1998) "Erosion and damage by sharp particles", *Wear*, **217**, 237-250.

Sparks, A. J., Hutchings, I. M., (1993) "Effects of erodent recycling in solid particle erosion testing", *Wear*, **162-164**, 139-147.

Srinivasan, S., Scattergood, R. O., (1987) "On lateral cracks in glass", *J. Mater. Sci.*, **22**, 3463-3469.

Srinivasan, S., Scattergood, R. O., (1988a) "Effect of erodent hardness on erosion of brittle materials" *Wear*, **128**, 139-152.

Srinivasan, S., Scattergood, R. O., (1988b) "Erosion of Mg-PSZ by solid particle impact", *Adv. Ceram. Mater.*, 3(4), 345-352.

Srinivasan, S., Scattergood, R. O., (1991) "*R* curve effects in solid particle erosion of ceramics" *Wear*, **142**, 115-133.

Steinbrech, R. W., Reichl, A., Schaarwächter, W., (1990) "*R*-curve behaviour of long cracks in alumina", *J. Am. Ceram. Soc.*, **73**, 2009-2015.

Sun, E. Y., Becher, P. F., Plucknett, K. P., Hsueh, C.-H., Alexander, K., B., Waters, S. B., Hirao, K., Brito, M. E., (1998) "Microstructural design of silicon nitride with improved fracture toughness: II, Effects of yttria and alumina additives", *J. Am. Ceram. Soc.*, **81**(11), 2831-2840.

Swain, M., (1994) *Structure and properties of ceramics*, VCH, Weinheim, Germany.

Ta, W., Cheng, Y.-B., Muddle, B., Hewett, C., Trigg, M., (2000) "Pressureless sintering of calcium alpha sialons", *Mater. Sci. Forum*, **325-326**, 199-206.

Tajima, Y., Urashima, K., (1994) "Improvement of strength and toughness of silicon nitride ceramics", in *Tailoring of Mechanical Properties of Si₃N₄ Ceramics*, ed. M. J. Hoffmann, G. Petzow, *NATO ASI Series, Series E: Applied Science*, **276**, Kluwer Academic Publishers, Dordrecht, The Netherlands, pp. 101-109.

Tanaka, I., Kleebe, H.-J., Cinibulk, M. K., Bruley, J., Clarke, D. R., Rühle, M., (1994) "Calcium concentration dependence of the intergranular film thickness in silicon nitride", *J. Am. Ceram. Soc.*, **77**(4), 911-914.

Thompson, D. P., (1977) "The crystal structures of 8H and 15R sialon polytypoids", in *Nitrogen Ceramics*, ed. F. L. Riley, Leyden, Noordhoof, pp. 129-135.

Thompson, D. P., Korgue, P., Hendry, A., (1983) "The structural characterisation of sialon polytypoids", in *Progress in Nitrogen Ceramics*, ed. F. L. Riley, Martinus Nijhoff, The Hague, Netherlands, pp. 61-74.

Thompson, D. P., (1988) Powder diffraction file JCPDS-ICDD, 33-261 (Joint Committee on Powder Diffraction Standards, Swarthmore, Pennsylvania).

Thompson, D. P., (1989) "The crystal chemistry of nitrogen ceramics", in *Materials Science Forum* **47**, ed. G. E. Murch (Editor-in-Chief), pp. 21-42.

Turenne, S., Fiset, M., Masounave, J., (1989) "The effect of sand concentration on the erosion of materials by a slurry jet", *Wear*, **133**, 95-106.

Turkdogan, E. T., Bills, P. M., Tippett, V. A., (1958) "Silicon nitrides: some physico-chemical properties", *J. Appl. Chem.*, **8**, 296-302.

van den Berg, P. H. J., de With, G., (1993) "Strength and residual stress of Mg-PSZ after grinding", *Wear*, **160**, 301-308.

van Rutten, J. W. T., Hintzen, H. T., Metselaar, R., (1996) "Phase formation of Ca-α-sialon by reaction sintering", *J. Euro. Ceram. Soc.*, **16**, 995-999.

van Tendeloo, G., Faber, K. T., Thomas, G., (1983) "Characterisation of AlN ceramics containing long-period polytypes", *J. Mater. Sci.*, **18**, 525-532.

Vetrano, J. S., Kleebe, H.-J., Hampp, E., Hoffmann, M. J., Cannon, R. M., (1992) "Epitaxial deposition of silicon nitride during post-sintering heat treatment", *J. Mater. Sci. Lett.*, **11**, 1249-1252.

Wada, S., Watanabe. N., (1986) *Yogyo-Kyokai-Shi*, **94**, 1157-1162.

Wada, S., Watanabe. N., (1987a) "Solid particle erosion of brittle materials (Part 4) – The erosive wear of thirteen kinds of commercial Al_2O_3 ceramic materials", *J. Ceram. Soc. Jpn. Inter. Ed.*, **95**(783-787), 783-787.

Wada, S., Watanabe. N., (1987b) "Solid particle erosion in brittle materials (Part 3) – The interaction with material properties of target and that of impingement particle on erosive wear mechanism", *Yogyo-Kyokai-Shi*, **95**, 573-578.

Wada, S., (1992) "Effects of hardness and fracture toughness of target materials and impact particles on erosion of ceramic materials", in *Erosion of ceramic materials*, ed. J. E. Ritter. Trans. Tech. Publications, Switzerland, pp. 51-74.

Wang, H., Cheng, Y.-B., Muddle, B. C., Gao, L., Yen, T. S, (1996a) "Preferred orientation in hot-pressed Ca α-SIALON ceramics", *Mater. Lett.*, **15**, 1447-1449.

Wang, P. L., Tu, H. Y., Wang, H., Sun, W. Y., Yan, D. S, (1996b) "Compositional design of α-β-YAG($Y_3Al_5O_{12}$) multiphase sialon ceramics", *Mater. Lett.*, **28**, 373-378.

Wang, L. L., Tien, T.-Y., Chen, I.-W., (1998) "Morphology of silicon nitride grown from a liquid phase", *J. Am. Ceram. Soc.*, 81(10), 2677-2686.

Wang, P. L., Zhang, C., Sun, W. Y., Yan, D. S., (1999a) "Characteristics of Ca-α-sialon-phase formation, microstructure and mechanical properties", *J. Euro. Ceram. Soc.*, **19**, 553-560.

Wang, P. L., Sun, W. Y., Yan, D. S, (1999b) "Mechanical properties of AlN-polytypoids – 15R, 12H and 21R", *Mater. Sci. Eng.*, **A272**, 351-356.

Wang, Y., Hsu, S. M., (1996) "Wear and wear transition mechanisms of ceramics", *Wear*, **195**, 112-122.

Weimer, A. W., (1997) *Carbide, nitride and boride materials synthesis and processing*, Chapman & Hall, London, pp. 159-164.

Werner, P.-E., (1969) "A fortran program for least-square refinement of crystal structure cell dimension", *Arkiv fur Kemi.*, **31**, 513-516.

Weiss, J., Lukas, H. L., (1989) "Calculated phase equilibria in silicon nitride systems", in *Materials Science Forum 47*, ed. G. E. Murch (Editor-in-Chief), pp. 43-57.

Werner, P.-E., (1969) "A fortran program for least-square refinement of crystal structure cell dimension", *Arkiv fur Kemi.*, **31**, 513-516.

Whitney, E. D., (1965) "Kinetics and mechanism of the transition of metastable tetragonal to monoclinic zirconia", *Trans. Faraday Soc.* **61**(513), 1991-2000.

Wiederhorn, S. M., Lawn, B. R., (1979) "Strength degradation of glass impacted with sharp particles: I, Annealed surfaces", *J. Am. Ceram. Soc.*, **62**(1-2), 66-70.

Wiederhorn, S. M., Hockey, B. J., (1983) "Effect of material parameters on the erosion resistance of brittle materials", *J. Mater. Sci.*, **18**, 766-780.

Wild, S., Grieveson, P., Jack, K. H., (1972) "The crystal structures of alpha and beta silicon and germanium nitrides", in *Special ceramics 5*, ed. P., Popper, British Ceramic Research Association, England, pp. 385-395.

Wood, C. A., Zhao, H., Cheng, Y.-B., (1999) "Microstructural development of calcium α-sialon ceramics with elongated grains", *J. Am. Ceram. Soc.*, **82**(2), 421-428.

Wood, C. A., Cheng, Y.-B., (2000) "Phase relationships and microstructures of Ca and Al-rich α-sialon ceramics", *J. Euro. Ceram. Soc.*, **20**, 357-366.

Wurst, J. C., Nelson, J. A., (1972) "Lineal intercept technique for measuring grain size in two-phase polycrystalline ceramics", *J. Am. Ceram. Soc.-Discussions and Notes*, 109.

Wyckoff, R. W. G., (1968) *Crystal Structures Vol 4*. Interscience.

Xu, H. H. K., Padture, N. P., Jahanmir, S., (1995) "Effect of microstructure on material-removal mechanisms and damage tolerance in abrasive machining of silicon carbide", *J. Am. Ceram. Soc.*, **78**(9), 2443-2448.

Xu, H. H. K., Jahanmir, S., Ives, L. K., Job, L. S., Ritchie, K. T., (1996) "Short-crack toughness and abrasive machining of silicon nitride", *J. Am. Ceram. Soc.*, **79**(12), 3055-3064.

Yen, T. S., (1994) "High performance silicon nitride composite ceramics through grain boundary and microstructural tailoring", in *Tailoring of Mechanical Properties of Si₃N₄ Ceramics*, ed. M. J. Hoffmann, G. Petzow, *NATO ASI Series, Series E: Applied Science*, **276**, Kluwer Academic Publishers, Dordrecht, The Netherlands, pp. 137-148.

Young, T., (1807) *A course of lectures on natural philosophy and the mechanical arts*, Printed for J. Johnson.

Yust, C. S., Crouse, R., S., (1978) "Melting at particle impact sites during erosion of ceramics", *Wear*, **51**, 193-196.

Zenotchkine, M., Shuba, R., Kim, J. S., Chen, I.-W., (2001) "R-curve behaviour of in situ toughened α-sialon ceramics", *J. Am. Ceram. Soc.*, **84**(4), 884-886.

Zerr, A., Miehe, G., Serghiou, G., Schwarz, M., Kroke, E., Riedel, R., FueB, H., Kroll, P., Boehler, R., (1999) "Synthesis of cubic silicon nitride", *Nature*, **400**, 340-342.

Zhan, G.-D., Mitomo, M., Nishimura, T., Xie, R.-J., Sakuma, T., Ikuhara, Y., (2000) "Superplastic behaviour of fine-grained β-silicon nitride material under compression", *J. Am. Ceram. Soc.*, **83**(4), 841-847.

Zhang, C., Narimatsu, E., Komeya, K., Tatami, J., Meguro, T., (2000a) "Control of grain morphology in Ca-α sialon ceramics by changing the heating rate", *Mater. Lett.*, **43**, 315-319.

Zhang, Y., Cheng, Y.-B., Lathabai, S., (2000b) "Erosion of alumina ceramics by air- and water-suspended garnet particles", *Wear*, **240**, 40-51.

Zhang, Y., Cheng, Y.-B., Lathabai, S., (2001a) "Influence of microstructure on the erosive wear behaviour of Ca α-sialon materials", *J. Euro. Ceram. Soc.*, **21**, 2435-2445.

Zhang, Y., Cheng, Y.-B., Lathabai, S., (2001b) "Erosion behaviour of advanced ceramics", *J. Aust. Ceram. Soc.*, **37**(1), 39-44.

Zhao, H., Swenser, S. P., Cheng, Y.-B., (1997) "Elongated α-sialon grains in pressureless sintered sialon ceramics", *J. Euro. Ceram. Soc.*, **18**, 1053-1057.

Zhou, J., Bahadur, S., (1991) "The effect of material composition and operational variables on the erosion of alumina ceramics", *Wear*, **150**, 343-354.

Zhou, J., Bahadur, S., (1993) "SEM studies of material damage in alumina ceramics by angular single and multiple particle impacts", *Wear*, **162-164**, 285-295.

Zhou, J., Bahadur, S., (1995) "Erosion characteristics of alumina ceramics at high temperatures", *Wear*, **181-183**, 178-188.

Zu, J. B., Hutchings, I. M., Burstein, G. T., (1990) "Design of a slurry erosion test rig", *Wear*, **140**, 331-344.

Zu, J. B., Burstein, G. T., Hutchings, I. M., (1991) "A comparative study of the slurry erosion and free-fall particle erosion of alumina", *Wear*, **149**, 73-84.